

AO-AU92 545

AIR FORCE INST OF TECH WRIGHT-PATTERSON AFB OH
RELATIVISTIC ELECTRON PRECIPITATION: AN OBSERVATIONAL STUDY. (U)
1980 L J. ANDREOLI
AFIT-CI-80-260

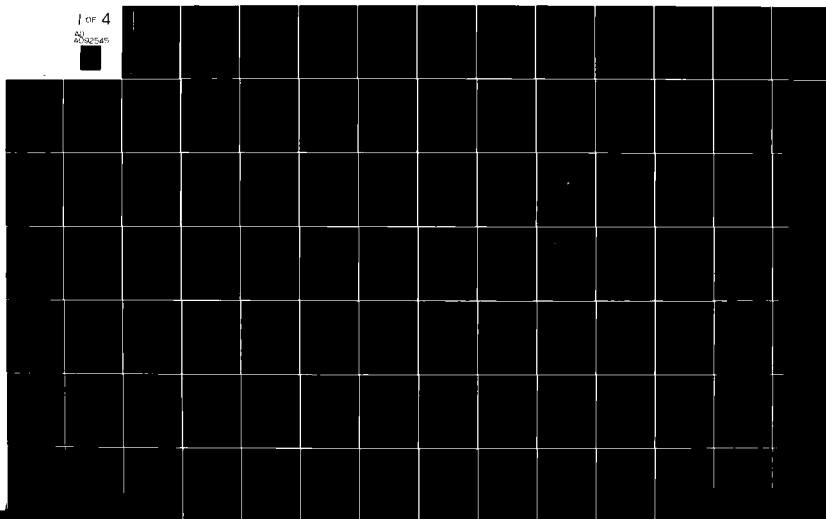
F/G 4/1

UNCLASSIFIED

NL

1 of 4

20250505



AD A092545

200 FILE COPY

14 UNCLASS		118211	
SECURITY CLASSIFICATION OF THIS PAGE (When Data Entered)		READ INSTRUCTIONS BEFORE COMPLETING FORM	
AFIT CI-REPORT DOCUMENTATION PAGE			
1. REPORT NUMBER	2. GOVT ACCESSION NO	3. RECIPIENT'S CATALOG NUMBER	
80-26D	AD A092545		
4. TITLE (and Subtitle)		5. TYPE OF REPORT & PERIOD COVERED	
Relativistic Electron Precipitation: An Observational Study		THESIS/DISSERTATION	
6. AUTHOR(s)		7. PERFORMING ORG. REPORT NUMBER	
Leopold Joseph Andreoli			
8. CONTRACT OR GRANT NUMBER(s)		9. PERFORMING ORGANIZATION NAME AND ADDRESS	
G Doctoral thesis		AFIT STUDENT AT: University of California, L.A.	
10. CONTROLLING OFFICE NAME AND ADDRESS		11. REPORT DATE	
AFIT/NR WPAFB OH 45433		1980	
12. MONITORING AGENCY NAME & ADDRESS (if different from Controlling Office)		13. NUMBER OF PAGES	
13 322		279	
14. DISTRIBUTION STATEMENT (of this Report)		15. SECURITY CLASS. (of this report)	
APPROVED FOR PUBLIC RELEASE; DISTRIBUTION UNLIMITED		UNCLASS	
16. DISTRIBUTION STATEMENT (of the abstract entered in Block 20, if different from Report)		15a. DECLASSIFICATION/DOWNGRADING SCHEDULE	
17. SUPPLEMENTARY NOTES		DTIC ELECTE DEC 08 1980 E	
APPROVED FOR PUBLIC RELEASE: IAW AFR 190-17 FREDRIC C. LYNCH, Major USAF Director of Public Affairs		Air Force Institute of Technology (ATC) Wright-Patterson AFB, OH 45433	
18. KEY WORDS (Continue on reverse side if necessary and identify by block number)			
19. ABSTRACT (Continue on reverse side if necessary and identify by block number)			
ATTACHED			

DD FORM 1 JAN 73 1473 EDITION OF 1 NOV 68 IS OBSOLETE

UNCLASS
SECURITY CLASSIFICATION OF THIS PAGE (When Data Entered)

012200

UNIVERSITY OF CALIFORNIA

Los Angeles

Relativistic Electron Precipitation:
An Observational Study

A dissertation submitted in partial satisfaction
of the requirements for the degree Doctor of Philosophy
in Atmospheric Sciences

by

Leopold Joseph Andreoli

1980

Accession For	
NTIS GRA&I	<input checked="checked" type="checkbox"/>
DDC TAB	<input type="checkbox"/>
Unannounced	<input type="checkbox"/>
Justification	
By	
Distribution/	
Availability Codes	
Dist	Avail and/or special
A	

© Copyright by
Leopold Joseph Andreoli
1980

The dissertation of Leopold Joseph Andreoli is approved.

Charles F. Kennel
Charles F. Kennel

Margaret G. Kivelson
Margaret G. Kivelson

George L. Siscoe
George L. Siscoe

S. V. Venkateswaran
S. V. Venkateswaran

Richard M. Thorne
Richard M. Thorne, Committee Chairman

UNIVERSITY OF CALIFORNIA, LOS ANGELES

1980

Dedicated to Kathleen, David, Michael and Donna.

TABLE OF CONTENTS

	Page
List of Tables	vi
List of Figures	viii
Acknowledgments	xix
Vita	xx
Abstract	xxi
Introduction	1
Chapter 1. Event Morphology	22
1.1 Results	22
1.2 Frequency of Occurrence and Magnetic Dependence	22
1.3 Local Time Dependence and Latitudinal Extent	36
1.4 Longitudinal Extent	44
1.5 REP - Proton Precipitation Correlation	44
1.6 Classification of REP Events	45
Chapter 2. Theory and Case Studies	53
2.1 Background	53
2.2 Resonant Populations	61
2.2.1 Whistler Mode Chorus	62
2.2.2 Electromagnetic Ion Cyclotron (EMIC) Waves	64
2.2.3 Electrostatic Ion Cyclotron (ESIC) Waves	67
2.3 Wave Amplitudes	72
2.3.1 Electromagnetic Waves	73
2.3.2 Electrostatic Amplitudes	75
2.4 Case Studies	77

	Page
2.4.1 Case 1, ESIC (rev 479, day 250, 6 SEP 1976).	77
2.4.2 Case 2, EMIC (rev 2484, day 132, 12 MAY 1977).	109
2.4.3 Case 3, Chorus (rev 1413, day 366, 31 DEC 1976).	123
Chapter 3. Atmospheric Consequences	130
3.1 Introduction and Background	130
3.2 REP Energy Spectra and Atmospheric Energy Deposition	132
3.3 REP Induced Hydrogen and Ozone Modifications	135
Chapter 4. Summary, Conclusions and Outlook	150
Appendix A OVI-19 Data Set and Analysis	154
Appendix B S3-3 Data Collection	199
Appendix C REP Event Identification and Catalog Use	226
Appendix D Computation of Electron and X-ray Energy Deposition Profiles	265
Bibliography	286

LIST OF TABLES

	Page
Table 2.1	Theoretical REP mechanisms and characteristics. 78
Table A-1	Low Energy Magnetic Spectrometer Channels, Energy, and Geometric Factors. 157
Table A-2	High Energy Magnetic Spectrometer Channels, Energy, and Geometric Factors. 159
Table B-1	S3-3 Scientific payloads with prime investigators in parenthesis. 204
Table B-2	S3-3 HEMS/LEMS Data Format. 211
Table C-1	Listing of individual microfiche by Readout REV NO (Station and Number), DATE OF REV (Last Digit of Yr, Month, Day), Beginning and Ending TIME OF REV IN SECS (Seconds), Precip Category ($1 \leq 235$ keV, $2 \leq 435$ keV, $3 \leq 655$ keV, $4 \leq 850$ keV), COMMENTS (12 = 12 keV electron channel, etc.; 80, 150 = 80, 150 keV Proton Channel, etc., L = L value). 234
Table C-2	Revs with strong precipitation ≥ 235 keV electrons by EVENT (one or more consecutive revs with strong precipitation), DATE (last digit of year, month, day), Readout REV (first letter of station, number), LAT (North, degrees), East LONG (degrees), L-VAL, MLT (hrs), $j(e/cm^2 s str keV)$ = differential flux value

of precipitating electrons from 235 keV to highest energy channel at which strong precipitation occurred, $J(p/cm^2 s \text{ str}) = \text{integral flux of strong diffusion precipitation of protons per energy channel if any, } 80 p^+$
 L-VAL = L value of 80 keV proton precipitation if any, strong precip 12, 33, L-VAL = check if 12, 33 keV electron channels had strong precip and L value of 12 keV channel
 UT (sec) = time at which 235 keV electron precip occurred.

251

Table D-1 Nomenclature (Spjeldvik, 1974). 256

Table D-2 Energy deposition function for Bremsstrahlung, for the case of uniform wide-area precipitation of an electron flux isotropic over the downward hemisphere. The quantity given is $A_{BR} (Z_m/T_o)$, in units of $cm^2 gm^{-1}$. Number in parenthesis indicates powers of ten. (Berger, Seltzer, Maeda, 1974). 269

Table D-3 $B_r(\text{keV/cm, column})$, stopping ratio, versus altitude for given incident electron energies. 274

Table D-4 Bremsstrahlung deposition computer listing. 279

LIST OF FIGURES

		Page
Figure 1	Illustration of one-hop skywave propagation via the ionosphere	2
Figure 2	Atmospheric penetration depths for protons and electrons assuming vertical incidence (adopted from <u>Aikin and Bauer, 1965</u>).	6
Figure 3	Time sequence of (A) HF absorption (dark shaded area) in Alaska; (b) VLF phase advance (shaded) from normal nighttime trace (dashed line); (c) AE index for 13-14 March 1969 from <u>Thorne and Larsen, 1976</u> .	11
Figure 4	Latitude-local time plot of all 425 keV electron spike observations from <u>Brown and Stone, 1972</u> .	16
Figure 5	Differential energy spectra of precipitating electrons of the following types: (A) Diffuse aurora (<u>Lui et al., 1977</u>); (B) Discrete aurora (<u>Lui et al., 1977</u>); (C) Balloon X-ray (<u>Bailey et al., 1970</u>); (D) Rocket (<u>Matthews and Simons, 1973</u>); (E) Satellite (<u>Larsen and Thomas, 1974</u>); (F) Satellite (<u>Vampola, 1971</u>).	18

Figure 1.1a,b,c	Daily values from 11 July 1976 to 29 September 1977. Plots are given of REPs with highest energy channel exhibiting strong diffusion (Panel A); the total number of outer zone passings, $L=4-8$ (Panel B); daily mean of the hourly Dst, γ (Panel C); A_p , equivalent daily planetary magnetic index, 2γ (Panel D).	23
Figure 1.2	Monthly REP event percentage of occurrence normalized to outer zone coverage for July 1976-September 1977.	28
Figure 1.3	Monthly percentage of REPs normalized to outer zone crossings ($L=4-8$) for magnetic conditions: $A_p > 30$ (Panel A); $20 \leq A_p < 30$ (Panel B); $10 \leq A_p < 20$ (Panel C); $A_p < 10$ (Panel D). Values for JAN and FEB in Panel A and $P=0.86$ and 0.39 for JAN and FEB respectively in Panel B.	30
Figure 1.4	REP event percentage of occurrence normalized to outer zone coverage ($L=4-8$) versus magnetic conditions for all months JUL 1976-SEP 1977. Total number of outer zone passes for each category are in parentheses.	32

		Page
Figure 1.5	Seven 2 day periods of AE index (γ) throughout 1977 with REPs indicated by arrows (\uparrow) and hours of noncoverage by shaded horizontal bar (\blacksquare). AE = AU (Upper Trace) - AL (Lower Trace).	34
Figure 1.6	REPs by date versus MLT (hrs). Hatched area indicates regions of coverage ($4 \leq L \leq 8$) around the local time of the orbit plane (skewed solid line).	37
Figure 1.7	Ratio of day (MLT 06-18) to night (MLT 18-06) for varying magnetic conditions.	40
Figure 1.8	REPs displayed by invariant latitude (degrees) versus MLT (hrs) for varying magnetic conditions. Lines indicate excursions of events in invariant latitude.	42
Figure 1.9	Flux versus UT plot of 12, 33, 235 keV electrons 80 keV protons for rev 1656 30 Jan 1977.	46
Figure 1.10	Percentage of revs (1-4 outer zone passes) with strong e^- or p^+ precipitation normalized to revs number by magnetic conditions.	48
Figure 1.11	REP events displayed according to invariant latitude and MLT for the following classes: dots and lines (.) for strong precipitation at energies ≤ 1 MeV with concurrent	

	proton precipitation; squares (\square) for strong precipitation at energies ≥ 1 MeV with concurrent proton precipitation; and circles (o) for strong precipitation at energies $\ll 1$ MeV without concurrent proton precipitation.	51
Figure 2.1	Velocity space surfaces for resonance with a wave of frequency ω and parallel refractive index $\mu_{ }$ for γ_{\perp} versus $\gamma_{ }$.	55
Figure 2.2	Minimum wave amplitudes required for electron strong diffusion scattering at $L=7$ versus electron energy for electron thermal energies 0.1, 1, 10 keV (Lyons, 1974).	59
Figure 2.3	Electron and proton resonant energies for the whistler mode chorus mechanism ($.1 \leq \frac{\omega}{\Omega_-} \leq .5$) [in keV] versus L for $N=10^4 \text{ cm}^{-3}$ for $L=4$ and $N=1, 10 \text{ cm}^{-3}$ for $L \geq 5$.	65
Figure 2.4	Resonant electron energies versus L for the ion cyclotron ($\frac{\omega}{\Omega_+} = 0.5$) wave mechanism for densities $N=1, 10 \text{ cm}^{-3}$ outside the plasma-sphere and $N=10^3 \text{ cm}^{-3}$ $L=4$ (Thorne and Kennel, 1971).	68
Figure 2.5a	Flux (counts/sec, every fourth data point) versus L value of low altitude (700 km) outer zone pass near local evening. Vertical arrows	

		Page
	(+) indicate singular precipitation and horizontal arrows (\rightarrow \leftarrow) indicate limits of extended precipitation.	81
Figure 2.5b	Same plots for high altitude (8000 km) passes at local dusk.	83
Figure 2.5c	Same for medium altitude (5000 km) passes at local morning.	85
Figure 2.6	Pitch angle versus flux (counts/sec) for 235-1610 keV electron channels for 3 times in the local evening outer zone of rev 479. The upward loss cone (L.C. = 50°) is indicated by the vertical line.	87
Figure 2.7	Enlargement of portions of Figure 2.5a.	90
Figure 2.8a	Spectrogram of plasma waves, 235 keV electrons, low energy electrons, low energy protons, 80 keV protons for the low altitude local evening pass.	92
Figure 2.8b	Same for the high altitude local dusk pass.	95
Figure 2.9	Kiruna raw magnetogram for 4-6 September 1976.	97
Figure 2.10	ATS-6 for 6 September 1976. Arrows indicate beginning and ending of event.	99
Figure 2.11	S3-2 (1,2,3) and S3-3 satellite (a,b,c) tracks for 6 September 1976 in invariant latitude versus MLT.	101

		Page
Figure 2.12a	S3-2 flux versus time plots of pass 1, Figure 2.11. Arrows indicate precipitation.	103
Figure 2.12b	Same for pass 2, Figure 2.11.	105
Figure 2.12c	Same for pass 3, Figure 2.11.	107
Figure 2.13a	Flux versus time plots of electrons for local evening pass of 12 May 1977.	110
Figure 2.13b	Same for higher energy electrons and protons.	112
Figure 2.14	Pitch angle versus flux plots for electrons with energies 160-1600 keV for 12 May 1977.	114
Figure 2.15	Spectrogram for 12 May 1977	116
Figure 2.16	Plasmapause relation to rev 2484, 12 May 1977 based on rough estimates.	119
Figure 2.17	ATS-6 for 12 May 1977.	121
Figure 2.18	Flux versus time plots for 31 December 1977. Arrows indicate strong diffusion precipitation.	124
Figure 2.19	Pitch angle distributions for 33, 235, 435 keV electron channels for 31 December 1976.	126
Figure 2.20	Spectrogram for low altitude early morning pass on 31 December 1976.	128
Figure 3.1	Energy spectra for cases 2,3 of Chapter 2.	133
Figure 3.2	Ion pair production rate versus altitude for ESIC, EMIC, and chorus events.	136
Figure 3.3	Altitude profile of the odd hydrogen formation rate related to ion pair production.	138

	Page
Figure 3.4a,b,c Ozone and hydroxyl concentrations [cm^{-3}] versus local time (hrs) for a. ESIC, b. EMIC, and c. chorus REP events.	141
Figure 3.5a,b,c Altitude [km] profiles of ozone concentration at time of maximum decrease, hydroxyl concentration at the same time, and hydroxyl concentration at the time of maximum enhancement for a. ESIC, b. EMIC, c. chorus REP events.	146
Figure A-1 OV3-3 180° Magnetic Focussing Spectrometer (shown without baffling) from <u>Vampola</u> , 1969.	155
Figure A-2 Geometric factor-energy response function assigned each channel for data analysis. Total area outside of the rectangle is about 15% but both functions contain equal areas. A slight bias towards higher energies for very steep spectra is produced (<u>Vampola</u> , 1969).	162
Figure A-3 Instrument response-pitch angle output.	164
Figure A-4 Analog record of 376 ± 28 keV electron data plotted as counting rate versus time on a pseudo-logarithmic scale. Universal time, magnetic field intensity, invariant latitude, L, altitude, and MLT are listed for 200-sec intervals. Pitch-angle distribution sampling	

	Page
	produces the large variations in counting rate in several regions of the plot (<u>Vampola</u> , 1971). 166
Figure A-5	Plots of instantaneous flux measurements versus L for the 712±137 keV electron channel from the OV3-3 magnetic spectrometer. The scatter in the data points is due to pitch-angle sampling. Envelope curves at the maximums and minimums are shown to emphasize the data that are iso- tropic in pitch angle (Koons et al., 1972). 168
Figure A-6	Flow chart illustrating process of elimination through the OV1-19 data set. 171
Figure A-7	Outer zone passes per day versus day of the year for the OV1-19 data set. Arrows indicate the three event days. 173
Figure A-8a	Differential electron fluxes versus UT (sec), B (Gauss), L, LAT (deg), ALT (km), for LEMS Proton, LEMS BREM, 822, 537, 444, 376 keV Electrons for DAY 134. 176
Figure A-8b	Differential electron fluxes versus UT (sec), B (Gauss), L, LAT (deg), ALT (km), for 312, 250, 192, 139, 92, 53 keV Electrons for DAY 134. 178
Figure A-9	Electron differential energy fluxes versus UT (hr), LT (hr), ALT (km), L, for 192, 537, 822 keV electrons for DAY 134 (14 MAY 1969). 180

		Page
Figure A-10	Flux versus Pitch Angle for electron channels 192, 537, and 822 keV for DAY 134. Flux upper limit in channel 822 keV is 2.696×10^1 since the high count rate meter coax cable from the HEMS to the satellite data system broke during launch.	182
Figure A-11a	Time sequence of differential electron flux versus pitch angle for the 537 keV channel on DAY 134.	185
Figure A-11b	Time sequence of differential electron flux versus pitch angle for the 444 keV channel on DAY 134.	187
Figure A-12	Dst for days 132 through 137; AE Index for parts of the UT day for days 134 and 135; Alaskan forward scatter absorption events are represented by the hatched boxes (Bailey, personal communication, 1973).	189
Figure A-13	REP frequency of occurrence for the OV1-19 Data Base.	193
Figure A-14	REP energy spectra for the three OV1-19 events in 1969 compared with the Vampola OV3-3 spectrum of 1971.	195
Figure A-15	Ion production rate versus altitude for the OV1-19 REP, solar radiation, galactic cosmic rays and the solar proton event of 1972.	197

		Page
Figure B-1	S3-3 Orbital parameters.	200
Figure B-2	Day of the year versus a) sun time of the orbit phase and b) latitude of apogee.	202
Figure B-3	S3-3 Payload Configuration.	207
Figure B-4	S3-3 HEMS/LEMS Layout.	209
Figure B-5	a) Electron channel component schematic; b) general response curve; c) channel values for E^0 with 100% efficiency.	214
Figure B-6	Typical three dimensional response curve for HEMS 435 keV electron channel.	217
Figure B-7	Typical instrument loss core response for the 655 keV electron channel for pitch angles 8^0 , 18^0 , and 28^0 .	219
Figure B-8	S3-3 Proton/alpha telescope data schematic.	224
Figure C-1	Logarithmic flux (counts/sec) versus UT (sec) for the 12, 235, 435, 655, 850 keV electron and 80 keV proton channel for rev 1661.	228
Figure C-2	Flux (counts/sec) versus pitch angle (degrees) for rev 1661 at 61092 UT (top) and 61109 UT (bottom) for the 235, 435, 655, 880 keV channels. Loss cone is 20^0 with the upward looking loss cone at 160^0 indicated by a vertical line.	230

		Page
Figure C-3	Microfiche layout with each logarithm of flux (counts/sec) as ordinate for each channel and abscissa the UT (sec) every 180 sec for 900 sec (16 samples/sec), ALT [km], LONG [deg-E], LAT [deg], B [Gauss], L [], ILAT [deg], MLT [hr]. E.G. Eight panels (15 min each) of 12, 33, 70 electrons, 8 panels 110, 160, 235 keV electrons, etc. P = Protons, A = Alphas, PD = Proton Detector, BG = Background.	232
Figure D-1	CIRA Reference Atmosphere of depth versus altitude (1965).	272
Figure D-2	$B_r(z,E)$ versus altitude.	276

ACKNOWLEDGEMENTS

I am grateful for having had the rare opportunity to work under the supervision of someone with the insight of Dr. Richard M. Thorne. I thank Dr. S. V. Venkateswaran for three and one-half years of guidance, inspiration, and friendship. Dr. George L. Siscoe has added significant breadth to my knowledge of the space sciences. Conversations with Drs. Charles F. Kennel and Margaret Kivelson were helpful and inspiring. I owe special thanks to Drs. Thorne and Kivelson for editing the manuscript and suggesting style changes.

Finally I thank Miss Sherry Lovell for typing this dissertation and Mrs. Dorothy Deutsch, Mr. Ted Doty, Mrs. Kathryn Drake and Mr. Wes Radlein for support and friendship. While a graduate student, I have been supported by the U. S. Air Force Institute of Technology.

The S3-2 and S3-3 data bases were provided by the prime investigator, Dr. A.L. Vampola, The Aerospace Corporation, ElSegundo, Ca. I am most grateful for many helpful conversations with him and Dr. J. Fennell and for their hospitality while I analyzed the data sets.

VITA

November 11, 1945--Born, Philadelphia, Pennsylvania

1967--B.S., Saint Joseph's College, Philadelphia

1967--Commissioned USAF

1970-1971--M.S., University of Michigan

1979--Major, USAF

ABSTRACT OF THE DISSERTATION

Relativistic Electron Precipitation:
An Observational Study

by

Leopold Joseph Andreoli

Doctor of Philosophy in Atmospheric Sciences

University of California, Los Angeles, 1980

Professor Richard M. Thorne, Chair

The object of this dissertation is to analyze satellite data to investigate the morphology of strong diffusion relativistic electron precipitation (REP) events with the ultimate purpose of gaining insights into the precipitation mechanism and determining atmospheric consequences. Analysis of fourteen (14) months of magnetic electron spectrometer and proton telescope data from the Air Force S3-3 satellite from July 1976 to September 1977 is presented. Analysis techniques and data catalogues are presented in detail. Three distinct classes of REPs were discovered: an overwhelming majority (96.5%) exhibited precipitation in a large range of energies below 1 MeV for electrons with concurrent proton precipitation; the smallest class (1.3%) also exhibited concurrent electron and proton precipitation but the electron

and proton precipitation but the electron precipitation occurred only at energies above 1 MeV; a third class (2.2%) had no associated proton precipitation and electrons precipitated only at energies below a few hundred keV. In addition, all REPs have a 10-20% frequency of occurrence that linearly increases with magnetic activity, show seasonal variation with equinoxial maxima and solstice minima, have mostly small latitudinal ($\sim 0.5L$) and large longitudinal (1000-10,000km) extents, and occur most frequently (9 out of 10) in the local nighttime sector.

A theoretical approach to the REP mechanism is presented. Interaction of the radiation belt electron and ring current proton populations with electrostatic and electromagnetic ion cyclotron and whistler mode chorus waves can account for the three classes of precipitation, respectively. Examples of each class are presented in detail.

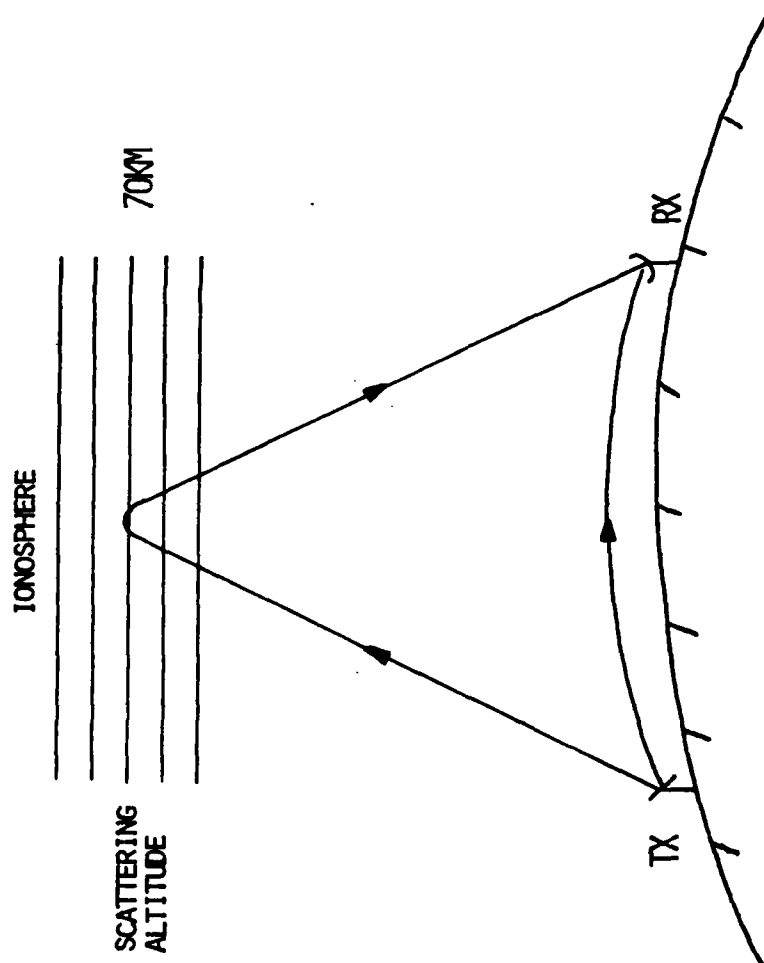
Finally, an investigation of the energy deposition rates from these events and their ultimate effect on the ionized and neutral atmosphere with emphasis on ozone modification is presented. The local hydroxyl concentration can be increased up to a factor of 10 and the local ozone concentration can be decreased by 10-30% by REP events.

Introduction

HF radio waves can propagate from transmitter to receiver via refractive interaction with the ionosphere (see Fig. 1). This propagation is known as forward scatter or skywave propagation. The received signal can be diminished (in power) if the electron density below the scattering altitude is enhanced in any way. Signal absorption occurs during the day due to the natural increase of free electrons below the scattering altitude by solar ionizing radiation ($1000\text{--}1100^{\circ}\text{A}$). Absorption can also be increased by precipitating energetic particles (e.g., solar protons) that reach altitudes below the scattering altitude. One well known class of absorption event is the Polar Cap Absorption (PCA) events which occur over the polar region following the outburst of energetic protons during flare activity on the sun. A lesser known but more frequent class of events involves the precipitation of relativistic electrons and these will be the subject of this dissertation.

Relativistic Electron Precipitation (REP) events were first observed as anomalous daytime absorption of forward scatter (more correctly - ionospheric refraction) HF signals by Bailey and Pomerantz (1965). The detection system used by Bailey and Pomerantz consisted of three paths each in Alaska and Antarctica operating near 23 MHz with skywave scattering points over the invariant latitude (Λ) range $58\text{--}77^{\circ}$ ($L = 3.6\text{--}20.0$). The scattering altitude was estimated to be ~ 70 km. Peak signal absorption typically occurred between $\Lambda = 62\text{--}66^{\circ}$ ($L = 4.5\text{--}6.0$); namely, within the region of long term trapping for

FIG 1. Illustration of one-hop skywave propagation via the
Ionosphere.



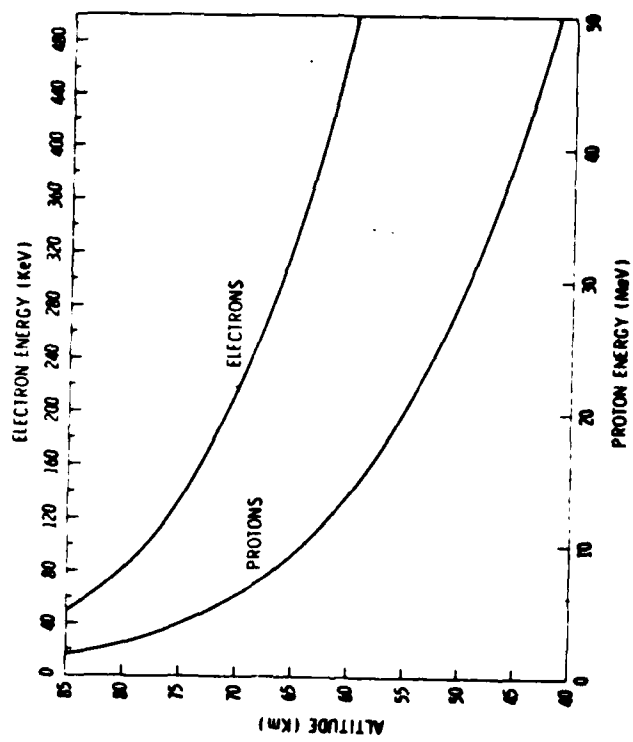
radiation belt particles.

Since solar protons could be ruled out due to the absence of absorption over the higher latitude polar cap region ($\Lambda > 72^\circ$; $L > 10$), absorption was attributed to a locally precipitated source of particles. These particles dissipate most of their energy at altitudes determined by their range in the atmosphere and thus by their energy (Aikin and Bauer, 1965). As shown in Fig. 2, protons require at least several MeV while electrons require only a few hundred keV of energy to penetrate below 70 km. This, however, immediately excludes the main bulk of auroral electrons (~ 1 -10 keV) as the precipitating particles causing absorption and indeed visible auroral activity (monitored by all sky cameras) was found to have no correlation with dayside HF absorption (Bailey et al., 1970). Since protons of several MeV energy are tenuous beyond ($L \sim 3.5$) and do not exhibit outer zone integral flux variations of the order estimated for strong ionospheric absorption ($\sim 40 \text{ cm}^{-2} \text{ str}^{-1} \text{ sec}^{-1}$ for protons), Bailey and Pomerantz concluded that trapped electrons at energies greater than 400 keV were the cause. In situ satellite measurements have also demonstrated that relativistic electrons trapped from $\Lambda = 55$ - 60° ($L = 3$ -4) can exhibit order of magnitude flux decreases during disturbed times (Frank, 1965). Furthermore, since the maximum observed absorption intensities occur at higher L values than the normally expected peak intensity of trapped electrons, Bailey and Pomerantz (1965) concluded the mechanism operates more efficiently near the trapping boundary.

Since Bailey and Pomerantz only observed the events during the daytime, they assumed, inconclusively, that the precipitating mechanism is more intense on the dayside. It must be noted that this type of measurement is highly frequency dependent. This is supported by the fact that as the forward scatter observing frequency changed from 50 MHz in the early 1950's to 35 MHz pre-IQSY (Int'l Quiet Sun Year) and finally to 23 MHz post IQSY, ability to detect less intense events improved. The day/night occurrence probability of REPs will be further discussed as we review subsequent measurements.

Other types of observations were soon employed to verify inferences based on the forward scatter results. Riometers which integrate the effect of precipitating particles (and radiation) of all energies were used to confirm signal absorption (Bailey et al., 1970). All sky cameras (observing auroral activity), ionosondes (for Es, sporadic E layer, detection), magnetometers (Bailey et al., 1966) and balloon X-ray measurements (for energy spectrum information) (Barcus and Rosenberg, 1966) basically confirmed signal absorption differences between daytime REPs and nighttime Es (absorption by precipitating 5-20 keV electrons). In addition, estimates of precipitating electron spectra for REP and Es conditions for quiet to severely disturbed magnetic conditions were constructed from X-ray and forward scatter measurements (Bailey et al., 1966; Bailey et al., 1970). Comparison of X-ray and forward-scatter-deduced spectra for the same event revealed the marked inability of the forward scatter system alone to detect the presence of relativistic electrons due

FIG 2. Atmospheric penetration depths for protons and electrons assuming vertical incidence (adopted from Aikin and Bauer, 1965).



to the large uncertainty in scattering altitude (Rosenberg et al., 1972). Spectra derived from various sources will be compared later.

Another drawback to estimating REP spectra from forward scatter measurements alone is the uncertainty of absolute absorption. The signal power received is enhanced by increases in the electron density at the scattering altitude as well as diminished by increases in electron density along the signal path below the scattering altitude, thus an accurate measure of absorption is difficult.

REPs (and PCAs) appear as absorption on forward scatter records by day. At night, although the scattering altitude is higher (by 10-20 km), there are insufficient free electrons below the scattering altitude to produce signal absorption and even the strongest precipitation events appear as signal enhancements. Riometers, however, continue to show absorption during such nighttime events (Bailey, 1968).

Two Alaskan paths at $\Delta = 65^\circ$ and 62° ($L = 5.7$ and 4.6) were chosen for long term statistical study (Bailey, 1968). For the period 1 March 1964 to 31 December 1966, REPs producing absorption ≥ 8 db occurred on 319 days with maxima at equinoxes and minima at solstices. The 93 medium and large REPs (absorption ≥ 14 db) for the same period are not associated with sudden commencement (SC) geomagnetic storms, but the events mostly occurred on magnetically disturbed days, lasted from 1-6 hours (with some seeming to last 24 hrs) and were mainly confined to the 12 hour period centered on local noon.

After 1967, the system detection capability became erratic due to the increasing solar activity. The system was terminated for various additional reasons early in 1973 (Sullivan, 1979). Attempts were made to obtain some 1969 forward scatter data for correlation and calibration with OV1-19 satellite spectrometer data (see Appendix A) but all of the forward scatter data except for the first five months of 1969 had been lost (Lincoln, 1978).

In 1968-1971, the Norwegian Defense Research Establishment (NDRE) undertook a program entitled "Omega Research in Norway" (Larsen, 1973). This program monitored the VLF (12.3 kHz) short hop (433 km) path between the transmitter at Aldra, $\Delta = 63.7^\circ$ ($L \sim 5.1$), and the receiver at Tromsø, $\Delta = 66.5^\circ$ ($L \sim 6.3$), both in Norway, for PCA, substorm, REP, and stratospheric warming research. Phase recordings of the VLF signal perpendicular (to propagation plane) and parallel magnetic components provide sensitive detection of ionization variations below the scattering altitude of about 60-65 km daytime and 80-90 km nighttime (Larsen, 1973). A diurnal effect is seen as an advance shift in baseline of 60-80 μsec from local night to day. REPs (and PCA/solar flare events) are readily observed both day and night as phase advances beyond the normal undisturbed levels.

Thorne and Larsen (1976) compared the Norwegian VLF and Alaskan HF observations of REPs and Auroral Electrojet (AE) Indices (for substorm identification) for the period January-May, 1969. They indicate "...a direct correlation between the onset of intense nighttime REP events with substorms while dayside REPs are far less frequent,

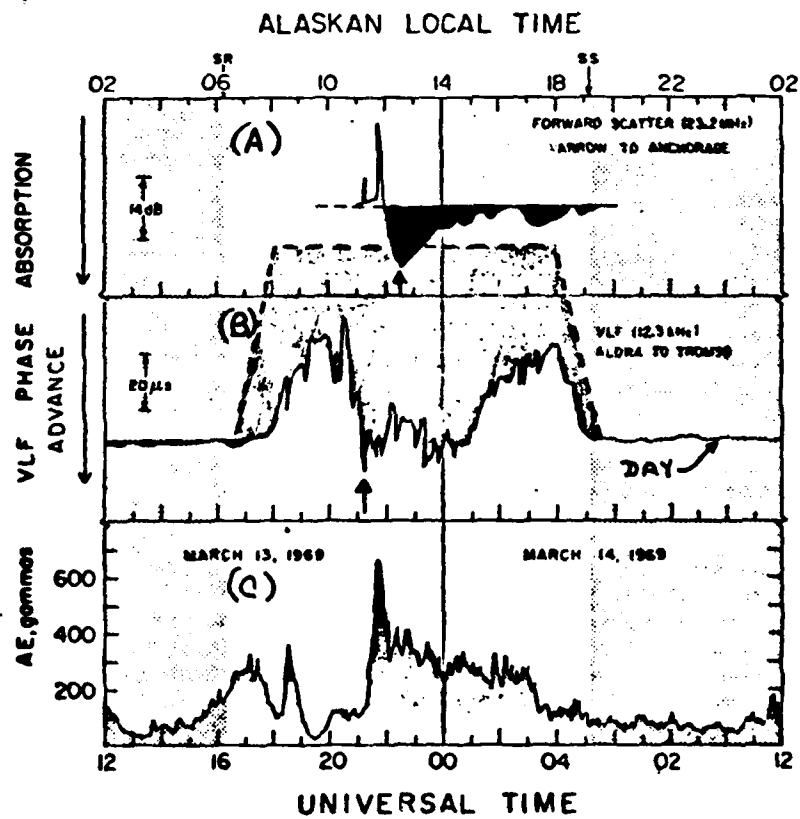
are shorter in duration and are often delayed by as much as several hours from the onset of substorm activity" (Thorne and Larsen, 1976). Figure 3 shows for example, a simultaneous increase in AE and VLF phase advance in Norway at 2100 UT followed 1-1 1/2 hrs later by the HF absorption in Alaska. This sequence agrees with the observation of the 25-26 August 1967 substorm by Hones et al., (1971) but not their inference of gradient drifting electrons injected at substorm onset since the gradient drift lifetimes of relativistic electrons are on the order of minutes (Thorne and Larsen, 1976). In addition, only a select class of substorms can trigger dayside REPs (Rosenberg et al., 1972; Thorne and Larsen, 1976) and substorm intensity is only weakly correlated in the selection of which substorm will spawn a REP (Thorne and Larsen, 1976).

Many observers using riometers (Brown, 1964; Jelly and Brice, 1967) and chains of riometers (Ansari, 1965; Lukkari et al., 1975; Lukkari and Kangas, 1976; Lukkari et al., 1977) have observed similar relations between subauroral energetic electron precipitation and slowly varying absorption (SVA), substorm onsets, and magnetic pulsations. Riometers observe total absorption occurring both above and below the scattering altitudes of VLF and HF systems and alone cannot determine where (in altitude) the absorption occurs nor yield a precise precipitation spectrum (Bailey, 1968).

Balloon-borne measurements of X-rays during REP events (usually with uncollimated NaI detectors near 32 km altitude) have the advantage over riometer measurements in sensitivity, time resolution, and the fact that they provide an

1

FIG 3. Time sequence of (A) HF absorption (dark shaded area) in Alaska; (b) VLF phase advance (shaded) from normal nighttime trace (dashed line); (c) AE index for 13-14 March 1969 from Thorne and Larsen, 1976.



energy spectrum (Bewersdorff et al., 1968). In addition to the disadvantages of imprecise balloon location (~ 100 km horizontally) and proton contamination of X-ray scintillators, the theoretically predicted X-ray spectrum (the scintillator measures mostly secondaries) is very sensitive to the assumed incident electron spectrum, usually in exponential form ($\propto \exp E/E_0$), and atmospheric depth (Bailey et al., 1970). Only six or seven X-ray measurement deduced electron energy spectra during energetic electron precipitation events have published and range from spectra constructed by the addition of soft ($E_0 = 9$ KEV) and hard ($E_0 = 40$ KEV) components (Bailey et al., 1970) to very hard ($E_0 = 180-200$ KEV) spectra (Rosenberg et al., 1972; Parks et al., 1979).

Rockets have carried spectral and integral electron spectrometers (Matthews and Simons, 1973; Vij et al., 1975; Matthews et al., 1976) as well as having boosted parachute-borne X-ray scintillators (Vij et al., 1975) during REP and auroral events. Simultaneous electron (rocket to 275 km apogee) and X-ray (rocket boost to 60 km) observations show fair agreement at least in the much "softer" auroral events (Vij et al., 1975). The spectrometers yield a more precise electron energy spectrum and, depending on instrument orientation and flight configuration, add pitch angle distribution information. An obvious drawback of this type of experiment for REP research is the lack of morphological statistics due to prohibitive logistics expense.

Satellite X-ray spectrometer experiments provide simultaneous measurements over a wide range of local times because of their extensive fields of view (Imhof et al., 1974) as well as opportunities for coordinated studies with particle spectrometers for improved spatial/temporal resolution (Imhof et al., 1975). Comparison of X-ray and particle measurements show agreement to only a few hundred keV and that impulsive (< 5 min duration) events near the energetic trapping boundary were substorm correlated (Imhof et al., 1978). Coordinated two satellites X-ray and particle measurements show significant variations in local time dependence of energetic electron precipitation though fluxes seemed greater in late morning than early morning.

The majority of satellite REP measurements have been made with integral (Brown and Stone, 1972; Larsen and Thomas, 1974; Morfill et al., 1975) and spectral (Vampola, 1969; Vampola, 1971 a and b; Imhof et al., 1973; Imhof et al., 1975) particle spectrometers. REP precipitation is observed to be a narrow ($\Delta L \sim .5-1.5$) phenomenon. Figure 4 shows an invariant latitude versus magnetic local time plot of electron precipitation spikes with $E > 425$ keV from the last five months of 1967 from the low polar orbit satellite OGO 4 (Brown and Stone, 1972). Notice a relative scarcity of events between 06-12 MLT. Also, the events extend from approximately the middle of the outer electron zone to the limit of closed field lines with the highest density clustered about the limit of stable trapping. A general shift to lower invariant latitudes is observed

with increasing geomagnetic activity. Event time scales range from several minutes to several hours. Approximately five times as many events occur at 2200 MLT as at 1000 MLT. This study was extended by the use of the > 500 keV measurements on board another low polar orbit satellite ESRO 4 with similar results (Morfill et al., 1975).

Another investigation of magnetic electron spectrometer data of precipitating electrons in the energy range $225 \text{ keV} < E < 2.47 \text{ MeV}$ aboard polar orbit satellite OV3-3 for the period August 1966-September 1967 show common occurrences of precipitation at local evening and midnight in a narrow region ($\Delta L \sim 0.5$) at the local limit of trapping (Vampola, 1971). Rare events (3) at local evening just inside the plasmopause where higher energy electrons ($> 1 \text{ MeV}$) are preferentially precipitating were also found.

Measurements of precipitating electrons from $> 48 \text{ keV}$ to $> 434 \text{ keV}$ on the polar orbit satellite ESRO 1A during the REP of 2 February 1969 at local morning at $\Delta = 63^\circ - 70^\circ$ ($L = 4.9 - 8.5$) have been reported by Larsen and Thomas (1974). The energy spectrum for this event is a bit "harder" than those previously obtained by rocket measurements (Matthews and Simons, 1973) but much harder than those deduced from balloon X-ray measurements (Bailey et al., 1970).

Figure 5 compares REP energy spectra from various sources previously discussed with typical discrete and diffuse auroral spectra (Lui et al., 1977). Satellite-borne spectrometers, particularly spectral spectrometers, have measured the hardest spectra in comparison with non satellite spectra and represent the most direct means of examining REPs of all intensities.

FIG 4. Latitude-local time plot of all 425 keV electron spike observations from Brown and Stone, 1972.

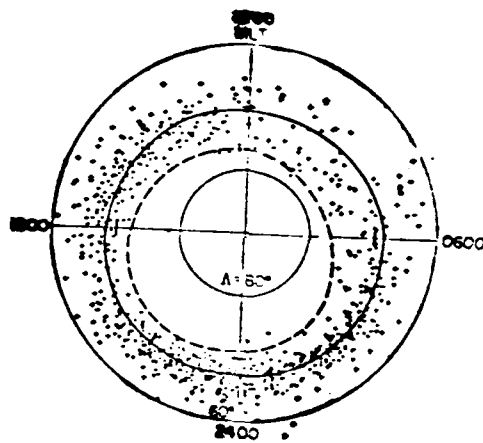
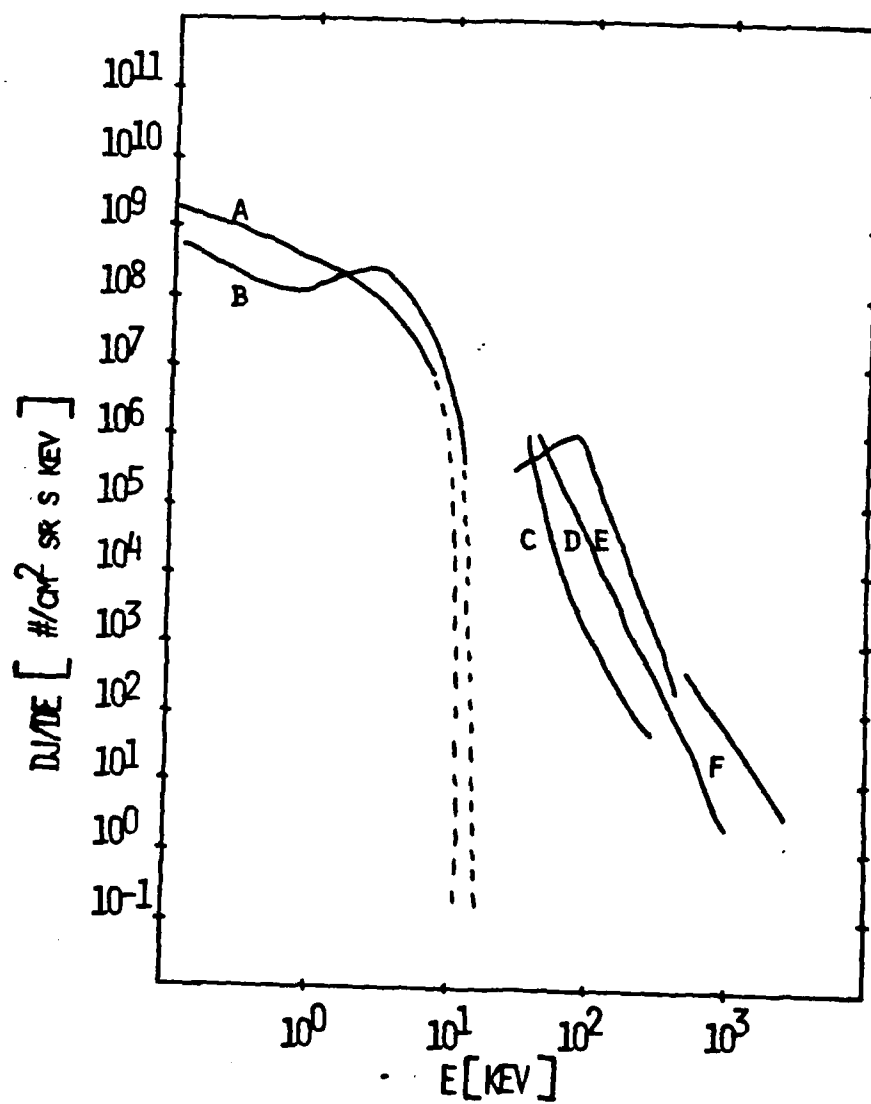


FIG 5. Differential energy spectra of precipitating electrons of the following types: (A) Diffuse aurora (Lui et al., 1977); (B) Discrete aurora (Lui et al., 1977); (C) Balloon X-ray (Bailey et al., 1970); (D) Rocket (Matthews and Simons, 1973); (E) Satellite (Larsen and Thomas, 1974); (F) Satellite (Vampola, 1971).



It was the purpose of this dissertation to determine the mechanisms responsible for REP events, their relative importance and atmospheric consequences through the study of satellite data. Magnetic electron spectrometer data on the low polar orbit satellites OV1-19 and S3-3 were graciously provided by the instrument builder and prime investigator, A. L. Vampola, Aerospace Corp., El Segundo, Ca. An exhaustive study of the OV1-19 data set was performed but for various reasons the data set yielded only marginally significant results. This study is described in detail with results in Appendix A. The S3-3 data set has few of the drawbacks of the OV1-19 data set and is the main source of study here. The S3-3 satellite orbit and orientation as well as particle and wave measurements are described in Appendix B.

This thesis is arranged with four main chapters. In Chapter 1, details of the S3-3 REP event morphology are presented. A description of the objective and subjective analysis of the data needed to identify events is contained in Appendix C.

Chapter 2 contains a general background of the types of mechanisms previously postulated and others newly discovered capable of explaining REPs. The mechanisms are compared with the classes of events found in Chapter 1. In addition, a case study of each type is presented with the view of advancing the knowledge of each mechanism.

Chapter 3 compares the atmospheric energy deposition profiles for REP and REP X-rays with profiles from other sources.

Profiles for REPs of various classes and intensities are presented as well as determinations of their importance and consequences in ionization production and ozone chemistry. The electron and X-ray deposition calculations are presented in Appendix D.

Chapter 4 summarizes the findings and discusses the conclusions and outlooks.

CHAPTER 1. EVENT MORPHOLOGY

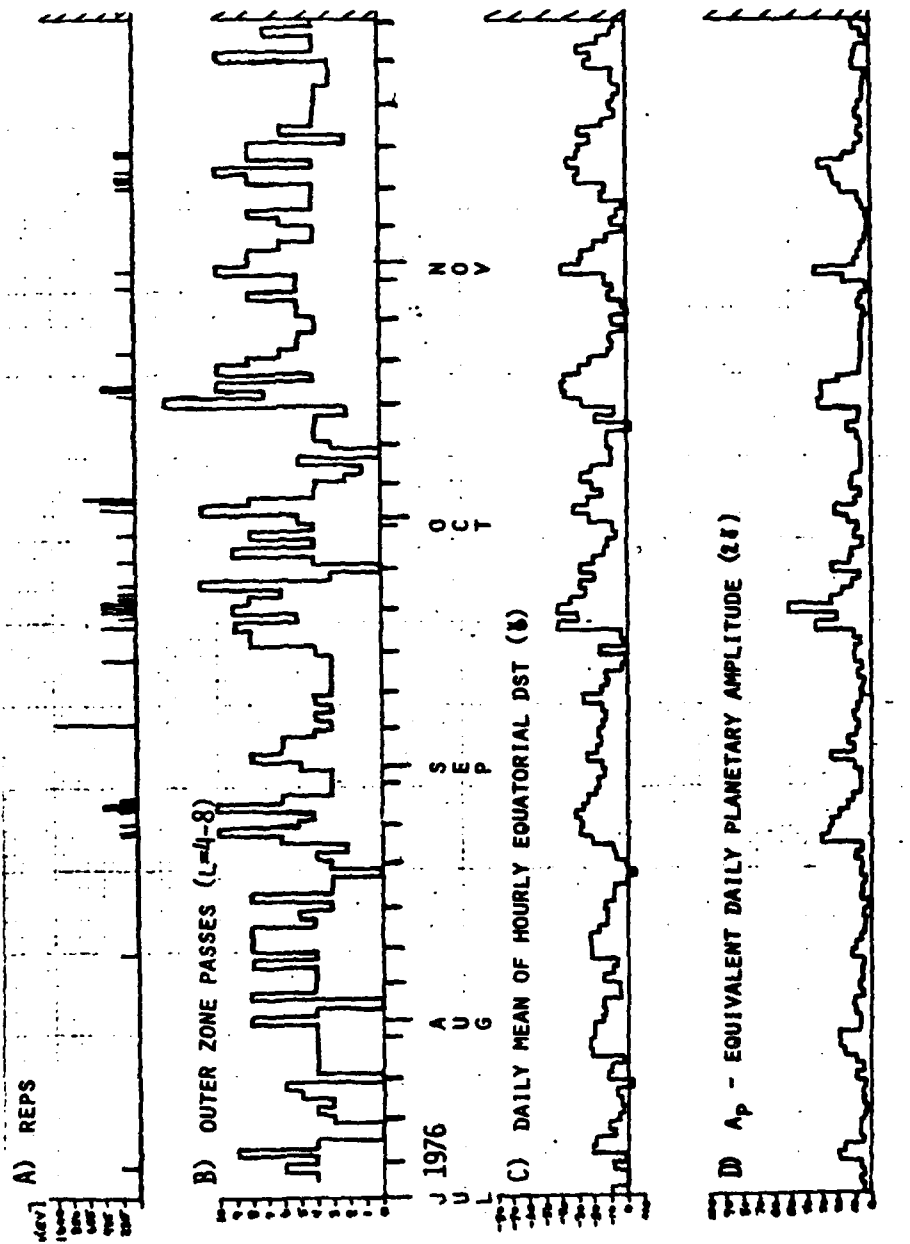
1.1 Results

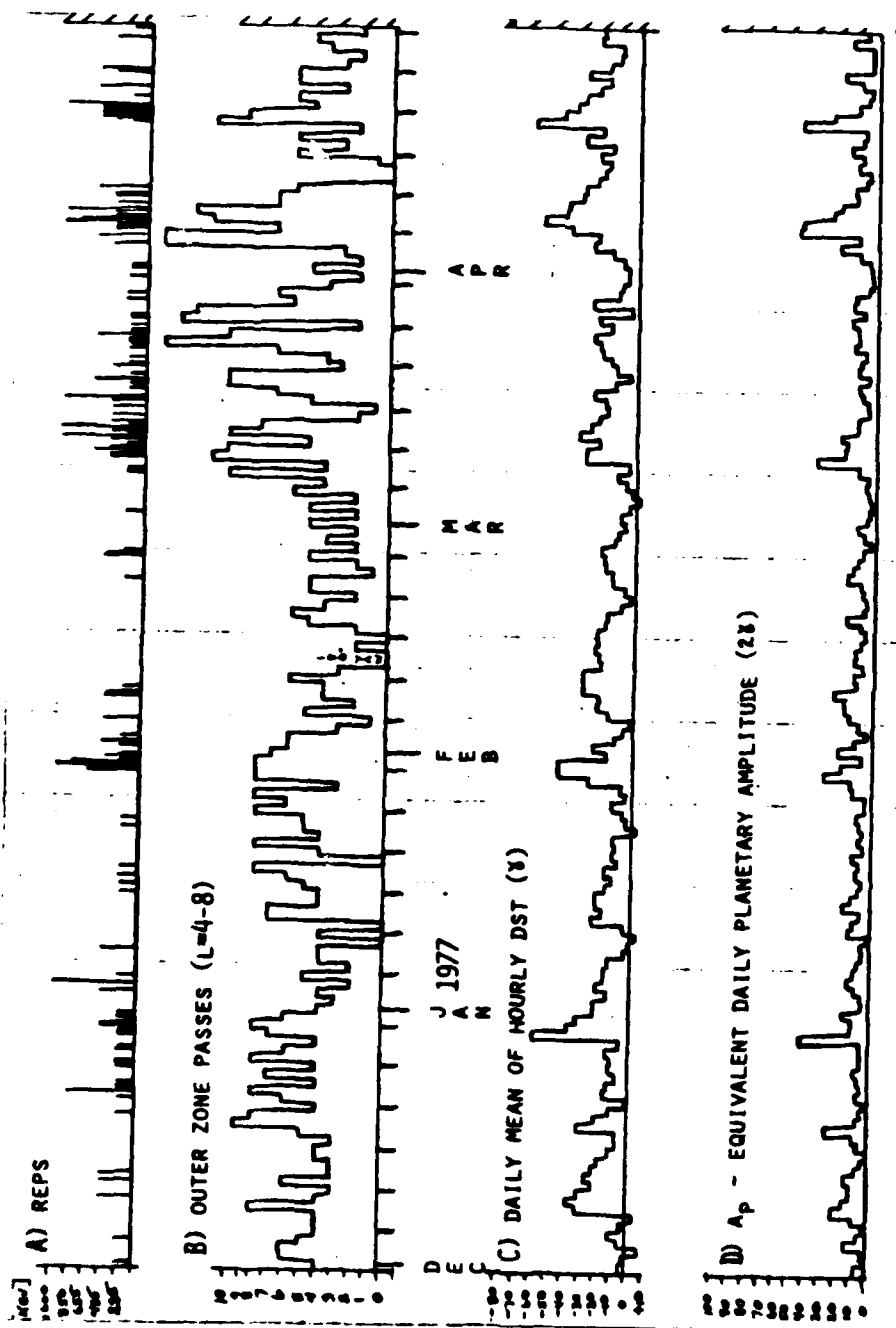
We present here the statistical data on REP occurrence measured on S3-3 during a 14 month period from 11 July 1976 to 29 September 1977. The S3-3 data collection specifications are described in Appendix B. The methodology of selecting REPs as well as the data base description is provided in Appendix C. Fig. 1.1, a-c, shows a summary of the S3-3 data set; the plot includes daily values of the highest energy channel (in keV) exhibiting strong diffusion precipitation (Panel A); the daily number of outer zone (L=4-8) passages (Panel B); the daily mean of the hourly equatorial DST in gamma units (Panel C); and the daily A_p , equivalent daily planetary magnetic amplitude in 2 gamma units (Panel D). Outer zone coverage (Panel B) was fairly uniform throughout the data set (although 29 days had no coverage) averaging a little over 5 outer zone passages per day. Coverage was a function of tape recorder capacity, power limitations, microfiche availability, etc. DST and A_p are presented to represent the relative magnetic condition of the magnetosphere since AE, the Auroral Electrojet Index, was not yet available for this time period. AE indices for five stations, AE (5), for seven 2 day periods in 1977, however, were available and are discussed in the next section. (Allen, private communication, 1979.)

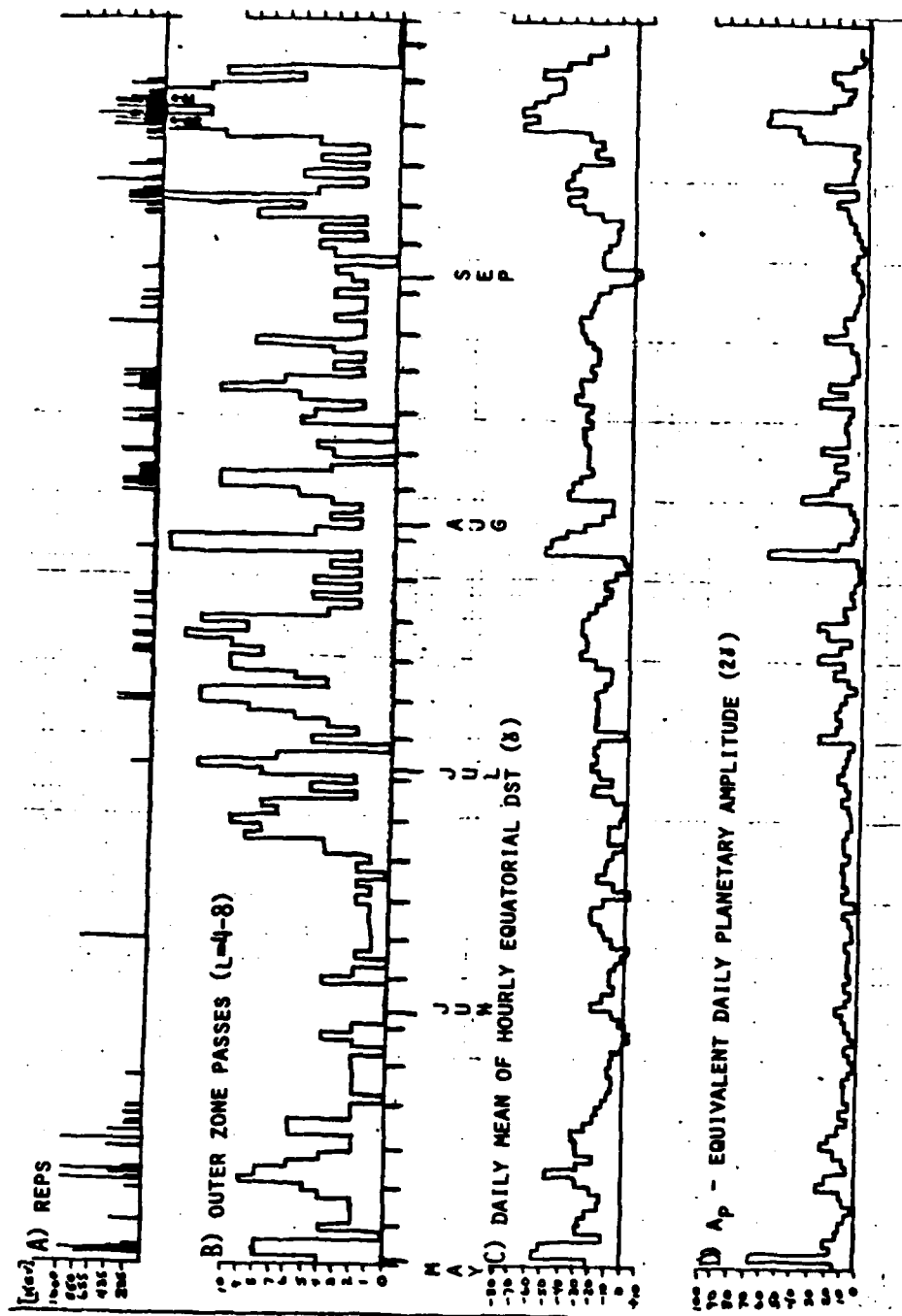
1.2 Frequency of Occurrence and Magnetic Dependence

The monthly average frequency of occurrence of REP events observed during the satellite transit of the outer radiation zone (L=4-8)

FIGURE 1.1a,b,c. Daily values from 11 July 1976 to 29 September 1977. Plots are given of REPs with highest energy channel exhibiting strong diffusion (Panel A); the total number of outer zone passings, $L=4-8$ (Panel B); daily mean of the hourly Dst, γ (Panel C); A_p , equivalent daily planetary magnetic index, 2γ (Panel D).







is represented in Fig. 1.2. Maximum occurrence is found near both (1976, 1977) autumnal equinoxes, at and slightly beyond vernal equinox, and near winter solstice while pronounced minima are evident near both (1976, 1977) summer solstices. This is generally consistent with the equinoxial maxima and solstice minima found by Bailey (1968). In this sense, the winter maxima is anomalous, but approximately five strong magnetically disturbed periods took place in Dec 1976-Jan 1977 (see Fig. 1.1b) probably accounting for the rise in activity. The magnetic dependence is apparent when the same monthly percentage of REPs normalized to outer zone coverage is plotted for days when $A_p > 30$ (Panel A), $20 \leq A_p < 30$ (Panel B), $10 \leq A_p < 20$ (Panel C), and $A_p < 10$ (Panel D) in Fig. 1.3. The anomalous winter maximum in Dec is apparent for $30 < A_p < 20$ while the Jan maximum is seen only for $20 < A_p < 30$. The remaining maxima and minima are fairly consistent with magnetic conditions.

Plotting the REP occurrence frequencies for all 14 months for different ranges of A_p (magnetospheric disturbance) (Fig. 1.4), one sees a nearly linear increase in REP occurrence with magnetic disturbances.

Fig. 1.5 shows S3-3 coverage of seven 2 day periods by AE index (Allen, private communication, 1979). This data is merely presented to support the fact that not all substorms trigger REPs (note particularly Panels A and E) in agreement with the findings of Rosenberg et al. (1972) and Thorne and Larsen (1976). The local times of collections for both Panels A (1 outer zone pass per rev) and E (2 outer zone passes

FIGURE 1.2 Monthly REP event percentage of occurrence normalized
to outer zone coverage for July 1976-September 1977.

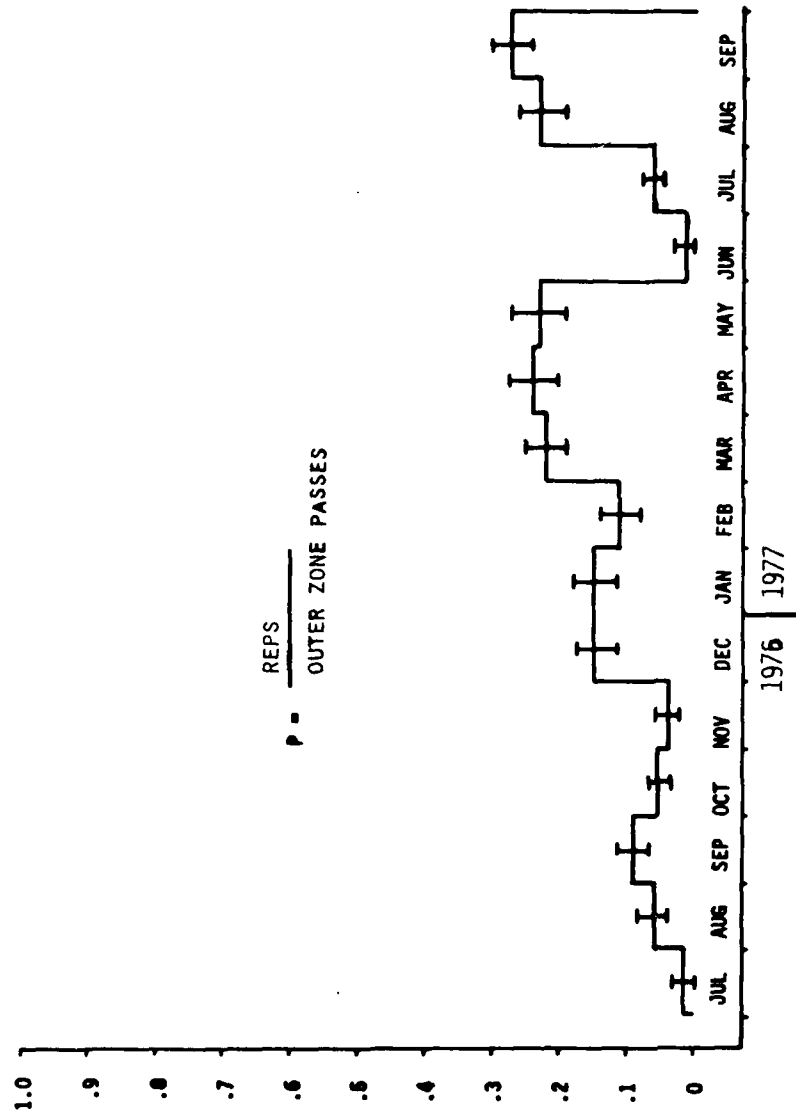


FIGURE 1.3 Monthly percentage of REPs normalized to outer zone crossings ($L=4-8$) for magnetic conditions: $A_p > 30$ (Panel A); $20 \leq A_p < 30$ (Panel B); $10 \leq A_p < 20$ (Panel C); $A_p < 10$ (Panel D). Values for JAN and FEB in Panels A and B overlap. $P=0$ for both JAN and FEB in Panel A and $P=0.86$ and 0.39 for JAN and FEB respectively in Panel B.

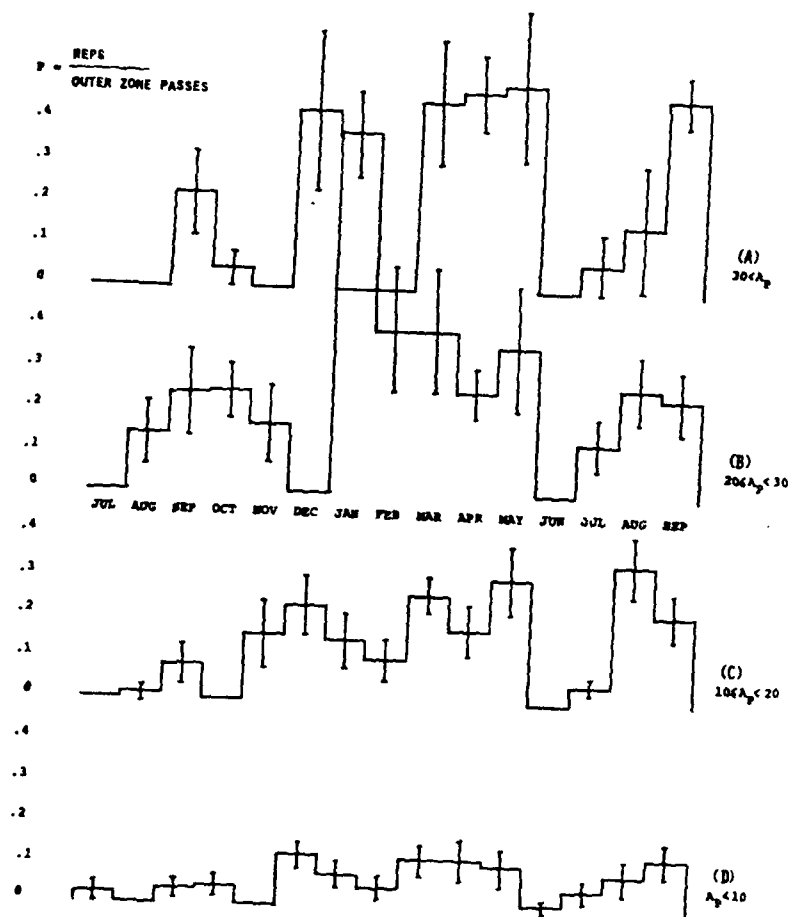


FIGURE 1.4 REP event percentage of occurrence normalized to outer zone coverage (L=4-8) versus magnetic conditions for all months JUL 1976-SEP 1977. Total number of outer zone passes for each category are in parentheses.

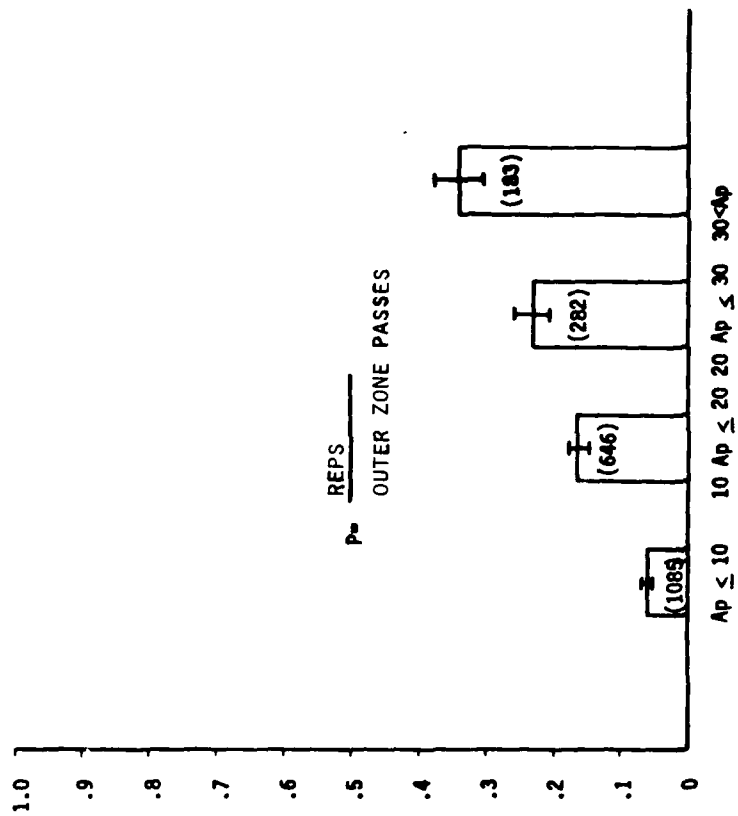
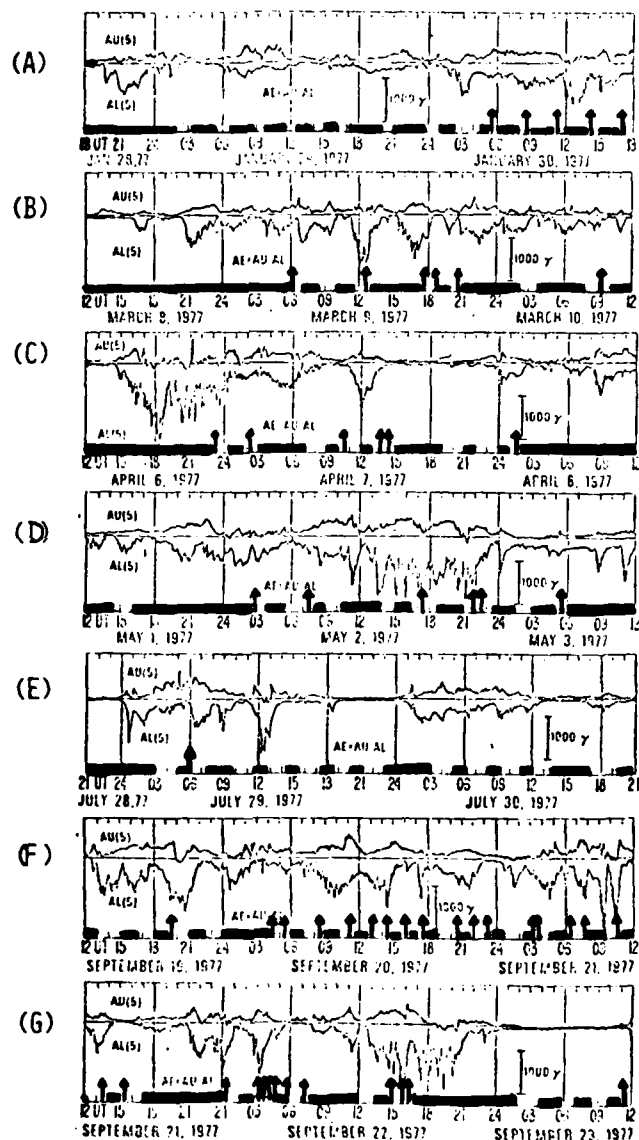


FIGURE 1.5 Seven 2 day periods of AE index (γ) throughout 1977 with REPs indicated by arrows (\uparrow) and hours of noncoverage by shaded horizontal bar (■). AE = AU (Upper Trace) - AL (Lower Trace).

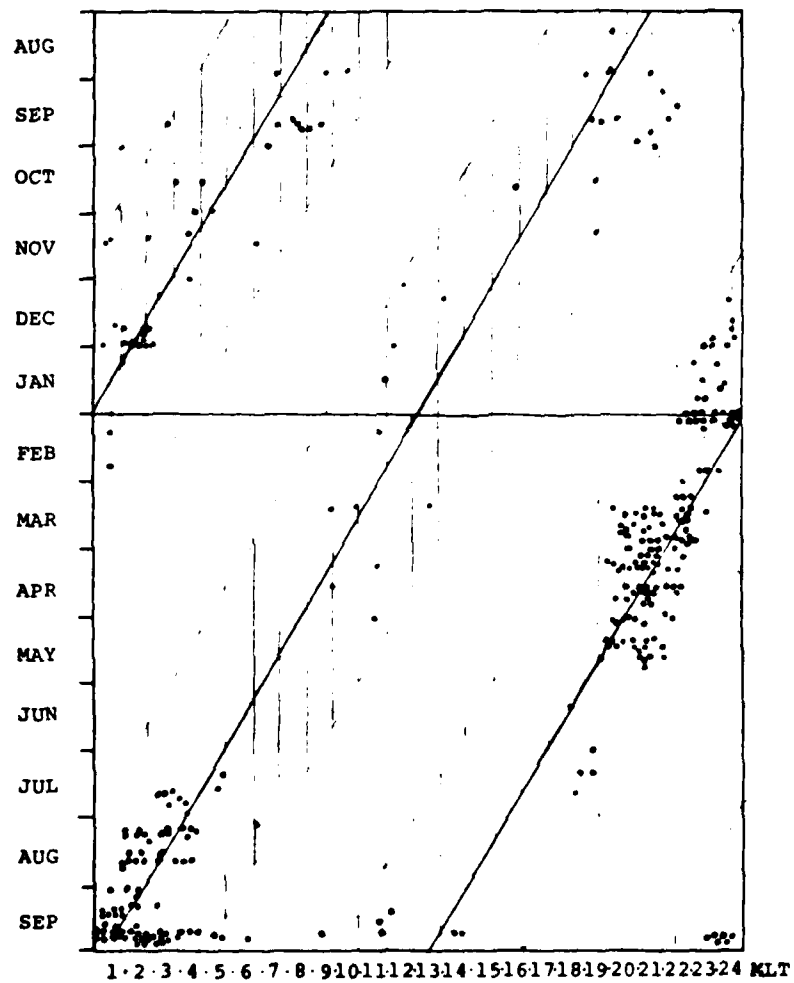


per rev) occurred near midnight where one would expect highest probability of detection (see Fig. 1.7 for example). Many of the outer zones, particularly the outer edge, in the passes of Panels A and E were very irregular showing trapped flux variations to nearly an order of magnitude though no precipitation was evident at the time of the pass. Also noticeable are times when substorms with large values ($\sim 900\gamma$) of AE do not spawn REPs (03-04L, 30 Jan 77, Panel A; 12-14L, 29 Jul 77, Panel E; 03-11L, 30 Jul 77, Panel E; 13-18L, 19 Sep 77, Panel F) while substorms corresponding to smaller AE may be associated with REPs (08-10L, 10 Mar 77, Panel B; 01-02L, 8 Apr 77, Panel C; 05-06L, 3 May 77, Panel D; 04-06L, 20 Sep 77, Panel F; 11-12L, 23 Sep 77, Panel G). This agrees again with Thorne and Larsen's (1976) finding of weak correlation between AE index and REP observations. An exception to this correlation is the REP activity at 03-04L, 22 Sep 77, Panel G, where a 1500 γ storm has associated REP activity for all four outer zone passes on the same revolution (see event catalogue, Appendix C, REV P 3569). This orbit was oriented in the 0200 and 1400 hrs MLT plane and could infer a longitudinal extent of nearly 10,000 km.

1.3 Local Time Dependence and Latitudinal Extent

To examine the local time morphology, REPs (Fig. 1.1, Panel A) were plotted for a given date versus magnetic local time (MLT) in Fig. 1.6. In order to test for any bias in the excursion of the orbit plane with time (skewed solid lines), we have sketched (hatched areas) the span of local times over which REPs could be observed in the range $4 \leq L \leq 8$ for a given local time orientation of this orbit plane. A

FIGURE 1.6 REPs by date versus MLT (hrs). Hatched area indicates regions of coverage ($4 \leq L \leq 8$) around the local time of the orbit plane (skewed solid line).



possible apogee-perigee bias in the orbit plane was investigated but after careful analysis (see Appendix C) the bias was found to be insignificant. The most striking feature is the pronounced night-day asymmetry with the greatest number of REPs occurring in the night sector. A plot of the ratio of day to night REPs is presented in Fig. 1.7 as a function of magnetically disturbed conditions. Overall there is a 9:1 preference for nighttime REP events. This local time asymmetry is less for highly disturbed ($A_p > 30$) conditions.

The actual local time morphology of REP events is shown in Fig. 1.8 (dots indicate very narrow localized events and lines are drawn for extended events) where they are plotted against invariant latitude for varying magnetic conditions. Most events show narrow latitudinal extends $\sim 0.5L$ (dots) while a few showed excursions up to 4-5L, mostly in the 235, 435 keV electron channels. Readily apparent is the relative lack of dayside REPs particularly during magnetically quiet days ($A_p \leq 10$). Furthermore, the scarcity of REPs over the local time range 1300-1900 remains apparent for $A_p \geq 10$. As can be seen from Fig 1.6 the orientation of the orbit plane for these MLTs covered roughly all months except the Mar-May maxima. Both autumnal equinoxes and the anomalous Dec-Jan maxima were covered so we believe that the statistics for the local afternoon hours are not biased by the orientation of the orbit plane: thus the tenuous afternoon statistics appear to be real. Also, for highly disturbed conditions ($A_p \geq 20$) the event location moves towards lower invariant latitudes; this is most noticeable for $A_p > 30$.

FIGURE 1.7. Ratio of day (MLT 06-18) to night (MLT 18-06) for
varying magnetic conditions.

$$\text{RATIO} = \frac{\text{DAY (MLT 06-18) REP}}{\text{NIGHT (MLT 18-06) REP}}$$

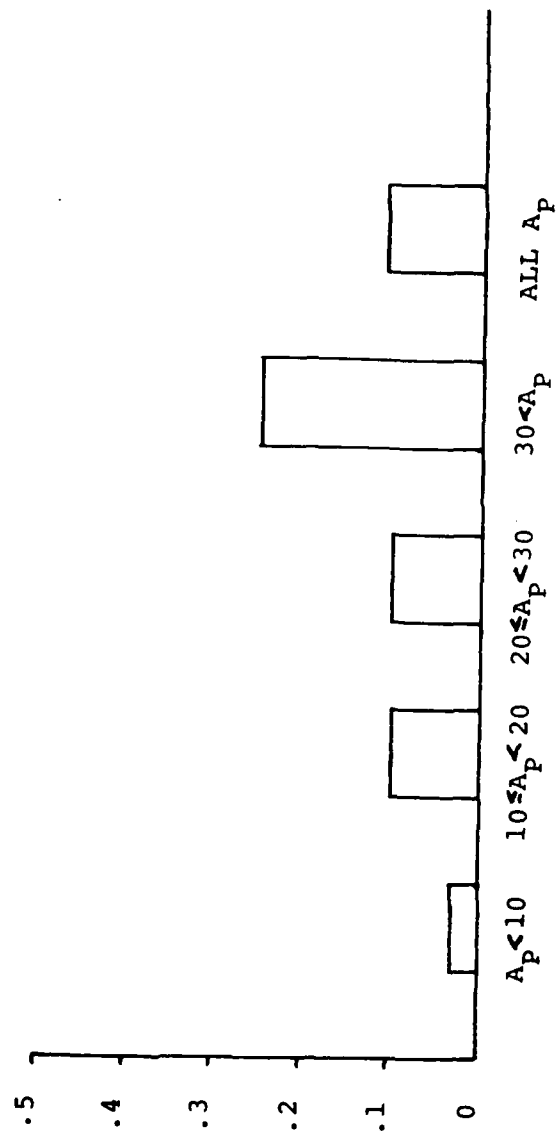
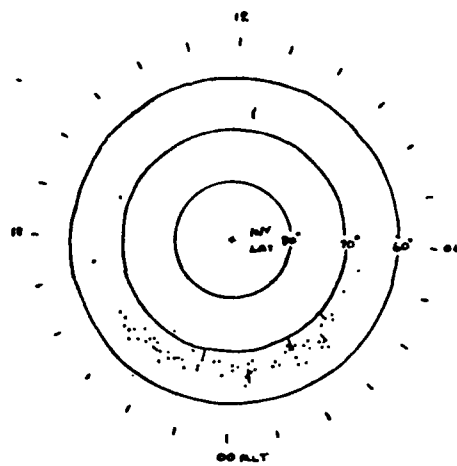
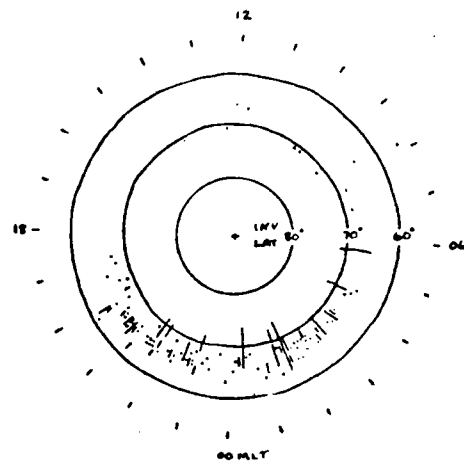


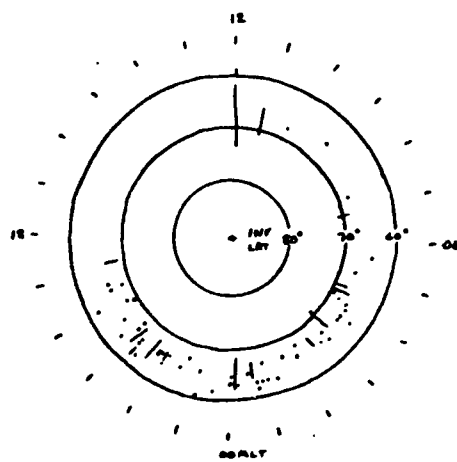
FIGURE 1.8 REPs displayed by invariant latitude (degrees) versus MLT (hrs) for varying magnetic conditions. Lines indicate excursions of events in invariant latitude.



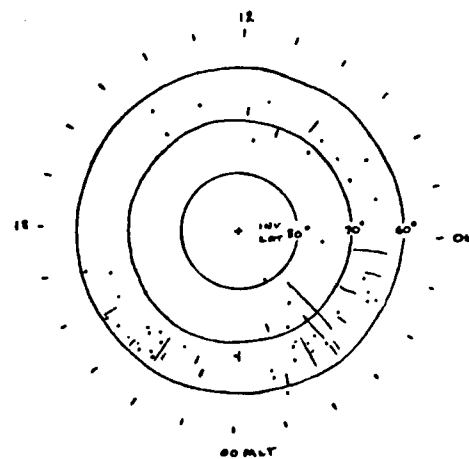
$A_P \leq 10$



$10 < A_P \leq 20$



$20 < A_P \leq 30$



$A_P > 30$

1.4 Longitudinal Extent

The slow (1.5 hr/month) excursion of the orbit plane in local time (see Appendix B) does not allow direct analysis of longitudinal extent. Estimates, however, can be made from previously published ground based events (e.g. Bailey, 1968) though these would probably be a lower limit. In addition, general limits could be estimated on an individual case basis from the satellite revisit times (~3 hrs) where consecutive coverage exists.

Duration of ground based REP events was observed to be 1-6 hrs with some events lasting for 24 hrs (Bailey, 1968). Several S3-3 REPs seemed to last for 24 hrs but continuity of these events is uncertain since events can occur over a period of many substorms (e.g. Fig 1.5, Panel F). The maximum longitudinal extent at 60° latitude is approximately 20,000 km. Bailey's 1 hr lower limit translates into 850 km which roughly agrees with Larsen's (1973) estimate of REPs extending greater than 1000 km. The 6 hour duration estimate translates to a 5,000 km longitudinal extent. For very disturbed times, all four outer zone crossings on the same 3 hour rev were on strong diffusion (see Fig 1.5, Panel (G), 22 Sep 1977, 0300-0500 UT) indicating longitudinal extents of 10000-15000 km.

1.5 REP - Proton Precipitation Correlation

In scanning through the data set it was immediately apparent that there was a high correlation between electron and proton precipitation (see catalogue remarks, Appendix C). Particularly noticeable was the similarity between precipitating fluxes in the 235 and 435 keV

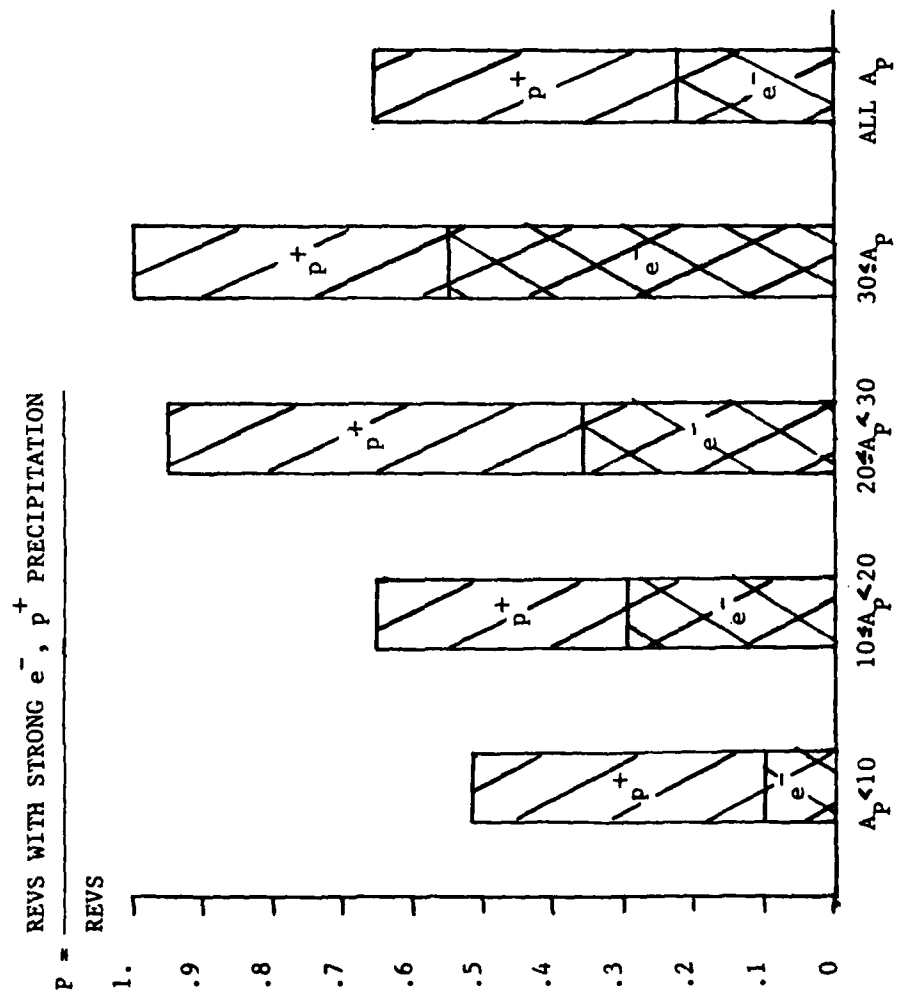
electron and the 80 keV proton channels. An example of this feature is presented in Fig 1.9 which shows the 12, 33, 235 keV electron channel and 80 keV proton channels for 30 Jan 1977. The 12 keV electrons are precipitating from 19590 UT to 20565 UT. Precipitation features for 33 and 235 keV electrons and >80 keV proton are evident at 19646-19700 UT, 19815 UT, and 20475 UT (proton precipitation began at 19580 UT). This suggests the precipitation mechanism for both electrons and protons may be either related or identical. Protons did, however, precipitate much more frequently than electrons and their zone of strong diffusion precipitation generally extended to lower latitude. This frequency difference can be readily seen in Fig 1.10 where the revs (1-4 outer zone passes per rev) with strong electron ($E_{\text{precip}}^- > 235 \text{ keV}$) and proton ($E_{\text{precip}}^+ > 80 \text{ keV}$) precipitation normalized to the number of revs is plotted for increasingly disturbed magnetic conditions. Note that proton precipitation is seen on 65% of revs while electrons on 22% of revs for all magnetic conditions. The high occurrence of proton precipitation in the energy range (100-200 keV) has been previously observed (e.g. On ESRO 1A, Lindalen et al., 1971).

1.6 Classification of REP Events

Due to the strong correlation of REPs with proton (>80 keV) precipitation, the data set was analyzed for REPs without concurrent strong proton precipitation. Only 7 of 313 outer zone passes fell in this category. In addition, all 7 cases had concurrent 33 keV electrons precipitating on strong diffusion and were found at altitudes below 1500 km.

FIGURE 1.9 Flux versus UT plot of 12, 33, 235 keV electrons and
80 keV protons for rev 1656 30 Jan 1977

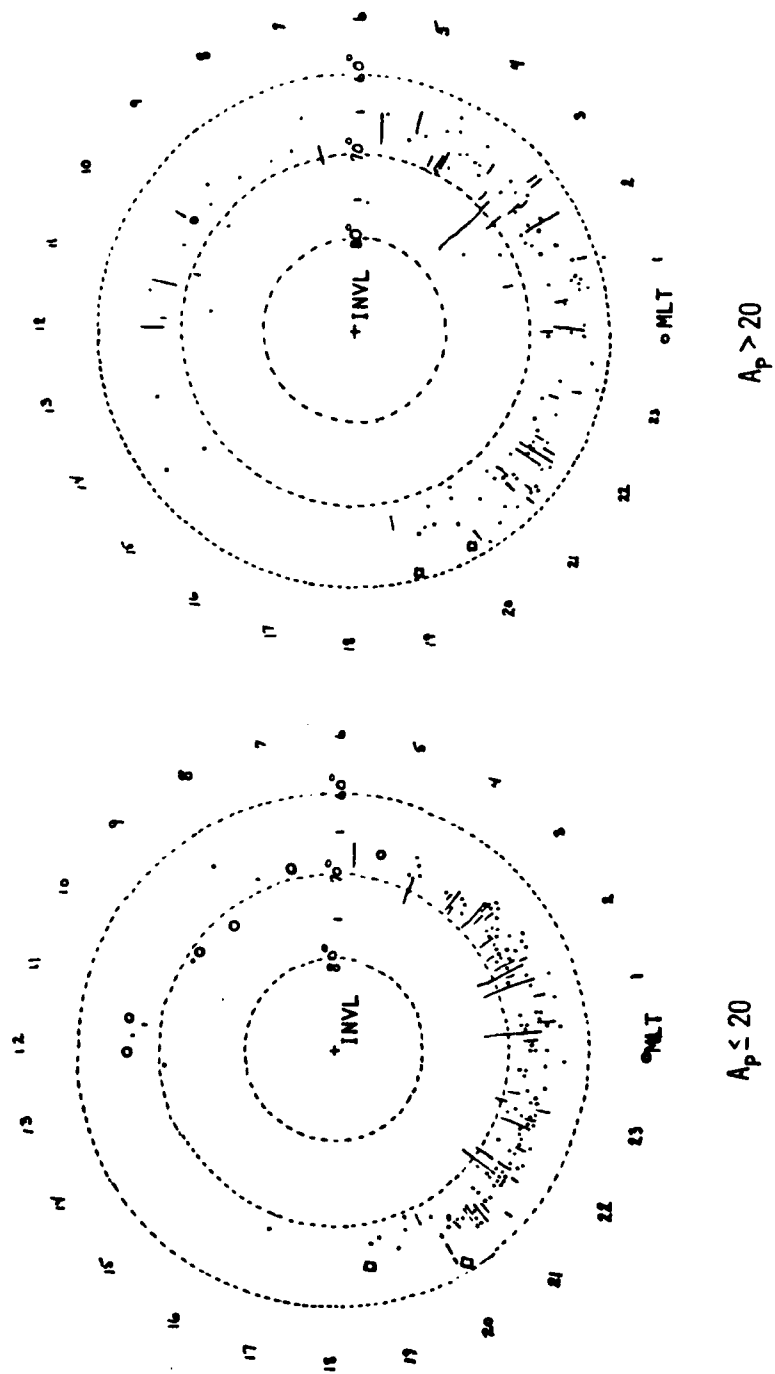
FIGURE 1.10 Percentage of revs (1-4 outer zone passes) with strong e^- or p^+ precipitation normalized to revs number by magnetic conditions.



Analysis of REP energy dependence revealed that the overwhelming majority of REPs had energies in the range 235-1000 keV on strong diffusion. Only 4 events had spectra such that only energies above 1 MeV were on strong diffusion. These same 4 cases were different in another way. They occurred equatorward of the outer edge of the outer zone; the remaining cases except for the seven above all occurred right at the outer edge or extended inward from the outer edge.

The four cases with strong precipitation only above 1 MeV were not among the seven cases which showed no concurrent proton precipitation. REPs could thus be divided into three distinct classes: those with strong diffusion precipitation below (302) and only above (4) 1 MeV with concurrent protons on strong diffusion and those with strong diffusion precipitation below 1 MeV but without strong proton precipitation (7). These classes are displayed in invariant latitude versus MLT in Fig1.11 and will be discussed in detail in Chapter 2.

FIGURE 1.11 REP events displayed according to invariant latitude and MLT for the following classes: dots and lines (. |) for strong precipitation at energies ≤ 1 MeV with concurrent proton precipitation; squares (\square) for strong precipitation at energies ≥ 1 MeV with concurrent proton precipitation; and circles (o) for strong precipitation at energies $\ll 1$ MeV without concurrent proton precipitation.



CHAPTER 2. THEORY AND CASE STUDIES

2.1 Background

To account for the observed subauroral radio signal absorption, Bailey (1968) estimated that the precipitating electrons at energies exceeding several hundred keV required fluxes $J_p \geq 10^3$ electrons/cm²s str. Such intense subauroral (closed field lines) precipitation requires pitch angle scattering of trapped radiation belt electrons near the strong diffusion limit. This leads to an isotropic pitch angle distribution, i.e., precipitated flux \approx trapped flux (Kennel, 1969). The rapid scattering can occur during resonant interaction between plasma waves and particles in the magnetosphere. Either of the first two adiabatic invariants (μ and J) can be violated during the pitch angle diffusion and this can provide a major loss mechanism for geomagnetically trapped particles (Thorne, 1975).

The condition for first order resonant scattering with relativistic electrons is:

$$1 - \mu_{||} \beta_{||} = \frac{\Omega_{-}}{\omega \gamma} \quad (1)$$

where $\mu_{||} = \frac{K_{||} c}{\omega}$, parallel (to ambient magnetic field)
refractive index

$\beta_{||} = \frac{v_{||}}{c}$, normalized parallel electron velocity

ω = wave frequency

$\frac{\Omega_{-}}{\gamma}$ = relativistic electron gyrofrequency

$\gamma = (1 - \beta^2)^{-1/2}$, relativistic mass
enhancement factor

c = speed of light in vacuo

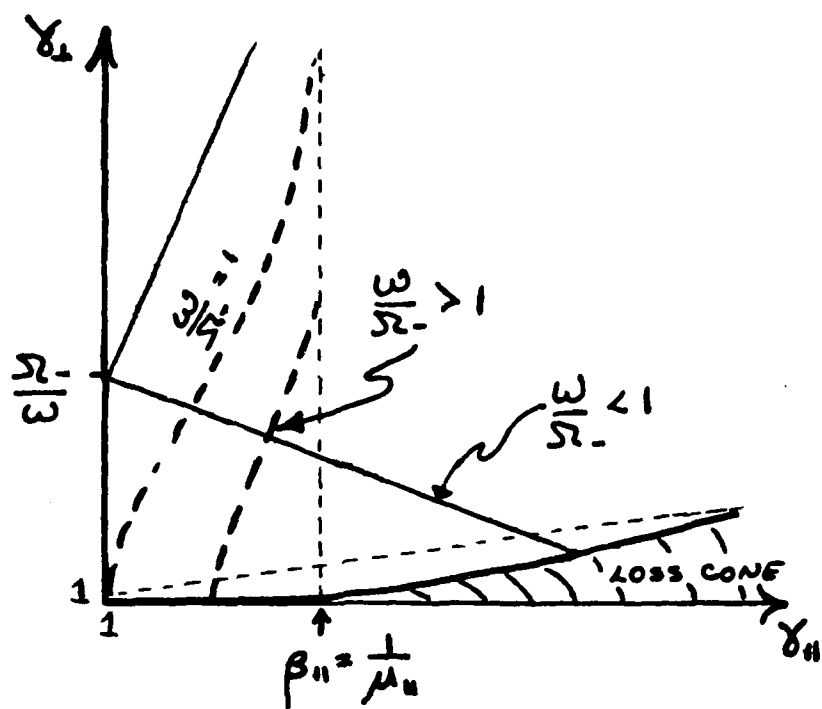
K_{\parallel} = parallel propagation constant

(wave number)

Thorne (1977) has scaled the general morphology of velocity space surfaces for resonance with a wave of a given frequency and refractive index (Fig 2.1). Waves with $\mu_{\parallel} > 1$ generally require $\omega < \Omega_{-}$ to resonate with relativistic electrons because only this surface ($\frac{\omega}{\Omega_{-}} < 1$) reaches the loss cone at relativistic energies. Waves with $\omega > \Omega_{-}$ even with $\mu_{\parallel} < 1$ as in the case of Auroral Kilometric Radiation (Kurth et al., 1975) do not usually resonate with relativistic electrons. A brief review of plasma waves follows.

Southwood (1978) has reviewed the plasma waves found in the magnetosphere. Four distinct classes of waves have been identified in the outer radiation zone $4 \leq L \leq 8$ where REP events are observed. The first class are electron electromagnetic waves at frequencies below the electron gyrofrequency; waves typically occur in the frequency band $.1 \leq \frac{\omega}{\Omega_{-}} \leq .5$. These so-called right hand polarized (Burton and Holzer, 1974) whistler mode "chorus" waves are generated at high altitudes (near the magnetic equator) outside the plasmasphere with typical wide band wave amplitudes ~ 10 mV (Dunckel and Helliwell, 1969, Anderson and Maeda, 1977). The waves propagate down the field lines to low altitudes where they are the most frequently occurring emission outside the plasmopause (Kennel and Thorne, 1967; Thorne and Kennel, 1967; Gurnett et al., 1969; Dunckel and Helliwell, 1969; Tsurutani and Smith, 1974). Dunckel and Helliwell (1969) examined emission

FIGURE 2.1 Velocity space surfaces for resonance with a wave of frequency ω and parallel refractive index μ_{\parallel} for γ_{\perp} versus γ_{\parallel} .



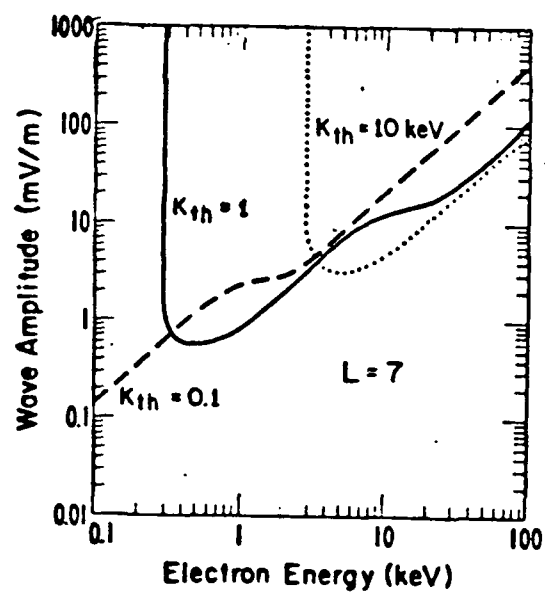
intensities for 300-500 Hz whistler mode chorus and found that they peak near 1000 MLT. Also, just outside the plasmapause, intensities increase abruptly at 0600 MLT and decrease gradually after 1400 MLT in agreement with OV3-3 1.3 kHz low altitude emissions (McPherson and Koons, 1970). A one year study of OGO-5 search coil magnetometer data show that equatorial chorus is strongly substorm correlated with two peaks: one at post midnight (L=5-8) and a second in the dawn to noon sector (L=7-11) (Tsurutani and Smith, 1977). The source of the waves is generation by loss cone instability associated with the pitch angle anisotropy of substorm injected electrons (Kennel and Petschek, 1966). Association of this wave phenomenon with precipitation of energetic electrons (10-100 keV) has been made by several authors (Dungey, 1963; Cornwall, 1964; Kennel and Petschek, 1966; Vampola et al., 1971; Thorne, 1974; Tsurutani and Smith, 1977).

The second class of waves are electron electrostatic waves found at frequencies above the electron gyrofrequency (Kennel et al., 1970). These so-called "n + 1/2" waves ($\frac{\omega}{\Omega_e} \simeq n + 1/2$) are found throughout the magnetosphere outside the plasmapause (Kennel et al., 1970; Shaw and Gurnett, 1975) and are thought to be generated by $\frac{\partial f}{\partial v} > 0$ electron distributions (Fredricks, 1971). The waves are localized about the geomagnetic equator from L=4-10 a majority of the time in the morning sector (Kennel et al., 1970; Fredericks and Scarf, 1973). Wave amplitudes range from 1-10 mV/m (Kennel et al., 1970) with excursions to 100 mV/m during substorms (Scarf et al., 1973). Theoretical parametric studies yielding realistic spatial growth rates

for these waves have been accomplished (Young et al., 1973; Karpman et al., 1975; Ashour-Abdalla and Kennel, 1976) and computations of the resonant electron population show energies of 1-10 keV (possibly accounting for the diffuse aurora, Lyons, 1974) or higher (~ 100 keV) during substorms (Scarf et al., 1973). However, this class of waves does not resonate effectively with relativistic electrons in strong diffusion, requiring wave amplitudes in excess of 100 mV/m to cause strong diffusion of 100 keV electrons (see Fig. 2.2, Lyons, 1974). This class will not be considered further in this study.

Analagous to the right hand electron electromagnetic waves which cut off at Ω_- , there is a third class, the left hand ion electromagnetic waves below Ω_+ (e.g., Cornwall, 1965). In the micropulsation literature these are sometimes referred to as "PCI or IPDP micropulsations" or periodic emissions: PCI ("Pearls") are dispersive waves propagating along field lines thought to be generated by the loss cone distribution of ring current protons just inside the plasmapause (Cornwall, 1965; Cornwall et al., 1970; Williams and Lyons, 1974; Kaye et al., 1979); "IPDP," intervals of pulsations of diminishing period are non-dispersive waves propagating near dusk during substorm expansion (McPherson et al., 1968; Lukkari and Kangas, 1976; Bossen et al., 1976). In a statistical study by Bossen et al. (1976) EMIC occurred mostly about the dusk meridian with frequencies $\frac{\omega}{\Omega_+} \sim .1-.2$ and wave amplitudes 1-7 γ during the main phase of geomagnetic storms. PCI turbulence has also been observed in detached plasma regions (Kivelson et al., 1972) prevalent in the late morning to dusk sector (Chappell,

FIGURE 2.2 Minimum wave amplitudes required for electron strong diffusion scattering at $L=7$ versus electron energy for electron thermal energies 0.1, 1, 10 keV (Lyons, 1974)



1974). Theoretical calculations show that these waves are candidates for hard REPs (precipitating electron energies ≥ 1 MeV) in the evening plasmopause (Thorne and Kennel, 1971) and possibly during the day in detached plasmas (Thorne, 1974).

The last class of waves to be discussed here are the electrostatic ion cyclotron waves predicted by Kennel et al. (1970) after the analogous electrostatic electron wave discovery and measured by Gurnett and Frank (1977) and Kintner et al., (1978). These waves have frequencies $\Omega_+ < \omega < \Omega_{LHR}$, amplitudes on the order of a few 10s of mV/m, and are found at all local times at $L > 6$ (Gurnett and Frank, 1977; Kintner et al., 1978). Generation of the waves is thought to be by current driven instability low on the field line to yield resonant Landau growth (Kindel and Kennel, 1971; Ashour-Abdalla and Thorne, 1978) and/or equatorial anisotropic pitch angle instability due to distributions of hot protons (Coroniti et al., 1972; Ashour-Abdalla and Thorne, 1977; Ashour-Abdalla and Thorne, 1978). Observations have indeed correlated REPs with intense ELF electrostatic waves (Koons et al., 1972) and shown that some cases can be explained only as a low altitude phenomenon (Vampola, 1977).

2.2 Resonant Populations

Since the observational data covers the electron energy range 12 keV-1.6 MeV and proton range > 80 keV, > 150 keV etc., it is important to determine the electron and proton resonant populations for each wave phenomena if any success at discrimination (between wave mechanism) is to be accomplished. We proceed with calculations for

each wave type.

2.2.1 Whistler Mode Chorus

The cold plasma dispersion relation for parallel whistler mode chorus propagation assuming $\Omega_+ \ll \omega \ll \Omega_-$ and $\mu_{||} \gg 1$ ($\omega_p \gg \Omega_-$) is given by Kennel and Petschek (1966):

$$\mu_{||}^2 \approx \frac{\omega_p}{\omega \Omega_-} \left(1 - \frac{\omega}{\Omega_-}\right)^{-1} \quad (2)$$

where ω_p = plasma frequency.

Using this dispersion relation and the condition for first order cyclotron resonance with relativistic electrons (eq. 1) assuming $\beta_{||} \approx \beta$ (valid near the loss cone), Thorne (1974) has derived an expression for resonant electron energies:

$$\left(\gamma^2 - 1\right)_{res} \approx \frac{2 E_m^- \Omega_-}{E_0^- \omega} \left(1 - \frac{\omega}{\Omega_-}\right)^3 \quad (3)$$

where $E_m^\pm = \frac{B^2}{8\pi N^\pm}$, magnetic energy per particle

B = local magnetic field value

N^\pm = particle number density

$E_0^\pm = m^*c^2$, particle rest energy.

Thus the expression for the resonant electron population with whistler mode chorus waves of frequency ω is:

$$E_r^- = \left[\left(\frac{2 E_m^- \Omega_-}{E_0^- \omega} \left(1 - \frac{\omega}{\Omega_-}\right)^3 + 1 \right)^{1/2} - 1 \right] E_0^- \quad (4)$$

where E_r^- is the resonant electron energy.

Since $B \approx \frac{B_0}{L^3}$ at the equator where $B_0 = .311$ Gauss and N varies from approximately $10^3/\text{cm}^3$ in the plasmasphere ($L=4$) to $1-10/\text{cm}^3$ in the plasma trough region ($L=5-8$) for a $K_p \sim 2-3$ (Chappell et al., 1970), we have a range of E_m^- of .5 keV ($L=4$, $N=10^3$) to 150 keV ($L=5$, $N=1$) at the equator. Down on the field line (away from the equator) where B increases and N is less than ionospheric densities ($< 10^4$) the value of E_m^- can reach a few 100 keV. Values of N not greater than 10^4 cm^{-3} are used since whistler mode chorus propagating down the field line rapidly becomes perpendicular to the local magnetic field line and reflects at frequencies near the lower hybrid resonance (Thorne and Kennel, 1967). [For propagation at angles to the field line, the cumulative contribution from parallel velocity resonances is appropriate since higher order resonances become important (Stix, 1962; Kennel and Petschek, 1966) although this is not the case for electromagnetic waves with $k_{\perp} \approx 0$.] So for $.1 \leq \frac{\omega}{\Omega_-} \leq .5$ (Tsurutani and Smith, 1977) and $E_m^- = .5-150$ keV (both typical equatorial values), we have $E_r^- = 1-800$ keV. Off the equator (down the field line where $\frac{\omega}{\Omega_-}$ is lower and E_m^- is higher) E_r^- is expected to reach values of nearly 10^3 keV.

For proton precipitation we use the resonance condition for first order ($n=1$) cyclotron resonance with protons

$$1 - \mu \beta_{\parallel} = \frac{\Omega_+}{\omega} \quad (5)$$

and the dispersion relation for whistlers to obtain

$$E_r^+ \approx \left(\frac{m^+}{m^-} \right) E_m^+ \left(\frac{\omega}{\Omega_-} \right) \left(1 - \frac{\omega}{\Omega_-} \right) \quad (6)$$

where $\frac{m^+}{m^-} = 1.837 \times 10^3$, proton to electron mass ratio. We take $E_m^+ \approx E_m^-$, since we assume the densities of electrons to be the same as protons (DeForest and McIlwain, 1971). Using the same range of values for $\frac{\omega}{\Omega_-}$ we can readily see that E_r^+ will typically be greater than an MeV (except in the dense plasmasphere) in agreement with Kennel and Petschek (1966).

Resonance energies for both electrons and protons are shown in Fig. 2.3. One readily sees that electrons can be resonant at energies up to several hundred keV while protons are resonant only at energies above 1 MeV.

2.2.2 Electromagnetic Ion Cyclotron (EMIC) Waves

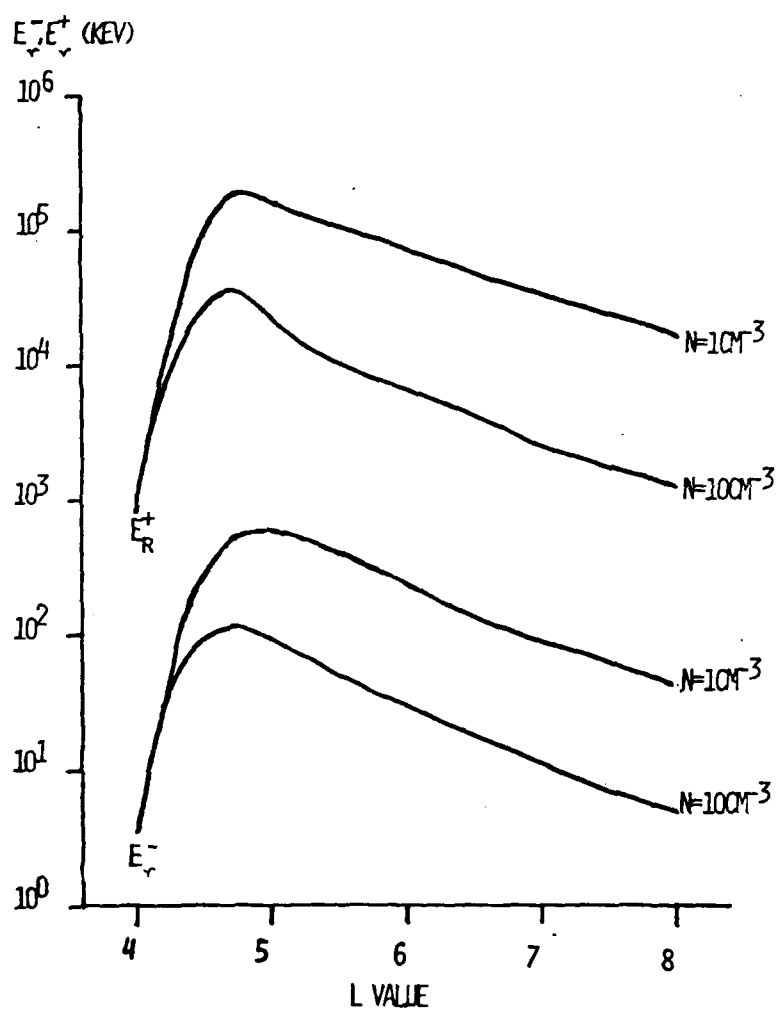
The cold plasma dispersion relation for parallel propagating EMIC waves below Ω_+ is given by Kennel and Petschek (1966):

$$\mu_{11}^2 = \frac{\omega_p^2}{\Omega_- \Omega_+} \left(1 - \frac{\omega}{\Omega_+} \right)^{-1} \quad (7)$$

Thorne and Kennel (1971) and Thorne (1974) have used equations (1) and (7) to derive the equation for resonant electrons with EMIC:

$$\left(\gamma^2 - 1 \right)_{res} \approx \frac{2 E_m^-}{E_o} \left(\frac{m^+}{m^-} \right) \left(\frac{\Omega_+}{\omega} \right)^2 \left(1 - \frac{\omega}{\Omega_+} \right) \quad (8)$$

FIGURE 2.3 Electron and proton resonant energies for the whistler mode chorus mechanism ($.1 \leq \frac{\omega}{\Omega_-} \leq .5$) [in keV] versus L for $N=10^4 \text{ cm}^{-3}$ for $L=4$ and $N=1, 10 \text{ cm}^{-3}$ for $L \geq 5$.



and we see that (8) becomes

$$E_r^- = \left\{ \left[\frac{2 E_m^- m^+ \Omega_+^2}{E_o^- m^- \omega^2} \left(1 - \frac{\omega}{\Omega_+} \right) + 1 \right]^{1/2} - 1 \right\} E_o^- \quad (9)$$

Using the previous value of E_m^\pm at $L=4$, $N=10^3 \text{ cm}^{-3}$, and $\frac{\omega}{\Omega_+} \simeq .1-.5$ (Bossen et al., 1976) we see that $E_r^- \sim \text{few MeV}$, see Fig 2.4. Even during intense injection events where EMIC waves may be generated outside the plasmasphere to $L=8$ due to enhanced ion fluxes and larger loss cone distributions (Coroniti et al., 1976), E_r^- for $L=8$, $N=10$, and $\frac{\omega}{\Omega_+} \sim .2$ is 5 MeV.

The equation for EMIC resonance with protons is given by Kennel and Petschek (1966):

$$E_r^+ = E_m^+ \left(\frac{\Omega_+}{\omega} \right)^2 \left(1 - \frac{\omega}{\Omega_+} \right)^3 \quad (10)$$

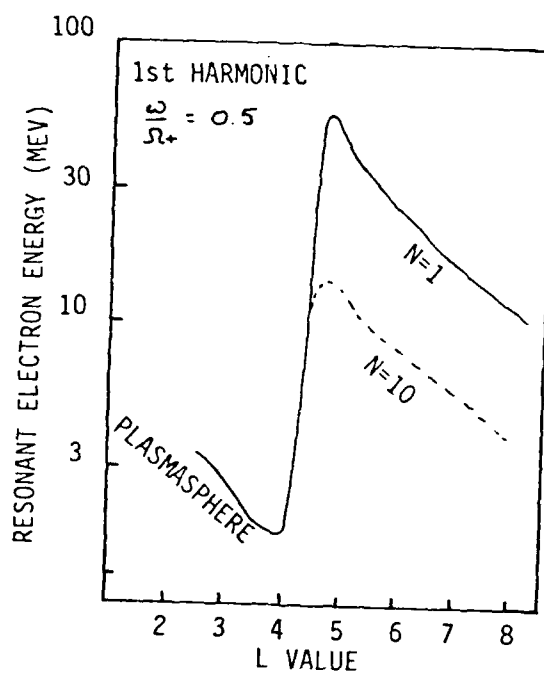
Using the same E_m^\pm values and $\frac{\omega}{\Omega_+} = .1-.2$ (Bossen et al., 1976) we see $E_r^+ \simeq 10\text{s}-100\text{s keV}$ near the outer edge of the plasmasphere.

In summary, EMIC waves resonate with electrons only at energies $\gg 1 \text{ MeV}$ and only near 1 MeV in the relatively dense plasmasphere or detached plasma regions where N is relatively large and at the equator where B is lowest. The resonant proton population for the same wave mechanism is on the order of 10's and 100's keV.

2.2.3 Electrostatic Ion Cyclotron (ESIC) Waves

Since the frequency of ESIC waves is near the Ω_+ , we can

FIGURE 2.4 Resonant electron energies versus L for the ion cyclotron ($\frac{\omega}{\Omega} = 0.5$) wave mechanism for densities $N=1, 10 \text{ cm}^{-3}$ outside the plasmasphere and $N=10^3 \text{ cm}^{-3}$ $L=4$ (Thorne and Kennel, 1971).



eliminate the unity term in (1) to obtain:

$$\gamma^2 \mu_{ii}^2 \beta_{ii}^2 = \left(\frac{\Omega_-}{\omega} \right)^2 \quad (11)$$

Using $\gamma^2 \beta_{ii}^2 \simeq \gamma^2 - 1$ (valid for particles near the loss cone) in (11) we have:

$$\gamma^2 - 1 = \mu_{ii}^{-2} \left(\frac{\Omega_-}{\omega} \right)^2 \quad (12)$$

By writing the wave refractive index $\mu_{ii}^2 = \frac{c^2 K_{ii}^2}{\omega^2} \frac{f_+^2 \Omega_+^2}{v_{th}^2}$, where Ω_+ is the ion gyroratio, v_{th} is the ion thermal speed, and $f_+ = v_{th}/\Omega_+$, eq. (12) becomes:

$$(\gamma^2 - 1)_{res} \simeq \left(\frac{\Omega_-}{\Omega_+} \right)^2 \left(\frac{v_{th}^+}{c} \right)^2 \left(\frac{1}{K_{ii} f_+} \right)^2 \quad (13)$$

Using $\left(\frac{v_{th}^+}{c} \right)^2 = 2 \frac{E_{th}^+}{E_o^+}$, where E_{th}^+ is the ion thermal energy, in (13) we have:

$$(\gamma^2 - 1)_{res} = \frac{2 E_{th}^+}{E_o^+} \left(\frac{m^+}{m^-} \right)^2 \left(\frac{1}{K_{ii} f_+} \right)^2 \quad (14)$$

The resonant electron energy for ESIC waves is thus:

$$E_e^- = \left\{ \left[\frac{2 E_{th}^+}{E_o^+} \left(\frac{m^+}{m^-} \right)^2 \left(\frac{1}{K_{ii} f_+} \right)^2 + 1 \right]^{1/2} - 1 \right\} E_o^- \quad (15)$$

Ashour-Abdalla and Thorne (1977 and 1978) have solved the electrostatic dispersion relation numerically and obtained k space contours of temporal and convective growth rates normalized to f_+ for typical equatorial and ionospheric conditions. If waves are excited by the current driven instability in the topside ionosphere with electron drifts just above the Kindel and Kennel (1971) marginal stability limit, 1 Re above the earth for $L \simeq 10$, $E_{th} \simeq 2\text{ev}$, the first three harmonics (typical of wave observations, Kintner et al., 1978) have typical values for $k_{||}$ $f_+ \simeq .26-.1$ (Ashour-Abdalla and Thorne, 1978). This yields values of $E_r^- \simeq 50-300$ keV. For excitation in the equatorial plasmasheet by the loss cone instability, typical equatorial parameters are $E_{th} \simeq 1$ keV, and $k_{||} f_+ \simeq .4-.5$ for the first five harmonics. This gives $E_r^- \simeq 100$ keV - 2 MeV. Again using the first order cyclotron relation for resonance with protons (eq. 5) we have:

$$1 - \mu_{||} \beta_{||} = \frac{\Omega_+}{\omega}$$

Rewriting, we have

$$\beta_{||}^2 = \frac{1}{\mu_{||}^2} \left(1 - \frac{\Omega_+}{\omega} \right)^2$$

or

$$\beta_{||}^2 = \left(\frac{\Omega_+}{\omega} \right)^2 \left(1 - \frac{\omega}{\Omega_+} \right)^2 \frac{1}{\mu_{||}^2}$$

Substituting for $\mu_{||}^2$, we have:

$$\beta_{||}^2 = \frac{v_{||}^2}{c^2} = \frac{\Omega_+^2}{c^2 k_{||}^2} \left(1 - \frac{\omega}{\Omega_+} \right)^2 \quad (16)$$

and

$$\frac{1}{2} m^+ v_{\perp}^2 = E_r^+ = \frac{v_{th}^2 m^+ c^2}{2 k_{\parallel}^2 f_+^2 c^2} \left(1 - \frac{\omega}{\Omega_+}\right)^2 \quad (17)$$

thus

$$E_r^+ = E_{th}^+ \left(\frac{1}{k_{\parallel} f_+}\right)^2 \left(1 - \frac{\omega}{\Omega_+}\right)^2 \quad (18)$$

Since $\left(\frac{1}{k_{\parallel} f_+}\right)^2 \left(1 - \frac{\omega}{\Omega_+}\right)^2$ is of the order one (1), $E_r^+ \approx E_{th}^+$, i.e., 2 eV - 1 keV. It must be noted, however, that higher order resonances must be taken into account since these electrostatic ion cyclotron waves have polarizations $\frac{k_{\perp}}{k_{\parallel}} \approx 10$ (Kintner et al., 1978). It will be shown in the next section that, unlike electromagnetic waves, resonant electrostatic wave amplitudes required for strong diffusion scattering decrease with increase in energy of the resonant population ($\gamma \rightarrow \infty$). Thus resonant energies for ions can easily reach a few 100 keV (Ashour-Abdalla and Thorne, 1978). So in summary, electrons with $E_r^+ \approx 50 \text{ keV} - 2 \text{ MeV}$ and ions with $E_r^+ \approx 1 - 100$'s keV can resonate with electrostatic ion cyclotron waves.

2.3 Wave Amplitudes

Now that the resonant electron and proton population is known for each wave mechanism, it is useful to determine the resonant wave amplitudes required for strong diffusion. We will relate the ability of observed wave amplitudes to

AD-A092 545

AIR FORCE INST OF TECH WRIGHT-PATTERSON AFB OH F/G 4/1
RELATIVISTIC ELECTRON PRECIPITATION: AN OBSERVATIONAL STUDY. (U)
1980 L J ANDREOLI
UNCLASSIFIED AFIT-CI-80-26D NL

2 of 4

AD-A092 545



populations on strong diffusion but the equations will help later when examining real cases.

The condition for strong diffusion, i.e., very rapid scattering, is

$$\tau_D \ll \tau_{1/4B} \quad (19)$$

where τ_D = diffusion loss time

$\tau_{1/4B}$ = 1/4 bounce time

This permits the particle distribution to become isotropic even over the loss cone ($= > J_p \approx J_t$). The loss time approaches a minimum value under strong diffusion and the diffusion coefficient, D , is larger than $1/\tau_{\min}$, where τ_{\min} is the minimum rate of diffusion loss. $\tau_{\min} \approx \frac{2 \tau_{1/4B}}{\alpha_L^2}$ where α_L is the pitch angle of the loss cone.

2.3.1 Electromagnetic Waves

The action of electromagnetic waves on particles is mainly via pitch angle scattering. The pitch angle scattering coefficient, $D_{\alpha\alpha}$, is given by Kennel and Petschek (1966):

$$D_{\alpha\alpha} = \frac{(\Delta\alpha)^2}{2 \Delta t} \approx \pi \Omega - \left(\frac{b}{B_0}\right)^2 \quad (20)$$

where b = wave amplitude

B_0 = ambient magnetic field value

and for strong diffusion scattering one requires

$$D_{\alpha\alpha} \approx D_{\alpha\alpha} \approx \frac{\alpha_L^2}{2 \tau_{1/4B}} \quad (21)$$

where α_L = loss cone pitch angle

D_{SD} = coefficient for strong diffusion.

Equation (20) can be rewritten including the relativistic mass correction and bounce averaging to obtain:

$$D_{aa} \approx \frac{\pi \Omega_-}{\gamma} \left(\frac{b}{B_0} \right)^2 f \quad (22)$$

where f = is the fraction of the electron bounce orbit spent in resonance with waves.

For equatorial loss cones, $\alpha_L^2 \approx \frac{1}{2L^3}$. For electrons, $\tau_{1/4B} \approx \frac{LR_0}{v^-} \approx \frac{LR_0}{c}$ where $R_0 = 1$ earth radius. Equating (22) and (20) with substitutions yields a fluctuating field wave amplitude for strong electron diffusion:

$$b_{SD}^- = \left(\frac{B_0^2 c \gamma}{4\pi L^4 R_0 \Omega_- f} \right)^{1/2} \quad (23)$$

and

$$b_{SD}^- = \frac{100 \gamma^{1/2}}{L^{7/2}} \text{ (gammas) for } f = \frac{1}{5} \quad (24)$$

For ions, $\tau_{1/4B} = \frac{LR_0}{v^+} = \frac{LR_0}{(2E^+/E_0^+)^{1/2} c}$, $\Omega_- = \frac{m^+}{m^-} \Omega_+$, and $\gamma \sim 1$ where E^+ and E_0^+ are the ion energy and ion rest energy respectively. Likewise, the fluctuating field wave amplitude for strong ion diffusion is

$$b_{SD}^+ = \left[\frac{m^+}{m^-} \left(\frac{2 E^+}{E_0^+} \right)^{1/2} \frac{B_0^2 c}{4 \pi L^4 R_0 \Omega_e} \right]^{1/2}$$

and

(25)

$$b_{SD}^+ = \frac{1.65 E^+{}^{1/4} (\text{KeV})}{L^{7/2}} (\text{gamma s})$$

Strong electron diffusion ($E_{\gamma}^- \sim 1/2 - 1$ MeV; $\gamma \sim 2-3$) thus requires amplitudes of 1 gamma at $L=4$ and 100 m γ at $L=8$. For ion strong diffusion ($E_{\gamma}^+ \sim 50$ keV), amplitudes of 3.5 gammas at $L=4$ and 300 m γ at $L=8$ are required. These values are within the range of amplitudes for both electrons and ions for EMIC waves (1-7 γ) found by Bossen et al. (1976) but only the most intense chorus events with amplitudes approximately 100 m γ (Tsurutani and Smith, 1977) meet the criteria for electrons at $L=8$.

2.3.2 Electrostatic Amplitudes

Electrostatic waves scatter electrons primarily by energy diffusion. Scattering by energy in the perpendicular (to the magnetic field line) direction at the edge of the loss cone requires a diffusion coefficient as follows:

$$D_{\perp\perp} = \frac{\langle \Delta v_{\perp} \rangle^2}{\Delta t} \quad (26)$$

For strong diffusion which can maintain isotropy over the loss cone one requires

$$D_{\perp\perp} \geq D_{SD} \approx \frac{V_{res}^2 \alpha_L^2}{\tau_{1/4B}} \approx \frac{V_{res}^2}{\tau_{1/4B}} \left(\frac{B_0}{B_A} \right) \quad (27)$$

where $B_A = B(100 \text{ km})$.

An approximate expression for $D_{\perp\perp}$ as a function of electrostatic wave amplitude can be derived (e.g. Ashour-Abdalla and Thorne, 1978):

$$D_{\perp\perp}^{\pm} = \frac{\Omega_{\pm}^2 c^2 \mathcal{E}_w^2}{\gamma^{\pm} B_0^2} \quad (28)$$

where \mathcal{E}_w is the electric field amplitude of the electrostatic wave. Equating eqs. (27) and (28) and using $\tau_{1/4B} = \frac{LR_0}{v} \sim \frac{LR_0}{c}$, we have for the fluctuating wave amplitude for electron strong diffusion

$$\mathcal{E}_w^{-} = \left[\frac{c}{LR_0} \left(\frac{B_0}{B_A} \right) \frac{B_0^2 \gamma^{-}}{\Omega^{-}} \right]^{1/2} \quad (29)$$

At the equator $\frac{B_0}{B_A} \approx \frac{1}{2L^3}$ and $\mathcal{E}_{w_{eq}}^{-} = [3.7 \times 10^8 \frac{\gamma^{-}}{L}]^{1/2} (\frac{mV}{m})$. For $\gamma^{-} = 2-3$, we have $\mathcal{E}_w^{-} = 20-250 \frac{mV}{m}$ for $L=8-4$. In the topside ionosphere near 1 Re, $\frac{B_0}{B_A} \approx \frac{1}{10}$, $B_0 \approx .05$, and $\mathcal{E}_{w_{1Re}}^{-} = [1.4 \times 10^7 \frac{\gamma^{-}}{L}]^{1/2} (\frac{mV}{m})$. For $\gamma^{-} = 2-3$, we have $\mathcal{E}_w^{-} \approx 1-3 \frac{V}{m}$ for $L=8-4$.

For the concomitant ion strong diffusion using eq. (27) and

$$D_{SD}^{+} = \Omega_{+}^2 c^2 \frac{\mathcal{E}_w^{+2}}{B_0^2} \quad (30)$$

we have

$$\mathcal{E}_\omega^+ = \left[\frac{c}{LR_0} \left(\frac{B_0}{B_A} \right) \left(\frac{B_0^2 \gamma^+ m^+}{\Omega_- m^-} \right) \left(\frac{2 E^+}{E_0^+} \right) \right]^{1/2} \quad (31)$$

and

$$\mathcal{E}_\omega^+ = \left[9.4 \times 10^6 \left(\frac{B_0}{B_A} \right) \frac{B_0 E^+ (\text{keV})}{L} \right]^{1/2} \left(\frac{\text{mV}}{\text{m}} \right) \quad (32)$$

Again for the equator $\frac{B_0}{B_A} \approx \frac{1}{2L^3}$ and $\gamma^+ = 1$ we have $\mathcal{E}_\omega^+ = 6 \frac{\text{mV}}{\text{m}} - 66 \frac{\text{V}}{\text{m}}$ at $L=8-4$ for a 50 keV ring current proton. At the 1 Re, $\frac{B_0}{B_A} \approx \frac{1}{10}$ $B \approx .05$ and $\gamma^+ = 1$, we have $\mathcal{E}_\omega^+ = 550 \frac{\text{mV}}{\text{m}} - 750 \frac{\text{mV}}{\text{m}}$ for a 50 keV ring current proton.

Electrostatic ion cyclotron waves have electric field amplitudes typically on the order of 10-100's $\frac{\text{mV}}{\text{m}}$ (Gurnett and Frank, 1977 and Kintner et al., 1978). Required wave amplitudes for both ions and electrons are easily met by these waves in the equatorial regime but not in the topside ionosphere.

Table 2.1 lists the range of parameters for strong ion and electron diffusion.

2.4 Case Studies

An example of each of the classes described in Section 1.6 is presented. Each example was selected as being most representative with amount of peripheral data available as an added factor.

2.4.1 Case 1, ESIC (rev 479, day 250, 6 SEP 1976).

The flux versus time plots for electron channels 12-1600 keV

TABLE 2.1 Theoretical REP mechanisms and characteristics.

THEORETICAL REP MECHANISMS

<u>WAVE</u>	<u>FREQ</u>	E^-_{RES}	E^+_{RES}	<u>MIN AMP S.D.</u> ELECTRONS	<u>MIN AMP S.D.</u> PROTONS
WHISTLER MODE CHORUS	$.1 < \omega / \omega_{ci}$	10-100s KEV	1-10 MEV	100ms- γ	300ms-3 γ
EM ION CYCL	$\omega < \omega_+$	1-10 MEV ($N=10^3$)	10 KEV-1 MEV	100ms- γ	300ms-3 γ
ES ION CYCL	$\omega_+ < \omega < \omega_{UH}$	10 KEV-2 MEV	100 EV-100s KEV	10s-1000ms/ γ	5-750ms/ γ

and protons 80-770 keV for three outer zone passes are shown in Fig 2.5 a,b,c, respectively. The low altitude outer zone pass at local evening (Fig 2.5a) shows an extended region of 12 keV precipitation (isotropic) at $L \approx 5-10$. This is actually an inverted V event which is bounded by 235 keV precipitation. At $L=5$ the precipitation extends to nearly 1 MeV electrons and 80 and 150 keV protons. This agrees well with the criteria of ESIC (Table 2.1). Fig 2.5b shows the outer zone pass at high altitude (~ 8000 km) near local dusk. Twelve (12) keV electrons are precipitating from $L \approx 7-9$ with two large spikes near $L \approx 8.4$. The two spikes are associated with two electrostatic shocks (Kintner, private communication) with perpendicular electric field $\mathcal{E}_\perp \approx 500$ mV/m. In addition > 80 and > 150 keV protons are precipitating from $L \approx 6$. Although there is significant trapped 235 keV electron flux from $L \approx 6.8-7.8$, there is no precipitation. The next pass (Fig 2.5c) is a medium altitude (~ 5000 km) pass near local morning. Twelve (12) keV electron precipitation is evident from $L \approx 6-13$. Extensive 33 keV is coincident although not on strong diffusion from $L \approx 9-12$. The 235 keV channel shows "moderate" precipitation at $L \approx 6-8$. Significant fluxes of > 80 keV protons are present to roughly $L \approx 12$ without any precipitation. This fits the criteria of whistler mode chorus in Table 2.1.

Pitch angle plots of the low altitude local evening outer zone pass of rev 479 are shown in Fig 2.6. Panel (A) at 5962 UT shows a normal pitch angle distribution both down (0°) and up (180°) the local magnetic field line. Panel (B) shows the next distribution towards

FIGURE 2.5a Flux (counts/sec, every fourth data point) versus L value of low altitude (700 km) outer zone pass near local evening. Vertical arrows (\uparrow) indicate singular precipitation and horizontal arrows ($\rightarrow \leftarrow$) indicate limits of extended precipitation.

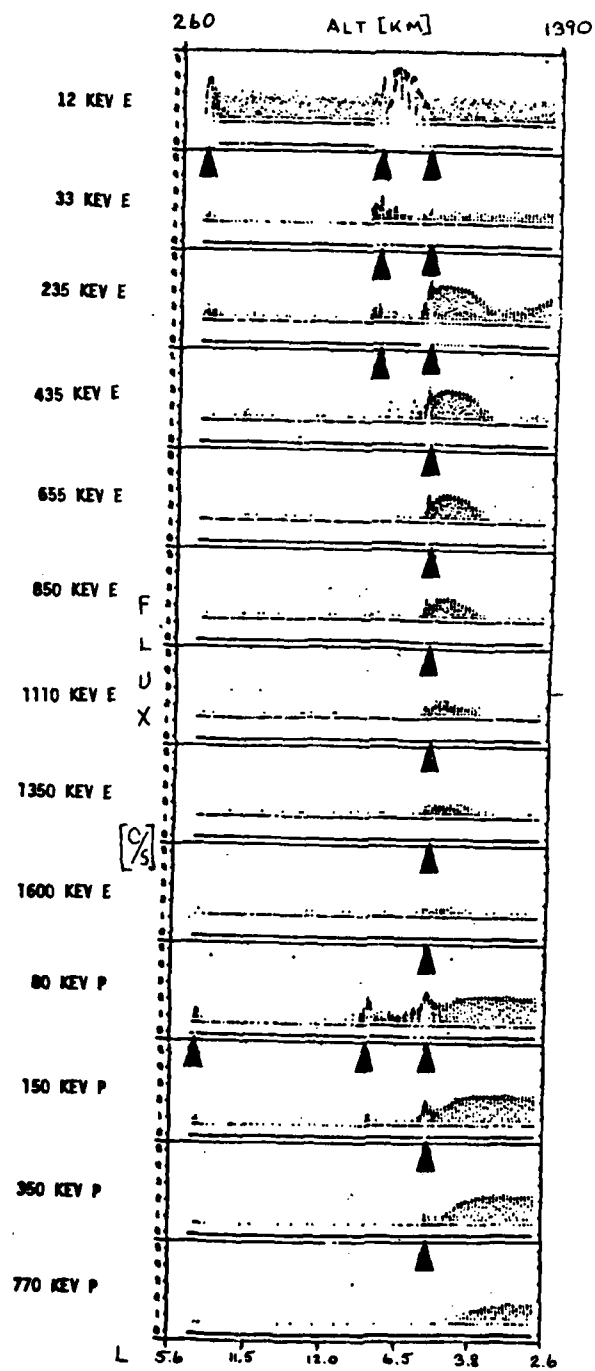


FIGURE 2.5b Same plots for high altitude (8000 km) passes at local dusk.

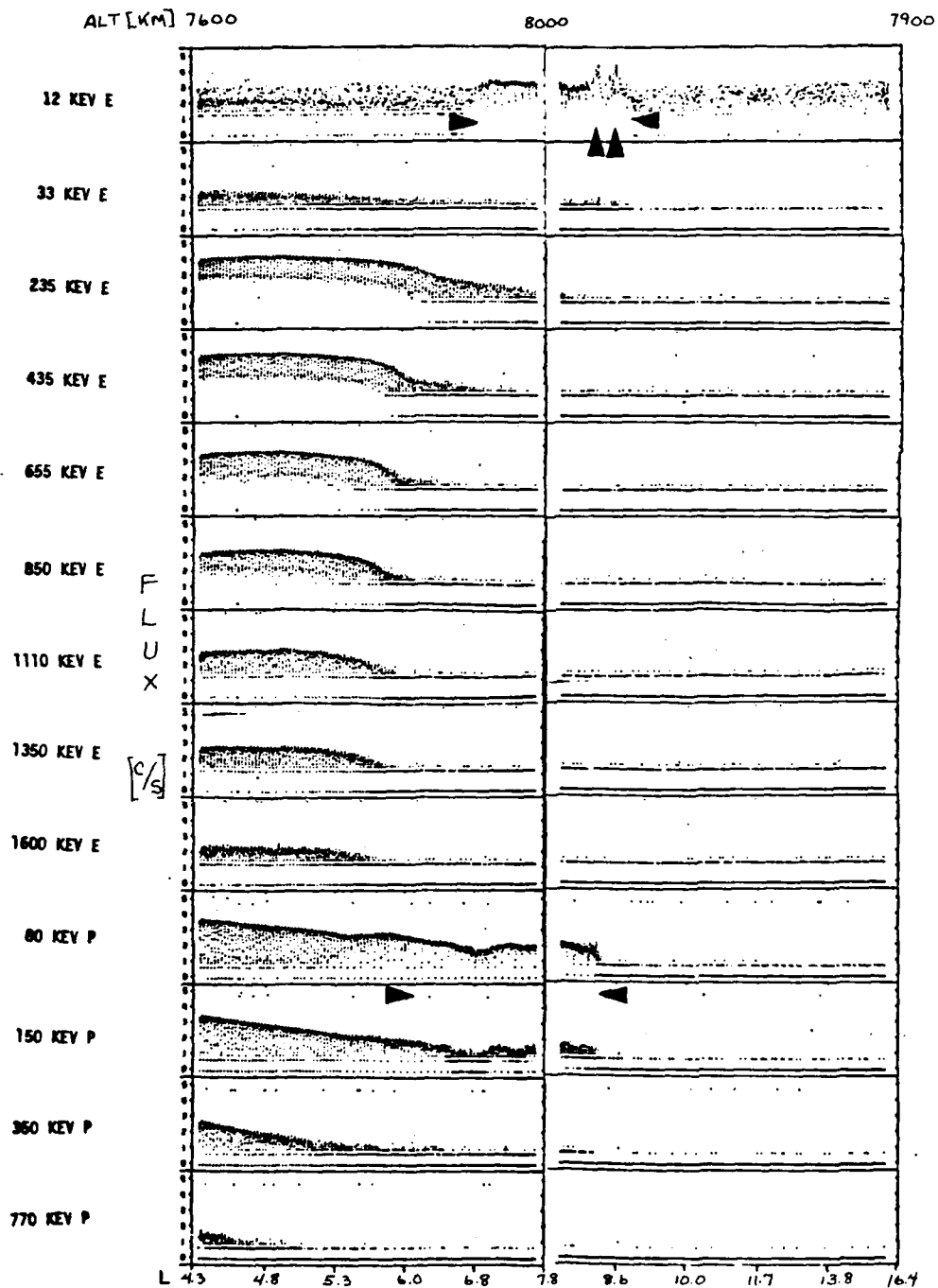


FIGURE 2.5c Same for medium altitude (5000 km) passes at
local morning.

ALT [KM] 6250

4550

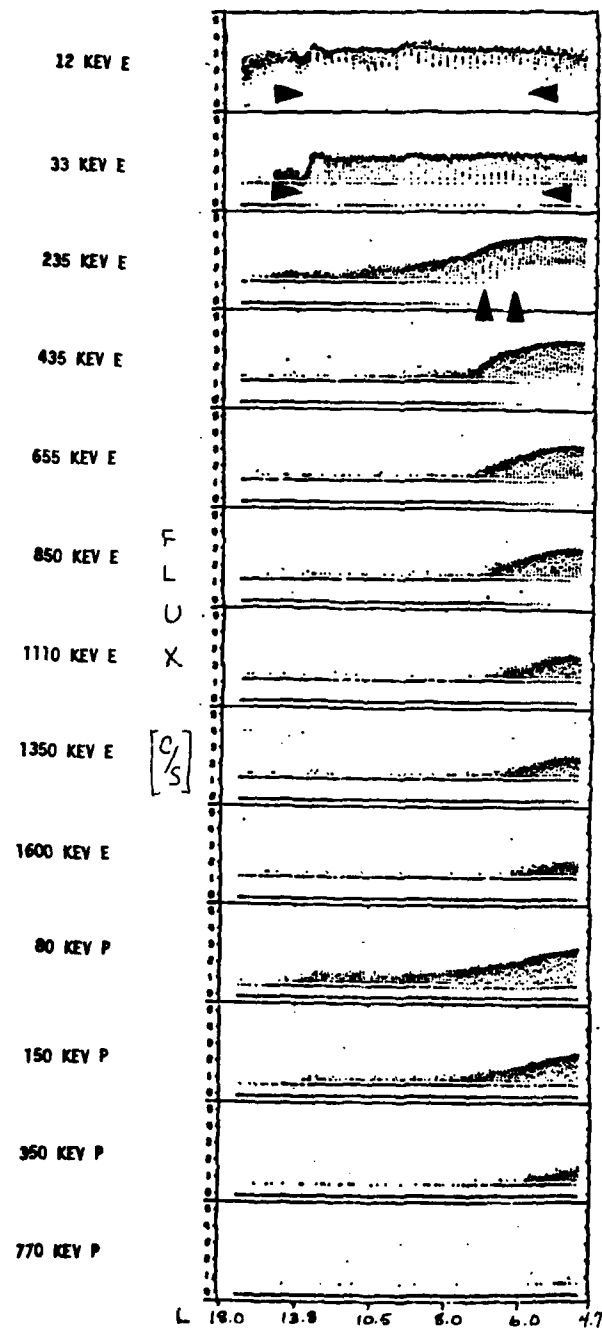
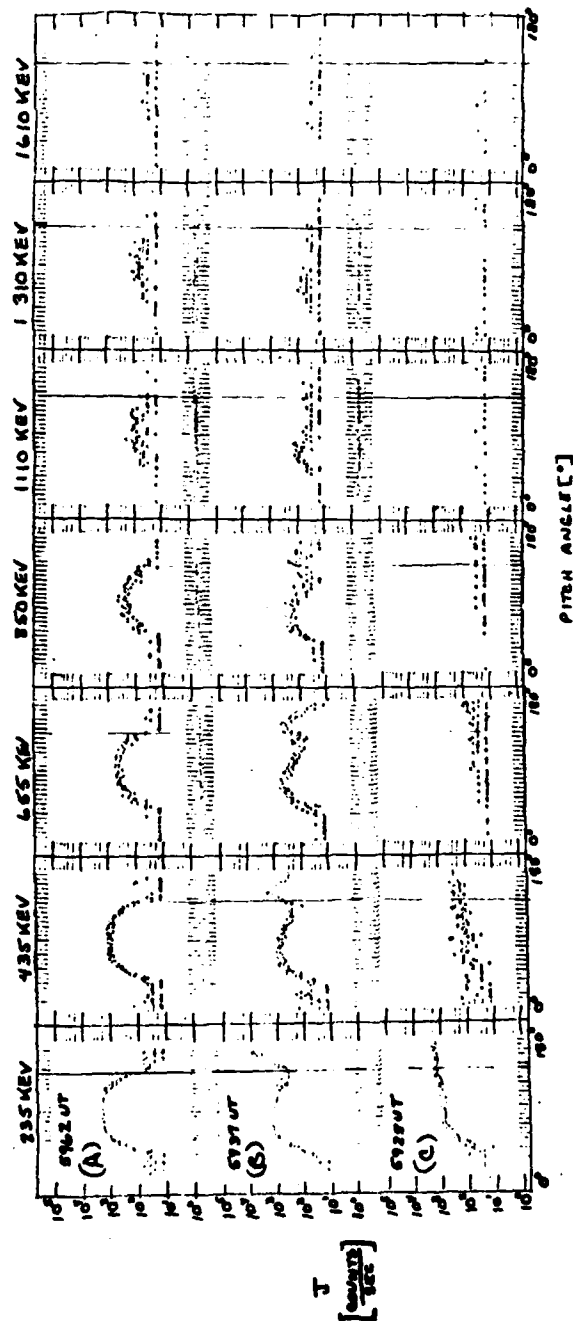


FIGURE 2.6 Pitch angle versus flux (counts/sec) for 235-1610 keV electron channels for 3 times in the local evening outer zone of rev 479. The upward loss cone (L.C. = 50°) is indicated by the vertical line.



the outer edge of the outer zone with a large spike in the upward viewing loss cone. The very next distribution Panel (C) shows isotropic flux in the upward loss cone. Isotropic fluxes are evident to ~ 1 MeV.

Since the precipitating flux is higher than the locally trapped flux, one can estimate the altitude at which pitch angle scattering occurred (Vampola, 1977). This is accomplished by tracing the precipitation flux to the shape of the outer zone as illustrated in Fig 2.7. At $L=4$ the trapped flux would be roughly 2×10^4 counts/sec up the field line where the precipitation occurred. Fig 2.5b shows fluxes near $L=4$ of approximately 2×10^4 counts/sec. The altitude of this pass is ~ 7600 km. It must be noted that this "spikey" event is very rare with the overwhelming majority of precipitation cases showing flat isotropic fluxes.

Resonance with 1 MeV electrons at ~ 1 Re would require $\frac{1}{k_{\parallel} \beta_+} \approx .008$, slightly smaller than values for first three harmonics calculated by Ashour-Abdalla and Thorne (1978). In addition, the wave amplitude is $\mathcal{E}_w \approx 350 \frac{mV}{m}$. Both these calculations indicate that higher harmonics may play a very important role in the mechanism.

Fig 2.8a shows time spectrograms for the filtered plasma wave data (frequency .03-100 KHz) and low energy electron (.2-33 keV) and protons (.1-3.9 keV), 235 keV electrons and > 80 keV protons of the low altitude local evening pass. The 80 keV proton and 235 keV electrons are seen to precipitate (upward loss cone filled) at 5815 UT and 5950 UT (the spike occurred here). Between these times is the inverted V electron event. Plasma turbulence is also evident but not well

FIGURE 2.7 Enlargement of portions of Figure 2.5a.

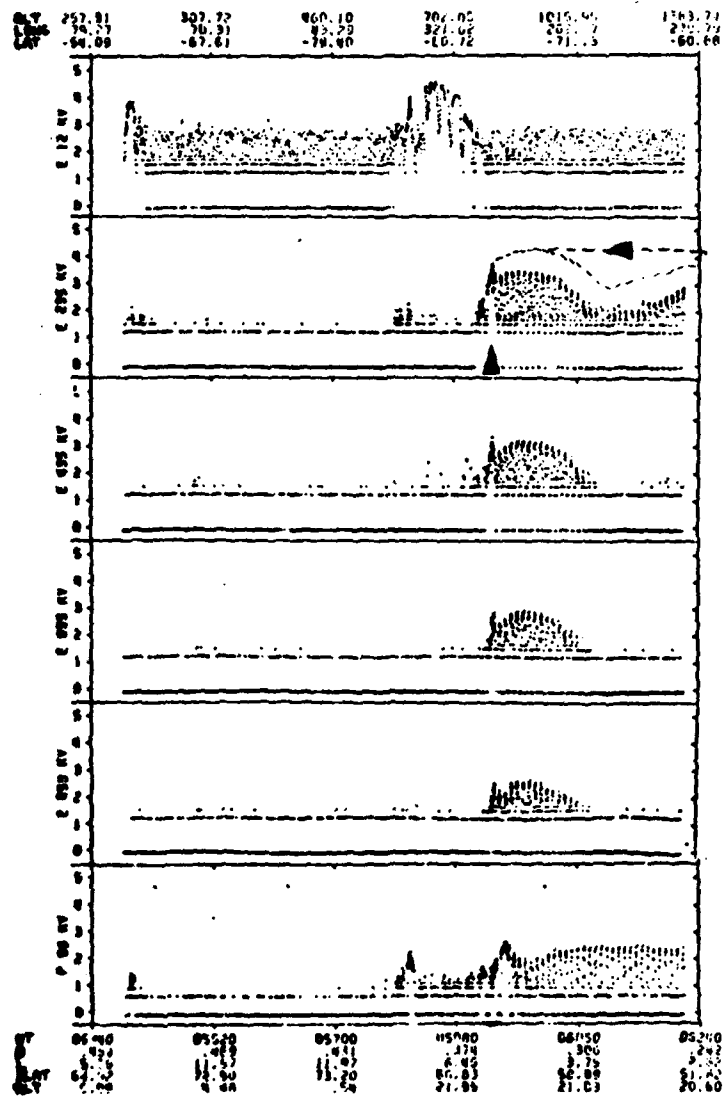
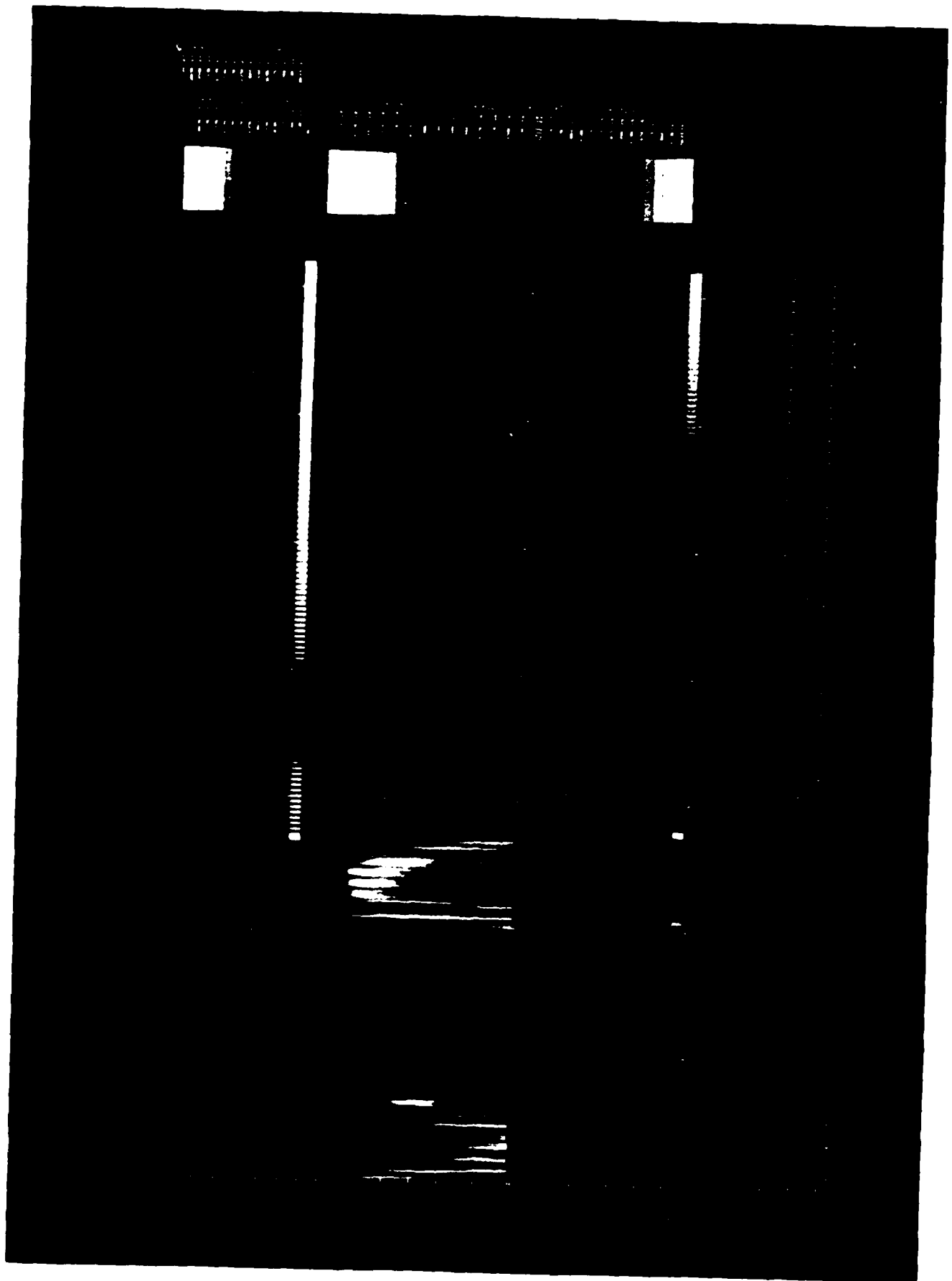


FIGURE 2.8a Spectrogram of plasma waves, 235 keV electrons, low energy electrons, low energy protons, 80 keV protons for the low altitude local evening pass.



defined. Fig 2.8b shows the high altitude local dusk pass with the inverted V electrons evident from 10500 UT to 10700 UT with ion beams also evident between these times. Plasma turbulence is also evident between these times but the 235 keV electrons have been depleted.

Fig 2.9 shows the raw magnetogram for Kiruna ($67^{\circ} 50'N$, $20^{\circ} 25'E$) for 4-6 September 1976. The period is relatively quiet from 0200 UT to 2200 UT 5 September 1976. A small substorm occurs shortly before midnight on 6 September and the estimate (to be shown later) of the extent of the precipitation in time is indicated by the arrows. In addition, the geosynchronous satellite, ATS-6, showed two small excursions in the 140-800 keV electron channel (see Fig 2.10).

The S3-2 satellite has a magnetic spectrometer similar to S3-3 (but only to electron energies of 400 keV). These satellites were coplanar at this time of year. The satellite tracks are shown in Fig 2.11. The X's indicate regions of precipitation for either satellite. The precipitation is first seen on S3-3 at 1.6 UT at 21.5 MLT (spike event). A similar spike event is then seen at 2.1 UT (both 200 and 400 keV channels) by S3-2 in the same location and altitude. Neither satellite observed precipitation electrons (protons were precipitating, Fig 2.5b) at local dusk. Both satellites observed precipitation near 200 keV at local morning at 3.05 UT (S3-2) and 3.8 UT (S3-3). The S3-2 satellite continues in orbit till precipitation at 200 keV is observed again at 3.65 UT at 3.0 MLT, 3.7 UT at 2.3 MLT, and 3.8 UT at 22.5 MLT. The extent of precipitation is thus ≈ 2.2 hrs. The actual S3-2 flux versus times are shown in Fig 2.12a,b,c.

FIGURE 2.8b Same for the high altitude local dusk pass.

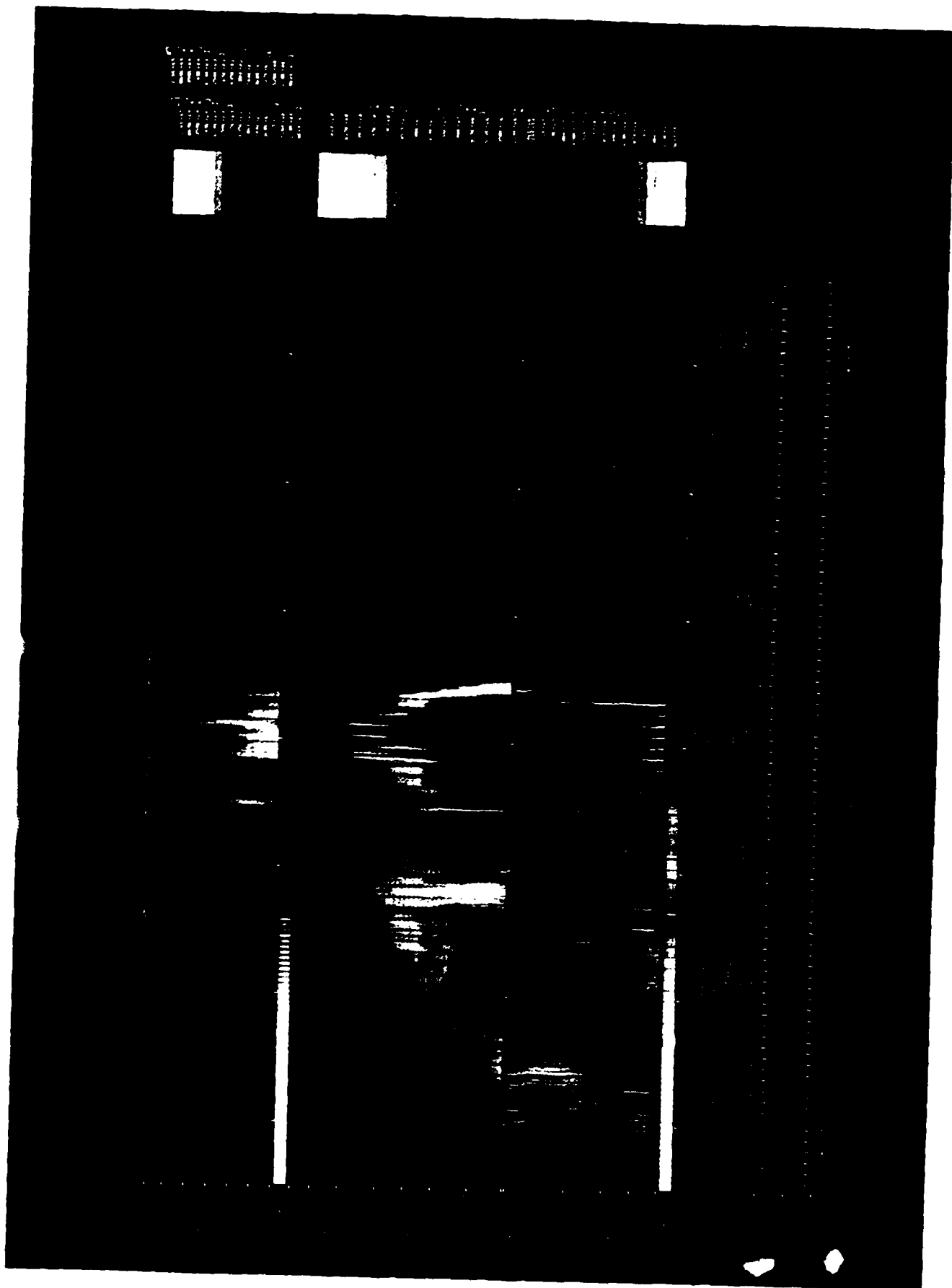


FIGURE 2.9 Kiruna raw magnetogram for 4-6 September 1976.

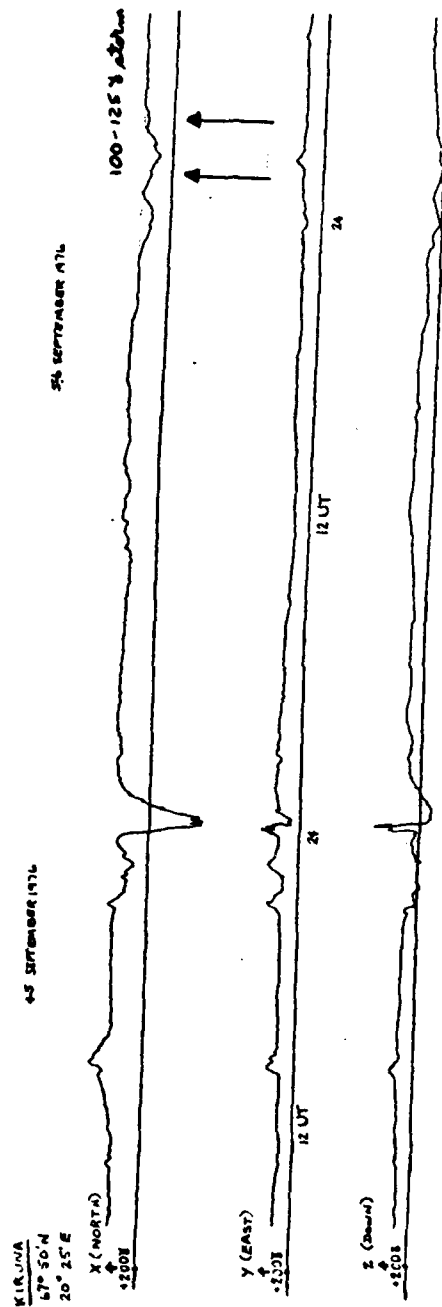


FIGURE 2.10 ATS-6 for 6 September 1976. Arrows indicate beginning
and ending of event.

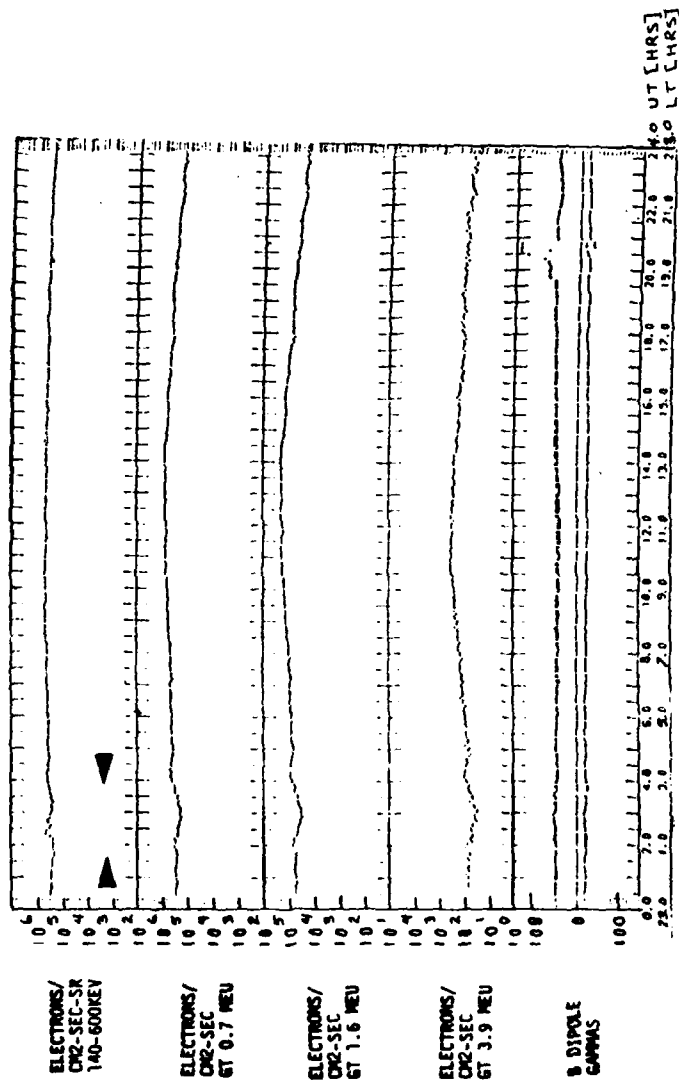


FIGURE 2.11 S3-2 (1, 2, 3) and S3-3 satellite (a, b, c) tracks for
6 September 1976 in invariant latitude versus MLT.

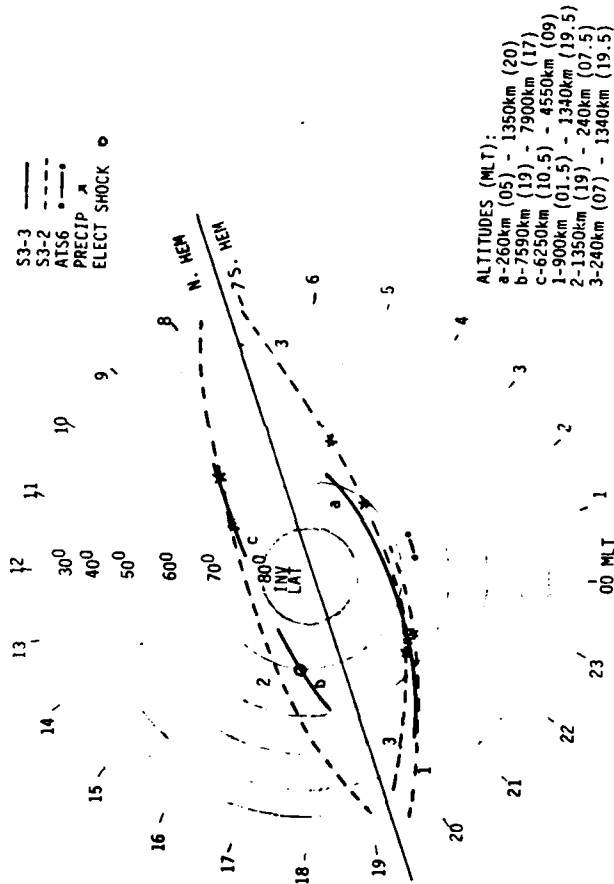
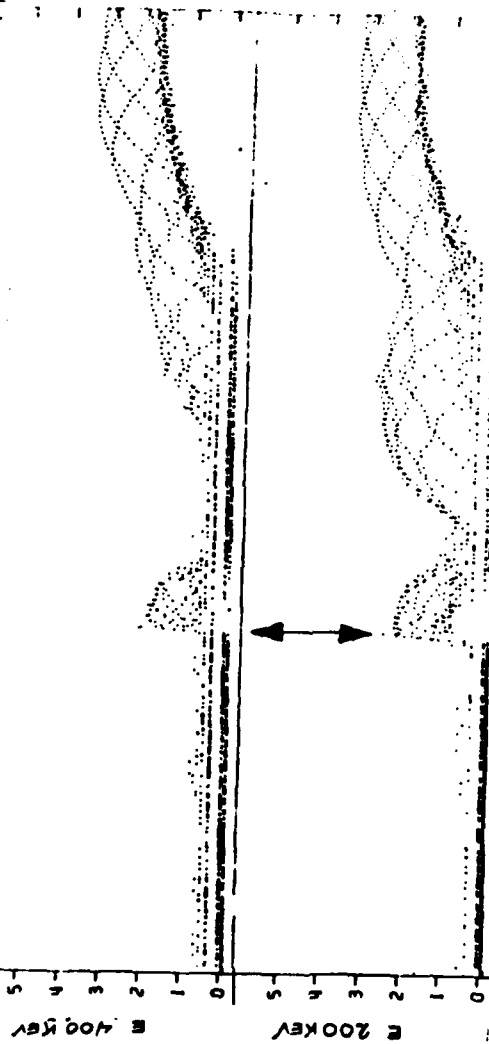


FIGURE 2.12a S3-2 flux versus time plots of pass 1, Figure 2.11.
Arrows indicate precipitation.

ALT	451.08	626.20	804.02	976.59	1129.55	1252.24	1337.12
LONG	55.52	46.94	294.23	268.52	261.28	257.06	253.78
LAT	-59.39	-78.08	-79.74	-63.72	-47.40	-31.53	-16.07



UT	06360	07260	07560	07860	08160	08460	08760
θ	419	401	365	303	243	182	174
L	6.98	12.67	5.83	2.84	1.82	1.41	1.34
ILAT	67.76	73.69	65.88	53.61	46.11	32.57	20.24
MUT	5.36	1.45	21.54	20.51	20.03	19.72	19.44

FIGURE 2.12b Same for pass 2, Figure 2.11.

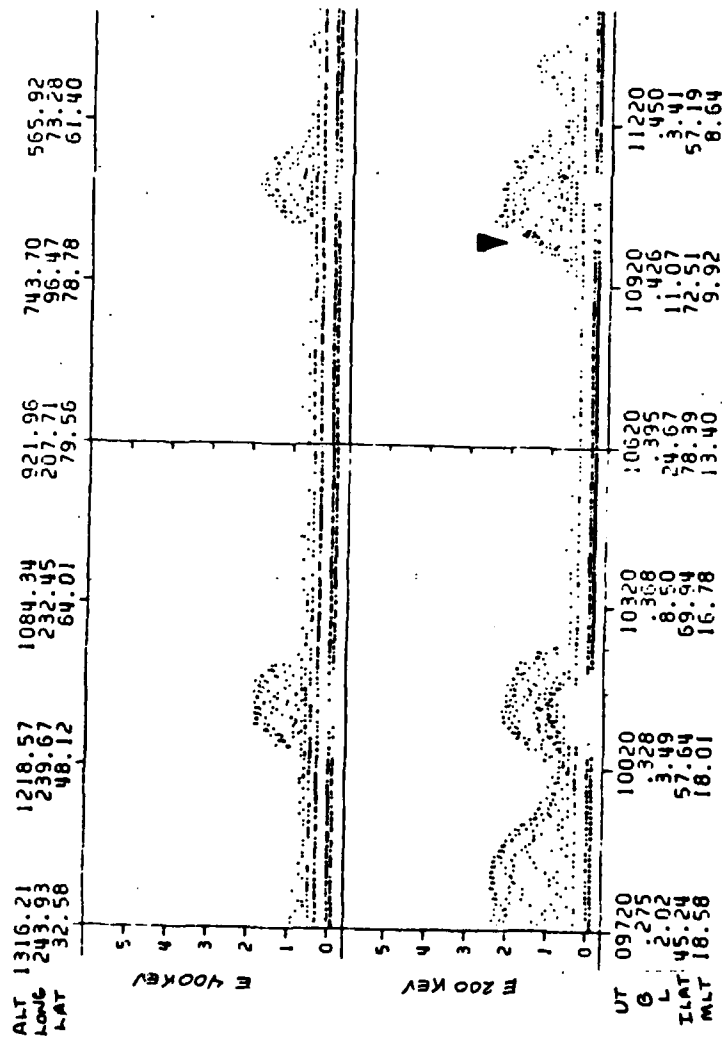
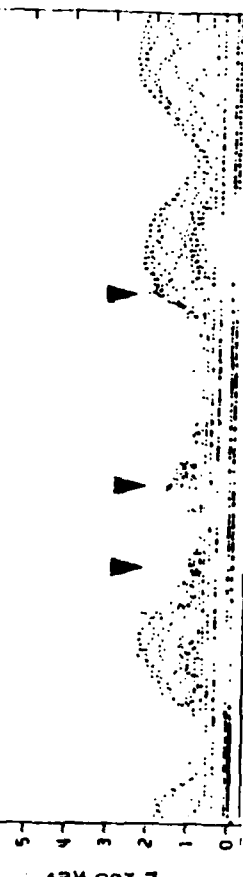
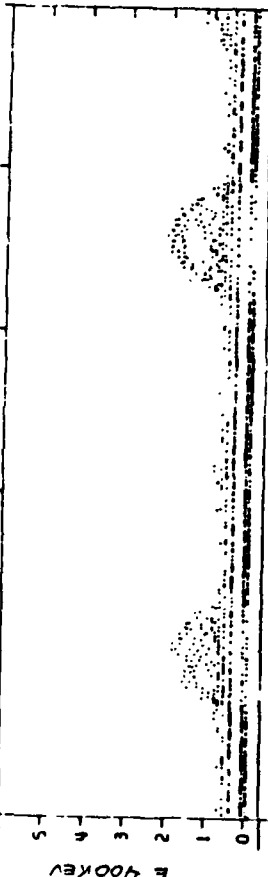


FIGURE 2.12c Same for pass 3, Figure 2.11.

ALT 328.96 461.00 626.19 804.08 976.65 1129.62
 LONG 50.16 43.34 22.21 269.71 243.38 236.06
 LAT -40.01 -59.78 -77.89 -79.91 -63.93 -47.61



UT 12720 13020 13320 13620 13920 14220
 O 322 348 379 381 345 290
 L 2.38 4.76 9.50 6.52 3.38 2.00
 ILAT 49.56 62.71 69.94 66.94 57.06 45.70
 MLT 6.28 5.19 2.28 22.48 20.95 20.20

In summary this event fits the criteria for ESIC mechanism at local evening with whistler mode chorus at local morning. This particular event seems to be a low altitude ($\sim 1.2 R_0$) phenomenon correlated with a 120γ substorm and inverted V event.

2.4.2 Case 2, EMIC (rev 2484, day 132, 12 May 1977)

The flux versus time plot for the EMIC example is shown in Fig 2.13a,b. No precipitation is seen in the 12 or 33 keV electron channels for this local evening, high altitude (~ 7800 km) pass. In the 235 keV channel, however, the flux at $L \approx 4.3$ falls an order of magnitude into the loss cone where normal loss cones are nearly 2 orders of magnitude deep. Proceeding up in energy, the loss cone at this same L value begins to fill until at 850 keV, the loss cones are nearly full (Fig 2.13b). Isotropic distributions are evident in the 1.1, 1.3, and 1.6 MeV channels. In addition, the > 80 keV protons are on strong diffusion from just equatorward of the electron precipitation and continuing poleward. The loss cone filling with increasing energy is evident in Fig 2.14 where pitch angle plots of flux for 160 keV to 1600 keV electron energies are shown. The upward observing loss cone is at 0° in these plots. This spectrum and concurrent proton precipitation is indicative of the EMIC mechanism.

The spectrogram for this pass is shown in Fig 2.15. Low energy electron and proton activity is evident poleward of the REP and only the > 80 keV is coincident. No plasma data was available for this pass.

No direct means of observing the plasmopause was available for

FIGURE 2.13a Flux versus time plots of electrons for local evening
pass of 12 May 1977.

ALT	7735.28	7805.36	7852.12	7875.63	7675.93	7853.01
LONG	241.89	240.47	239.10	237.77	236.49	235.23
LAT	40.78	37.73	34.71	31.69	28.68	25.66

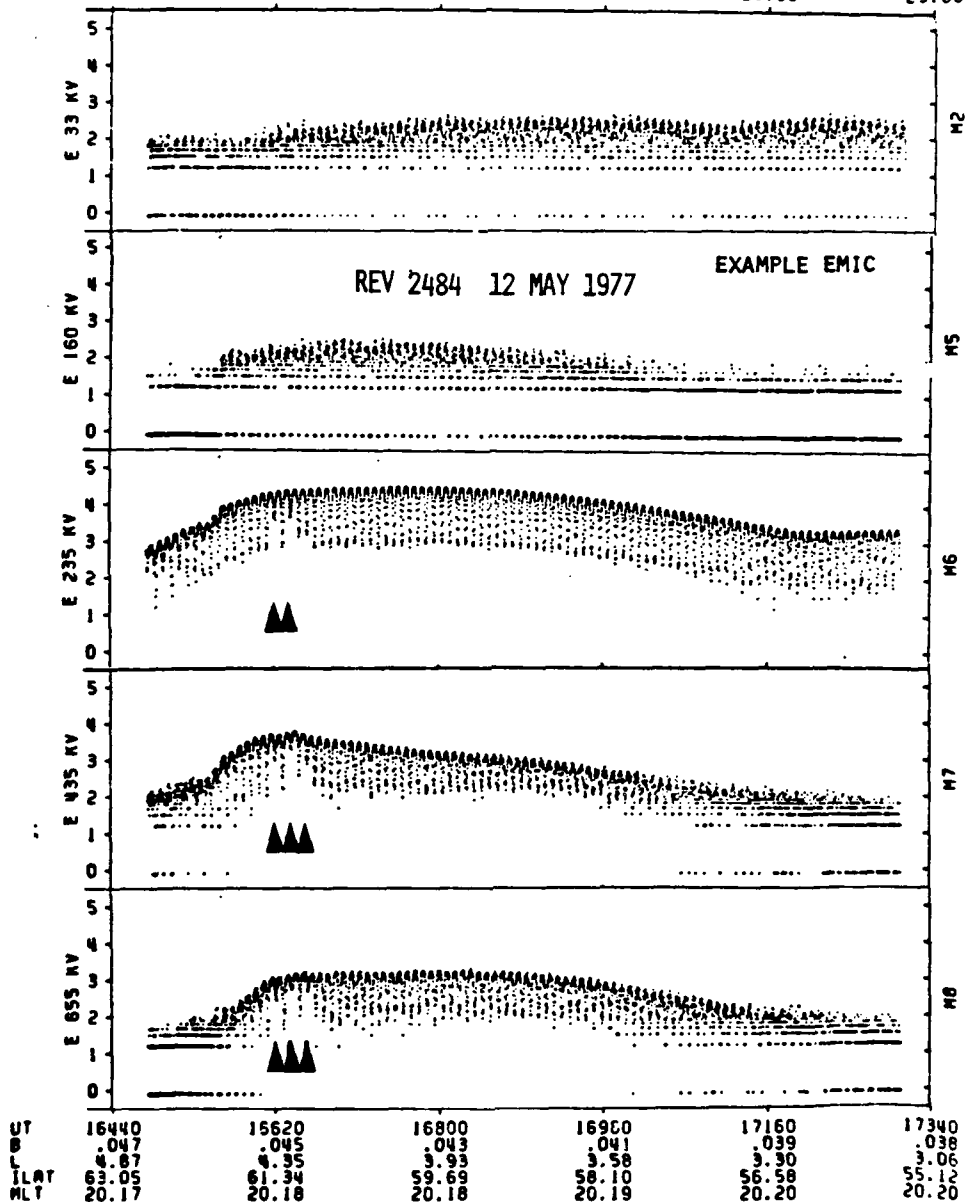


FIGURE 2.13b Same for higher energy electrons and protons.

ALT	7735.28	7805.36	7852.12	7875.63	7875.93	7853.01
LONG	241.89	240.47	239.10	237.77	236.49	235.23
LAT	40.78	37.73	34.71	31.69	28.68	25.66

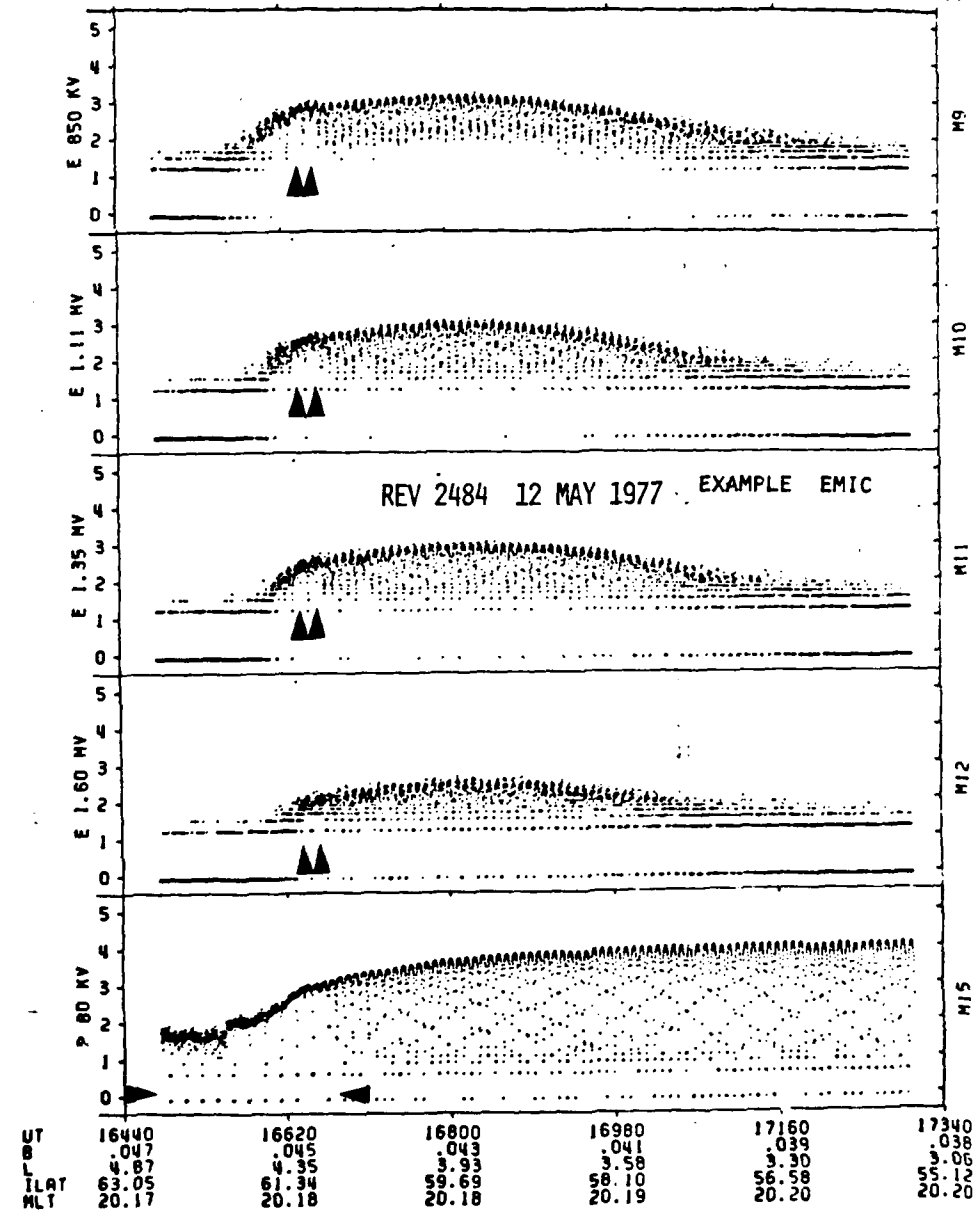


FIGURE 2.14 Pitch angle versus flux plots for electrons with energies 160-1600 keV for 12 May 1977.

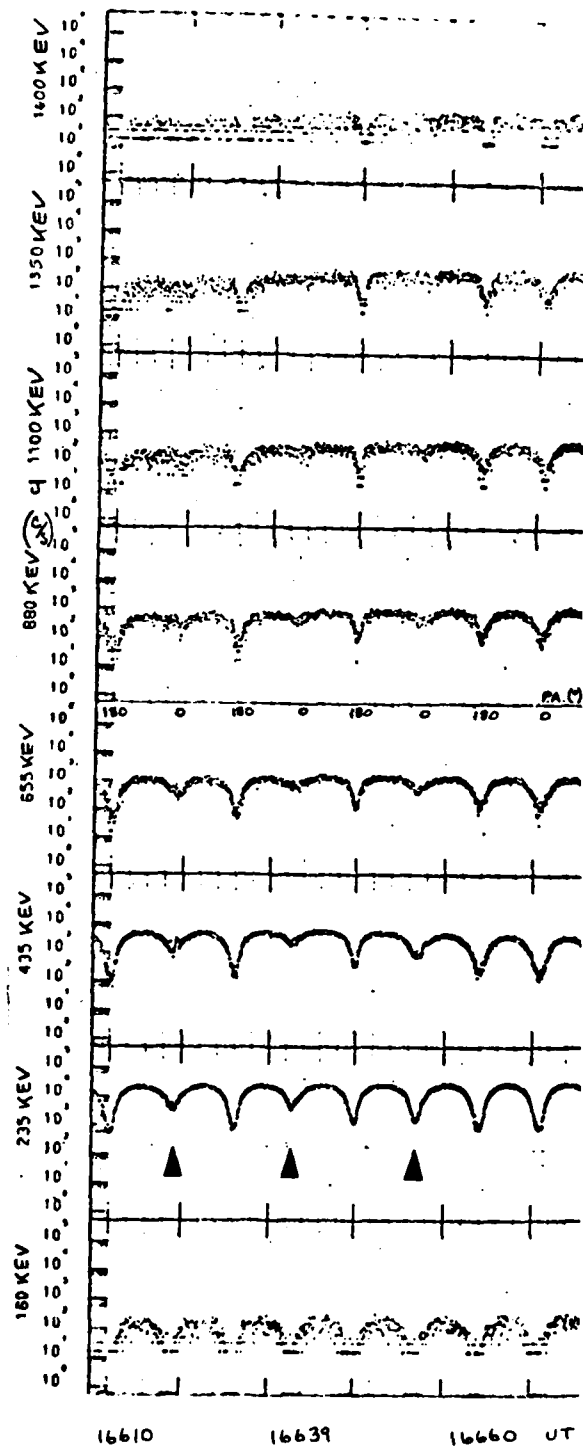
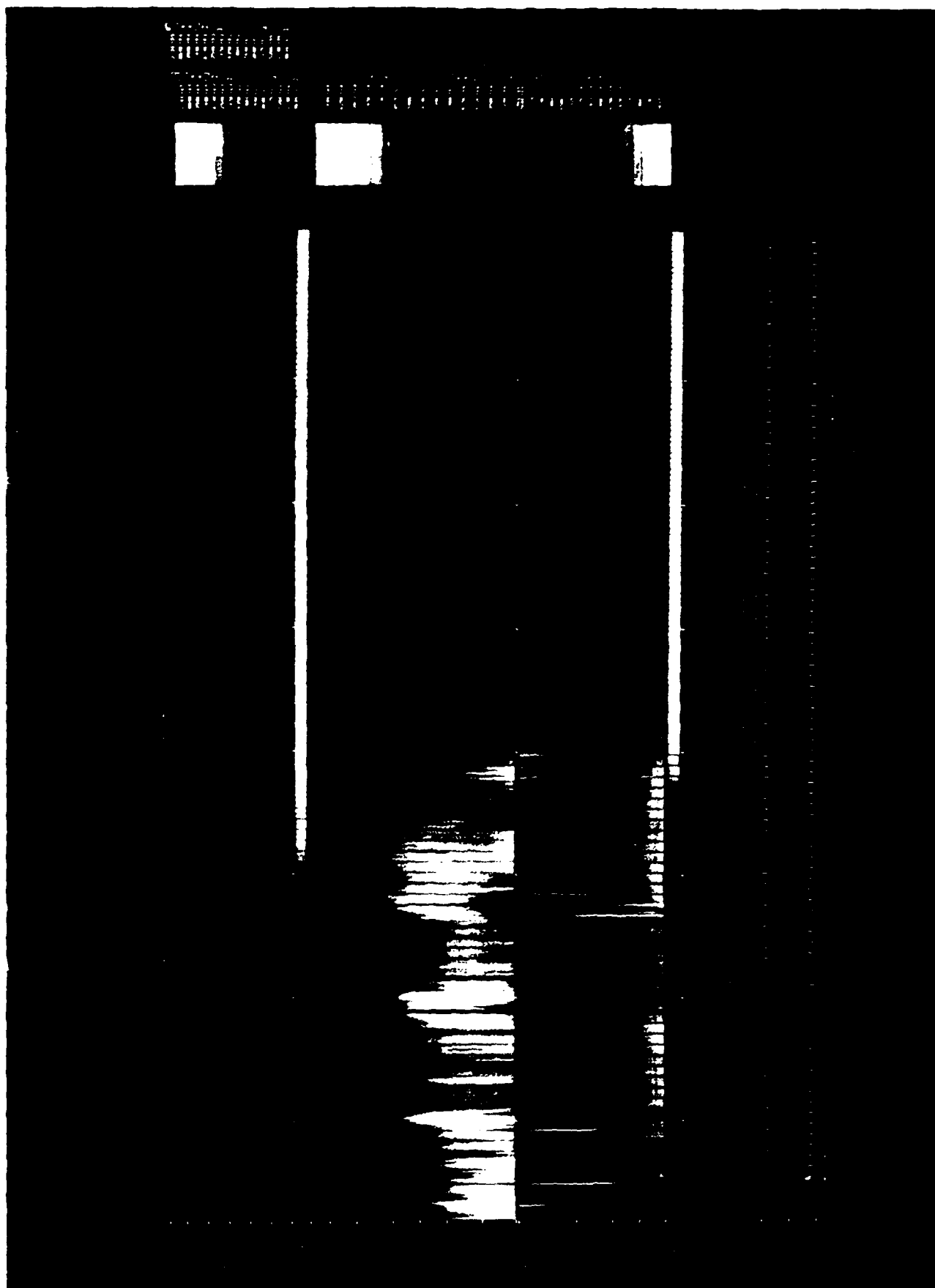


FIGURE 2.15 Spectrogram for 12 May 1977.



this pass. However Mizera (1974) has shown that the midnight plasma-pause is ~ 8 L equatorward of the energetic proton precipitation boundary. The electron and proton precipitation are nearly coincident at local evening. Since the plasmasphere bulges poleward from midnight to dusk, the REP may indeed be just within the plasmopause. Another rough approximation to the L value of the midnight-dawn plasmopause location is given empirically by Carpenter and Park (1973) from ATS-5 data:

$$L_{pp} = 5.7 - 0.47 K_p \quad (29)$$

where K_p is the maximum geomagnetic planetary three-hour-range indices 12 hours previous to the event. The same formula may be used with K_p as the actual value at the time of the event. For UT of 4.6 hrs on 12 May 1977 the K_p at the time of event was ~ 4.5 and the max 12 hrs previous was 5.0. These two values yield $L_{pp} = 3.3-3.9$ as the midnight-dawn-noon plasmopause and approximately twice that value for the dusk plasmopause. These are sketched in Fig 2.16. For these rough approximations, the location of the precipitation of rev 2484 is clearly within the plasmasphere.

Finally, Fig 2.17 shows the ATS-6 electron data on 12 May 1977. The REP occurred during a highly disturbed period as indicated in the 140-600 keV electron channel. In addition, S3-3 showed precipitation (ESIC) at energies up to 435 keV on the preceding and following passes at the same local time. Only four of these events ($E_p^- \geq 1$ MeV) were observed for the entire data set.

FIGURE 2.16 Plasmopause relation to rev 2484, 12 May 1977 based
on rough estimates.

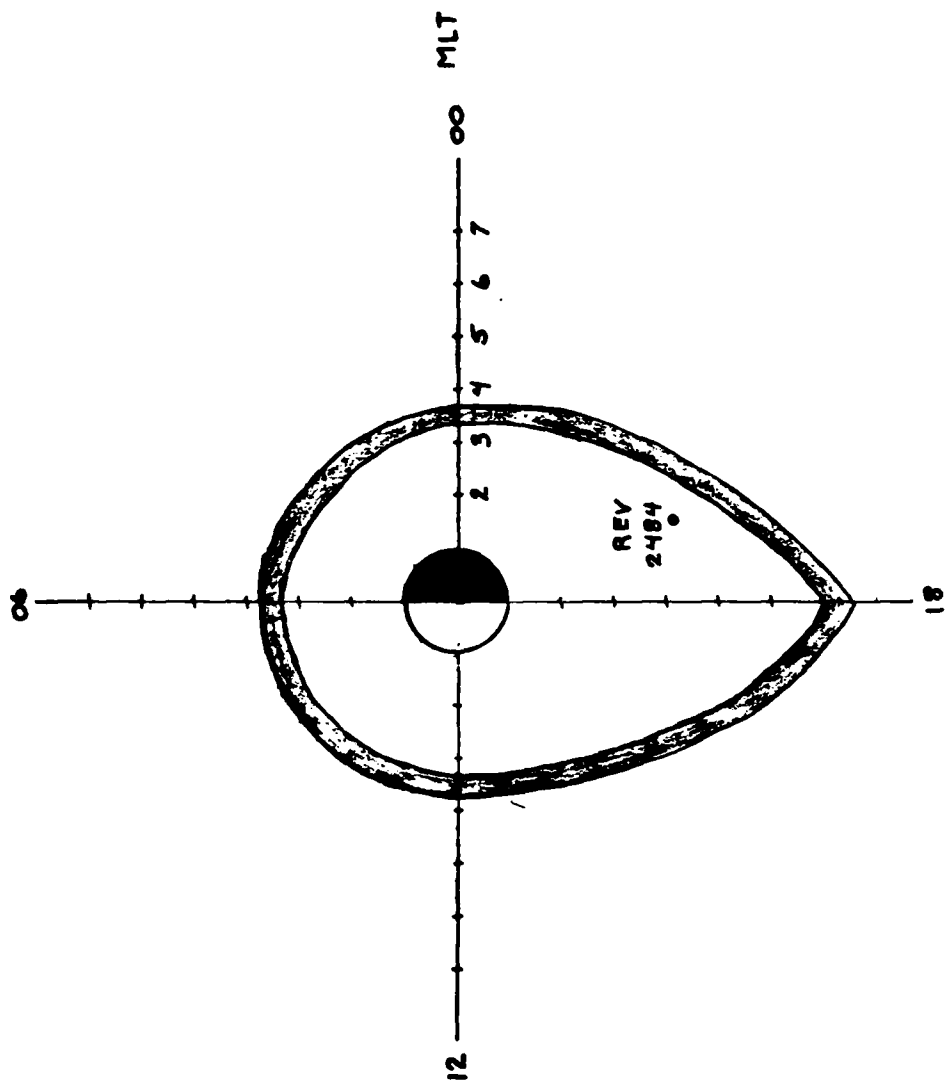
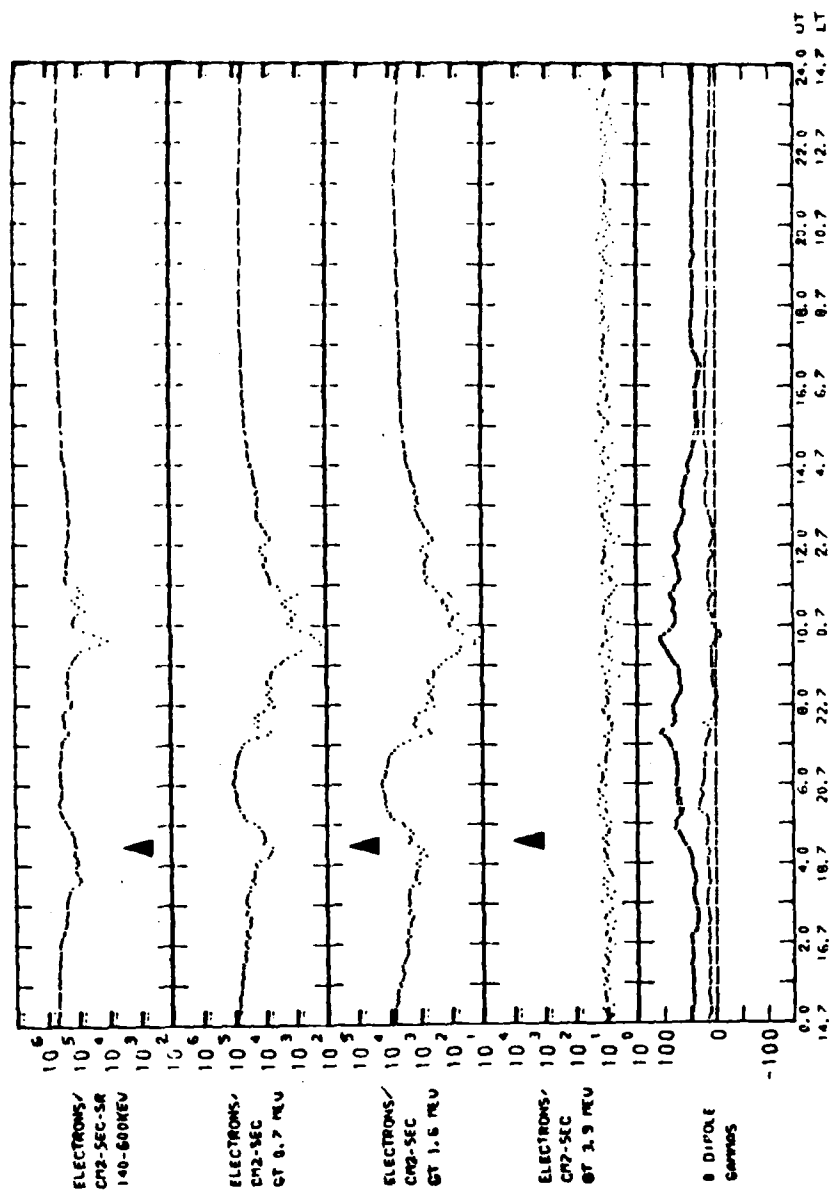


FIGURE 2.17 ATS-6 for 12 May 1977.



2.4.3 Case 3, Chorus (rev 1413, day 366, 31 December 1976)

The flux versus time plot for 31 December 1976 is shown in Fig 2.18. Only 33 and 235 keV electron precipitation is evident just prior to local noon at low altitude (550 km). No protons were precipitating on strong diffusion though they were present. The pitch angle plot for this event is shown in Fig 2.19 where the loss cone $\approx 55^\circ$. Normal distributions are evident at 12812 UT but at the later times, 33 and 235 keV channels are isotropic in the upward viewing loss cone.

The spectrogram (Fig 2.20) shows evidence of plasma noise just above 30 Hz at and poleward of the REP (12820 UT). A faint band near 10 kHz is also evident.

FIGURE 2.18 Flux versus time plots for 31 December 1977. Arrows indicate strong diffusion precipitation

ALT	1567.20	1179.00	836.03	556.72	356.78	257.58
LONG	154.81	150.49	143.79	126.84	95.69	2.99
LAT	49.61	59.61	64.83	70.17	82.15	72.62

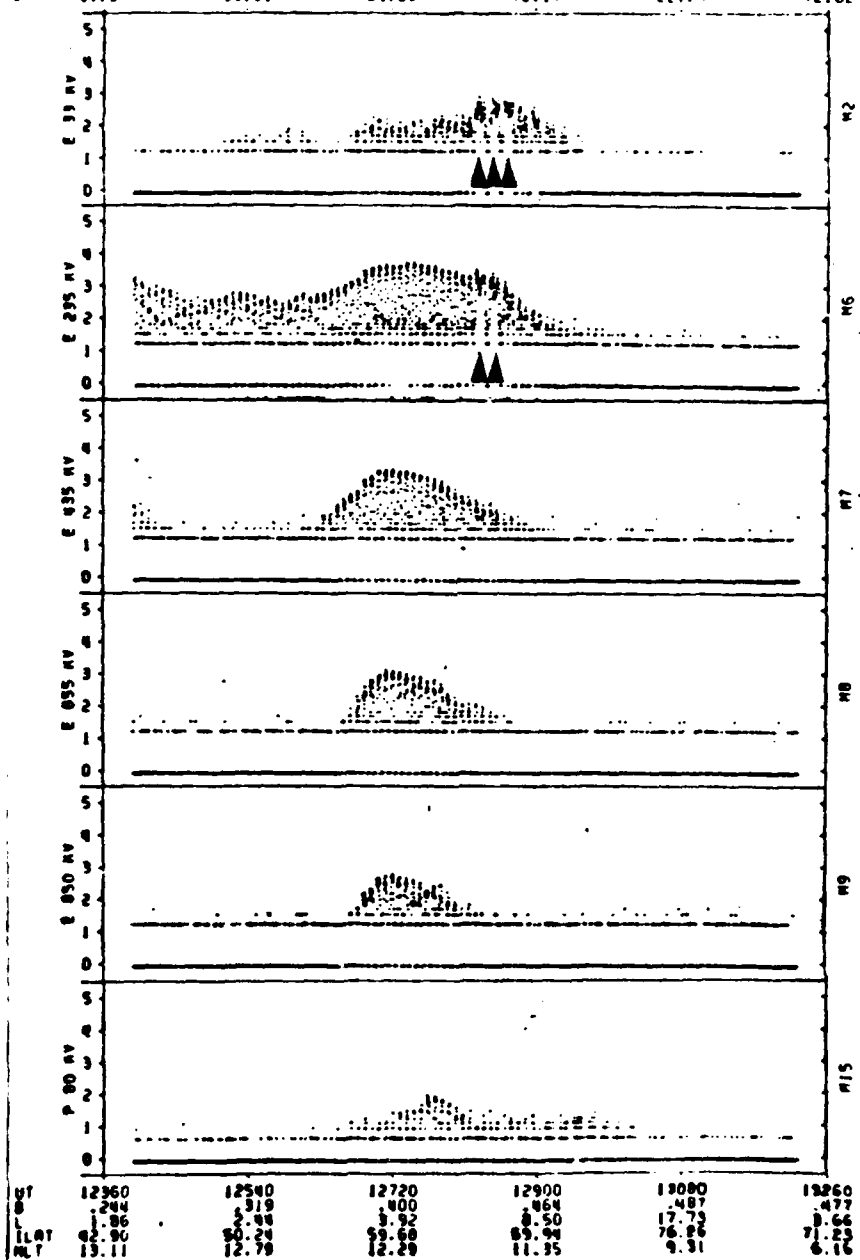


FIGURE 2.19 Pitch angle distributions for 33, 235, 435 keV electron channels for 31 December 1976.

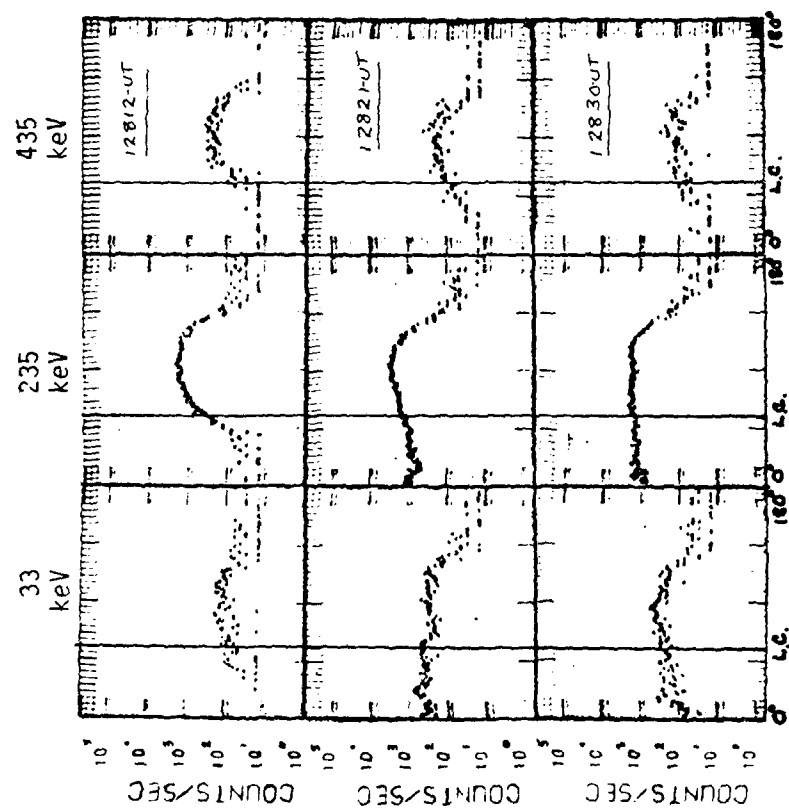


FIGURE 2.20 Spectrogram for low altitude early morning pass
on 31 December 1976.

CHAPTER 3. ATMOSPHERIC CONSEQUENCES

3.1 Introduction and Background

The earth's atmosphere below 100 km has been the object of intense investigation over the past 10-15 years. It is well known that a variety of electromagnetic and particle radiation can deposit energy in this region and thus modify the local chemistry. The remainder of this section describes the ionization and neutral chemistry with special emphasis on ozone removal. In subsequent sections we examine the three examples in Chapter 2 and their effect on ozone.

The ionosphere below 100 km, known as the "D region," has been studied by several authors with respect to ionization by solar and galactic cosmic rays (Webber, 1962), primarily in the polar cap region ($\Lambda \geq 75^\circ$): energetic electron precipitation in the auroral region, $\Lambda \simeq 70-75^\circ$ (Rees, 1963; Lerfold and Little, 1964; Bailey et al., 1970) and subauroral regions, $\Lambda \simeq 60-70^\circ$ (Bailey, 1968; Larsen, 1973; Reagan, 1977; Thorne, 1977b) and at mid latitudes, $\Lambda \leq 60^\circ$ (Potemra and Znuda, 1970; Spjeldvik and Thorne, 1975a,b; Larsen et al., 1976). Solar UV, especially HLy α at 1216 Å and HLy β at 1025 Å, produces the dominant primary ion in the quiet mesosphere through ionization of NO. Also, solar UV scattered from the sunlit hemisphere has long been thought to be an important ionizing radiation source at night. Solar UV (and X-ray) radiation is strongly absorbed below about 85 km where positive ion composition is dominated by multiply hydrated ion clusters of the type $H^+(H_2O)_n$, $NO^+(H_2O)_n$, and $H_3O^+(H_2O)_n$ (Johannesen and

Krankowski, 1972). O_2^- , the dominant negative ion below 80 km, is produced by electron attachment and interacts with CO, NO, HCO and $(H_2O)_n$ to form heavy negative ion and large water clusters.

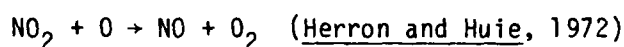
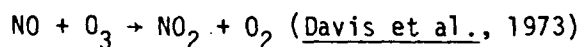
Although the precipitating particle energy is usually negligible compared to other ionizing sources below 100 km, it can be the dominant ionization source during disturbed conditions below 80 km (Thorne, 1977b). Particulate energy produces mostly primary ions O_2^+ and N_2^+ , N^+ , and O^+ of which ~94% are rapidly converted to O_2^+ through charge exchange with O_2 (Reagan et al., 1978) and ~6% to NO^+ by ion-atom interchange with N_2 and O_2 (Gunton et al., 1977). This disturbed increase in O_2^+ can thus modify the complex clustering reactions in the D-region.

A comparison of several ionizing sources is presented in Fig A.15 (Appendix A) where the overwhelming dominance of the largest solar proton event (SPE) of August 1972 is evident. Immense SPEs such as August 1972 are relatively rare and indeed REPs can frequently be the dominant ionization source below 100 km (Spjeldvik and Thorne, 1975a; Thorne, 1977b).

The production and removal of odd oxygen (O , O_3) is of paramount importance in neutral atmospheric chemistry below 100 km. Odd oxygen is produced primarily by photodissociation of molecular oxygen. The Chapman (1930) process, $O + O_3 \rightarrow 2O_2$, is now well known to account for only ~20% removal of odd oxygen. The major removal process includes catalytic loss cycles with chlorine compounds (e.g. Crutzen and Howard, 1978), and odd nitrogen and odd hydrogen species (Blake

and Lindzen, 1973). The latter two are of particular interest here since they can be significantly modified by intense particle precipitation (Thorne, 1977a,b; 1979).

The bulk of odd oxygen depletion is through the following nitrogen chemistry important particularly below 50 km (Blake and Lindzen, 1973):



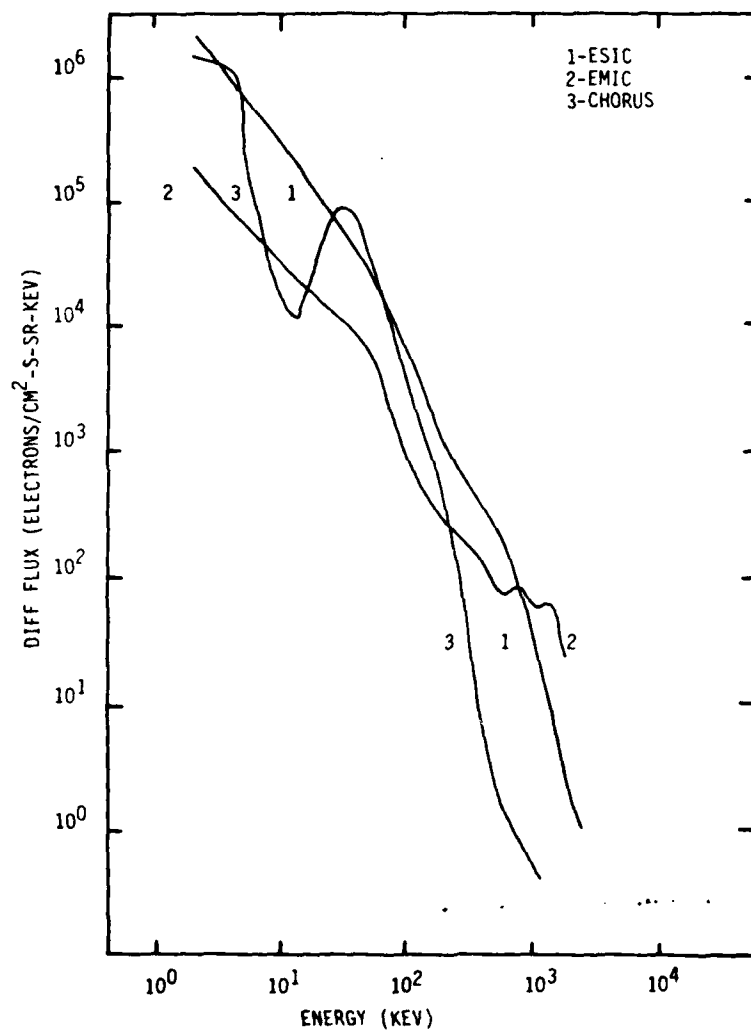
REPs can be the dominant source of NO production by dissociation of N_2 in the mesosphere and a competing source with nitrous oxide upwelling from the Earth's surface in the upper stratosphere (Thorne, 1979).

Above 40 km the odd hydrogen chemistry begins to dominate in the removal of odd oxygen (Blake and Lindzen, 1973). Here the odd hydrogen is produced mainly by dissociation of water vapor by photons and O ('D) atoms and as a by-product of O_2^+ production by energetic particle precipitation (Rowe et al., 1974). In this way, the increase in O_2^+ during REPs may also affect the mesospheric removal of odd oxygen. Since energy deposition by REPs can dominate in the mesosphere, we shall subsequently examine the removal of odd oxygen by the enhanced odd hydrogen chemistry and its ozone consequences for the three REP examples of Chapter 2.

3.2 REP Energy Spectra and Atmospheric Energy Deposition

The precipitation spectra for the three cases presented in Chapter 2 are shown in Fig 3.1. The ESIC spectrum (Case 1) has the

FIGURE 3.1 Energy spectra for cases 1,2,3 of Chapter 2.



highest flux in the 100-800 keV range. The EMIC spectrum (Case 2) dominates at energies above 1 MeV and is comparable to the previously published spectrum of Vampola (1971). The chorus event is relatively weak dominating only near 3 and 30 keV. These REP spectra were input to the UCLA (Spjeldvik, 1974) electron precipitation model (see Appendix D). The ion pair production (assuming 35 keV per pair) versus altitude is shown in Fig 3.2. The Bremsstrahlung X-ray deposition profiles were also plotted in Fig 3.2. As expected, the ESIC curve dominates in the 70 km region, and EMIC in the 50-60 km region. Whistler events are relatively non-competitive with other REP spectra but may dominate local chemistry.

The ESIC case of Chapter 2 was used to model a typical REP to calculate the total energy deposition. The latitudinal extent was approximately 200-300 km based on the invariant latitude excursions of both S3-2 and S3-3. The longitudinal extent based on local time duration was 7,000-10,000 km. The event lasted approximately 2.2 hours. The peak ion production rate occurred at ~73 km altitude with a value of $6.8 \times 10^{-3} \text{ (cm}^{-3} \text{ sec}^{-1}\text{)}$. Assuming precipitation was nearly constant and uniform throughout the events (which is not likely), a peak value of $\sim 1 \times 10^{24} \text{ ion pairs cm}^{-1} \text{ (column)}$ or $3.5 \times 10^{22} \text{ keV}$ of energy was deposited during this event.

3.3 REP Induced Hydrogen and Ozone Modifications

The REP ion production rates versus altitude were processed to produce odd hydrogen (and thus hydroxyl) according to the chemical modelling of Heaps (1978). Fig 3.3 presents this model of odd hydrogen

FIGURE 3.2 Ion pair production rate versus altitude for ESIC,
EMIC, and chorus events.

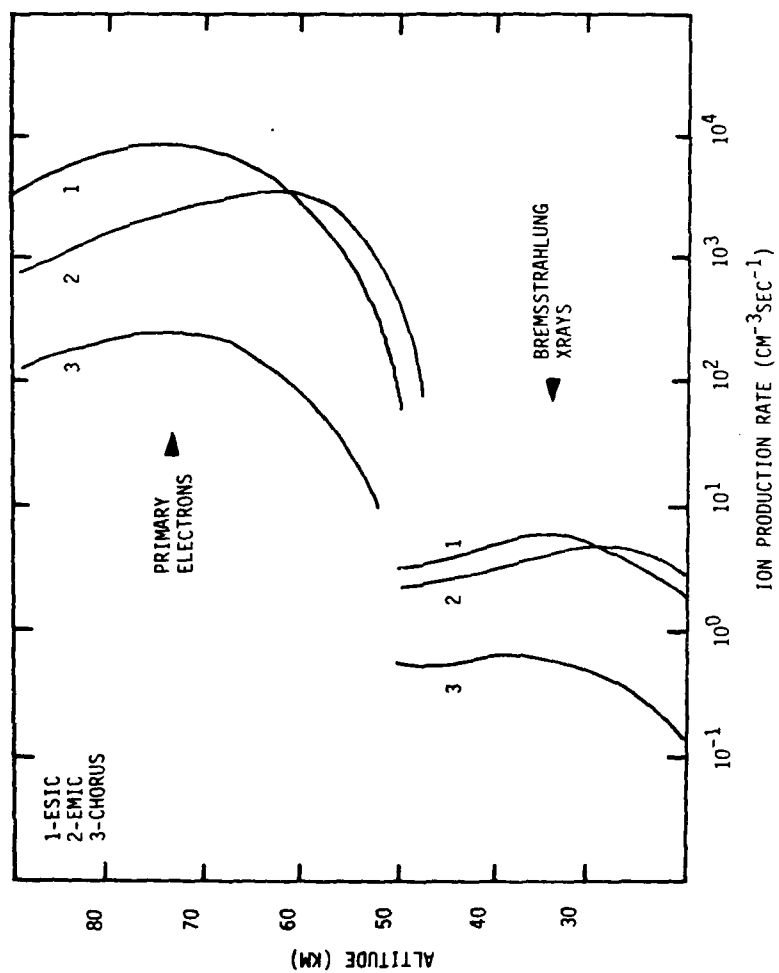
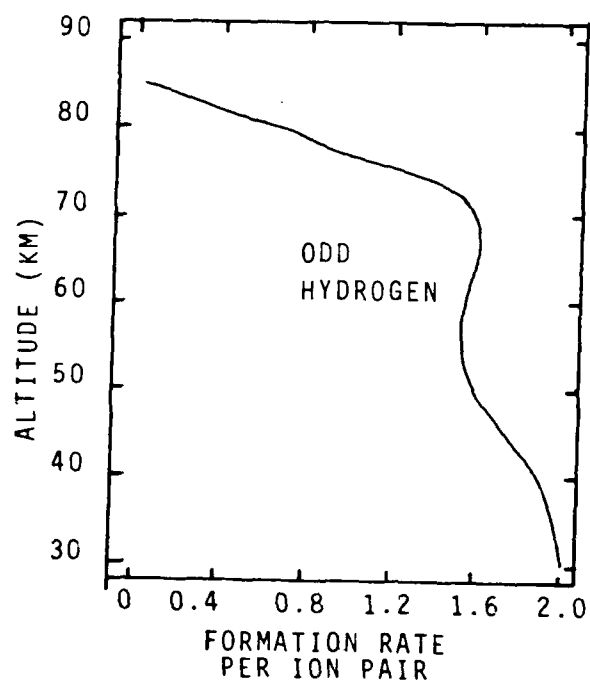


FIGURE 3.3 Altitude profile of the odd hydrogen formation rate
related to ion pair production.



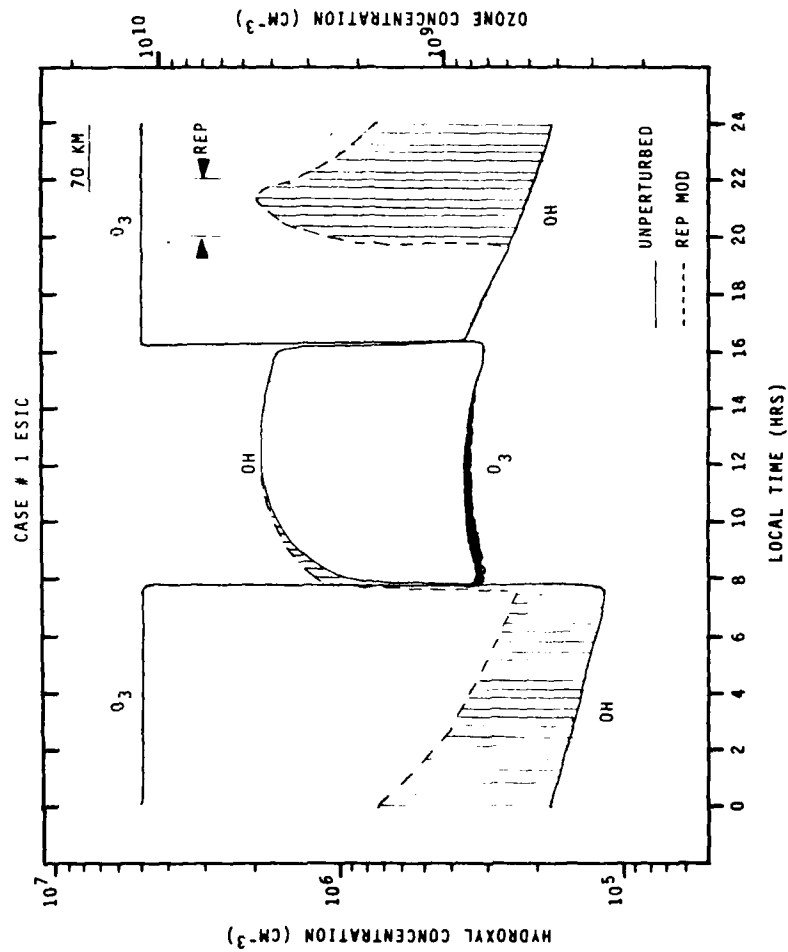
production as a function of ion pair production for disturbed conditions (higher ion production rate). The higher altitude limit for cluster ion formation is clearly indicated by the trailoff above 80 km. Since the nitrogen cycle dominates in the stratosphere, odd hydrogen is not expected to be important below 40 km.

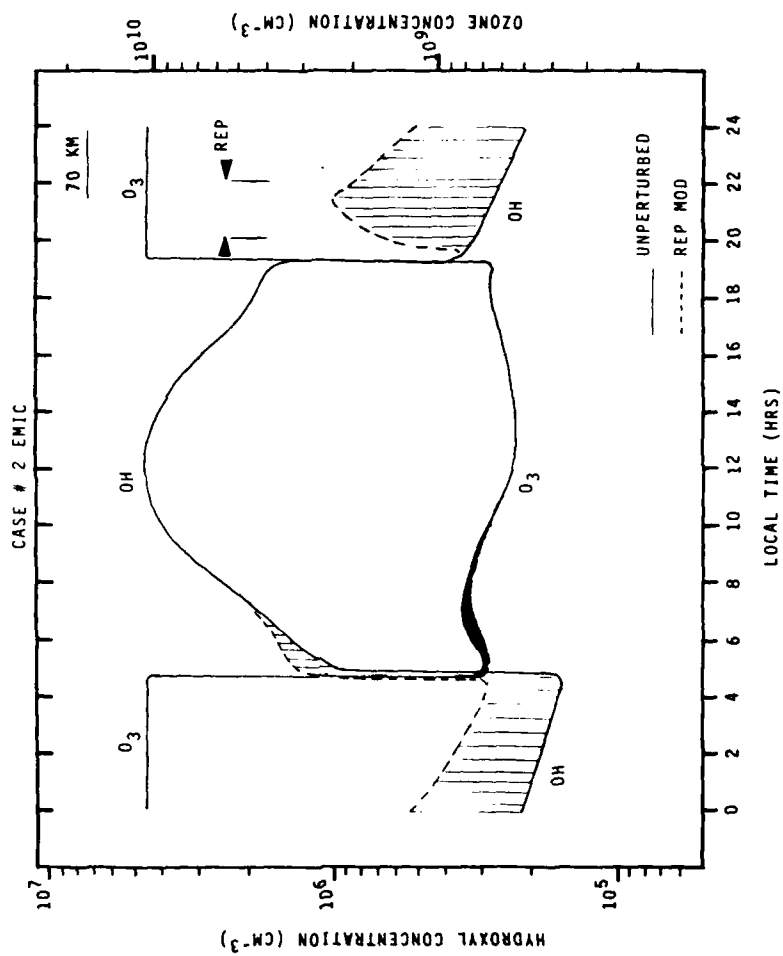
After modelling the OH increases to the REP ionization rates, a numerical simulation fashioned after Blake and Lindzen (1973) was performed to calculate the relative change in ozone concentrations. The numerical simulation differs from Blake and Lindzen's model in that two reactions (OH nighttime source reaction and Chapman's (1930) original 3 body atomic oxygen collision equation to form O_2) are added, reaction rates are updated, and solar flux and ozone concentrations vary with time of day (DeVore, 1977).

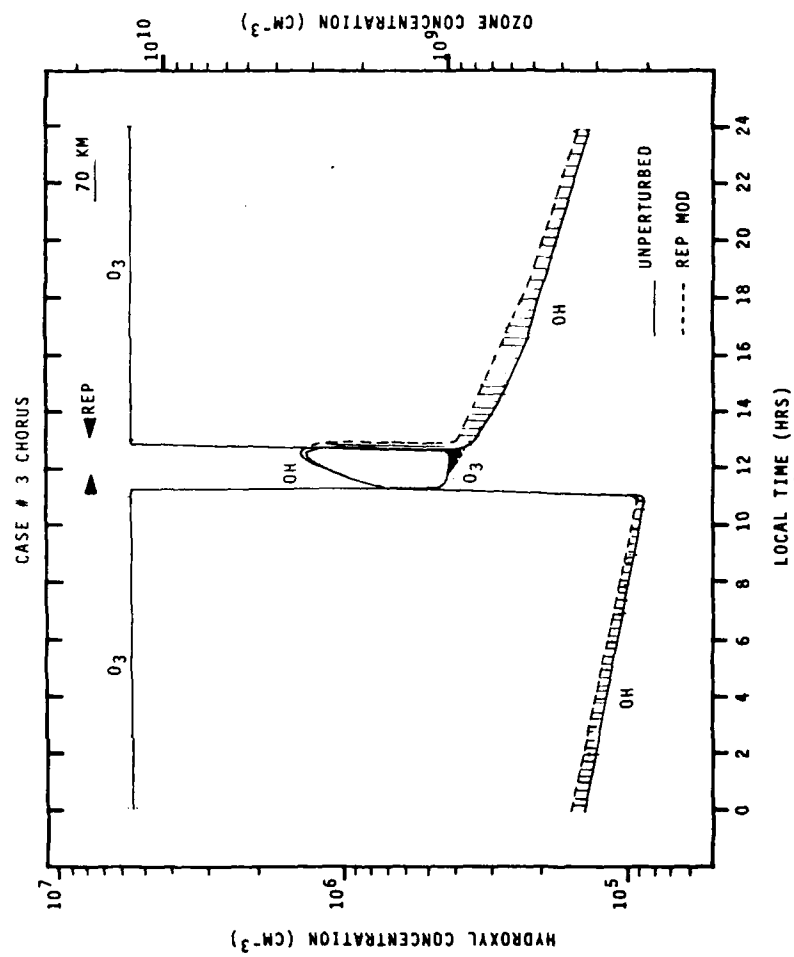
The results for Case 1 and 2 (Fig 3.4a and b) are similar since they both occur during local evening. Factors of 10 and 4 increase in OH concentrations at 70 km immediately after precipitation commenced occurred for the ESIC and EMIC cases respectively. The enhancement continued throughout the night and several hours into the day. Ozone was not affected until sunrise due to the low nighttime O concentration but showed sunrise decreases of 10-15% for both cases. These diminished ozone concentrations lasted for several hours.

The chorus event (Case 3, Fig. 3.4c) occurred near local noon with a small enhancement in OH concentration and throughout the succeeding night. The ozone concentration showed an immediate response dropping by nearly 20%. The diminution of ozone ended at local sunset.

FIGURE 3.4a,b,c Ozone and hydroxyl concentrations [cm^{-3}] versus local time (hrs) for a. ESIC, b. EMIC, and c. chorus REP events.



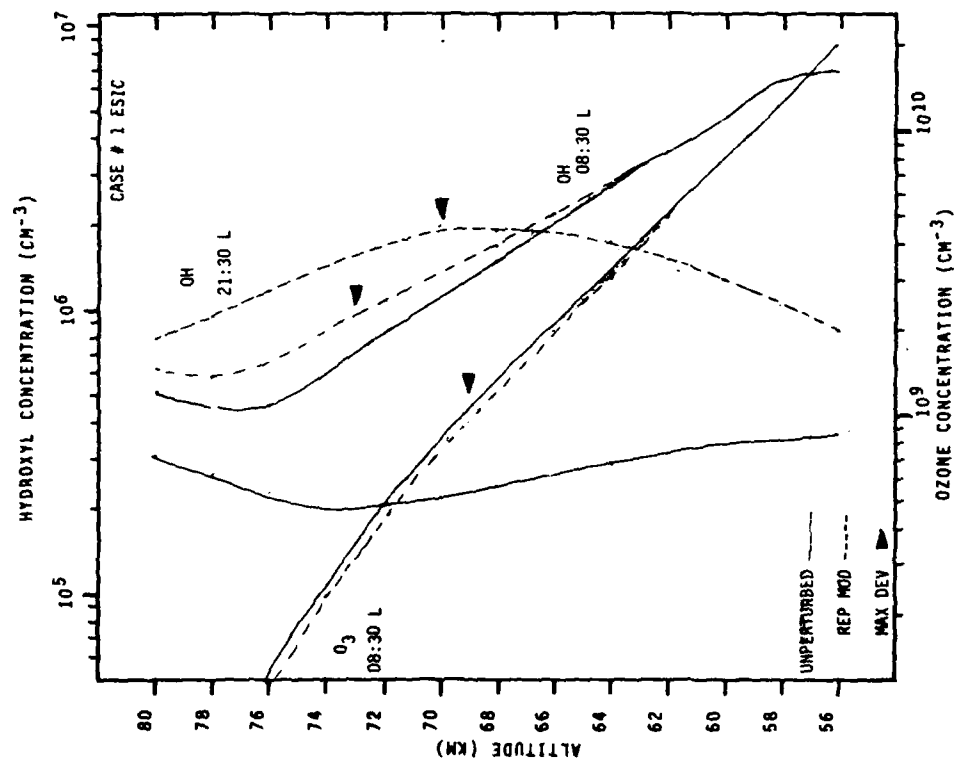


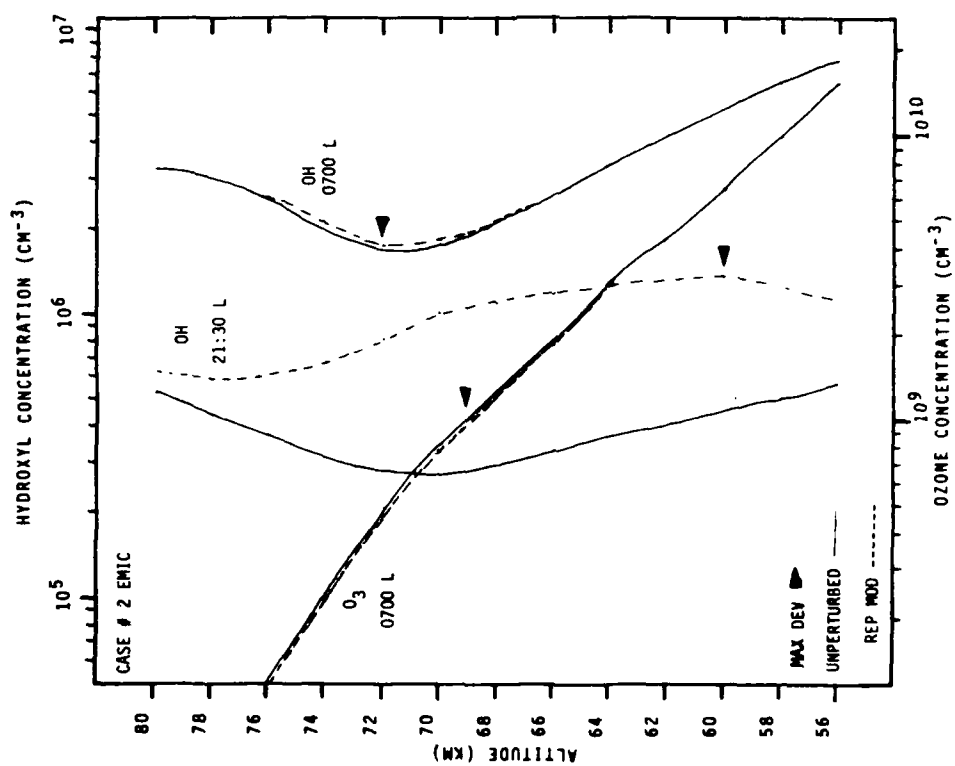


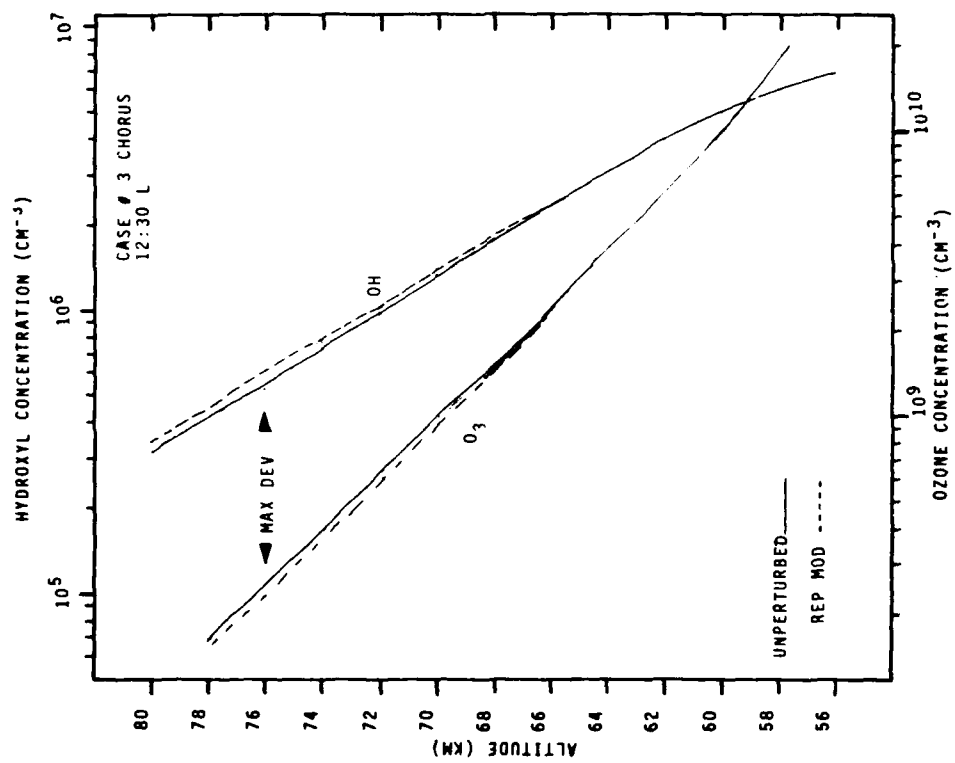
A similar simulation with an intense REP modelled after the ESIC case, this time occurring at local noon, showed only a 17% increase in OH but more than a 30% decrease in ozone.

Altitude profiles of the ozone concentrations at the local time of maximum decrease, OH concentrations at the same time and at time of maximum OH enhancement for the three cases are presented in Figs 3.5a,b,c. Maximum ozone decreases occurred at 69 km for both the ESIC and EMIC cases and at 76 km for the chorus case. Only in the chorus case, where onset of OH enhancement and ozone diminution were simultaneous, did the deviations occur at the same altitude.

FIGURE 3.5a,b,c Altitude [km] profiles of ozone concentration at time of maximum decrease, hydroxyl concentration at the same time, and hydroxyl concentration at the time of maximum enhancement for a. ESIC, b. EMIC, c. chorus REP events.







CHAPTER 4. SUMMARY, CONCLUSIONS AND OUTLOOK

I have presented here the results of two years of data analysis of fourteen months of satellite outer radiation zone coverage (Chapter 1). Theory and examples have been provided in an attempt to explain the types of REPs discovered in the analysis (Chapter 2). Finally, some atmospheric consequences were investigated (Chapter 3).

For the first time the properties of strong diffusion REPs have been studied using a relatively extensive, dense satellite data set and the following results have been obtained:

- o REPs show a seasonal variation with equinoxial maxima and solstice minima in agreement with Bailey (1968).
- o The occurrence frequency of REPs is nearly linear with general magnetic conditions again in agreement with Bailey (1968).
- o Correlation of REP producing substorms and substorm indices (AE) are weak in the limited number of cases examined in agreement with Thorne and Larson (1976) and not all substorms produce REPs in agreement with Rosenberg et al. (1972) and Thorne and Larson (1976).
- o Overall, only one out of ten REPs occur in daytime but as magnetic conditions become disturbed there is an increase in daytime REPs approaching three out of ten.
- o REPs are estimated to extend in longitude from 1000 km to 10-15,000 km in general agreement with Larsen, 1973, and Bailey, 1966.

- o 98% of all REPs occur concurrently with protons (≥ 80 keV) precipitating on strong diffusion and many features of the precipitation are similar.
- o Three distinct classes of REPs occurred: an overwhelming majority (96.5%) had strong diffusion precipitating spectra from hundreds to a thousand keV energy and all these events occurred near the outer bound of trapping simultaneously with proton precipitation; the smallest group (1.3%) had strong diffusion precipitating spectra only for electrons ≥ 1 MeV and again with concurrent proton precipitation but inward from the outer bound of trapping and probably within the plasmasphere; a slightly larger group (2.2%) had strong diffusion precipitation spectra only for electrons of a few hundred keV but with protons present with normal loss cone distributions (not precipitating on strong diffusion).

The theoretical investigation shows that REPs can be caused by radiation belt plasma interactions with plasma waves and that the electrostatic ion cyclotron (ESIC), electromagnetic ion cyclotron (EMIC) and whistler mode chorus waves can respectively account for the three distinct types of REPs discussed above.

Atmospheric consequences were investigated with the following results:

- o ESIC and EMIC REPs deposit more energy into the atmosphere than chorus REPs.
- o Immediate increases in the OH concentration up to a factor

of 10 are observed during REP occurrence and gradually return to normal within 24 hours.

- o Ozone diminution only occurs simultaneously with daytime REPs, only after sunrise with nighttime REPs, and return to normal in several hours.

The following main conclusions may be drawn from these results:

- o The ESIC wave interaction is by far the dominant cause of REPs.
- o REPs are locally important in reducing ozone concentration (10-30%).

Based on all of the above, future considerations should include the following areas of endeavor:

- o Although the concurrent proton precipitation seems to point to the anisotropic pitch angle instability at the equator rather than to a current driven instability low on the field line, results are inconclusive (Kintner et al. 1979). Resolution of the location of the instability would lead to better understanding of the trigger mechanism for REPs.
- o Relativistic electron precipitation at rates less than strong diffusion were not analyzed here due to the difficulty with distinction of the pitch angle distribution and the instrument response limits for small loss cones. Weaker events (moderate diffusion) may be locally important to ozone chemistry particularly if they occur during the daytime.

- o Though REPs locally increase the OH concentrations day or night, an investigation of long term effects on the atmosphere are important since it may be possible to dry out the mesosphere over a year's time and actually account for long term ozone buildups (Crutzen, private communication, 1980).

Appendix A - OVI-19 Data Set and Analysis

The data used for this study was collected by two magnetic spectrometers aboard Air Force Office of Aerospace Research satellite 1969-25C designated OV1-19 and provided by the instrument builder and prime investigator, A. L. Vampola, Aerospace Corp., El Segundo, Ca. The purpose of this study was to find the frequency of occurrence of REP events and determine the suitability of this type of data for future study.

The OV1-19 satellite was launched on 18 March 1969 into an elliptical orbit with apogee/perigee at 5790/467 km. Inclination was 104.8° and the period 154 min. The satellite was spin stabilized at 8.4 rpm. A three-axis magnetometer tabulated aspect information. Four hours of continuous data was collected and transmitted each tape recorder dump. Over the life of the satellite, approximately 25% data coverage was achieved.

The two spectrometers were of the 180° magnetic focusing type similar to those onboard AF/OAR satellite OV3-3 and schematically presented in Fig. A-1. (Vampola, 1969). One unit, the Low Energy Magnetic Spectrometer (LEMS), had eight electron channels from 53-444 keV with geometric factors as shown in Table A-1 and the other, the High Energy Magnetic Spectrometer (HEMS), had 16 electron detectors from 537 keV to 5.1 MeV as shown in Table A-2. The look direction of each instrument was perpendicular to the satellite spin axis (for pitch angle scanning) which was nominally perpendicular to the orbit plane. Flux counting rates were sampled once per second. As with

FIG A-1. OV3-3 180⁰ Magnetic Focussing Spectrometer (shown without baffling) from Vampola, 1969.

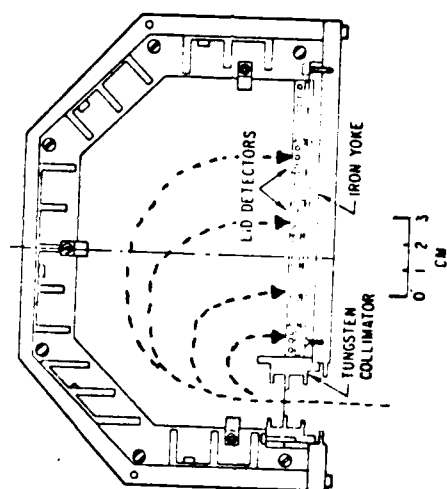


TABLE A-1. Low Energy Magnetic Spectrometer Channels, Energy, and Geometric Factors.

TABLE A-1. Low-Energy Magnetic Spectrometer

Detector	Electron Energy, kev	Geometric Energy Efficiency Factor, cm ² ster kev
1	53-14 ⁺¹⁵	0.00205
2	92-16 ⁺¹⁹	0.0833
3	139-21 ⁺²²	1.36
4	192 ± 24	2.53
5	250 ± 26	2.34
6	312 ± 27	2.16
7	376 ± 28	2.01
8	444 ± 29	1.86
9	Protons > 35 Mev, bremsstrahlung back- ground detection	

TABLE A-2. High Energy Magnetic Spectrometer Channels, Energy,
and Geometric Factors.

TABLE A-2. High-Energy Magnetic Spectrometer

Detector	Energy, Mev	Geometric Energy Factor, cm ² ster kev
1	0.537- $11.4^{+1.10}_{-1.10}$	45.7
2	0.822- $11.4^{+1.10}_{-1.10}$	36.5
3	1.112- $11.4^{+1.10}_{-1.10}$	30.1
4	1.409- $11.4^{+1.10}_{-1.10}$	25.5
5	1.711- $11.4^{+1.10}_{-1.10}$	22.1
6	2.018- $11.4^{+1.10}_{-1.10}$	19.4
7	2.321- $11.4^{+1.10}_{-1.10}$	17.3
8	2.632- $11.4^{+1.10}_{-1.10}$	15.7
9	2.932- $11.4^{+1.10}_{-1.10}$	14.3
10	3.245- $11.4^{+1.10}_{-1.10}$	13.1
11	3.557- $11.4^{+1.10}_{-1.10}$	12.1
12	3.863- $11.4^{+1.10}_{-1.10}$	11.3
13	4.169- $11.4^{+1.10}_{-1.10}$	10.5
14	4.476- $11.4^{+1.10}_{-1.10}$	9.87
15	4.783- $11.4^{+1.10}_{-1.10}$	9.29
16	5.091- $11.4^{+1.10}_{-1.10}$	8.67
17	Protons >130 Mev, bremsstrahlung background detection	

the OV3-3 units, the flux determinations were limited at low counting rates by statistical fluctuations and at high counting rates by telemetry quantization (Vampola, 1969). In addition, a rectangular energy versus geometric factor response is assigned for each actual channel response for data analysis as illustrated in Fig. A-2. Instrument response to an input spectrum zero everywhere in the loss cone and isotropic at some level outside the loss cone is shown for Channel 4 of the low energy unit in Fig. A-3. An order of magnitude drop in flux response roughly occurs 7° into the loss cone.

A typical high to low altitude pass for Channel 7 of the low energy unit is shown in Fig. A-4. Inner zone (A), slot region (B), outer zone (C), and polar region (D) are distinctive features of the pass. The large variation in count rate is due to pitch angle sampling.

Fig. A-5 for an OV3-3 sample shows the outer zone at low altitude from L=3-6 with envelopes drawn for the top and bottom of the sampling scatter. The top envelope is representative of the locally trapped flux and the bottom is the flux furthest into the loss cone. When the two curves touch, as in Fig. A-5 at L=5.6, this indicates an isotropic pitch-angle distribution, as predicted for strong pitch angle diffusion. The analysis mode is then to view all of the available passes for this envelope closure. Final determination is made when flux vs pitch angle plots show isotropic fluxes filling the upward looking (downward flowing) loss cone.

In order to accomplish the task of analyzing the data set

FIG A-2. Geometric factor-energy response function assigned each channel for data analysis. Total area outside of the rectangle is about 15% but both functions contain equal areas. A slight bias towards higher energies for very steep spectra is produced (Vampola, 1969).

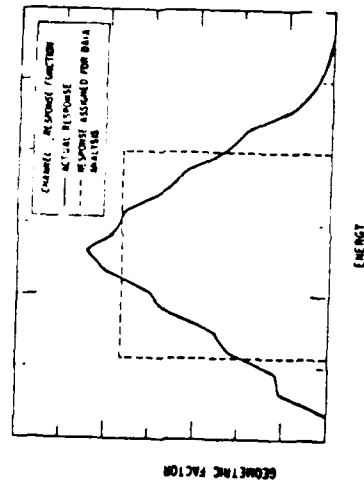


FIG A-3. Instrument response-pitch angle output.

QVI-19 LEMS CHANNEL 4 (.197 MEV) 30 DEGREE LOSS-CONE

INPUT RESPONSE: 0 FOR P.A. $\leq 30^\circ$ AND $\geq 150^\circ$
 1 FOR P.A. $> 30^\circ$ AND $< 150^\circ$

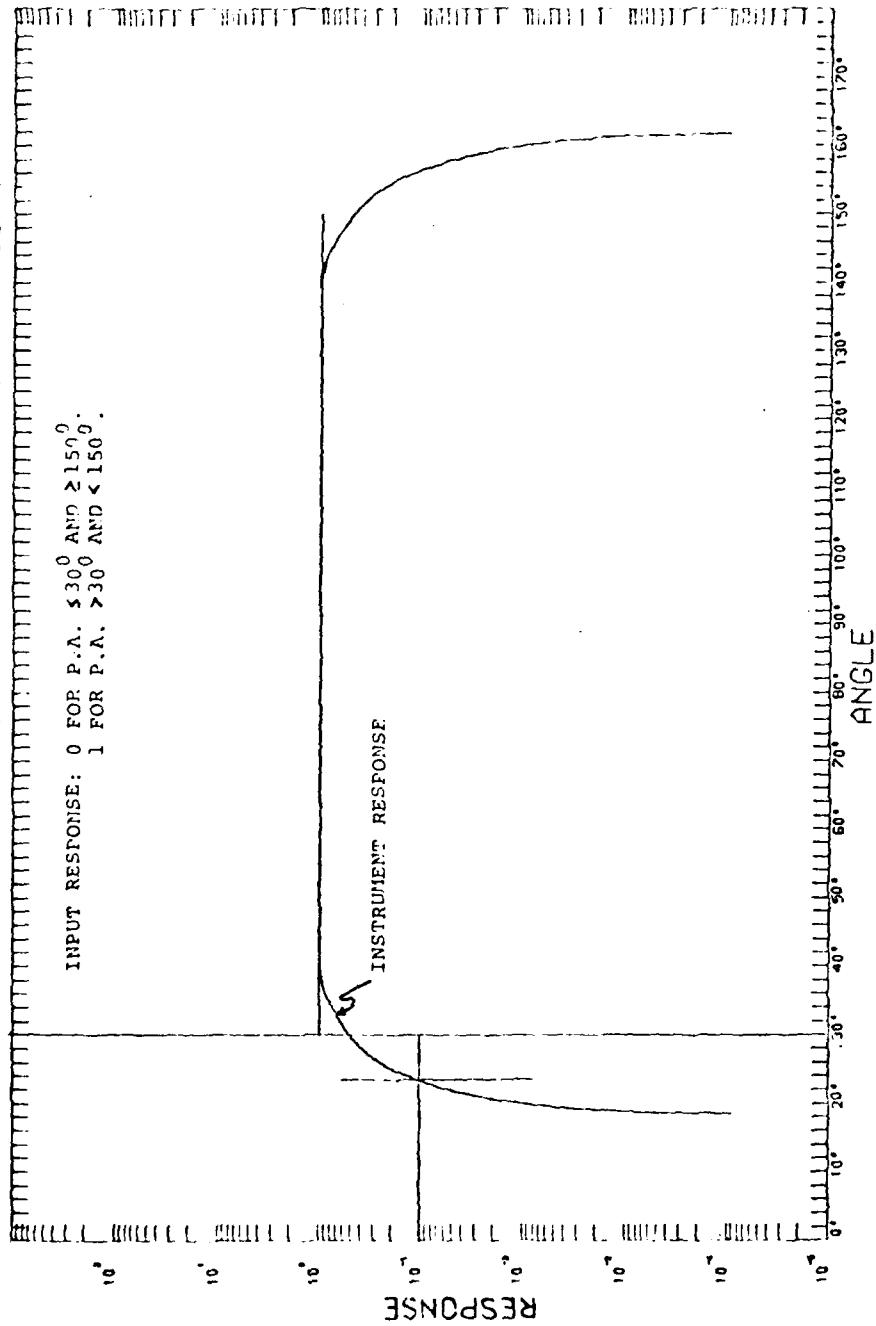


FIG A-4. Analog record of 376 ± 28 keV electron data plotted as counting rate versus time on a pseudo-logarithmic scale. Universal time, magnetic field intensity, invariant latitude, L, altitude, and MLT are listed for 200-sec intervals. Pitch-angle distribution sampling produces the large variations in counting rate in several regions of the plot (Vampola, 1971).

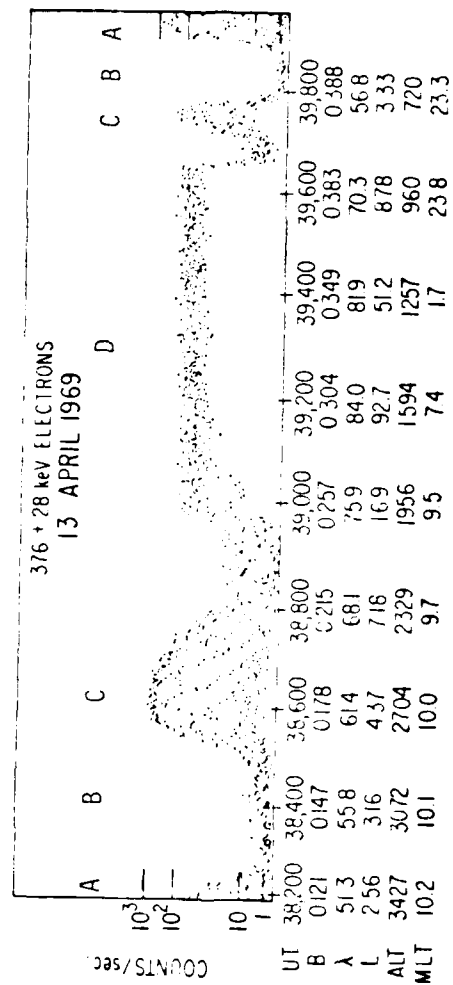


FIG A-5. Plots of instantaneous flux measurements versus L for the 712 ± 137 keV electron channel from the OV3-3 magnetic spectrometer. The scatter in the data points is due to pitch-angle sampling. Envelope curves at the maximums and minimums are shown to emphasize the data that are isotropic in pitch angle (Koons et al, 1972).

AD-A092 545

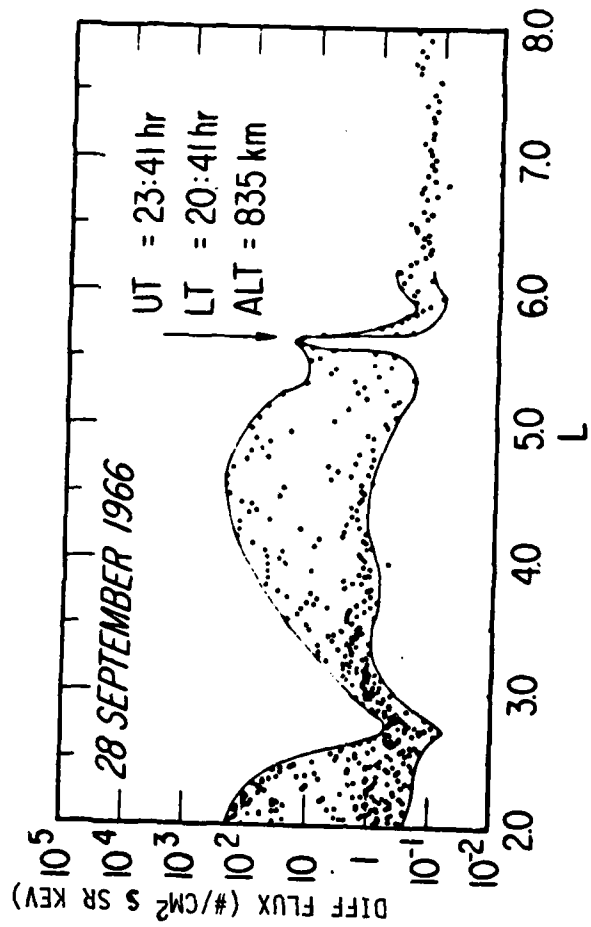
AIR FORCE INST OF TECH WRIGHT-PATTERSON AFB OH F/G 4/1
RELATIVISTIC ELECTRON PRECIPITATION: AN OBSERVATIONAL STUDY.(U)
1980 L J ANDREOLI
AFIT-CI-80-26D NL

UNCLASSIFIED

3 of 4

AD
A092 545





as objectively as possible, a set of criteria was developed for REP event identification. These are illustrated in flow chart form in Fig. A-6. The first criteria was that only data in the L range 4-7 would be studied. A total of 320 passes, clustered as high as 4 passes on a given day, was extracted from a data set spanning from day 77 of 1969 to day 13 of 1970 (301 days). Because of the finite width of the field-of-view ($\sim 10^\circ$) and the fact that the satellite orbit precluded pitch angle sampling to 0° (and 180°) everywhere in the orbit, it was determined that data below 1000 km would yield loss cones large enough for a high frequency of complete loss cone sampling. This criteria eliminated 88 cases. The third criteria demanded that REP fluxes be high at higher energies ($1 \text{ MeV} \pm 500 \text{ keV}$). Seventy-two cases failed on this criteria. Next we determined that if we had data at least 10° into the loss cone, we could identify real precipitation based on the channel response previously described. This eliminated 39 cases of which 17 were less than 10° into the loss cone and 22 did not sample the loss cone at all. In some cases (19), count rate sampling and pitch angle modulation were phased in such a way as to make event evaluation impossible. These cases were labeled "instrument problems" and eliminated. Finally, 103 cases remained in which an analysis could reasonably be made. These passes are shown as passes per day versus day of the year in Fig. A-7. Of these 103 "clean cases", only three exhibited isotropic fluxes into the loss cone at relativistic energies (identified by arrows on Fig. A-7).

The REP of 14 May 1969 (day 134) is of particular interest since it exhibited the "hardest" spectrum of the three REPs (spectra

**FIG A-6. Flow chart illustrating process of elimination through the
OV1-19 data set.**

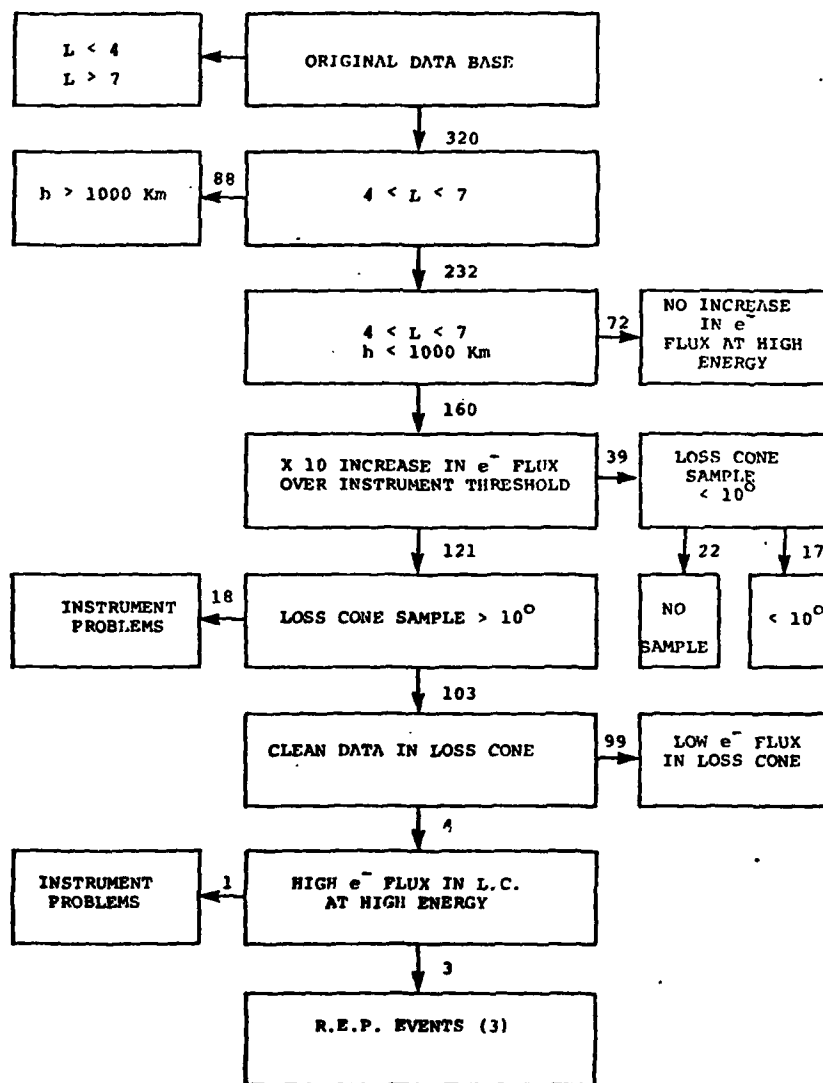
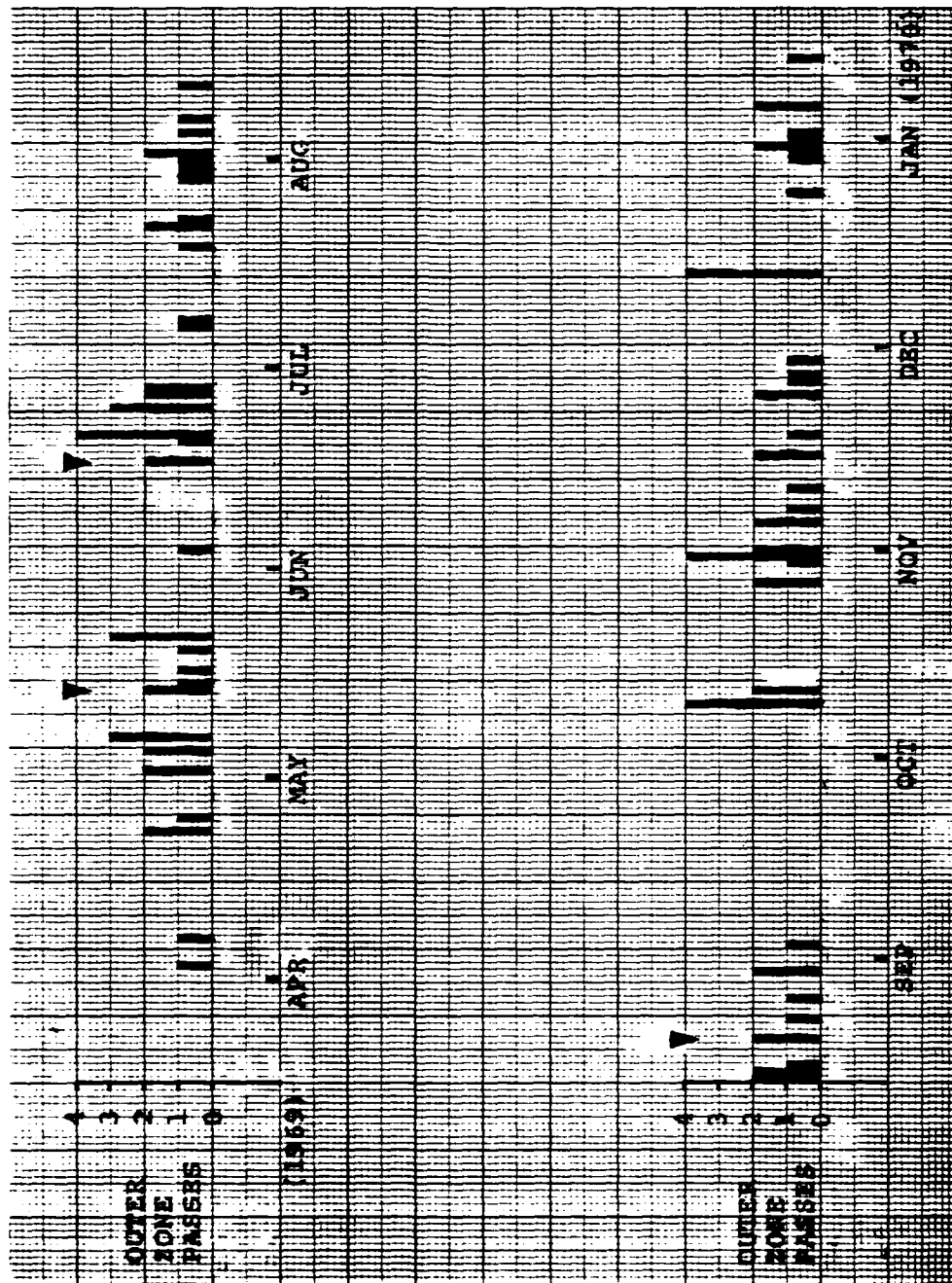


**FIG A-7. Outer zone passes per day versus day of the year for the
OV1-19 data set. Arrows indicate the three event days.**



will be compared later) and falls in a period where Alaska forward scatter data exists. Figures A-8, a and b, show plots of differential electron fluxes versus U.T. (in seconds) for the various energy channels, LEMS Bremsstrahlung (background), and LEMS protons (>55 keV) for day 134. The higher energy electron channels exhibited low fluxes and are not shown. The outer edge of the outer zones at local morning (07:20 MLT: 79642-79659 U.T.) and local midnight (00:18 MLT; 80184-80225 U.T.) exhibit envelope closure. The local morning outer zone exhibited very high trapped fluxes (see Fig. A-9) at all energies but the loss cone ($\sim 55^\circ$) was not sampled.

The pitch angle distribution for the local midnight (80196-80225 U.T.) outer zone transit are shown in Fig. A-10 for energy channels 192, 537, 822 keV. The nominal loss cone is $\sim 66^\circ$ and the symbols "+/o" represent instrument viewing positions up/down the local magnetic field line. The plots show high fluxes in the upward viewing loss cone at several instances in all energy channels while the downward viewing loss cone generally show normal trail-off to lower values. The large variation in precipitating fluxes is due either to the transition of the satellite through regions of strong and not so strong precipitation or spatial variations in trapped flux during the 30 seconds duration of the pitch and angle plot. The plots represent approximately seven complete ($0-180^\circ$) pitch angle distributions each and 537 keV channel has each data sample labeled with the last three digits of the U.T. in seconds. Deep in the loss cone two orders of magnitude variation occur between 210 and 218 whereas a half order of magnitude between 205 and 220 or 201 and 197 occur in the trapped distribution.

FIG A-8a. Differential electron fluxes versus UT (sec), B (Gauss),
L, LAT (deg), ALT (km), for LEMS Proton, LEMS BREM, 822,
537, 444, 376 keV Electrons for DAY 134.

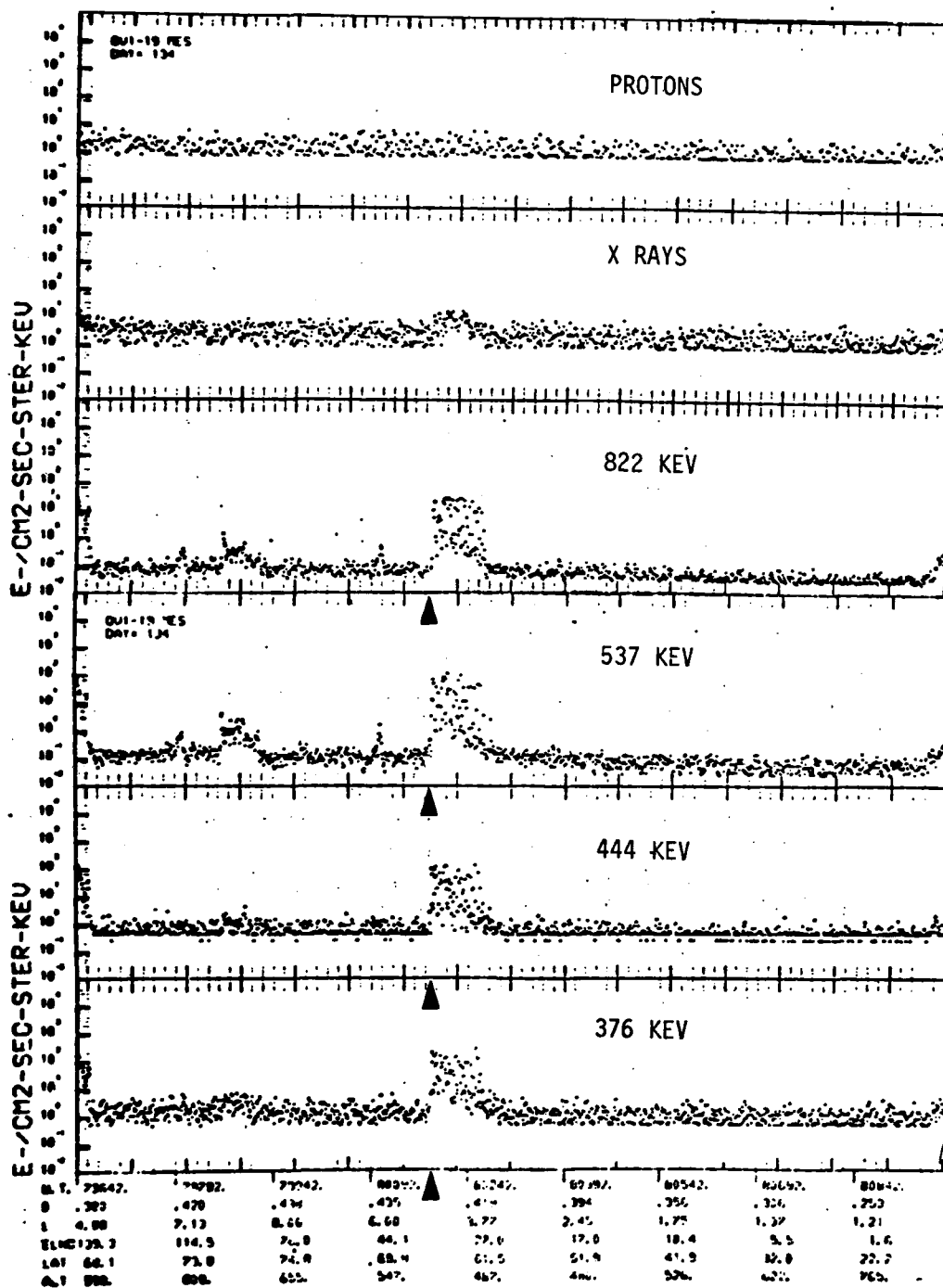


FIG A-8B. Differential electron fluxes versus UT (sec), B (Gauss),
L, LAT (deg), ALT (km), for 312, 250, 192, 139, 92,
53 keV Electrons for DAY 134.

FIG A-9. Electron differential energy fluxes versus UT (hr), LT (hr),
ALT (km), L, for 192, 537, 822 keV electrons for DAY 134
(14 MAY 1969).

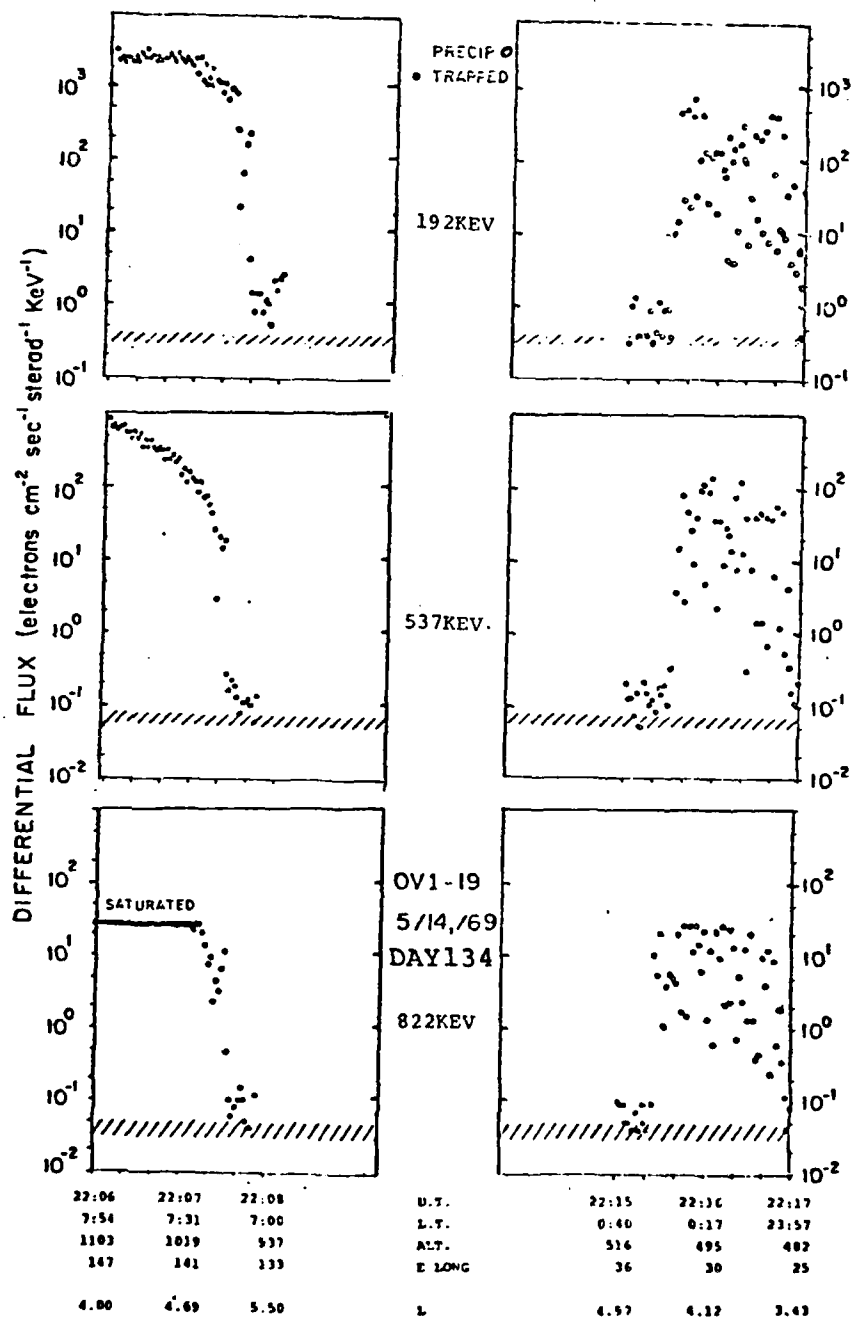
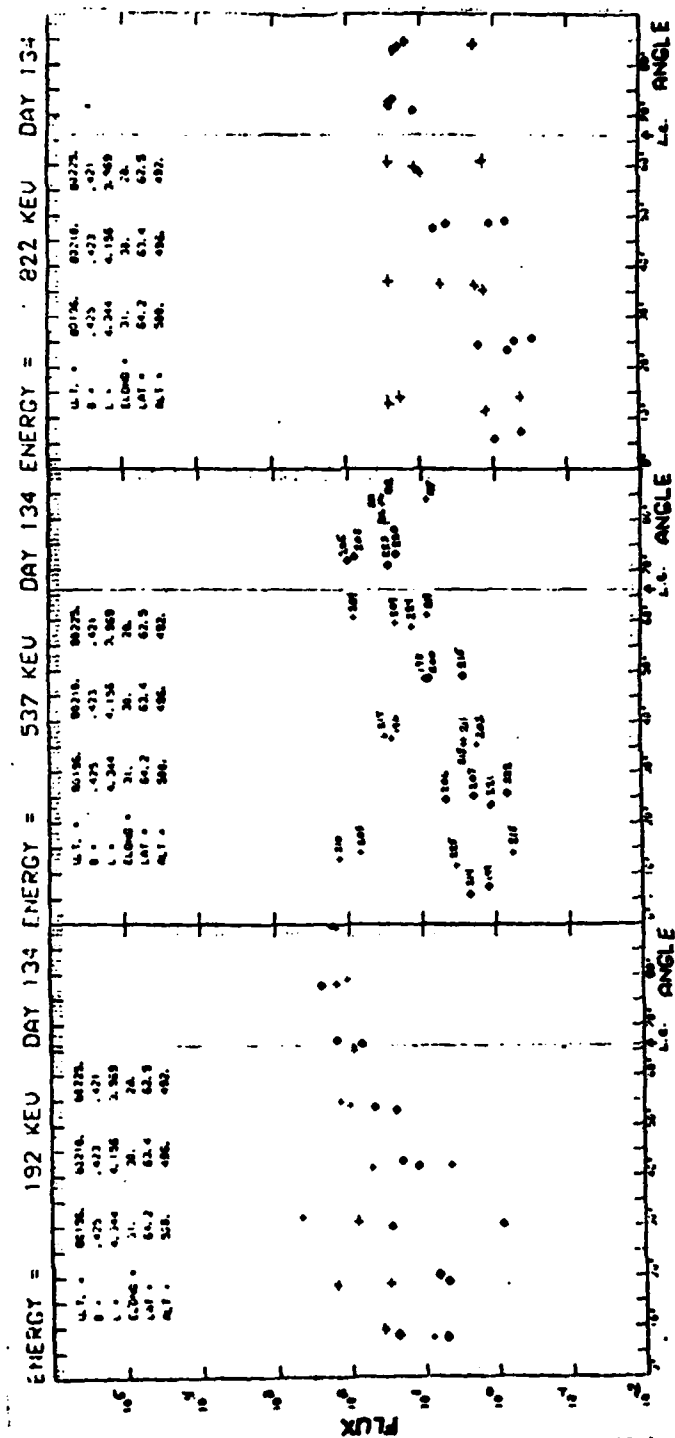


FIG A-10. Flux versus Pitch Angle for electron channels 192, 537, and 822 keV for DAY 134. Flux upper limit in channel 822 keV is 2.696×10^1 since the high count rate meter coax cable from the HEMS to the satellite data system broke during launch.



A time sequence in pitch angle versus differential flux for the same local midnight outer zone pass (day 134) for channels 444, and 537 keV are shown in Figs. A-11 a and b respectively. Data samples are subjectively connected to display the most "normal" distribution. This is difficult because of the wide spread in pitch angles ($\sim 50^\circ$) between samples and compounded by a few missing samples. The 444 keV channel is the highest energy measured by the LEMS whereas the 537 keV channel is the lowest for the HEMS. Thus, Fig. A-11 a is 165° out of phase with Figs. A-11b. Each sample is identified by the last three digits of the U.T. in seconds. "Normal" upward and downward loss cone distributions are evident at all energies after sample 213. The upper envelope (dashed line -U) connects the locally trapped flux (pitch angles $\sim 90^\circ$) and the lower (dashed line-L) connects the lowest flux into the loss cones (pitch angles $\sim 0^\circ, 180^\circ$). It is evident that the envelopes nearly close in at least a few places towards the outer edge of the outer zone though the instrument is viewing almost $2\frac{1}{2}$ orders of magnitude into the loss cone. Most notable is the isotropic (upward viewing loss cone) flux in Fig. A-11b at sample 188 (80188 U.T.).

The magnetic activity for this event as well as Alaska forward scatter absorption are illustrated in Fig. A-12. The Alaska forward scatter absorption on day 134 was greater than 10 db from 19:40 to 02:10 U.T. (09:40-16:10 Alaskan local time) with a peak absorption of 19 db at 20:12 U.T. The only other absorption recorded was early on days 132 and 137. Dst shows disturbed conditions

FIG A-11a. Time sequence of differential electron flux versus pitch angle for the 537 key channel on DAY 134.

DIFF FLUX (E/CM² SR S KEV)

537 KEV CHANNEL

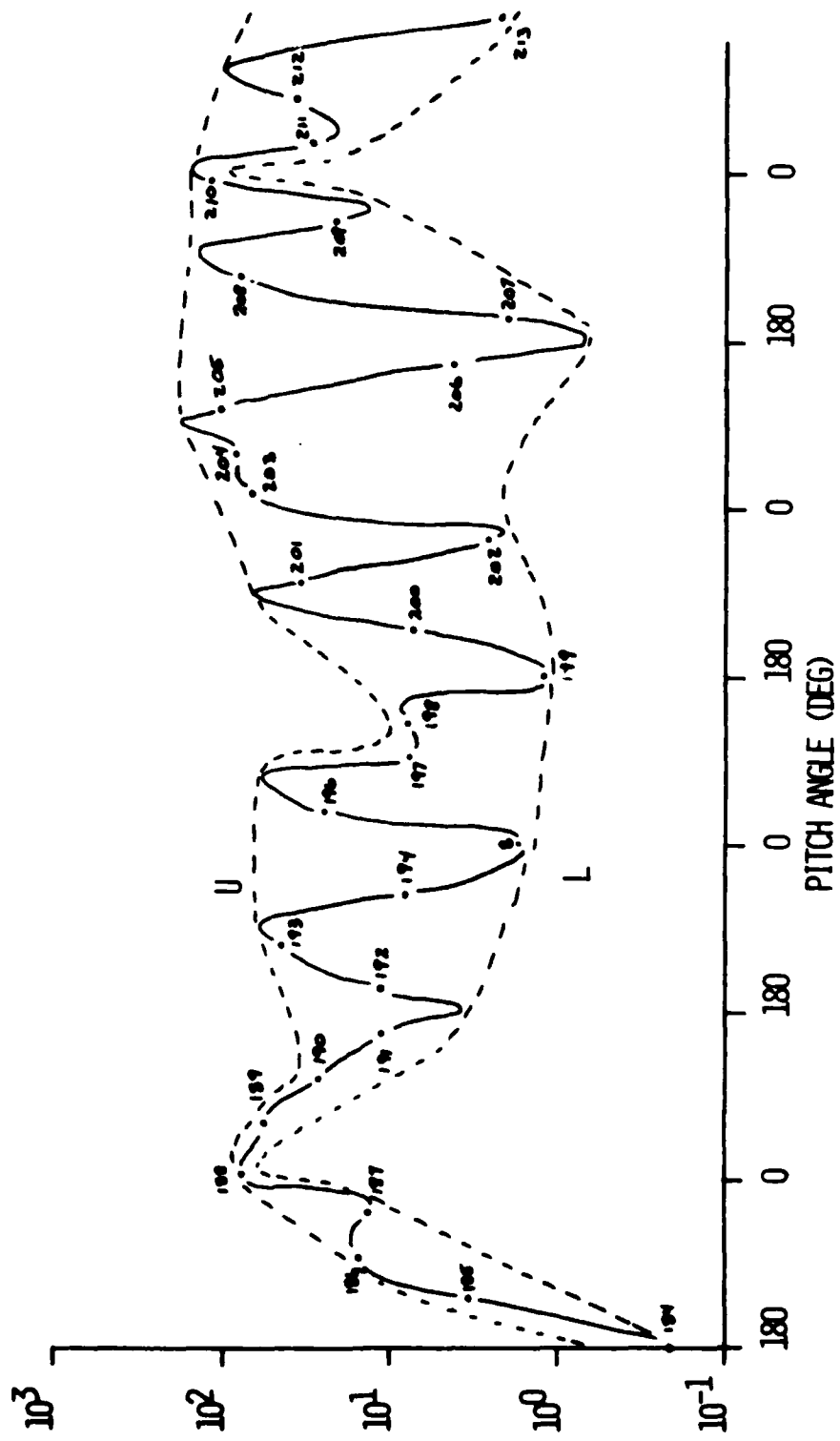


FIG A-11b. Time sequence of differential electron flux versus pitch angle for the 444 keV channel on DAY 134.

DIFF FLUX (E/CM² SR S KEV)

444 KEV CHANNEL

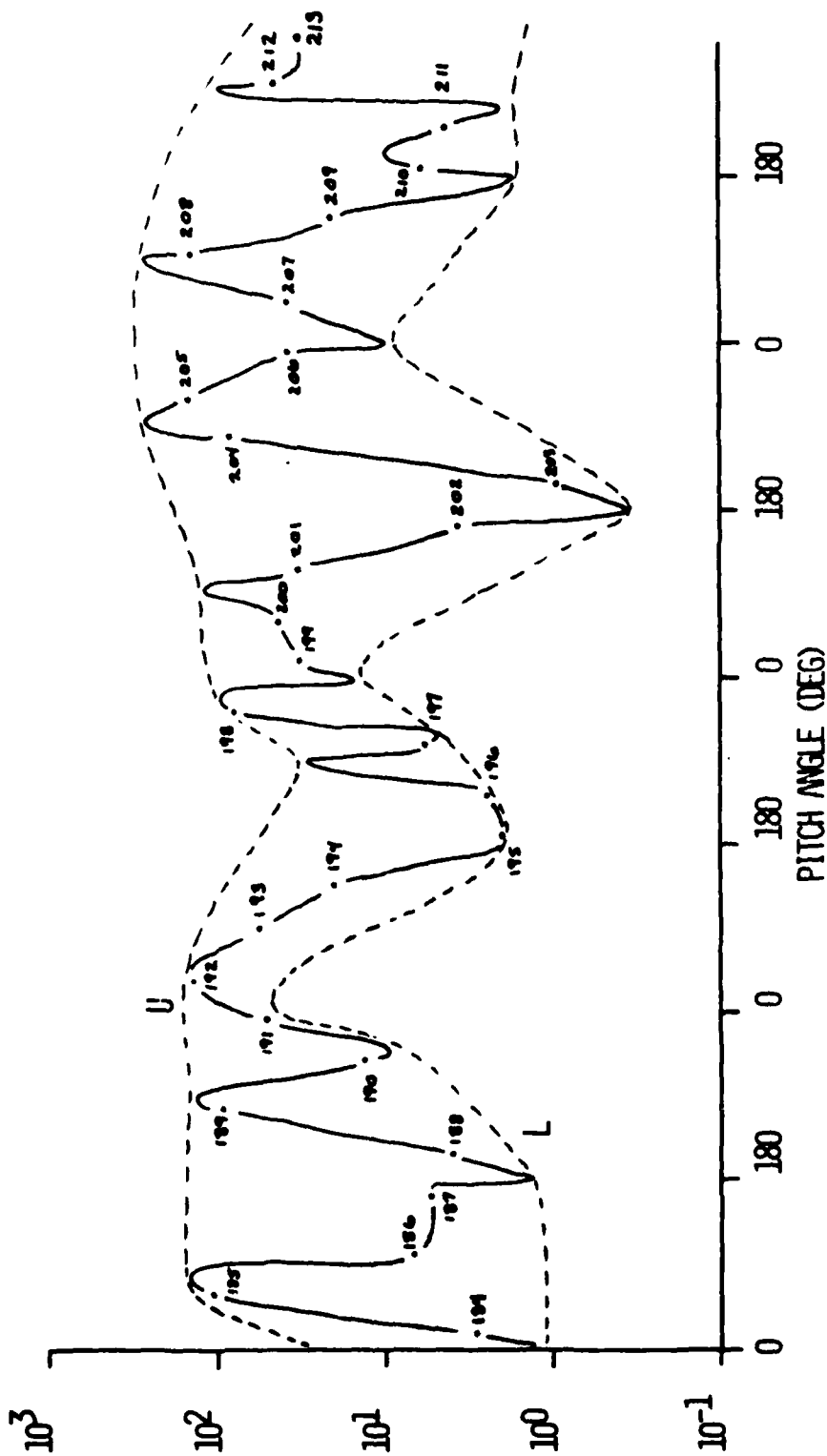
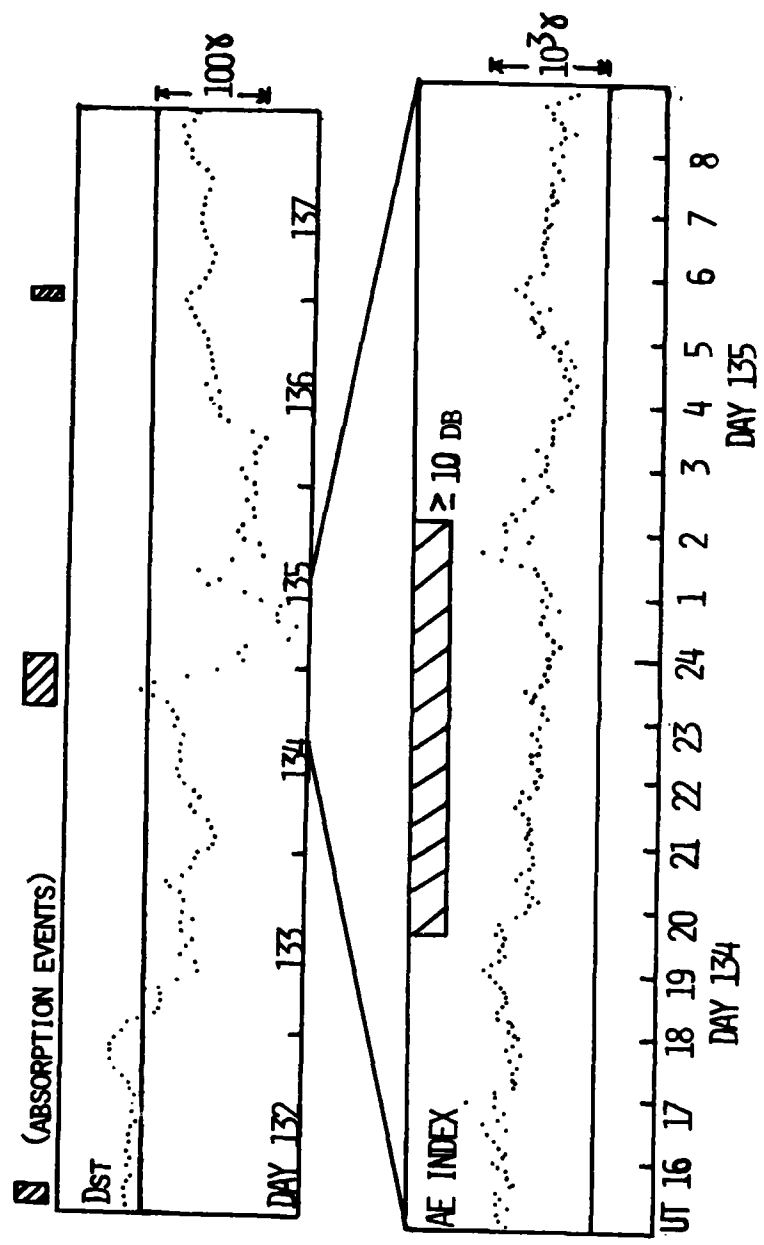


FIG A-12. Dst for days 132 through 137; AE Index for parts of the UT day for days 134 and 135; Alaskan forward scatter absorption events are represented by the hatched boxes (Bailey, Personal Communication, 1973).



from late on day 132 through recovery on day 137. A positive excursion is particularly noticeable near 22 U.T. on day 134 near the time of the satellite REP observation. This is followed by a $>100\gamma$ depression early on day 135. AE shows a 1500γ increase at 20 U.T. on day 134 two hours before the satellite observation. It is interesting to note that although day 133 and 135 are strongly disturbed no forward scatter absorption occurred above Alaska (Thorne and Larsen, 1976). A local early morning and late evening pass by OV1-19 occurred on day 135. The local early morning pass did not sample the loss cone but even though the evening pass did, no REP was observed.

All three REPs observed occurred between local midnight and local dawn. The expected frequency of occurrence of REPs based on this study is 1-13% with a 90% confidence interval. The 50% confidence level indicates a frequency of 5% (see Fig. A-13). This is consistent with 5% frequency for moderate (>8 db absorption) REPs found by Bailey (1968).

The energy spectra for the three OV1-19 REPs are compared with the OV3-3 REP measured by Vampola (1971) in Fig. A-14. It is evident that they are comparable in hardness (approach to isoenergetic). So it is not surprising that the REPs will have a similarly predicted effect on the deposition of energy (represented by ion production) in the atmosphere as shown in Fig. A-15.

The conclusions of this study are that the OV1-19 was capable of observing strong diffusion events (REPs) from a few hundred keV to 1 keV energies. More REPs would probably have been observed if

the loss cones were sampled more frequently. A similar data set with better statistics would yield more morphological information and possibly a clue to the type and relative importance of various mechanisms for causing REPs.

FIG A-13. REP frequency of occurrence for the OV1-19 Data Base.

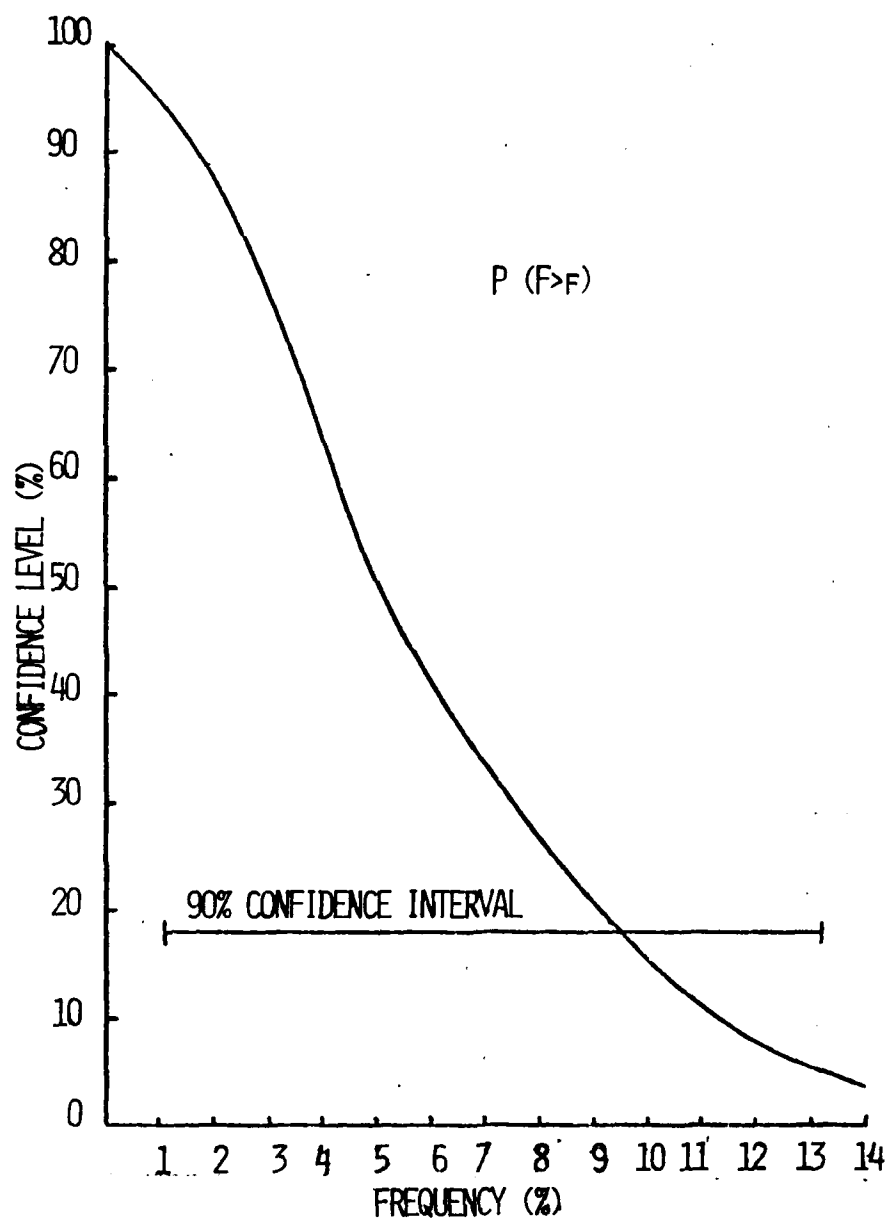


FIG A-14. REP energy spectra for the three OV1-19 events in 1969
compared with the Vampola OV3-3 spectrum of 1971.

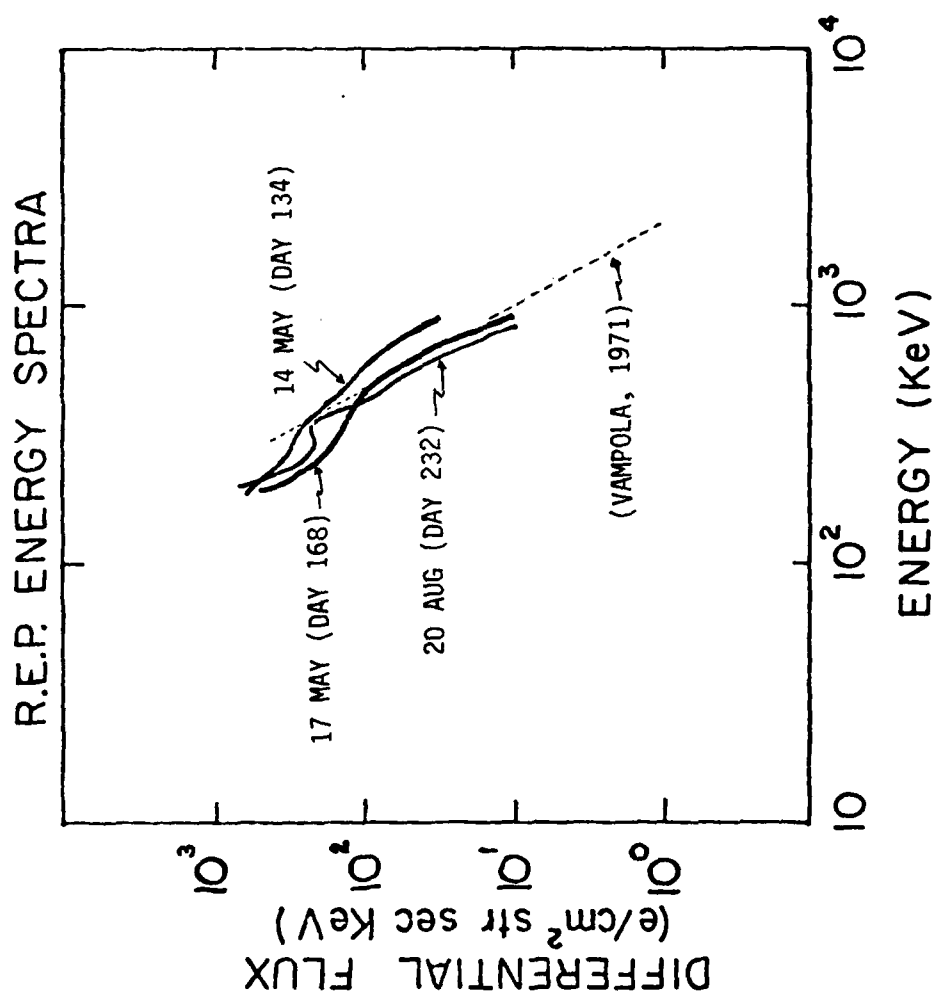
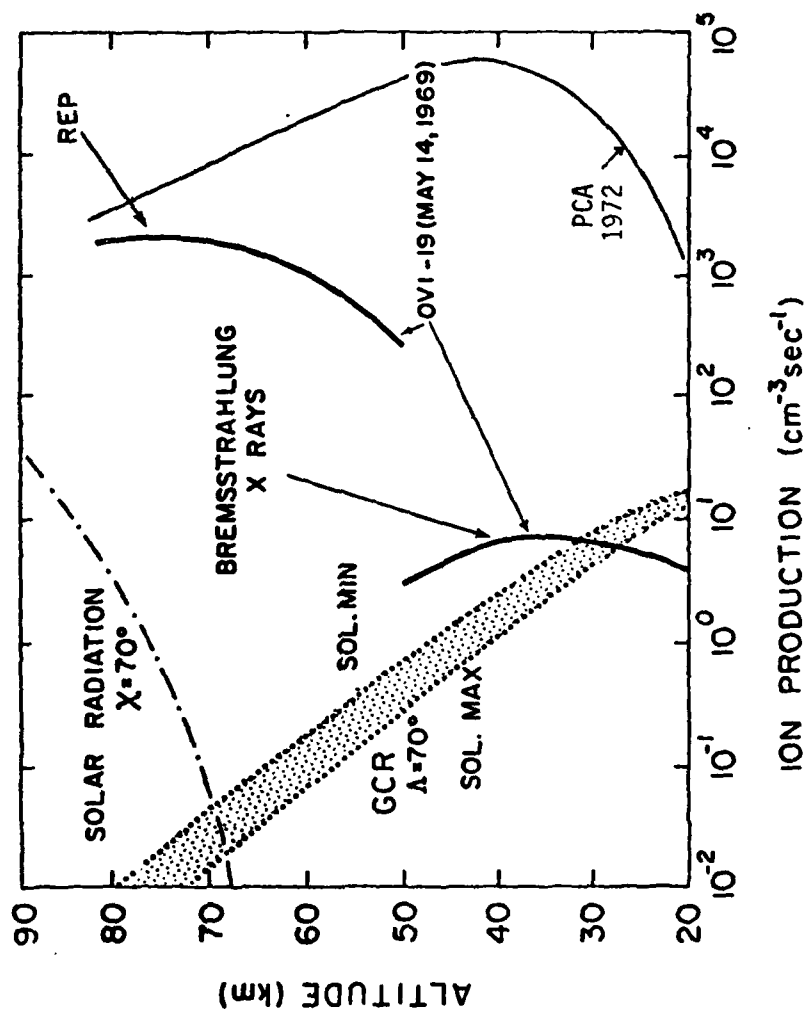


FIG A-15. Ion production rate versus altitude for the OV1-19 REP,
solar radiation, galactic cosmic rays and the solar proton
event of 1972.



Appendix B - S3-3 Data Collection

The primary data set used in this dissertation was collected by a magnetic spectrometer aboard Air Force Space Test Program satellite STP 74-2 designated S3-3 launched in the summer of 1976. The S3-3 orbit is highly elliptical (schematically shown in Fig. B-1) with apogee/perigee nominally 8000/250 km. The maximum apogee of 8035 km was reached on 3 August 1976 and continues to decrease at a rate of 0.35 km/day. Orbit inclination is 97° with a period of 180 minutes. The nodal drift rate is 0.27° /day westward, i.e., the local time of orbit nodal crossing decreases 0.049 hr/day from launch values of 10:30 (ascending node) and 22:30 (descending node) as shown in Fig. B-2, panel a. The line of apsides (major axis of orbit) was initially placed less than 90° from equator on the sun side (Fig. B-1) and slowly rotates toward the dark side at the rate of 0.94° /day from a launch value of 63° as shown in Fig. B-2, panel b. The satellite spin rate was maintained at approximately 3 rpm with the spin vector perpendicular to the orbit plane. In order to maintain the solar cells facing toward the sun (and the backside away for thermal control), the satellite was yawed 180° on days 40-48 (around 14 February) 1977.

The S3-3 scientific payloads are listed with brief descriptions in Table B-1. Of prime interest is the CRLS-217 which will be described here in detail. Data from ONR-104 and CRLS-218 are referred to in Chapter 2 and only brief details will be provided.

FIG B-1. S3-3 Orbital parameters.

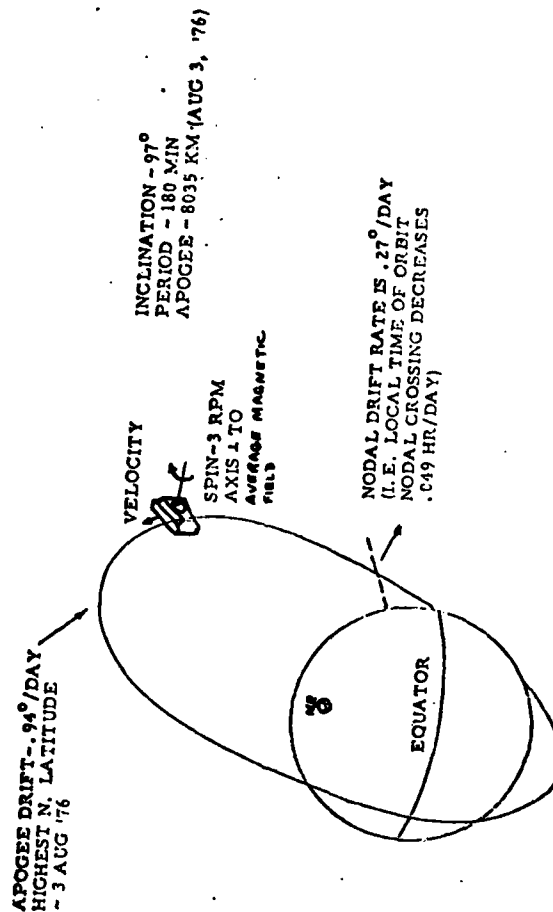
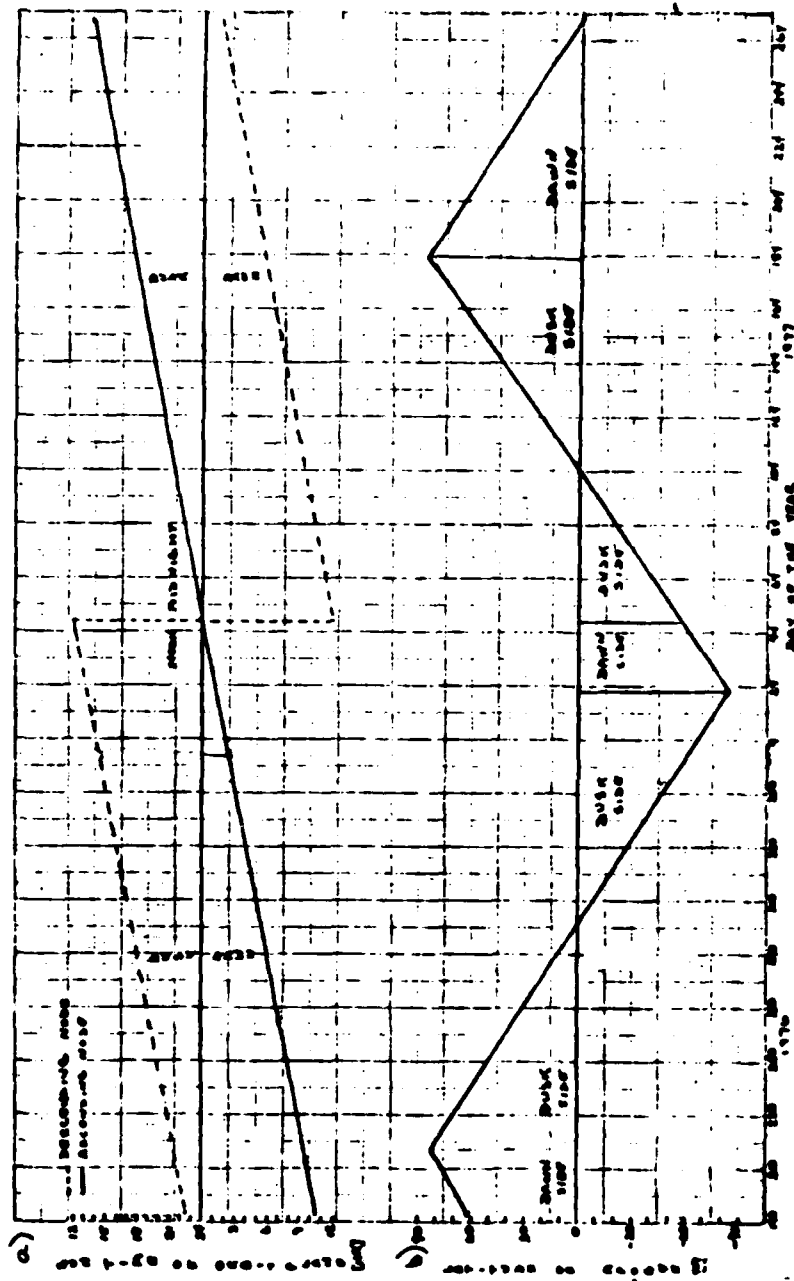


FIG B-2. Day of the year versus a) sun time of the orbit phase
and b) latitude of apogee.



**TABLE B-1. S3-3 Scientific payloads with prime investigators
in parenthesis.**

CRL-214 Trapped Proton Monitoring (Yates) AFGL

Solid state detectors are used to measure the spatial distributions, angular distribution and energy spectrum of protons with energy between .1 and 100 MeV.

ONR-118 Low Energy Particle Spectrometer (Sharp) Lockheed

Ions and electrons with energy between 0.5 to 16 KeV and 0.07 to 24 KeV, respectively, are detected using channel multipliers. Particle energy is determined using either magnetic deflection or penetration of particles through thin foils.

ONR-104 Electric Field Measurements (Moser) UC Berkeley

3 dipoles are used to measure the three components of the DC & AC electrostatic electric field.

CRL-215 Electric Fields and Ion Drifts (Wildman) AFGL

Plasma probes are used to detect the bulk flow of plasma and hence to infer the electric field strength. Four electrostatic analyzers are sensitive to ions in the energy range of 0.1 to 30 eV.

CRLS-217 Energetic Electron Environment (Vampola) Aerospace

A magnetic spectrometer with solid state detectors is used to measure the differential electron flux between 0.012 and 1.6 MeV, protons from 0.08 to 3 MeV, and alphas above 4 MeV.

CRLS-218 Magnetospheric Hydrogen-Electron Abundance (Fennell) Aerospace

An electrostatic analyzer is used to measure the fluxes of low energy electrons and ions at several energies; electrons from 0.17 to 8.4 KeV, ions from 0.09 + 3.9 KeV/Q.

CRLS-225 ELF/VLF Fields (Koons) Aerospace

An air core magnetic loop and a dipole antenna are used to measure the intensity of magnetic and electric fields in the 0.1 to 20.0 KHz frequency range.

The satellite payload configuration is shown in Fig. B-3 with the spin vector perpendicular to the page. The CRLS-217 location is such that penetration thresholds are approximately 10 MeV for electrons and 100 MeV for protons.

CRLS-217 is a twelve differential energy channel magnetic electron spectrometer with an eight channel integral proton and alpha (1 channel) telescope. Permanent magnets (.53 and 1.64 kiloGauss) momentum analyze electrons entering the instrument aperture focusing them onto 12 silicon semiconductor detectors at the primary focus (180°). The instrument configuration is similar to the OV3-3 and OV1-19 instruments described in Appendix A except that the Low Energy Magnetic Spectrometer (LEMS) and High Energy Magnetic Spectrometer (HEMS) are built into one unit as shown in Fig. B-4. Pulseheight analysis of the energy deposits in the detectors is used to discriminate against bremsstrahlung, noise, and penetrating ion background. Also, an additional shielded detector is used to monitor the background. The electron output of each detector channel corresponds to the uni-directional electron intensity of a given energy bin (typically ± 15 keV for LEMS, ± 100 keV for HEMS) and from these outputs an energy spectrum can be obtained.

The data format is presented in Table B-2. Included are the identification code, channel, sample rate, bits/sample, and geometric energy factor for 28 CRLS-217 and 2 (21, 22) CRLS-218 measurements. Measurements 1-5 are the 5 LEMS channels while 6-12 are the HEMS, with all channel accumulators read out every 1/16 second. Note that

FIG B-3. S3-3 Payload Configuration.

FIG B-4. S3-3 HEMS/LEMS Layout.

TABLE B-2. S3-3 HEMS/LEMS Data Format.

MEAS.	ID CODE	CHANNEL	SAMPLES/SEC	BITS/SAMPLE	GEOMETRIC-ENERGY FACTOR
1	ME1	E ₀ ~ 12 KeV	16	12**	0.0088 cm ² ster KeV
2	ME2	E ₀ ~ 33 KeV			0.0029
3	ME3	E ₀ ~ 70 KeV			0.0141
4	ME4	E ₀ ~ 110 KeV			0.0036
5	ME5	E ₀ ~ 160 KeV			0.0147
6	ME6	E ₀ ~ 235 KeV			0.54
7	ME7	E ₀ ~ 435 KeV			6.52
8	ME8	E ₀ ~ 655 KeV			6.12
9	ME9	E ₀ ~ 880 KeV			5.65
10	ME10	E ₀ ~ 1.11 MeV			5.17
11	ME11	E ₀ ~ 1.35 MeV			4.57
12	ME12	E ₀ ~ 1.60 MeV	16		4.04 cm ² ster KeV
13	MP1-S	E _p > 50 KeV			
14	MP2-S	E _p > 100 KeV	4		0.012 cm ² ster
15	MP3-S	E _p > 200 KeV			
16	MP4 "	E _p > 300 KeV			
17	MP5 "	E _p > 400 KeV			
18	MP6 "	E _p > 500 KeV			
19	MP7 "	E _p > 600 KeV			
20	MP8 "	E _p > 700 KeV			
21	S	E ₀ > 1.55 MeV			
22	L	E ₀ > 4.0 MeV - 13.2 MeV			0.012 cm ² ster
23	ESA STEP	ESA STEP			
24	E1	E ₀ ~ 12 KeV	4		
25	E2	E ₀ ~ 33 KeV			
26	E3	E ₀ ~ 70 KeV			
27	E4	E ₀ ~ 110 KeV			
28	E5	E ₀ ~ 160 KeV			
29	E6	E ₀ ~ 235 KeV			
30	E7	E ₀ ~ 435 KeV			
31	E8	E ₀ ~ 655 KeV			
32	E9	E ₀ ~ 880 KeV			
33	E10	E ₀ ~ 1.11 MeV			
34	E11	E ₀ ~ 1.35 MeV			
35	E12	E ₀ ~ 1.60 MeV			
36	E13	E ₀ ~ 1.80 MeV			
37	E14	E ₀ ~ 2.00 MeV			
38	E15	E ₀ ~ 2.20 MeV			
39	E16	E ₀ ~ 2.40 MeV			
40	E17	E ₀ ~ 2.60 MeV			
41	E18	E ₀ ~ 2.80 MeV			
42	E19	E ₀ ~ 3.00 MeV			
43	E20	E ₀ ~ 3.20 MeV			
44	E21	E ₀ ~ 3.40 MeV			
45	E22	E ₀ ~ 3.60 MeV			
46	E23	E ₀ ~ 3.80 MeV			
47	E24	E ₀ ~ 4.0 MeV			
48	E25	E ₀ ~ 4.2 MeV			
49	E26	E ₀ ~ 4.4 MeV			
50	E27	E ₀ ~ 4.6 MeV			
51	E28	E ₀ ~ 4.8 MeV			
52	E29	E ₀ ~ 5.0 MeV			
53	E30	E ₀ ~ 5.2 MeV			
54	E31	E ₀ ~ 5.4 MeV			
55	E32	E ₀ ~ 5.6 MeV			
56	E33	E ₀ ~ 5.8 MeV			
57	E34	E ₀ ~ 6.0 MeV			
58	E35	E ₀ ~ 6.2 MeV			
59	E36	E ₀ ~ 6.4 MeV			
60	E37	E ₀ ~ 6.6 MeV			
61	E38	E ₀ ~ 6.8 MeV			
62	E39	E ₀ ~ 7.0 MeV			
63	E40	E ₀ ~ 7.2 MeV			
64	E41	E ₀ ~ 7.4 MeV			
65	E42	E ₀ ~ 7.6 MeV			
66	E43	E ₀ ~ 7.8 MeV			
67	E44	E ₀ ~ 8.0 MeV			
68	E45	E ₀ ~ 8.2 MeV			
69	E46	E ₀ ~ 8.4 MeV			
70	E47	E ₀ ~ 8.6 MeV			
71	E48	E ₀ ~ 8.8 MeV			
72	E49	E ₀ ~ 9.0 MeV			
73	E50	E ₀ ~ 9.2 MeV			
74	E51	E ₀ ~ 9.4 MeV			
75	E52	E ₀ ~ 9.6 MeV			
76	E53	E ₀ ~ 9.8 MeV			
77	E54	E ₀ ~ 10.0 MeV			
78	E55	E ₀ ~ 10.2 MeV			
79	E56	E ₀ ~ 10.4 MeV			
80	E57	E ₀ ~ 10.6 MeV			
81	E58	E ₀ ~ 10.8 MeV			
82	E59	E ₀ ~ 11.0 MeV			
83	E60	E ₀ ~ 11.2 MeV			
84	E61	E ₀ ~ 11.4 MeV			
85	E62	E ₀ ~ 11.6 MeV			
86	E63	E ₀ ~ 11.8 MeV			
87	E64	E ₀ ~ 12.0 MeV			
88	E65	E ₀ ~ 12.2 MeV			
89	E66	E ₀ ~ 12.4 MeV			
90	E67	E ₀ ~ 12.6 MeV			
91	E68	E ₀ ~ 12.8 MeV			
92	E69	E ₀ ~ 13.0 MeV			
93	E70	E ₀ ~ 13.2 MeV			
94	E71	E ₀ ~ 13.4 MeV			
95	E72	E ₀ ~ 13.6 MeV			
96	E73	E ₀ ~ 13.8 MeV			
97	E74	E ₀ ~ 14.0 MeV			
98	E75	E ₀ ~ 14.2 MeV			
99	E76	E ₀ ~ 14.4 MeV			
100	E77	E ₀ ~ 14.6 MeV			
101	E78	E ₀ ~ 14.8 MeV			
102	E79	E ₀ ~ 15.0 MeV			
103	E80	E ₀ ~ 15.2 MeV			
104	E81	E ₀ ~ 15.4 MeV			
105	E82	E ₀ ~ 15.6 MeV			
106	E83	E ₀ ~ 15.8 MeV			
107	E84	E ₀ ~ 16.0 MeV			
108	E85	E ₀ ~ 16.2 MeV			
109	E86	E ₀ ~ 16.4 MeV			
110	E87	E ₀ ~ 16.6 MeV			
111	E88	E ₀ ~ 16.8 MeV			
112	E89	E ₀ ~ 17.0 MeV			
113	E90	E ₀ ~ 17.2 MeV			
114	E91	E ₀ ~ 17.4 MeV			
115	E92	E ₀ ~ 17.6 MeV			
116	E93	E ₀ ~ 17.8 MeV			
117	E94	E ₀ ~ 18.0 MeV			
118	E95	E ₀ ~ 18.2 MeV			
119	E96	E ₀ ~ 18.4 MeV			
120	E97	E ₀ ~ 18.6 MeV			
121	E98	E ₀ ~ 18.8 MeV			
122	E99	E ₀ ~ 19.0 MeV			
123	E100	E ₀ ~ 19.2 MeV			
124	E101	E ₀ ~ 19.4 MeV			
125	E102	E ₀ ~ 19.6 MeV			
126	E103	E ₀ ~ 19.8 MeV			
127	E104	E ₀ ~ 20.0 MeV			
128	E105	E ₀ ~ 20.2 MeV			
129	E106	E ₀ ~ 20.4 MeV			
130	E107	E ₀ ~ 20.6 MeV			
131	E108	E ₀ ~ 20.8 MeV			
132	E109	E ₀ ~ 21.0 MeV			
133	E110	E ₀ ~ 21.2 MeV			
134	E111	E ₀ ~ 21.4 MeV			
135	E112	E ₀ ~ 21.6 MeV			
136	E113	E ₀ ~ 21.8 MeV			
137	E114	E ₀ ~ 22.0 MeV			
138	E115	E ₀ ~ 22.2 MeV			
139	E116	E ₀ ~ 22.4 MeV			
140	E117	E ₀ ~ 22.6 MeV			
141	E118	E ₀ ~ 22.8 MeV			
142	E119	E ₀ ~ 23.0 MeV			
143	E120	E ₀ ~ 23.2 MeV			
144	E121	E ₀ ~ 23.4 MeV			
145	E122	E ₀ ~ 23.6 MeV			
146	E123	E ₀ ~ 23.8 MeV			
147	E124	E ₀ ~ 24.0 MeV			
148	E125	E ₀ ~ 24.2 MeV			
149	E126	E ₀ ~ 24.4 MeV			
150	E127	E ₀ ~ 24.6 MeV			
151	E128	E ₀ ~ 24.8 MeV			
152	E129	E ₀ ~ 25.0 MeV			
153	E130	E ₀ ~ 25.2 MeV			
154	E131	E ₀ ~ 25.4 MeV			
155	E132	E ₀ ~ 25.6 MeV			
156	E133	E ₀ ~ 25.8 MeV			
157	E134	E ₀ ~ 26.0 MeV			
158	E135	E ₀ ~ 26.2 MeV			
159	E136	E ₀ ~ 26.4 MeV			
160	E137	E ₀ ~ 26.6 MeV			
161	E138	E ₀ ~ 26.8 MeV			
162	E139	E ₀ ~ 27.0 MeV			
163	E140	E ₀ ~ 27.2 MeV			
164	E141	E ₀ ~ 27.4 MeV			
165	E142	E ₀ ~ 27.6 MeV			
166	E143	E ₀ ~ 27.8 MeV			
167	E144	E ₀ ~ 28.0 MeV			
168	E145	E ₀ ~ 28.2 MeV			
169	E146	E ₀ ~ 28.4 MeV			
170	E147	E ₀ ~ 28.6 MeV			
171	E148	E ₀ ~ 28.8 MeV			
172	E149	E ₀ ~ 29.0 MeV			
173	E150	E ₀ ~ 29.2 MeV			
174	E151	E ₀ ~ 29.4 MeV			
175	E152	E ₀ ~ 29.6 MeV			
176	E153	E ₀ ~ 29.8 MeV			
177	E154	E ₀ ~ 30.0 MeV			
178	E155	E ₀ ~ 30.2 MeV			
179	E156	E ₀ ~ 30.4 MeV			
180	E157	E ₀ ~ 30.6 MeV			
181	E158	E ₀ ~ 30.8 MeV			
182	E159	E ₀ ~ 31.0 MeV			
183	E160	E ₀ ~ 31.2 MeV			
184	E161	E ₀ ~ 31.4 MeV			
185	E162	E ₀ ~ 31.6 MeV			
186	E163	E ₀ ~ 31.8 MeV			
187	E164	E ₀ ~ 32.0 MeV			
188	E165	E ₀ ~ 32.2 MeV			
189	E166	E ₀ ~ 32.4 MeV			
190	E167	E ₀ ~ 32.6 MeV			
191	E168	E ₀ ~ 32.8 MeV			
192	E169	E ₀ ~ 33.0 MeV			
193	E170	E ₀ ~ 33.2 MeV			
194	E171	E ₀ ~ 33.4 MeV			
195	E172	E ₀ ~ 33.6 MeV			
196	E173	E ₀ ~ 33.8 MeV			
197	E174	E ₀ ~ 34.0 MeV			
198	E175	E ₀ ~ 34.2 MeV			
199	E176	E ₀ ~ 34.4 MeV			
200	E177	E ₀ ~ 34.6 MeV			
201	E178	E ₀ ~ 34.8 MeV			
202	E179	E ₀ ~ 35.0 MeV			
203	E180	E ₀ ~ 35.2 MeV			
204	E181	E ₀ ~ 35.4 MeV			
205	E182	E ₀ ~ 35.6 MeV			
206	E183	E ₀ ~ 35.8 MeV			
207	E184	E ₀ ~ 36.0 MeV			
208	E185	E ₀ ~ 36.2 MeV			
209	E186	E ₀ ~ 36.4 MeV			
210	E187	E ₀ ~ 36.6 MeV			
211	E188	E ₀ ~ 36.8 MeV			
212	E189	E ₀ ~ 37.0 MeV			
213	E190	E ₀ ~ 37.2 MeV			
214	E191	E ₀ ~ 37.4 MeV			
215	E192	E ₀ ~ 37.6 MeV			
216	E193	E ₀ ~ 37.8 MeV			
217	E194	E ₀ ~ 38.0 MeV			
218	E195	E ₀ ~ 38.2 MeV			
219	E196	E ₀ ~ 38.4 MeV			
220	E197	E ₀ ~ 38.6 MeV			
221	E198	E ₀ ~ 38.8 MeV			
222	E199	E ₀ ~ 39.0 MeV			
223	E200	E ₀ ~ 39.2 MeV			
224	E201	E ₀ ~ 39.4 MeV			
225	E202	E ₀ ~ 39.6 MeV			
226	E203	E ₀ ~ 39.8 MeV			
227	E204	E ₀ ~ 40.0 MeV			
228	E205	E ₀ ~ 40.2 MeV			
229	E206	E ₀ ~ 40.4 MeV			
230	E207	E ₀ ~ 40.6 MeV			
231	E208	E ₀ ~ 40.8 Me			

the geometric energy factor decreases with energy for the LEMS and HEMS, i.e., sensitivity decreases with increase in energy (given flux will produce less counts/sec for a reduced geometric energy factor). In addition, S3-3 HEMS channels are more than a factor of 2.5 higher in geometric energy factor than OV1-19 LEMS channels to ~450 keV (see Table A-1) but more than a factor of 5.8 lower than OV1-19 HEMS channels to ~1.1 MEV (see Table A-2). Measurements 13-19 and 20 show specs for the integral proton and alpha channels which were also sampled at a rate of 1/sec.

A functional block diagram of the instrument is shown in Fig. B-5a. The lower level discriminator is set at 50% of the minimum expected energy deposit to reject bremsstrahlung and noise and the upper level discriminator is set at an upper threshold of 110% of the maximum expected energy to reject penetrating particles (cosmic rays and energetic protons).

Each electron energy channel is calibrated to find the channel response curve from which the absolute peak (EAPeAK), minimum (EAMIN), and maximum (EAMAX) values are determined (see Fig. B-5 b). A triangle which best matches the slopes of the response curve then yields its peak (E), minimum (ERMIN), and maximum (ERMAX) values. Center values of the two triangle slopes determine EMIN and EMAX. Vertical lines are extended through EMIN and EMAX. The vertical extension of these two lines continues until the resulting rectangle area formed with line segment H equals the area under the actual response curve. This representative rectangle is then used as the

FIG B-5. a) Electron Channel component schematic; b) general response curve; c) channel values for E^0 with 100% efficiency.

channel response for data analysis. (This is identical to the description in Appendix A and depiction in Fig. A-2 for instruments OV3-3 or OV1-19.) Values for the above parameters for an assumed spectrum of E^0 with 100% efficiency are listed in Fig. B-5 c. A typical three dimensional response is shown in Fig. B-6 for the 435 KEV channel.

The instrument loss cone response for 655 keV channel is shown in Figs. B-7 a-c as the result of an input distribution isotropic everywhere outside the loss cone and falling off about an order of magnitude per 2^0 in the loss cone for pitch angles of 8^0 , 18^0 , 28^0 , respectively. Response to a sharp cutoff can be demonstrated by a zero input distribution at the loss cone but is not represented here. Except for pitch angles less than $\sim 10^0$, an order of magnitude drop in response is about 9^0 into the loss cone. This response obviously affects the subjective selection of isotropic distributions in the loss cone and is further discussed in Appendix C.

The spin rate of ~ 3 RPM allows the instrument to complete a pitch angle plot ($0-180^0$) in approximately 10 seconds (compared to ~ 4 seconds for OV1-19). At 16 samples/sec, the instrument will collect ~ 150 samples for a pitch angle plot, nearly a factor of 40 better than the OV1-19. The S3-3 advantage is clear when the two data sets are compared for analysis.

The proton/alpha telescope consists of two silicon detectors in series as shown in Fig. B-8. Detector D1 (100 μ m thick) has a

FIG B-6. Typical three dimensional response curve for HEMS 435 keV
electron channel.

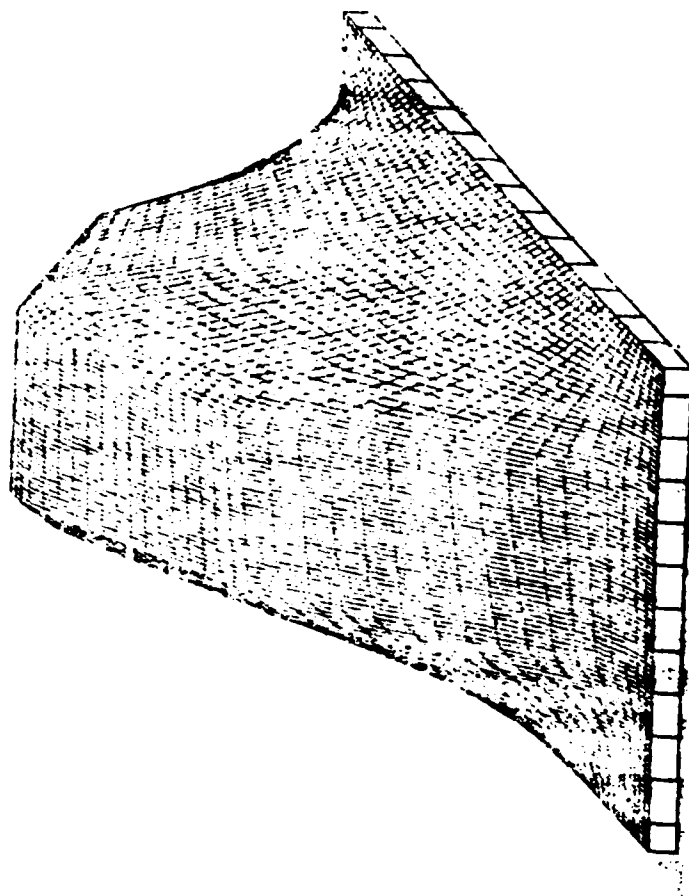
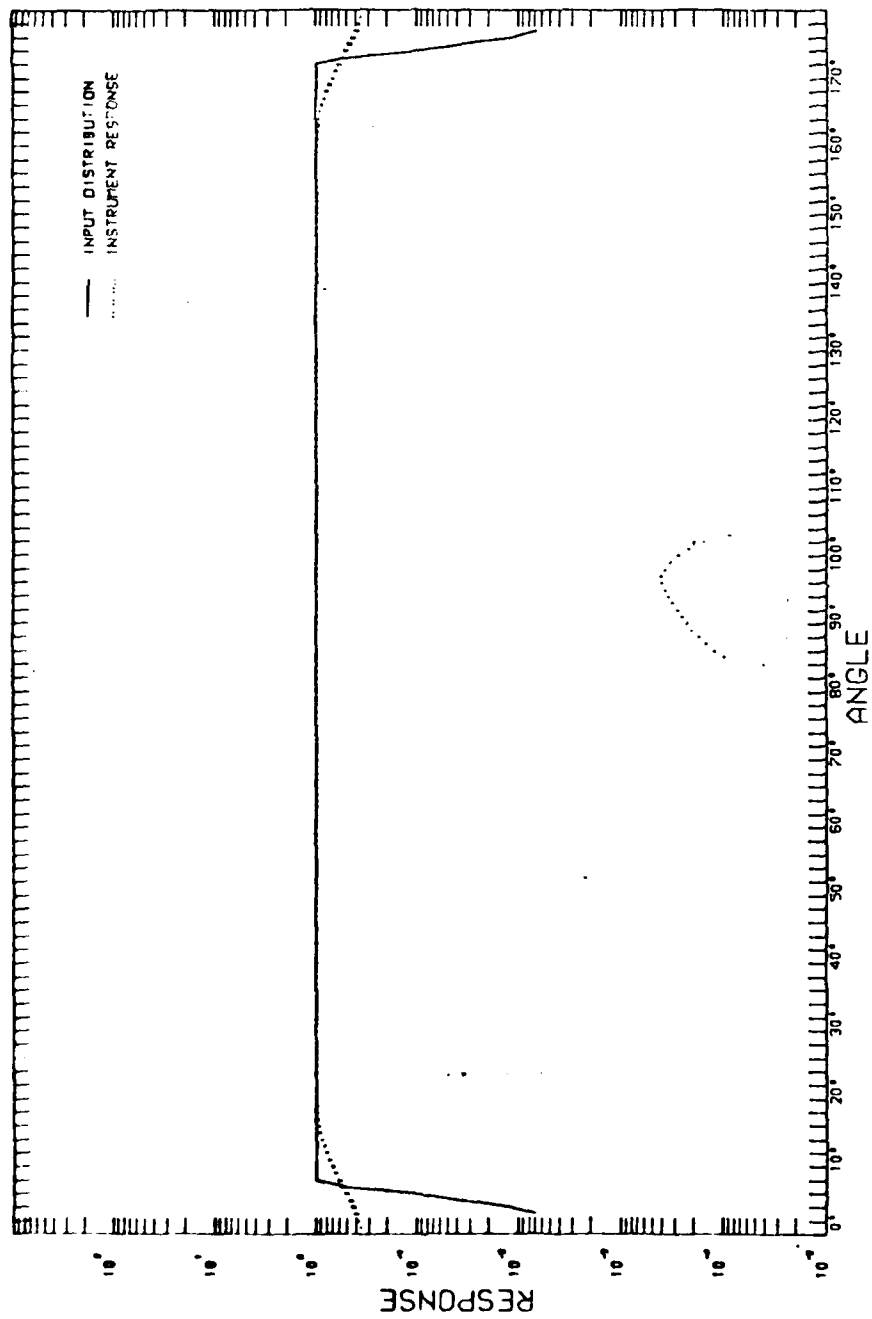
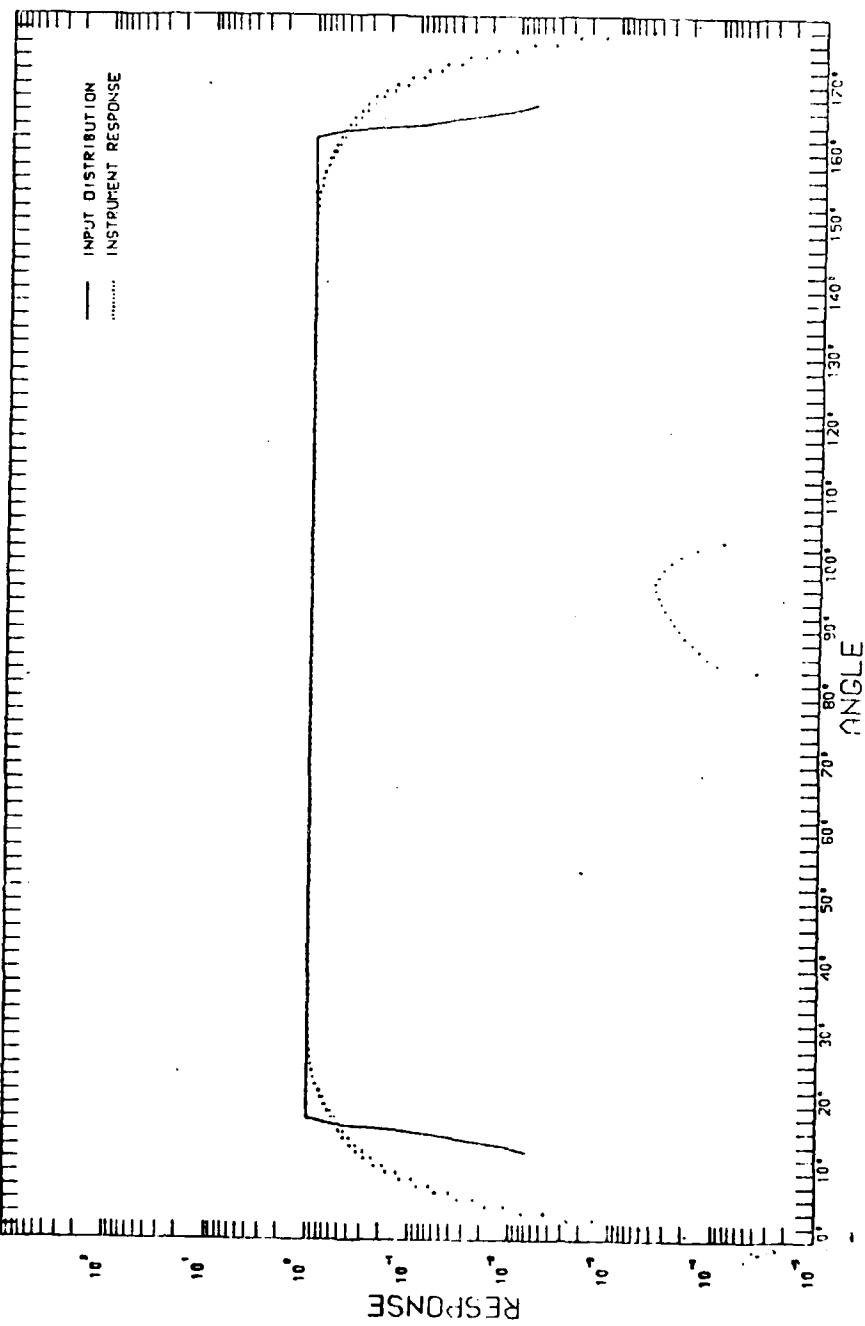


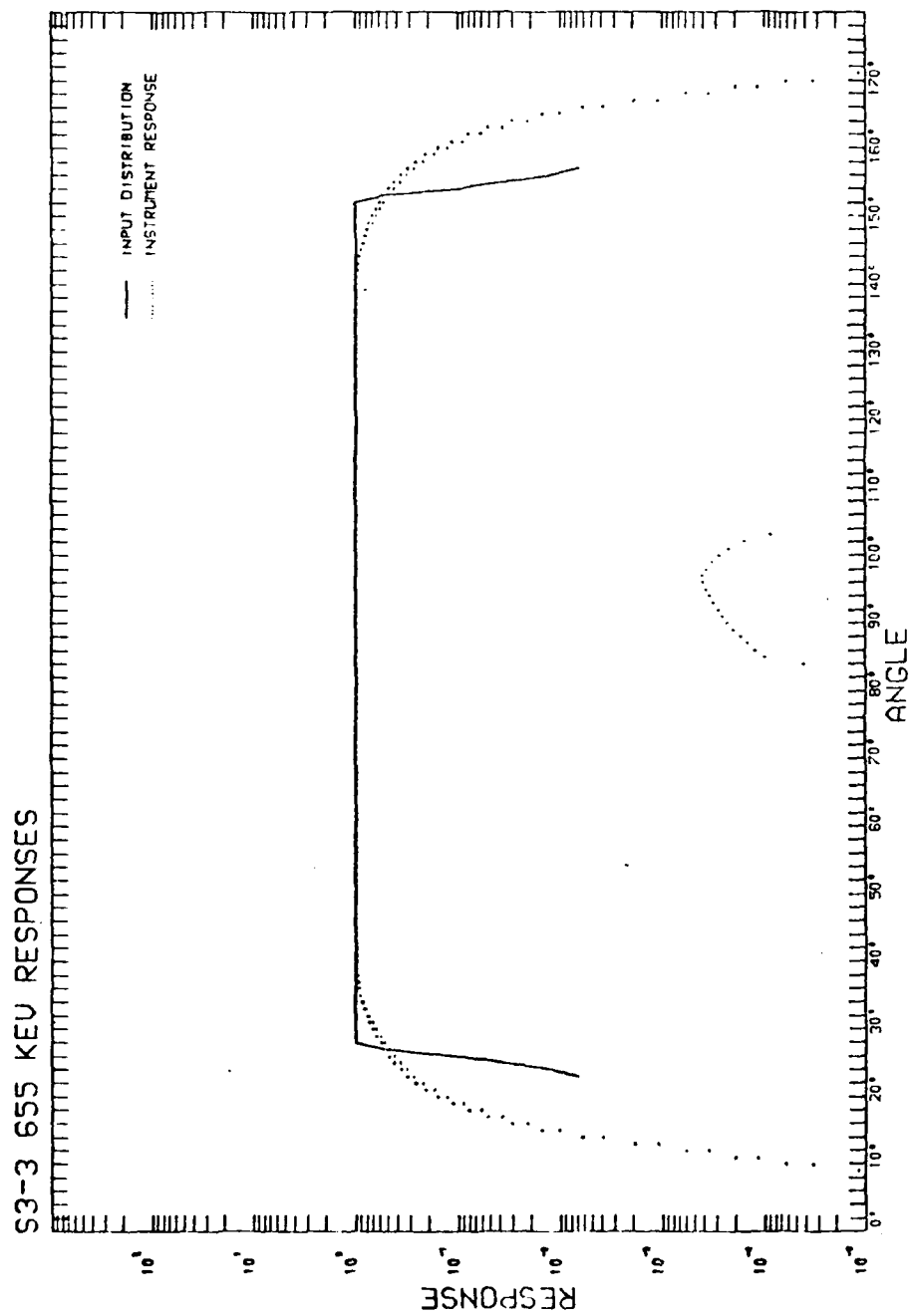
FIG B-7. Typical instrument loss cone response for the 655 keV electron channel for pitch angles 8° , 18° , and 28° .

S3-3 655 KEV RESPONSES



S3-3 655 KEV RESPONSES

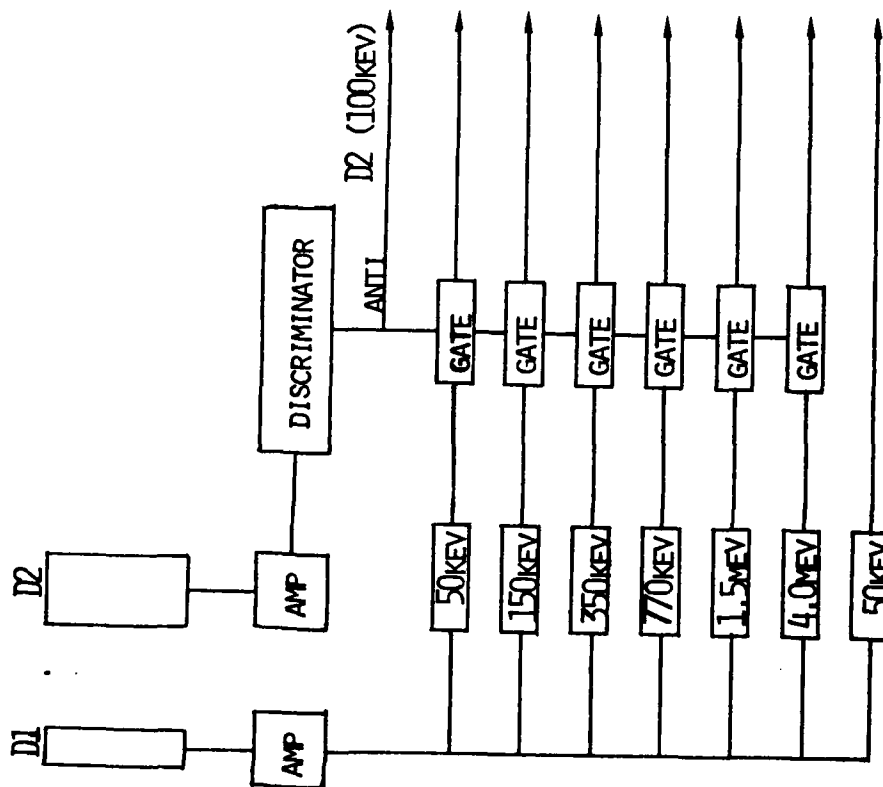




lower threshold of 50 keV and detector D2 (200 um thick) has a lower threshold of 100 keV and is the anti to reject energetic protons and cosmic rays penetrating through D1. Particles depositing more than about 4 MeV are assumed to be alphas since $p^+ > 3.2$ MeV would pass through D1 and be antied out by D2. All channels are sampled at 4 samples/sec and $E_p > 80$ keV and $E_\alpha > 4.0$ MeV are also sampled at 1/sec.

The S3-3 wave experiment by the Berkeley group (Mozer et al., 1977) obtained the three orthogonal components of the static or fluctuating electric field by measuring the potential differences between three orthogonal pairs of separated spheres. Two pairs of spheres were separated by 37 m in the satellite spin plane and one pair by 6 m along the spin axis. One sphere on the long boom could be operated as a Langmuir probe to make relative density fluctuations. Broadband signals (.05 - 16 kHz) were transmitted in real time to ground stations for 15 min periods on about 25% of the orbits (Kintner et al., 1978). The percentage of concurrent real time wave data and stored plasma data (CRLS 217) is much less. Only filtered wave data in bands from .03-100 kHz are available for most of the stored plasma data presented here.

FIG B-8. S3-3 Proton/alpha telescope data schematic.



TO DATA BOX AND
TELEMETRY

Appendix C - REP Event Identification and Catalog Use

In order to select REP events, it was necessary to be able to identify regions of isotropic fluxes on microfiche time plots of the electron and proton fluxes indicative of strong diffusion. Fig. C-1 shows such a plot for the 12, 235, 435, 655 and 850 keV electron and 80 keV proton channels for rev 1661 on a logarithmic scale; UT is measured in sec. The microfiche displays only every fourth data point. The variation in fluxes are due to pitch angle modulation. The key feature one must recognize is the missing upward viewing loss cone indicative of a full or isotropic loss cone. This feature is readily evident throughout the 12 keV electron channel from $L = 4.0 - 8.0$ and the 80 keV proton channel from $L = 4.5 - 6.0$. The 235, 435, 655, and 850 keV channels exhibit missing loss cones at $L \sim 4.5$ with the rest of the outer zone mostly eroded. Effects such as data drops and low altitude diminished flux values similarly appear as missing loss cones so it is extremely important to follow up with examination of the actual pitch-angle plot. Fig. C-2 shows pitch-angle plots for the 235, 435, 655, and 850 keV channels of the example in Fig. C-1 for UT 61092 and 61109 secs. The magnetic field direction is zero in the southward direction at the equator so for this Southern Hemisphere example, 180° is the up-the-field-line direction. The pitch angle is approximately 20° . Also, every data point is displayed and differential flux values can be obtained by dividing by the geometric value per channel (Table B-2). The top panel shows normal loss cone distributions both up and down the field line indicative of expected

radiation belt distributions. (However, the belts are disturbed since normally quiet times produce loss cones 3 1/2 orders of magnitude down from trapped flux). The bottom panel (data toward the outer edge of the outer zone) shows the pitch angle 17 secs later. Although normal distributions are evident down the field line, viewing up the field line shows isotropic distributions in all channels. Similar plots can be obtained for the proton channels.

Since the satellite spin axis is not always directly perpendicular to the local magnetic field line and the instrument has a field of view of approximately 5° (half angle), we chose only those cases with data at least 10° into the local loss cone. A few exceptions were made when the excursion into the loss cone was greater than 6° and isotropic fluxes were measured on previous and succeeding revs. Less than 3% of the 325 events selected for further pitch-angle analysis were rejected for the 'less than 10° in the loss cone' criteria.

Apogee/perigee bias in the flux data was investigated and found to be not important except in the actual appearance of the flux versus time distributions. At apogee the loss cones are small and the counting rates are high. Here we merely insisted on the '10° into the loss cone' criteria for validation. At perigee the loss cones are large, the extent (in time) of the entire outer zone is narrow, and the flux counting rates of both trapped and precipitated particles is small. The learning process to identify isotropic fluxes on the microfiche plots was accomplished by a series of trial and error analyses taking about 3 months of time and 150 samples. A high

Fig. C-1. Logarithmic flux (counts/sec) versus UT (sec) for the 12, 235, 435, 655, 850 keV electron and 80 keV proton channel for rev 1661.

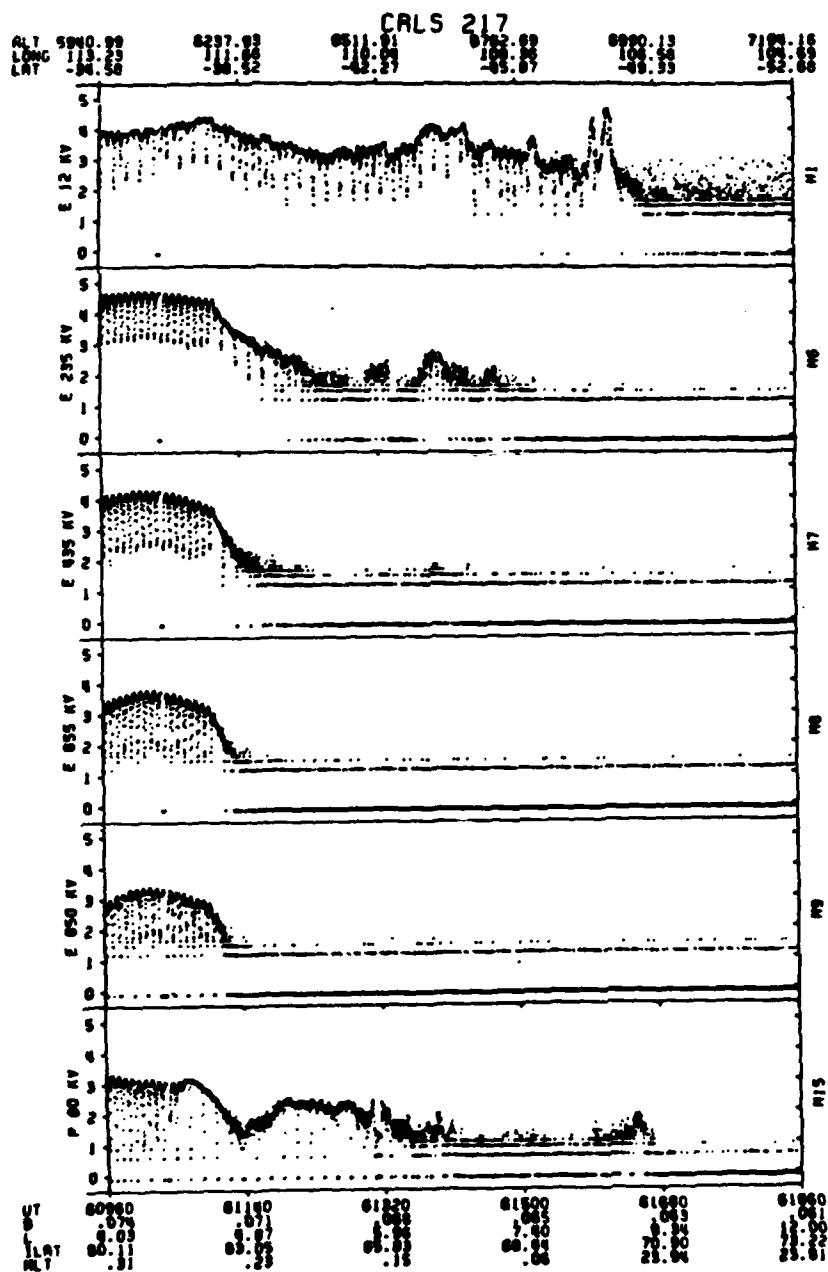


Fig. C-2. Flux (counts/sec) versus pitch angle (degrees) for rev 1661 at 61092 UT (top) and 61109 UT (bottom) for the 235, 435, 655, 880 keV channels. Loss cone is $\sim 20^\circ$ with the upward looking loss cone at 160° indicated by a vertical line.

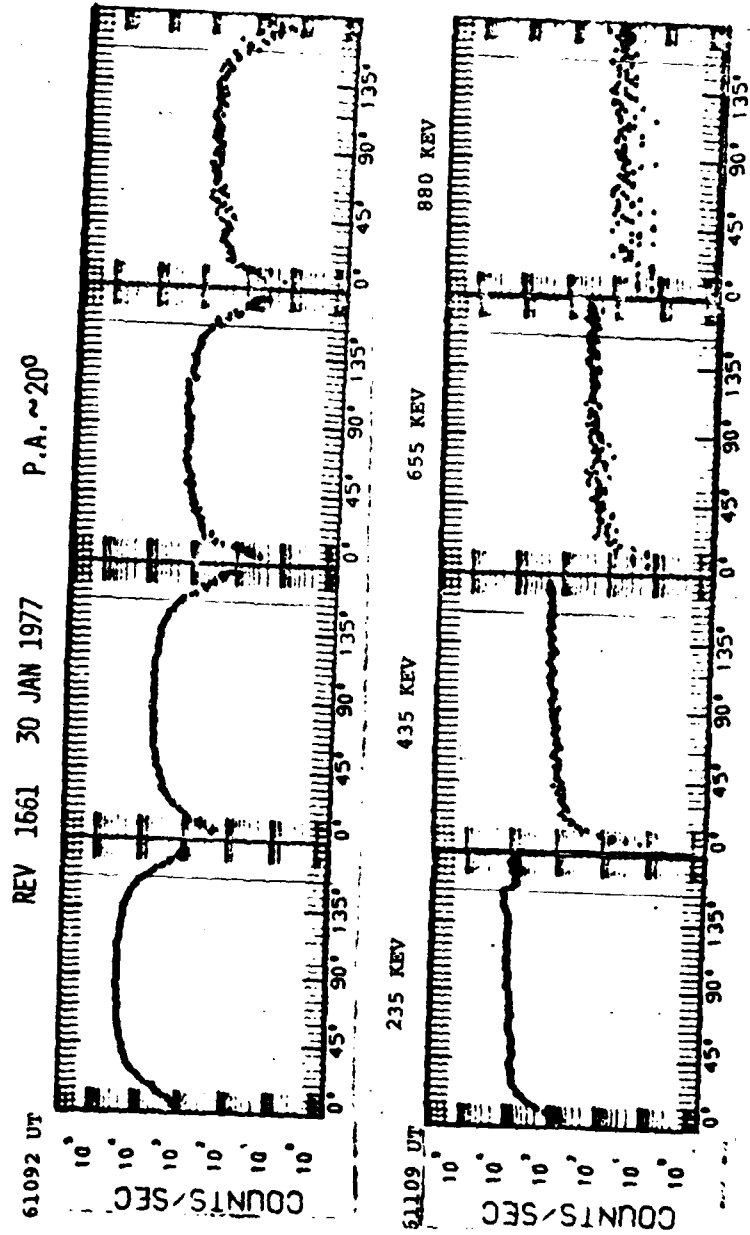


Fig. C-3. Microfiche layout with each logarithm of flux (counts/sec) as ordinate for each channel and abscissa the UT (sec) every 180 sec for 900 sec (16 samples/sec), ALT [km], LONG [deg-E], LAT [deg], B [Gauss], L [], ILAT [deg], MLT [hr]. E.G. Eight panels (15 min each) of 12, 33, 70 electrons, 8 panels 110, 160, 235 keV electrons, etc. P = Protons, A = Alphas, PD = Proton Detector, BG = Background.

16 SAMPLES/SEC								1 SAMPLE/SEC
12 } KEV 33 } 70 }	15 MIN ▶	"	"	"	"	"	"	861 } 862 }
"	110 } KEV 160 } 235 }	"	"	"	"	"	"	1 HR ▶
"	"	"	"	"	"	"	"	12 } KEV 70 } 235 }
"	"	"	"	1.11 } MEV 1.35 } 1.60 }	"	"	"	"
"	"	"	"	"	"	P17 } P12 } P80 KEV	"	850 } KEV 880 } 94.0 MEV
"	"	"	"	"	"	"	P150 } KEV P350 } P770 }	"
"	"	"	"	"	"	"	81.55 } MEV 84.00 }	"

Table C-1. Listing of individual microfiche by Readout REV NO
(Station and Number), DATE of REV (Last Digit of Yr,
Month, Day), Beginning and Ending TIME OF REV IN
HRS (Hours, Minutes, Seconds), Beginning and Ending
TIME OF REV IN SECS (Seconds), Precip Category
(1 \leq 235 keV, 2 \leq 435 keV, 3 \leq 655 keV, 4 \leq 850 keV),
COMMENTS (12 = 12 keV electron channel, etc.; 80,
150 = 80, 150 keV Proton Channel, etc; L = L value).

- 1 - Aug 65
- 2 - 235, 435
- 3 - 235, 435, 655
- 4 - 235, 435, 655, 880 on...

[illegible]

120 L-6-21 800 L-5-7

29: 4 - made again 2-2-6

[illegible]

73C-28

1. Introduction

1998-11-30 1998-11-30

1.34-4.8.2 PG 19/1-5.5.2

12 Dec 1969 POP - 407-2

7. 352 = 6, 6-12 PD 100' 6-5-6

12, 330' 6" 6.7 2350' 6" 6.80, 10' 6"

30, 105-400

12.32c 6.5.7 Ref. 6.5.7-6

100-602

~~1235-10-00-0-6-V~~, 10, ГОР° 674
~~1235-10-00-0-6-V~~, 11, ГОР° 674

120-668

120-679

١٢٧

... ..

126. 4-7 ROP. 4-65

135-672 NO 100-42-5

02-27-8

130-654-9 400' 6" 6"

12.33.6 - 6.7.6

120° 4-12.8 800° 2=55-2

—

[illegible]

120-670

1957-1958

... 4-28

120-627

These are the

• • • • •

1962

1977

1. The first part of the document is a list of names and titles, including "The Hon. Mr. Justice" and "The Hon. Mr. Justice".

100

12. 1000 1000

1

70-100-235

Let $C = \{C_1, C_2, \dots, C_n\}$

179.65 6-7 8

[illegible]

REV NO.	DATE	TIME OF REV	TIME OF REV
OF REV		IN MRS	IN SECS
BOS 0819	61010	05513	102241
IND 0818	61010	102258	120936
BOS 0824	61019	408	12206
BUA 0823	61019	12222	30224
POG 0820	61019	04615	101523
IND 0827	61019	101123	115003
BOS 0832	61019	235236	10213
COO 0831	61020	10230	25049
IND 0835	61020	03520	100620
COO 0836	61020	100637	114630
BOS 0840	61020	234102	5220
MUL 0839	61021	8236	23915
BOS 0846	61021	82407	90002
COO 0845	61021	94810	113455
BOS 0851	61022	00450	93617
COO 0850	61022	93632	112310
COO 0861	61023	75437	02405
BOS 0860	61023	92422	111101
BOS 0869	61024	104726	120706
IND 0867	61024	120722	135719
POG 0877	61025	100039	111709
BOS 0875	61025	111726	125039
BOS 0884	61026	101131	115240
BOS 0883	61026	115305	133300
COO 0893	61027	45024	04213
BOS 0891	61027	04230	102222
BOS 0897	61028	11504	22610
MUL 0896	61028	22627	41314
COO 0902	61028	100232	110831
COO 0901	61028	112040	130041
COO 0911	61029	92052	110255
COO 0910	61029	110312	125631
COO 0918	61030	91313	110029
COO 0917	61030	110133	124421
BOS 0924	61031	91443	105039
POG 0923	61031	105054	123157
BUA 0928	61031	175354	192731
MUL 0927	61031	192747	112710
BOS 0932	61101	00000	100000
BOS 0932	61101	00000	100000
IND 0931	61101	104909	121912
MUL 0936	61101	101622	193233
MUL 0934	61101	193249	211424
BOS 0940	61102	00820	102613
POG 0939	61102	102630	120625
IND 0946	61102	100335	192120
MUL 0943	61102	192146	210130
BOS 0949	61103	115359	131134
BOS 0948	61103	131153	148205
BOS 0957	61103	234730	10525
IND 0955	61104	10542	20542
IND 0962	61104	234551	4135
MUL 0960	61105	4152	23255
MUL 0949	61105	23211	3310
COO 0948	61106	3332	22011
COO 0974	61106	111541	122651
COO 0973	61106	122707	141347
IND 0979	61107	20745	32535
GUA 0978	61107	32551	50546
COO 0984	61107	140116	151235
COO 0982	61107	151251	165917
IND 0988	61108	79114	90907
POG 0987	61108	90923	104914
IND 0994	61109	43932	85720
IND 0994	61109	55936	73733
BOS 1005	61110	102311	114054
IND 1004	61110	114110	132113
IND 1011	61111	11482	23904
MUL 1009	61111	23921	41251
GUA 1018	61111	220309	231417
GUA 1017	61111	231432	10109
BOS 1021	61112	91006	103805
IND 1020	61112	103822	124047
MUL 1025	61112	214940	230052
GUA 1024	61112	230109	4740
COO 1030	61113	124127	140652
BOS 1029	61113	140708	154035
BOS 1034	61114	3447	14538
GUA 1033	61114	14553	33246
COO 1036	61114	122005	135022
BOS 1037	61114	135039	152205
BOS 1045	61115	91621	102729
IND 1044	61115	102751	121410
GUA 1050	61115	210926	222707
GUA 1049	61115	222724	722
POG 1059	61116	235350	11133
GUA 1057	61117	111449	25146
COO 1063	61117	114454	131046
POG 1061	61117	131105	144452
COO 1072	61118	93629	70051
MUL 1071	61118	70107	83424
BOS 1070	61119	111912	125020
IND 1076	61119	125035	141707
GUA 1090	61120	170150	101247
MUL 1088	61120	101304	199907
COO 1095	61121	100187	100906
COO 1096	61121	120922	134917
COO 1103	61122	14221	30441
BOS 1101	61122	30457	44014
BOS 1111	61123	102230	114446

2. 3. 4. 5. 6. 7. 8. 9. 10. 11. 12. 13. 14. 15. 16. 17. 18. 19. 20. 21. 22. 23. 24. 25. 26. 27. 28. 29. 30. 31. 32. 33. 34. 35. 36. 37. 38. 39. 40. 41. 42. 43. 44. 45. 46. 47. 48. 49. 50. 51. 52. 53. 54. 55. 56. 57. 58. 59. 60. 61. 62. 63. 64. 65. 66. 67. 68. 69. 70. 71. 72. 73. 74. 75. 76. 77. 78. 79. 80. 81. 82. 83. 84. 85. 86. 87. 88. 89. 90. 91. 92. 93. 94. 95. 96. 97. 98. 99. 100. 101. 102. 103. 104. 105. 106. 107. 108. 109. 110. 111. 112. 113. 114. 115. 116. 117. 118. 119. 120. 121. 122. 123. 124. 125. 126. 127. 128. 129. 130. 131. 132. 133. 134. 135. 136. 137. 138. 139. 140. 141. 142. 143. 144. 145. 146. 147. 148. 149. 150. 151. 152. 153. 154. 155. 156. 157. 158. 159. 160. 161. 162. 163. 164. 165. 166. 167. 168. 169. 170. 171. 172. 173. 174. 175. 176. 177. 178. 179. 180. 181. 182. 183. 184. 185. 186. 187. 188. 189. 190. 191. 192. 193. 194. 195. 196. 197. 198. 199. 200. 201. 202. 203. 204. 205. 206. 207. 208. 209. 210. 211. 212. 213. 214. 215. 216. 217. 218. 219. 220. 221. 222. 223. 224. 225. 226. 227. 228. 229. 230. 231. 232. 233. 234. 235. 236. 237. 238. 239. 240. 241. 242. 243. 244. 245. 246. 247. 248. 249. 250. 251. 252. 253. 254. 255. 256. 257. 258. 259. 260. 261. 262. 263. 264. 265. 266. 267. 268. 269. 270. 271. 272. 273. 274. 275. 276. 277. 278. 279. 280. 281. 282. 283. 284. 285. 286. 287. 288. 289. 290. 291. 292. 293. 294. 295. 296. 297. 298. 299. 300. 301. 302. 303. 304. 305. 306. 307. 308. 309. 310. 311. 312. 313. 314. 315. 316. 317. 318. 319. 320. 321. 322. 323. 324. 325. 326. 327. 328. 329. 330. 331. 332. 333. 334. 335. 336. 337. 338. 339. 340. 341. 342. 343. 344. 345. 346. 347. 348. 349. 350. 351. 352. 353. 354. 355. 356. 357. 358. 359. 360. 361. 362. 363. 364. 365. 366. 367. 368. 369. 370. 371. 372. 373. 374. 375. 376. 377. 378. 379. 380. 381. 382. 383. 384. 385. 386. 387. 388. 389. 390. 391. 392. 393. 394. 395. 396. 397. 398. 399. 400. 401. 402. 403. 404. 405. 406. 407. 408. 409. 410. 411. 412. 413. 414. 415. 416. 417. 418. 419. 420. 421. 422. 423. 424. 425. 426. 427. 428. 429. 430. 431. 432. 433. 434. 435. 436. 437. 438. 439. 440. 441. 442. 443. 444. 445. 446. 447. 448. 449. 450. 451. 452. 453. 454. 455. 456. 457. 458. 459. 460. 461. 462. 463. 464. 465. 466. 467. 468. 469. 470. 471. 472. 473. 474. 475. 476. 477. 478. 479. 480. 481. 482. 483. 484. 485. 486. 487. 488. 489. 490. 491. 492. 493. 494. 495. 496. 497. 498. 499. 500. 501. 502. 503. 504. 505. 506. 507. 508. 509. 510. 511. 512. 513. 514. 515. 516. 517. 518. 519. 520. 521. 522. 523. 524. 525. 526. 527. 528. 529. 530. 531. 532. 533. 534. 535. 536. 537. 538. 539. 540. 541. 542. 543. 544. 545. 546. 547. 548. 549. 550. 551. 552. 553. 554. 555. 556. 557. 558. 559. 560. 561. 562. 563. 564. 565. 566. 567. 568. 569. 570. 571. 572. 573. 574. 575. 576. 577. 578. 579. 580. 581. 582. 583. 584. 585. 586. 587. 588. 589. 590. 591. 592. 593. 594. 595. 596. 597. 598. 599. 600. 601. 602. 603. 604. 605. 606. 607. 608. 609. 610. 611. 612. 613. 614. 615. 616. 617. 618. 619. 620. 621. 622. 623. 624. 625. 626. 627. 628. 629. 630. 631. 632. 633. 634. 635. 636. 637. 638. 639. 640. 641. 642. 643. 644. 645. 646. 647. 648. 649. 650. 651. 652. 653. 654. 655. 656. 657. 658. 659. 660. 661. 662. 663. 664. 665. 666. 667. 668. 669. 670. 671. 672. 673. 674. 675. 676. 677. 678. 679. 680. 681. 682. 683. 684. 685. 686. 687. 688. 689. 690. 691. 692. 693. 694. 695. 696. 697. 698. 699. 700. 701. 702. 703. 704. 705. 706. 707. 708. 709. 710. 711. 712. 713. 714. 715. 716. 717. 718. 719. 720. 721. 722. 723. 724. 725. 726. 727. 728. 729. 730. 731. 732. 733. 734. 735. 736. 737. 738. 739. 740. 741. 742. 743. 744. 745. 746. 747. 748. 749. 750. 751. 752. 753. 754. 755. 756. 757. 758. 759. 760. 761. 762. 763. 764. 765. 766. 767. 768. 769. 770. 771. 772. 773. 774. 775. 776. 777. 778. 779. 780. 781. 782. 783. 784. 785. 786. 787. 788. 789. 790. 791. 792. 793. 794. 795. 796. 797. 798. 799. 800. 801. 802. 803. 804. 805. 806. 807. 808. 809. 810. 811. 812. 813. 814. 815. 816. 817. 818. 819. 820. 821. 822. 823. 824. 825. 826. 827. 828. 829. 830. 831. 832. 833. 834. 835. 836. 837. 838. 839. 840. 841. 842. 843. 844. 845. 846. 847. 848. 849. 850. 851. 852. 853. 854. 855. 856. 857. 858. 859. 860. 861. 862. 863. 864. 865. 866. 867. 868. 869. 870. 871. 872. 873. 874. 875. 876. 877. 878. 879. 880. 881. 882. 883. 884. 885. 886. 887. 888. 889. 890. 891. 892. 893. 894. 895. 896. 897. 898. 899. 900. 901. 902. 903. 904. 905. 906. 907. 908. 909. 910. 911. 912. 913. 914. 915. 916. 917. 918. 919. 920. 921. 922. 923. 924. 925. 926. 927. 928. 929. 930. 931. 932. 933. 934. 935. 936. 937. 938. 939. 940. 941. 942. 943. 944. 945. 946. 947. 948. 949. 950. 951. 952. 953. 954. 955. 956. 957. 958. 959. 960. 961. 962. 963. 964. 965. 966. 967. 968. 969. 970. 971. 972. 973. 974. 975. 976. 977. 978. 979. 980. 981. 982. 983. 984. 985. 986. 987. 988. 989. 990. 991. 992. 993. 994. 995. 996. 997. 998. 999. 1000.

[illegible]

| REV NO. | DATE | TIME OF REV | TIME OF REV |
|----------|--------|-------------|-------------|
| OF REV | IN HRS | IN SECS | |
| IND 1829 | 70220 | 132554 | 152430 |
| MUL 1834 | 70221 | 911350 | 110944 |
| IND 1839 | 70221 | 170532 | 190344 |
| MUL 1844 | 70222 | 91045 | 111655 |
| BOS 1849 | 70222 | 201008 | 220819 |
| POB 1845 | 70222 | 113859 | 133702 |
| IND 1864 | 70225 | 42556 | 62344 |
| IND 1870 | 70225 | 111740 | 131815 |
| POB 1880 | 70226 | 105359 | 120413 |
| MUL 1886 | 70227 | 104423 | 124227 |
| COO 1871 | 70227 | 183801 | 203611 |
| MUL 1893 | 70220 | 102520 | 122340 |
| MUL 1901 | 70301 | 100649 | 120454 |
| BOS 1907 | 70301 | 235554 | 15356 |
| MUL 1909 | 70302 | 94803 | 114407 |
| MUL 1917 | 70303 | 92916 | 112720 |
| BOS 1922 | 70303 | 231813 | 114449 |
| MUL 1933 | 70303 | 85143 | 104947 |
| POB 1937 | 70305 | 194304 | 214211 |
| MUL 1941 | 70306 | 83254 | 103100 |
| IND 1944 | 70306 | 104417 | 204220 |
| BOS 1947 | 70307 | 33721 | 53525 |
| MUL 1948 | 70307 | 63450 | 83305 |
| IND 1952 | 70307 | 182930 | 202341 |
| MUL 1956 | 70308 | 31835 | 51639 |
| MUL 1964 | 70308 | 51244 | 71045 |
| MUL 1965 | 70309 | 82612 | 100822 |
| MUL 1967 | 70309 | 113013 | 130554 |
| POB 1968 | 70309 | 170301 | 181425 |
| COO 1968 | 70309 | 181445 | 190104 |
| POB 1970 | 70309 | 200553 | 215030 |
| BOS 1972 | 70310 | 15606 | 35348 |
| MUL 1973 | 70310 | 78054 | 98057 |
| IND 1975 | 70310 | 148314 | 168408 |
| IND 1977 | 70310 | 200103 | 215918 |
| COO 1980 | 70311 | 13623 | 33425 |
| BOS 1984 | 70311 | 211840 | 234337 |
| BOS 1987 | 70312 | 11712 | 31506 |
| POB 1988 | 70312 | 41440 | 61235 |
| MUL 1990 | 70312 | 100929 | 120731 |
| IND 1992 | 70312 | 160425 | 180226 |
| BOS 1994 | 70312 | 220008 | 235017 |
| MUL 1996 | 70313 | 35522 | 55326 |
| POB 1998 | 70313 | 95034 | 114835 |
| POB 2000 | 70313 | 154539 | 174344 |
| BOS 2002 | 70313 | 214059 | 233855 |
| IND 2006 | 70314 | 122844 | 142647 |
| MUL 2010 | 70315 | 34749 | 74547 |
| POB 2020 | 70316 | 22950 | 42747 |
| MUL 2029 | 70316 | 211335 | 231124 |
| IND 2037 | 70317 | 110120 | 125928 |
| IND 2038 | 70317 | 151840 | 162448 |
| IND 2039 | 70317 | 182321 | 202126 |
| BOS 2035 | 70317 | 204329 | 221949 |
| COO 2036 | 70318 | 21643 | 41448 |
| COO 2038 | 70318 | 81145 | 100947 |
| MUL 2040 | 70318 | 140443 | 160447 |
| POB 2041 | 70318 | 170412 | 190218 |
| BOS 2043 | 70318 | 200145 | 215949 |
| COO 2044 | 70319 | 19451 | 39449 |
| POB 2045 | 70319 | 45419 | 65221 |
| POB 2047 | 70319 | 104915 | 124719 |
| IND 2048 | 70319 | 134431 | 154449 |
| BOS 2051 | 70319 | 194140 | 213950 |
| COO 2052 | 70320 | 13452 | 33449 |
| IND 2050 | 70320 | 185005 | 204802 |
| MUL 2063 | 70321 | 02623 | 124234 |
| BOS 2067 | 70321 | 193127 | 212925 |
| POB 2071 | 70322 | 09504 | 110235 |
| MUL 2072 | 70322 | 120744 | 132050 |
| IND 2073 | 70322 | 155804 | 175510 |
| BOS 2075 | 70322 | 185408 | 205108 |
| COO 2076 | 70323 | 48445 | 68443 |
| BOS 2077 | 70323 | 34953 | 54344 |
| POB 2079 | 70323 | 64313 | 84104 |
| IND 2080 | 70323 | 123745 | 143543 |
| IND 2082 | 70323 | 153804 | 173501 |
| BOS 2083 | 70323 | 212946 | 232739 |
| COO 2084 | 70324 | 1704 | 27047 |
| MUL 2085 | 70324 | 32424 | 52418 |
| COO 2086 | 70324 | 62139 | 81934 |
| POB 2087 | 70324 | 91859 | 111819 |
| BOS 2099 | 70325 | 80194 | 99953 |
| MUL 2103 | 70326 | 74044 | 93425 |
| POB 2104 | 70326 | 112550 | 132351 |
| IND 2109 | 70326 | 142310 | 162114 |
| IND 2106 | 70326 | 175143 | 194839 |
| BOS 2107 | 70326 | 201759 | 221400 |
| BOS 2108 | 70326 | 231527 | 251140 |
| MUL 2109 | 70327 | 12255 | 32447 |
| POB 2112 | 70327 | 51544 | 69989 |
| POB 2113 | 70327 | 80744 | 99954 |
| COO 2113 | 70327 | 84552 | 102067 |
| IND 2113 | 70327 | 140224 | 160022 |
| IND 2115 | 70327 | 169904 | 189748 |
| BOS 2119 | 70327 | 215433 | 235105 |
| COO 2117 | 70328 | 18201 | 34954 |
| POB 2119 | 70328 | 45001 | 64672 |
| POB 2120 | 70329 | 194634 | 214424 |
| COO 2126 | 70329 | 38988 | 57704 |

12, 13, 14, 15, 16, 17, 18, 19, 20, 21, 22, 23, 24, 25, 26, 27, 28, 29, 30, 31, 32, 33, 34, 35, 36, 37, 38, 39, 40, 41, 42, 43, 44, 45, 46, 47, 48, 49, 50, 51, 52, 53, 54, 55, 56, 57, 58, 59, 60, 61, 62, 63, 64, 65, 66, 67, 68, 69, 70, 71, 72, 73, 74, 75, 76, 77, 78, 79, 80, 81, 82, 83, 84, 85, 86, 87, 88, 89, 90, 91, 92, 93, 94, 95, 96, 97, 98, 99, 100, 101, 102, 103, 104, 105, 106, 107, 108, 109, 110, 111, 112, 113, 114, 115, 116, 117, 118, 119, 120, 121, 122, 123, 124, 125, 126, 127, 128, 129, 130, 131, 132, 133, 134, 135, 136, 137, 138, 139, 140, 141, 142, 143, 144, 145, 146, 147, 148, 149, 150, 151, 152, 153, 154, 155, 156, 157, 158, 159, 160, 161, 162, 163, 164, 165, 166, 167, 168, 169, 170, 171, 172, 173, 174, 175, 176, 177, 178, 179, 180, 181, 182, 183, 184, 185, 186, 187, 188, 189, 190, 191, 192, 193, 194, 195, 196, 197, 198, 199, 200, 201, 202, 203, 204, 205, 206, 207, 208, 209, 210, 211, 212, 213, 214, 215, 216, 217, 218, 219, 220, 221, 222, 223, 224, 225, 226, 227, 228, 229, 230, 231, 232, 233, 234, 235, 236, 237, 238, 239, 240, 241, 242, 243, 244, 245, 246, 247, 248, 249, 250, 251, 252, 253, 254, 255, 256, 257, 258, 259, 260, 261, 262, 263, 264, 265, 266, 267, 268, 269, 270, 271, 272, 273, 274, 275, 276, 277, 278, 279, 280, 281, 282, 283, 284, 285, 286, 287, 288, 289, 290, 291, 292, 293, 294, 295, 296, 297, 298, 299, 300, 301, 302, 303, 304, 305, 306, 307, 308, 309, 310, 311, 312, 313, 314, 315, 316, 317, 318, 319, 320, 321, 322, 323, 324, 325, 326, 327, 328, 329, 330, 331, 332, 333, 334, 335, 336, 337, 338, 339, 340, 341, 342, 343, 344, 345, 346, 347, 348, 349, 350, 351, 352, 353, 354, 355, 356, 357, 358, 359, 360, 361, 362, 363, 364, 365, 366, 367, 368, 369, 370, 371, 372, 373, 374, 375, 376, 377, 378, 379, 380, 381, 382, 383, 384, 385, 386, 387, 388, 389, 390, 391, 392, 393, 394, 395, 396, 397, 398, 399, 400, 401, 402, 403, 404, 405, 406, 407, 408, 409, 410, 411, 412, 413, 414, 415, 416, 417, 418, 419, 420, 421, 422, 423, 424, 425, 426, 427, 428, 429, 430, 431, 432, 433, 434, 435, 436, 437, 438, 439, 440, 441, 442, 443, 444, 445, 446, 447, 448, 449, 450, 451, 452, 453, 454, 455, 456, 457, 458, 459, 460, 461, 462, 463, 464, 465, 466, 467, 468, 469, 470, 471, 472, 473, 474, 475, 476, 477, 478, 479, 480, 481, 482, 483, 484, 485, 486, 487, 488, 489, 490, 491, 492, 493, 494, 495, 496, 497, 498, 499, 500, 501, 502, 503, 504, 505, 506, 507, 508, 509, 510, 511, 512, 513, 514, 515, 516, 517, 518, 519, 520, 521, 522, 523, 524, 525, 526, 527, 528, 529, 530, 531, 532, 533, 534, 535, 536, 537, 538, 539, 540, 541, 542, 543, 544, 545, 546, 547, 548, 549, 550, 551, 552, 553, 554, 555, 556, 557, 558, 559, 560, 561, 562, 563, 564, 565, 566, 567, 568, 569, 570, 571, 572, 573, 574, 575, 576, 577, 578, 579, 580, 581, 582, 583, 584, 585, 586, 587, 588, 589, 590, 591, 592, 593, 594, 595, 596, 597, 598, 599, 600, 601, 602, 603, 604, 605, 606, 607, 608, 609, 610, 611, 612, 613, 614, 615, 616, 617, 618, 619, 620, 621, 622, 623, 624, 625, 626, 627, 628, 629, 630, 631, 632, 633, 634, 635, 636, 637, 638, 639, 640, 641, 642, 643, 644, 645, 646, 647, 648, 649, 650, 651, 652, 653, 654, 655, 656, 657, 658, 659, 660, 661, 662, 663, 664, 665, 666, 667, 668, 669, 670, 671, 672, 673, 674, 675, 676, 677, 678, 679, 680, 681, 682, 683, 684, 685, 686, 687, 688, 689, 690, 691, 692, 693, 694, 695, 696, 697, 698, 699, 700, 701, 702, 703, 704, 705, 706, 707, 708, 709, 710, 711, 712, 713, 714, 715, 716, 717, 718, 719, 720, 721, 722, 723, 724, 725, 726, 727, 728, 729, 730, 731, 732, 733, 734, 735, 736, 737, 738, 739, 740, 741, 742, 743, 744, 745, 746, 747, 748, 749, 750, 751, 752, 753, 754, 755, 756, 757, 758, 759, 760, 761, 762, 763, 764, 765, 766, 767, 768, 769, 770, 771, 772, 773, 774, 775, 776, 777, 778, 779, 780, 781, 782, 783, 784, 785, 786, 787, 788, 789, 790, 791, 792, 793, 794, 795, 796, 797, 798, 799, 800, 801, 802, 803, 804, 805, 806, 807, 808, 809, 810, 811, 812, 813, 814, 815, 816, 817, 818, 819, 820, 821, 822, 823, 824, 825, 826, 827, 828, 829, 830, 831, 832, 833, 834, 835, 836, 837, 838, 839, 840, 841, 842, 843, 844, 845, 846, 847, 848, 849, 850, 851, 852, 853, 854, 855, 856, 857, 858, 859, 860, 861, 862, 863, 864, 865, 866, 867, 868, 869, 870, 871, 872, 873, 874, 875, 876, 877, 878, 879, 880, 881, 882, 883, 884, 885, 886, 887, 888, 889, 890, 891, 892, 893, 894, 895, 896, 897, 898, 899, 900, 901, 902, 903, 904, 905, 906, 907, 908, 909, 910, 911, 912, 913, 914, 915, 916, 917, 918, 919, 920, 921, 922, 923, 924, 925, 926, 927, 928, 929, 930, 931, 932, 933, 934, 935, 936, 937, 938, 939, 940, 941, 942, 943, 944, 945, 946, 947, 948, 949, 950, 951, 952, 953, 954, 955, 956, 957, 958, 959, 960, 961, 962, 963, 964, 965, 966, 967, 968, 969, 970, 971, 972, 973, 974, 975, 976, 977, 978, 979, 980, 981, 982, 983, 984, 985, 986, 987, 988, 989, 990, 991, 992, 993, 994, 995, 996, 997, 998, 999, 1000, 1001, 1002, 1003, 1004, 1005, 1006, 1007, 1008, 1009, 1010, 1011, 1012, 1013, 1014, 1015, 1016, 1017, 1018, 1019, 1020, 1021, 1022, 1023, 1024, 1025, 1026, 1027, 1028, 1029, 1030, 1031, 1032, 1033, 1034, 1035, 1036, 1037, 1038, 1039, 1040, 1041, 1042, 1043, 1044, 1045, 1046, 1047, 1048, 1049, 1050, 1051, 1052, 1053, 1054, 1055, 1056, 1057, 1058, 1059, 1060, 1061, 1062, 1063, 1064, 1065, 1066, 1067, 1068, 1069, 1070, 1071, 1072, 1073, 1074, 1075, 1076, 1077, 1078, 1079, 1080, 1081, 1082, 1083, 1084, 1085, 1086, 1087, 1088, 1089, 1090, 1091, 1092, 1093, 1094, 1095, 1096, 1097, 1098, 1099, 1100, 1101, 1102, 1103, 1104, 1105, 1106, 1107, 1108, 1109, 1110, 1111, 1112, 1113, 1114, 1115, 1116, 1117, 1118, 1119, 1120, 1121, 1122, 1123, 1124, 1125, 1126, 1127, 1128, 1129, 1130, 1131, 1132, 1133, 1134, 1135, 1136, 1137, 1138, 1139, 1140, 1141, 1142, 1143, 1144, 1145, 1146, 1147, 1148, 1149, 1150, 1151, 1152, 1153, 1154, 1155, 1156, 1157, 1158, 1159, 1160, 1161, 1162, 1163, 1164, 1165, 1166, 1167, 1168, 1169, 1170, 1171, 1172, 1173, 1174, 1175, 1176, 1177, 1178, 1179, 1180, 1181, 1182, 1183, 1184, 1185, 1186, 1187, 1188, 1189, 1190, 1191, 1192, 1193, 1194, 1195, 1196, 1197, 1198, 1199, 1200, 1201, 1202, 1203, 1204, 1205, 1206, 1207, 1208, 1209, 1210, 1211, 1212, 1213, 1214, 1215, 1216, 1217, 1218, 1219, 1220, 1221, 1222, 1223, 1224, 1225, 1226, 1227, 1228, 1229, 1230, 1231, 1232, 1233, 1234, 1235, 1236, 1237, 1238, 1239, 1240, 1241, 1242, 1243, 1244, 1245, 1246, 1247, 1248, 1249, 1250, 1251, 1252, 1253, 1254, 1255, 1256, 1257, 1258, 1259, 1260, 1261, 1262, 1263, 1264, 1265, 1266, 1267, 1268, 1269, 1270, 1271, 1272, 1273, 1274, 1275, 1276, 1277, 1278, 1279, 1280, 1281, 1282, 1283, 1284, 1285, 1286, 1287, 1288, 1289, 1290, 1291, 1292, 1293, 1294, 1295, 1296, 1297, 1298, 1299, 1300, 1301, 1302, 1303, 1304, 1305, 1306, 1307, 1308, 1309, 1310, 1311, 1312, 1313, 1314, 1315, 1316, 1317, 1318, 1319, 1320, 1321, 1322, 1323, 1324, 1325, 1326, 1327, 1328, 1329, 1330, 1331, 1332, 1333, 1334, 1335, 1336, 1337, 1338, 1339, 1340, 1341, 1342, 1343, 1344, 1345, 1346, 1347, 1348, 1349, 1350, 1351, 1352, 1353, 1354, 1355, 1356, 1357, 1358, 1359, 1360, 1361, 1362, 1363, 1364, 1365, 1366, 1367, 1368, 1369, 1370, 1371, 1372, 1373, 1374, 1375, 1376, 1377, 1378, 1379, 1380, 1381, 1382, 1383, 1384, 1385, 1386, 1387, 1388, 1389, 1390, 1391, 1392, 1393, 1394, 1395, 1396, 1397, 1398, 1399, 1400, 1401, 1402, 1403, 1404, 1405, 1406, 1407, 1408, 1409, 1410, 1411, 1412, 1413, 1414, 1415, 1416, 1417, 1418, 1419, 1420, 1421, 1422, 1423, 1424, 1425, 1426, 1427, 1428, 1429, 1430, 1431, 1432, 1433, 1434, 1435, 1436, 1437, 1438, 1439,

[illegible]

| REV. NO. | DATE OF REV | TIME OF REV IN HRS | TIME OF REV IN SECS |
|----------------|-------------|--------------------|---------------------|
| COO 3000 70714 | 111055 | 123295 | 40259 45548 |
| COO 3002 70714 | 146450 | 103233 | 60340 76045 |
| COA 3003 70714 | 193140 | 212904 | 70002 77346 |
| IMO 3004 70716 | 222812 | 2838 | 80830 10000 |
| POG 3005 70715 | 17445 | 32212 | 5005 12321 |
| POG 3007 70715 | 17875 | 19521 | 56277 33381 |
| COO 3008 70715 | 18000 | 10000 | 50000 10000 |
| MUL 3009 70715 | 133045 | 150030 | 40065 45118 |
| MUL 3010 70715 | 168741 | 105050 | 80061 68105 |
| IMO 3012 70715 | 220054 | 236010 | 79254 96030 |
| COO 3014 70716 | 35005 | 35117 | 10320 21077 |
| BOS 3015 70716 | 45110 | 04750 | 24670 31670 |
| BOS 3016 70716 | 021013 | 114427 | 37263 42277 |
| MUL 3017 70716 | 124335 | 144059 | 45815 50859 |
| COO 3018 70716 | 124335 | 144059 | 45815 50859 |
| IMO 3020 70716 | 213315 | 133040 | 77595 96040 |
| POG 3021 70717 | 2272 | 87214 | 1792 8054 |
| BOS 3023 70717 | 62256 | 82021 | 22976 30021 |
| BOS 3024 70717 | 93504 | 111454 | 34504 40412 |
| COO 3025 70717 | 124920 | 141332 | 46140 81212 |
| MUL 3026 70717 | 155313 | 171005 | 57193 65105 |
| BOS 3027 70717 | 180913 | 200637 | 65353 72057 |
| COO 3028 70717 | 200637 | 200637 | 65353 72057 |
| COO 3030 70718 | 25857 | 45611 | 10137 17779 |
| COO 3031 70718 | 60538 | 78255 | 21358 28375 |
| COO 3032 70718 | 93410 | 104928 | 34450 39640 |
| COO 3033 70718 | 114462 | 134049 | 45252 49458 |
| COA 3034 70718 | 144516 | 144234 | 53114 60154 |
| POG 3035 70718 | 174146 | 193909 | 63706 70479 |
| BOS 3036 70718 | 211643 | 223544 | 74603 81344 |
| COO 3037 70718 | 23131 | 42649 | 9003 16149 |
| COO 3038 70718 | 23131 | 42649 | 9003 16149 |
| POG 3040 70719 | 82436 | 102157 | 30274 37117 |
| COO 3041 70719 | 112556 | 131031 | 41156 47947 |
| POG 3042 70719 | 134540 | 161504 | 52540 58506 |
| POG 3044 70719 | 201052 | 220013 | 72652 79306 |
| POG 3046 70720 | 20405 | 40120 | 7645 14400 |
| POG 3047 70720 | 51621 | 65753 | 18061 23513 |
| MUL 3048 70720 | 83951 | 95422 | 31133 35452 |
| COO 3049 70720 | 95422 | 95422 | 31133 35452 |
| COO 3050 70720 | 143910 | 154722 | 52785 58645 |
| BOS 3052 70720 | 194256 | 214018 | 70974 78010 |
| MUL 3053 70720 | 234630 | 13540 | 45710 57408 |
| BOS 3055 70721 | 43321 | 62949 | 14351 23349 |
| IMO 3056 70721 | 72151 | 92420 | 27131 33960 |
| MUL 3059 70721 | 133039 | 151923 | 40639 55163 |
| MUL 3063 70722 | 94249 | 114012 | 39419 48212 |
| BOS 3064 70722 | 93123 | 32180 | 35900 10980 |
| COO 3074 70722 | 151123 | 160000 | 50000 50000 |
| COO 3082 70724 | 114308 | 134032 | 42106 49232 |
| MUL 3087 70725 | 22533 | 42287 | 8733 17517 |
| COO 3093 70725 | 151022 | 170704 | 50422 61444 |
| BOS 3094 70726 | 93455 | 65121 | 17431 24601 |
| COO 3106 70727 | 72255 | 91945 | 26545 33505 |
| COO 3109 70727 | 161155 | 180912 | 50313 63532 |
| COA 3117 70728 | 154043 | 174707 | 64643 63667 |
| COO 3120 70728 | 155252 | 155252 | 13122 13212 |
| COO 3121 70728 | 82436 | 78255 | 21357 28375 |
| MUL 3122 70729 | 93028 | 115113 | 34228 40046 |
| MUL 3123 70729 | 122204 | 141739 | 45424 51459 |
| COA 3124 70729 | 153164 | 171405 | 55004 62048 |
| BOS 3125 70729 | 182137 | 201304 | 65397 72634 |
| IMO 3126 70729 | 211141 | 230116 | 76501 82074 |
| BOS 3128 70730 | 30145 | 48954 | 10945 17996 |
| BOS 3129 70730 | 61126 | 79624 | 21206 26606 |
| COO 3130 70730 | 72255 | 91945 | 26545 33505 |
| COO 3131 70730 | 118150 | 134914 | 42718 49736 |
| COA 3133 70730 | 175046 | 194213 | |

aliability in identifying REPs was obtained.

Fig. C-3 shows how each microfiche is layed out and Table C-1 is a listing of the individual microfiche by Rev Number, Date, UT of Rev in hrs and secs, and notes on electron and proton precipitation events. Approximately 1212 microfiche were examined three times by one individual (the author) and once by another graduate student (T. Kelley) for comparison. A list of 358 outer zone transits were identified for further discrimination by pitch-angle. 313 outer zone REP revs were confirmed by the pitch-angle analysis and are listed in Table C-2. The remaining case was eliminated by the loss-cone criteria previously described, bad data drop outs, low flux values, and spike events. This table also subjectively groups the revs into 173 'events' by combining consecutive revs with strong precipitation. Since each revs last 3 hrs and there was no AE data set available to determine substorm duration this grouping maybe off as much as 25% in total event number.

Table C-2. Revs with strong precipitation \geq 235 keV electrons by EVENT (one or more consecutive revs with strong precipitation), DATE (last digit of year, month, day), Readout REV (first letter of station, number), LAT (North, degrees), East LONG (degrees), L-VAL, MLT (hrs), $j(e/cm^2 \text{ s str keV})$ = differential flux value of precipitating electrons from 235 keV to highest energy channel at which strong precipitation occurred, $J(p/cm^2 \text{ s str})$ = integral flux of strong diffusion precipitation of protons per energy channel if any, 80 p⁺ L-VAL = L value of 80 keV proton precipitation if any, strong precip 12, 33, L-VAL = check if 12, 33 keV electron channels had strong precip and L value of 12 keV channel, UT (sec)= time at which 235 keV electron precip occurred.

| EVE
N | DATE | REV | LAT | LONG | LVAL | MLT | J [°/hr. obs.] | | | | J [°/hr. obs.] | | | | POP.
LVAL | STATION | | I | | |
|----------|-------|------|------|-------|------|------|----------------|--------|--------|--------|----------------|-------|--------|--------|--------------|---------|-----|---|--------|------|
| | | | | | | | 485 | 485 | 485 | 485 | 1.1 | 1.35 | 1.6 | 80 | | 150 | 850 | | 1.2 | 3.3 |
| 1 | 60714 | B49 | 68.1 | 295.4 | 6.17 | 21.2 | 306+1 | | | | | | | 1.66+4 | 6.66+3 | 6.5-6 | ✓ | ✓ | 6-12 | 16.2 |
| 2 | 60809 | C258 | 62.0 | 598 | 6.4 | 20.4 | 765+1 | | | | | | | 3.33+4 | 8.33+3 | 5-6.5 | ✓ | ✓ | 6-4 | 15.8 |
| 3 | 60824 | A375 | 65.1 | 528 | 7.0 | 10.3 | 306+2 | | | | | | | 8.33+3 | | 9-10 | ✓ | ✓ | 6-8.5 | 8.6 |
| 4 | 60824 | A381 | 47.6 | 314.2 | 7.1 | 20.1 | 163+1 | | | | | | | 2.5+4 | 8.33+3 | 6.7-6.6 | ✓ | ✓ | 6-2.5 | 22.5 |
| 5 | 60825 | C386 | 56.8 | 354.8 | 7.8 | 20.2 | 306+1 | | | | | | | 3.5+5 | 8.33+4 | 5.3-2.5 | ✓ | ✓ | 6-2.5 | 19.5 |
| 6 | 60827 | M398 | 82.2 | 12.0 | 7.9 | 21.8 | 306+1 | | | | | | | 1.66+4 | 2.5+3 | 5-10 | ✓ | ✓ | 5-10 | .2 |
| | 60827 | M398 | 42.5 | 274.7 | 6.2 | 19.5 | 1.53+2 | 3.07+1 | | | | | | 8.33+4 | 2.5+4 | 5-7 | ✓ | ✓ | | 1.2 |
| 7 | 60827 | C405 | 44.3 | 319.9 | 5.7 | 20.1 | 46+2 | 3.53+1 | | | | | | 4.5+4 | 8.33+3 | 4-8 | ✓ | ✓ | 6 | 22.1 |
| 8 | 60828 | C407 | 55.9 | 321.9 | 9.5 | 9.7 | 6.12+1 | | | | | | | | | | ✓ | ✓ | 8-11 | 11.2 |
| 9 | 60828 | P410 | 63.1 | 192.5 | 7.5 | 7.7 | 4.6+2 | | | | | | | 6.66+3 | | 8-10 | ✓ | ✓ | 6-12 | 20.1 |
| 10 | 60906 | B477 | 77.9 | 305.3 | 5.3 | 22.0 | 1.0+3 | 1.98+2 | 8.66+1 | 3.54+1 | 7.7+0 | 6.5+0 | 4.85+0 | 2.5+4 | 8.33+3 | 5-6.8 | ✓ | ✓ | 5-7-9 | 1.7 |
| 11 | 60914 | C547 | 65.4 | 206.5 | 6.4 | 22.5 | 1.53+2 | 9.2+0 | | | | | | 7.5+3 | 1.3+3 | 5-6 | ✓ | ✓ | 5-7 | 6.4 |
| 12 | 60918 | B575 | 45.0 | 157.3 | 4.3 | 20.3 | 2.65+1 | 1.8+1 | | | | | | 1.1+5 | 2.5+4 | 4-7 | ✓ | ✓ | 4-7 | 8.9 |
| 13 | 60919 | I584 | 50.4 | 308.1 | 5.4 | 8.3 | 9.2+2 | | | | | | | 8.3+3 | 6.7+2 | 7-9 | ✓ | ✓ | 5-6 | 10.9 |
| 14 | 60920 | M589 | 67.5 | 95.9 | 7.0 | 8.5 | 1.1+3 | 2.8+1 | | | | | | 8.3+3 | | 9-12 | ✓ | ✓ | 6-10 | 1.7 |
| | 60920 | I592 | 63.0 | 2.2 | 7.1 | 9.5 | 7.65+1 | | | | | | | 2.5+3 | | 9-12 | ✓ | ✓ | 6-9 | 7.7 |
| | 60920 | B595 | 71.3 | 219.8 | 7.5 | 7.8 | 1.4+3 | 2.3+1 | | | | | | 1.5+3 | | 10-20 | ✓ | ✓ | 5-20 | 14.3 |
| 15 | 60921 | B599 | 61.4 | 55.5 | 6.0 | 3.7 | 3.06+1 | 6.1+0 | | | | | | 7.5+8 | 1.0+4 | 5-6 | ✓ | ✓ | 4.5-20 | 2.2 |
| | 60921 | B599 | 77.0 | 285.0 | 6.1 | 22.2 | 3.06+2 | 3.06+1 | | | | | | 1.0+5 | 1.6+4 | 5-6 | ✓ | ✓ | 5-8 | 2.3 |
| | 60921 | B599 | 65.0 | 50.5 | 6.0 | 9.1 | 1.2+3 | | | | | | | 9.3+4 | 3.3+4 | 5-6 | ✓ | ✓ | 6-11 | 4.5 |
| | 60921 | B602 | 47.5 | 118.6 | 6.0 | 19.4 | 4.6+1 | | | | | | | | | | ✓ | ✓ | 6-8 | 11.4 |
| 16 | 60922 | I608 | 74.8 | 110.8 | 10.5 | 8.7 | 3.06+1 | | | | | | | | | | ✓ | ✓ | 1.2-17 | 1.3 |

| E
V
T | DATE | REV | LAT | (g) | L-VAL | MLT | $d \left[\frac{1}{\sqrt{2}} \sqrt{\frac{1}{2} \frac{1}{\sqrt{2}} \frac{1}{\sqrt{2}}} \right]$ | | | | | $\tau \left[\frac{1}{\sqrt{2}} \sqrt{\frac{1}{2} \frac{1}{\sqrt{2}} \frac{1}{\sqrt{2}}} \right]$ | | | 10 ⁰⁰
L-VAL | stroke count | | L-VAL
(HAI)
UT | 2 |
|-------------|-------|--------|-------|-------|-------|------|--|--------|-------|-----|----|---|-------|-------|---------------------------|--------------|-----|----------------------|------|
| | | | | | | | 235 | 435 | 655 | 850 | 11 | 1.35 | 1.6 | 80 | | 150 | 350 | | |
| 17 | 60829 | C 619 | -51.2 | 123.1 | 8.0 | 19.6 | 1.2E2 | | | | | | 2.5+5 | 6.6+4 | 2.5+3 | ✓ | ✓ | 6-10 | 11.1 |
| 18 | 60926 | C 644 | -76.8 | 290.2 | 6.7 | 21.5 | 3.5+1 | | | | | | 3.3+4 | 4.2+3 | | ✓ | | 5-6 | 1.5 |
| 19 | 60929 | C 665 | -59.0 | 182.0 | 6.9 | 21.1 | 1.5+2 | | | | | | 2.3+2 | | | ✓ | | 6-8 | 7.01 |
| 20 | 61002 | I 639 | -53.4 | 288.0 | 7.2 | 7.4 | 7.6+2 | 3.07+1 | | | | | 2.3+3 | | | ✓ | ✓ | 5-12 | 11.8 |
| 21 | 61003 | I 697 | -75.8 | 14.1 | 7.2 | 2.0 | 4.6+1 | 1.5+1 | | | | | 7.5+3 | | | ✓ | | 6-8 | 3.2 |
| | 61003 | I 697 | -73.5 | 280.1 | 6.0 | 21.8 | 1.5+2 | 2.0+1 | 7.0+0 | | | | 4.2+4 | 6.7+3 | | ✓ | | 6-7 | 3.5 |
| 22 | 61016 | I 803 | -76.2 | 264.6 | 6.7 | 5.0 | 6.1+2 | | | | | | 1.0+4 | 5.8+3 | | ✓ | ✓ | 5-8 | 9.8 |
| 23 | 61017 | C 808 | -58.0 | 62.0 | 6.2 | 4.0 | 4.6+1 | 1.4+1 | | | | | 8.3+3 | 1.6+3 | | ✓ | ✓ | 4-8 | .6 |
| | 61017 | C 808 | -73.0 | 290.0 | 6.0 | 19.6 | 4.6+2 | 4.6+1 | | | | | 2.8+4 | 8.3+3 | | ✓ | ✓ | >5 | .9 |
| 24 | 61021 | C 845 | -69.3 | 283.8 | 7.3 | 16.7 | 4.6+1 | | | | | | 7.5+3 | | | | | 6-6.5 | 1.1 |
| 25 | 61028 | C 901 | -56.0 | 253.7 | 6.5 | 5.2 | 1.1+2 | | | | | | | | | ✓ | ✓ | 6.5 | 12.9 |
| 26 | 61031 | C 924 | -75.3 | 255.7 | 6.0 | 4.7 | 7.7+1 | | | | | | 8.3+4 | 5.0+4 | | ✓ | ✓ | 4-7 | 9.9 |
| 27 | 61110 | I 1004 | -59.5 | 272.7 | 6.4 | 4.4 | 4.6+1 | | | | | | 2.5+3 | | | ✓ | ✓ | 6-9 | 13.2 |
| 28 | 61111 | I 1011 | -65.3 | 255.5 | 6.4 | 1.6 | 9.1+1 | | | | | | 1.6+4 | 7.5+3 | | | | | 1.6 |
| | 61111 | I 1011 | -69.4 | 238.0 | 7.3 | 19.6 | 4.6+1 | | | | | | 2.5+3 | | | | | | 1.9 |
| 29 | 61112 | I 1025 | -50.5 | 85.2 | 5.5 | 3.0 | 3.0+1 | | | | | | 2.5+4 | 7.5+3 | | ✓ | ✓ | 5 | 22.1 |
| 30 | 61114 | C 1034 | -64.3 | 35.2 | 7.1 | 1.5 | 2.0+1 | | | | | | 4.2+4 | 1.7+4 | | ✓ | ✓ | 6.5-6 | .9 |
| | 61114 | C 1033 | -71.9 | 39.0 | 7.5 | 7.0 | 1.4+2 | | | | | | | | | ✓ | ✓ | 6-10 | 3.3 |
| 31 | 61201 | C 1174 | -58.9 | 178.0 | 7.2 | 4.5 | 1.8+1 | | | | | | 2.5+3 | | | ✓ | ✓ | 4.5 | 14.8 |
| 32 | 61204 | C 1202 | -70.5 | 188.5 | 8.7 | 12.4 | 5.0+1 | | | | | | 8.3+3 | | | ✓ | ✓ | 7-12 | 1.5 |
| 33 | 61209 | C 1239 | -74.0 | 273.8 | 7.0 | 2.3 | 4.6+1 | 4.6+0 | | | | | 6.7+3 | 2.5+3 | | ✓ | ✓ | 5-9 | 7.1 |

| STATION | DATE | REV | LAT | LONG | (G) | L-VAL | MLT | Δ [°/km²/decade] | | | Δ [°/km²/decade] | | | S [°/km²/decade] | | | BOPT | STATUS | REMARK | 3 |
|---------|---------|-------|------|-------|------|-------|-------|-------------------------|-------|-----|-------------------------|------|-----|------------------|-------|-------|-------|--------|--------|-----------|
| | | | | | | | | 485 | 655 | 850 | 1.1 | 1.35 | 1.6 | 80 | 150 | 350 | | | | |
| 34 | 6/12/11 | I1250 | 632 | 22.9 | 7.0 | 0.5 | 0.5 | 6.1+1 | 7.7+0 | | | | | 1.25+4 | 3.3+3 | | 5-6 | ✓ | ✓ | 5-9 6 |
| 35 | 6/12/12 | M1260 | 52.3 | 272.5 | 8.8 | 14.0 | 0.6 | 1.5+2 | 4.6+1 | | | | | 6.7+3 | 8.3+2 | | 6-8 | ✓ | ✓ | 6-13 20.2 |
| 36 | 12/19 | P1317 | 60.4 | 4.7 | 51-6 | 0.6 | 2.0+1 | | | | | | | 4.2+4 | 1.7+4 | | 5-5.4 | ✓ | ✓ | 5-6 1.6 |
| 37 | 6/12/21 | M1338 | 48.5 | 109.7 | 7.0 | 1.82 | 3.0+1 | | | | | | | 8.3+3 | 1.7+3 | | 7 | ✓ | ✓ | 7 18.7 |
| 38 | 6/12/22 | G1340 | 67.9 | 322.5 | 5.6 | 0.6 | 6.1+1 | 1.2+1 | 7.5+0 | | | | | 2.5+4 | 5.8+3 | | 5-6.3 | ✓ | ✓ | 3.9 |
| 39 | 6/12/22 | D1342 | 64.9 | 236.6 | 5.8 | 2.9 | 9.2+0 | | | | | | | 5.0+3 | | | 5.5 | ✓ | ✓ | 5-6 9.8 |
| 40 | 6/12/22 | E1345 | 49.0 | 157.2 | 5.4 | 2.9 | 2.0+1 | | | | | | | 8.3+3 | | | 5.4 | ✓ | ✓ | 4-6 15.5 |
| 41 | 6/12/23 | I1350 | 66.2 | 338.2 | 6.1 | 2.8 | 1.5+1 | | | | | | | 1.7+3 | | | 6 | ✓ | ✓ | 5 18.5 |
| 42 | 6/12/25 | I1369 | 50.3 | 166.0 | 58.3 | 2.9 | 1.1+2 | | | | | | | 2.5+4 | 6.7+3 | | 5.3-6 | ✓ | ✓ | 6 9.5 |
| 43 | 6/12/27 | G1380 | 67.8 | 338.1 | 6.5 | 0.1 | 1.5+1 | | | | | | | 3.3+3 | 9.2+2 | | 7 | ✓ | ✓ | 5-8 14.8 |
| 44 | 6/12/27 | M1386 | 49.5 | 128.1 | 7.3 | 2.0 | 1.5+1 | | | | | | | 8.3+3 | | | 6 | ✓ | ✓ | 20.7 |
| 45 | 6/12/29 | I1398 | 59.8 | 302.0 | 5.8 | 1.2 | 3.0+1 | | | | | | | 2.5+3 | | | 6-7 | ✓ | ✓ | 23.4 |
| 46 | 6/12/29 | G1404 | 55.5 | 128.1 | 7.3 | 2.0 | 1.5+1 | | | | | | | 2.5+3 | | | 6 | ✓ | ✓ | 2.6 |
| 47 | 6/12/30 | I1406 | 71.5 | 272.6 | 7.3 | 0.6 | 1.5+1 | 6.1+0 | | | | | | 8.3+3 | 1.7+3 | | 6-7 | ✓ | ✓ | 12.2 |
| 48 | 6/12/31 | G1413 | 73.0 | 130.0 | 6.0 | 12.1 | 2.0+2 | | | | | | | 1.7+5 | 7.5+4 | 8.3+3 | 3-5 | ✓ | ✓ | 5.0 |
| 49 | 6/12/31 | G1420 | 58.8 | 202.0 | 7.0 | 2.5 | 1.4+1 | | | | | | | 2.5+4 | 1.7+4 | 3.3+3 | 4-6 | ✓ | ✓ | 8.0 |
| | | | | | | | | | | | | | | 7.5+4 | 1.7+4 | | 5-7 | ✓ | ✓ | 22.7 |
| | | | | | | | | | | | | | | 9.2+3 | 2.5+3 | | 6-7 | ✓ | ✓ | 4.9 |
| | | | | | | | | | | | | | | 8.3+3 | 8.3+3 | | 5.5-7 | ✓ | ✓ | 7.8 |
| | | | | | | | | | | | | | | | | | 6-8 | ✓ | ✓ | 3.6 |
| | | | | | | | | | | | | | | 3.3+3 | 8.3+2 | | 6.0 | ✓ | ✓ | 9.7 |
| | | | | | | | | | | | | | | 2.5+3 | | | 6.5 | ✓ | ✓ | 10.4 |

| F
V
E
N | DATE | REV | LAT | LONG | (S) | VAL | MLT | D [P/m ² ·s·mm] | | | | S [P/m ² ·s·mm] | | | BOP
LVAL | STR PROSLIN | | LVAL | MRS
UT | |
|------------------|---------------|-------|-------|-------|------|-------|-------|----------------------------|-------|-------|-------|----------------------------|------|-----|-------------|-------------|-------|------|-----------|------|
| | | | | | | | | 285 | 435 | 655 | 850 | 1.1 | 1.35 | 1.6 | | 80 | 150 | | | 370 |
| 50 | 70103 | 01408 | 57.8 | 12.0 | 5.8 | 23.8 | 2.2 | 1.5+2 | 1.5+1 | | | | | | 1.7+4 | 2.3+3 | | ✓ | 6 | .4 |
| 51 | 70104 | 01450 | -44.0 | 156.0 | 5.2 | 2.2 | 1.5+2 | 1.2+2 | 6.5+1 | 2.3+1 | 7.7+0 | | | | 4.2+4 | 8.3+3 | | ✓ | >5 | 15.1 |
| 52 | 70105 | 01455 | 64.5 | 236.2 | 6.5 | 2.1 | 1.5+1 | | | | | | | | 1.7+4 | 2.5+3 | | | | 9.5 |
| 53 | 70108 | 01485 | -49.2 | 77.7 | 6.6 | 0.3 | 1.5+2 | 3.1+1 | | | | | | | 8.3+3 | 1.7+3 | | | | 20.0 |
| 54 | 70115 | 01535 | 71.0 | 98.5 | 6.5 | 11.8 | 1.5+2 | | | | | | | | 8.3+3 | | | ✓ | >5 | 5.5 |
| 55 | 70116 | 01547 | -71.0 | 308.0 | 7.8 | 23.2 | 3.0+1 | | | | | | | | 6.7+3 | | | ✓ | 8 | 9.4 |
| 56 | 70117 | 01557 | -44.0 | 107.1 | 6.0 | 0.6 | 1.4+1 | | | | | | | | 4.2+3 | | | ✓ | 6 | 17.6 |
| 57 | 70118 | 01560 | 62.3 | 270.5 | 5.0 | 0.5 | 3.0+1 | | | | | | | | 2.5+4 | 8.3+3 | | ✓ | 5-5.5 | 5.7 |
| 58 | 70123 | 01600 | 69.2 | 277.8 | 7.1 | 23.7 | 4.6+1 | | | | | | | | 2.5+3 | | | ✓ | 7 | 4.5 |
| 59 | 70124 | 01608 | 69.2 | 293.0 | 7.0 | 23.6 | 1.5+1 | | | | | | | | 1.7+3 | | | ✓ | >6 | 4.2 |
| 60 | 70130 | 01656 | 63.0 | 275.5 | 5.0 | 0.04 | 4.6+2 | 7.7+1 | 1.5+1 | | | | | | 2.5+4 | 6.7+3 | | ✓ | >5 | 5.5 |
| | 70130 | 01658 | 56.8 | 255.8 | 5.0 | 1.06 | 6.1+1 | 1.5+1 | 4.9+0 | | | | | | 1.7+4 | 2.5+3 | | ✓ | >4.5 | 8.4 |
| | 70130 | 01658 | -49.2 | 195.8 | 5.0 | 0.8 | 3.0+2 | 4.6+1 | 1.6+1 | | | | | | 1.7+4 | 2.3+3 | | ✓ | >5 | 11.2 |
| | 70130 | 01659 | -45.4 | 154.1 | 4.6 | 0.8 | 1.4+2 | 1.5+1 | | | | | | | 7.5+4 | 8.3+3 | | ✓ | >4.5 | 14.1 |
| | 70130 | 01661 | 37.9 | 112.4 | 4.85 | 0.2 | 1.5+3 | 3.1+2 | 5.4+1 | 1.8+1 | 4.5+0 | | | | 8.3+4 | 2.5+4 | 1.7+3 | ✓ | 4-9 | 17.0 |
| | 70130 | 01661 | -44.8 | 19.7 | 4.5 | 23.6 | 6.1+2 | 7.7+1 | 1.6+1 | 4.1+0 | | | | | 4.2+4 | 1.7+4 | 6.7+3 | ✓ | 4-6 | 20.0 |
| | 70130 | 01662 | -44.8 | 19.7 | 4.2 | 23.2 | 1.5+2 | 4.6+1 | 8.2+0 | 5.3+0 | | | | | 7.5+4 | 2.5+4 | 3.8+3 | ✓ | 4-5 | 23.0 |
| | 70131 | 01664 | 63.2 | 323.2 | 5.9 | 22.9 | 4.6+1 | | | | | | | | 7.5+4 | 1.7+4 | | ✓ | 5-6 | 2.9 |
| | 70131 | 01664 | 61.3 | 280.4 | 4.95 | 22.9 | 3.0+1 | | | | | | | | NO DATA | | | ✓ | 4.8 | 5.2 |
| | (70131) 01665 | 62.2 | 285.5 | 4.95 | 22.9 | 3.0+1 | | | | | | | | | | | | | | |
| 61 | 70131 | 01665 | 49.7 | 199 | 5.1 | 1.0 | 1.7+1 | | | | | | | | 3.3+4 | 2.5+3 | | ✓ | 5 | 10.9 |
| 62 | 70131 | 01668 | 44.1 | 113.8 | 5.7 | 0.1 | 4.6+2 | 6.1+1 | | | | | | | 8.2+3 | 2.5+3 | | ✓ | 6 | 16.8 |
| | 70131 | 01670 | 46.4 | 67.0 | 6.2 | 23.2 | 3.0+1 | | | | | | | | 8.3+3 | 4.2+3 | | ✓ | 6 | 19.8 |
| 63 | 70202 | 01681 | 50.7 | 205.3 | 4.95 | 0.9 | 3.0+1 | | | | | | | | 7.5+4 | 1.7+4 | | ✓ | 4.2-5 | 10.4 |
| | 70202 | 01684 | -47.4 | 162.5 | 5.6 | 0.1 | 2.0+1 | | | | | | | | 2.5+4 | 2.5+3 | | ✓ | 4.2-5 | 13.9 |

| DATE | REV | LAT | LONG | L-VAL | MIT | 235 | 435 | 65 | 850 | 1.1 | 1.35 | 1.6 | $\bar{r} (\% \pm)$ | | | 12 | 33 | 1MAL | UT | 5 |
|-------|--------|------|---------|---------|------|-------|-------|-------|-------|-------|------|-----|--------------------|-------|-------|-------|----|--------|------|---|
| 70202 | I 1894 | 40.5 | 121.2 | 49.25 | 8.9 | 6.1+1 | 7.6+0 | | | | | | 80 | 150 | 350 | 5-9 | ✓ | 5-15 | 16.2 | |
| 70202 | H 1486 | 19.2 | 235.435 | 15.5 | 24.5 | 6.1+1 | 7.6+0 | | | | | | 4.2+4 | 8.3+3 | | | | | | |
| 70203 | Q 1488 | 1.4 | 235.435 | 16.5 | | | | | | | | | | | | | | | | |
| 70203 | M 620 | 7.9 | | | | | | | | | | | | | | | | | | |
| 70203 | I 1692 | 46.9 | 160.2 | 5.9 | 0.8 | 2.2+1 | | | | | | | 6.7+4 | | | 6 | ✓ | 6-7 | 13.0 | |
| 70205 | Q 1708 | 48.3 | 172.5 | 6.2 | 0.8 | 1.5+2 | 2.0+1 | | | | | | 1.7+4 | 6.7+3 | | 65.6 | ✓ | 6 | 12.5 | |
| 70208 | H 1734 | 75.2 | 148.1 | 57.10 | 1.4 | 1.5+2 | 3.0+1 | | | | | | 1.6+4 | 8.3+3 | | 5-10 | ✓ | 4-10 | 16.6 | |
| 70208 | H 1734 | 41.0 | 97.5 | 5.7 | 28.4 | 1.5+2 | 2.0+1 | | | | | | 8.3+4 | 1.7+4 | | 4-10 | ✓ | 4-10 | 17.5 | |
| 70209 | I 1741 | 73.5 | 50.1 | 6.8 | 11.2 | 3.0+2 | | | | | | | 2.5+3 | | | 4-10 | ✓ | 4-10 | 7.3 | |
| 70222 | Q 1849 | 68.4 | 57.3 | 6 | 1.5 | 4.6+1 | | | | | | | 8.3+3 | | | 6 | ✓ | 4-8 | 21.8 | |
| 70225 | I 1864 | 51.2 | 280.1 | 6.7 | 0.2 | 1.2+2 | 1.5+1 | | | | | | 2.5+4 | 7.5+3 | | 6.8 | ✓ | 7-6 | 5.6 | |
| 70225 | I 1870 | 41.9 | 201.3 | 6.8 | 23.3 | 1.5+2 | 3.0+1 | | | | | | 1.7+4 | 5.0+4 | | 7 | ✓ | 7 | 11.5 | |
| 70225 | I 1870 | 41.9 | 156.2 | 7.6 | 23.7 | 3.0+1 | | | | | | | 8.3+3 | 4.2+3 | | 6-7 | ✓ | 6-8 | 12.7 | |
| 70302 | Q 1909 | 64.9 | 219.1 | 7.8 | 22.8 | 1.5+1 | | | | | | | 6.7+3 | 8.3+2 | | 6 | ✓ | 5-10 | 9.9 | |
| 70307 | Q 1927 | 66.9 | 270.8 | 6.2 | 22.4 | 1.4+1 | | | | | | | 1.7+3 | | | 5.7 | ✓ | 6.5 | 4.0 | |
| 70307 | H 1948 | 59.0 | 232.0 | 6.0 | 23.1 | 1.5+1 | | | | | | | 3.3+3 | | | 5.5 | ✓ | 5-7 | 6.8 | |
| 70307 | H 1948 | 56.0 | 235.5 | 5.8 | 22.7 | 9.2+0 | | | | | | | DATA | DATA | | | | 8.3 | | |
| 70309 | H 1964 | 56.6 | 243.5 | 48.5 | 23.1 | 4.6+2 | 2.0+1 | | | | | | 4.2+4 | 8.3+3 | | 4.8-5 | ✓ | 4.6-5 | 6.1 | |
| 70309 | Q 1965 | 72.7 | 2.4 | 9-26 | 10.7 | 1.5+1 | | | | | | | 8.3+3 | | | 8 | ✓ | 7-8 | 12.7 | |
| 70309 | P 1963 | 41.9 | 75.9 | 5.8 | 21.8 | 1.5+2 | 1.5+1 | | | | | | 6.7+4 | 1.7+4 | | 4.4-9 | ✓ | 4.1-10 | 17.7 | |
| 70309 | Q 1968 | 73.0 | 273.8 | 6.0 | 13.3 | 1.5+3 | | | | | | | 8.3+3 | | | 7-14 | ✓ | 6-7 | 18.6 | |
| 70309 | P 1970 | 51.3 | 244 | 5.7 | 21.3 | 6.6+2 | 7.7+1 | 6.5+0 | | | | | 5.0+4 | 2.5+3 | | 4.8-7 | ✓ | 5.6 | 20.8 | |
| 70310 | Q 1972 | 3.0 | 174.4 | 35.2 | 5.6 | 21.3 | | | | | | | | | | | | | | |
| 70310 | H 1975 | 65.2 | 41.5 | 9.3 | 9.9 | 7.2+1 | | | | | | | 7.5+3 | | | 12 | ✓ | 7-10 | 9.4 | |
| 70310 | I 1975 | 43.6 | 121.6 | 6.8 | 22.6 | 2.7+3 | 4.6+1 | | | | | | 5.8+4 | 2.5+3 | | 6.8 | ✓ | 6-8 | 14.5 | |
| 70310 | I 1977 | 56.6 | 25.1 | 7.0 | 20.1 | 1.5+1 | | | | | | | 3.5+4 | | | 5.5+5 | ✓ | 6.6 | 20.6 | |
| 70311 | Q 1980 | 68.1 | 285.5 | 62.46 | 21.8 | 4.6+2 | 3.5+1 | | | | | | 8.3+3 | 6.7+3 | | 55.70 | ✓ | 6-8 | 2.7 | |
| 70311 | B 1986 | 62.0 | 340.8 | 5.3-5.6 | 21.0 | 7.6+2 | 1.6+2 | 8.2+1 | 3.5+1 | 7.7+0 | | | 8.3+4 | 2.5+4 | 2.5+3 | 4.9+0 | ✓ | 5.8 | 23.3 | |

| E
V
E
N
T | DATE | REV | LAT | LONG | L-VAL | MLT | σ (0.1% at 400) | | | | σ (0.1% at 400) | | | | σ (0.1% at 400) | | | | 33 | 12 | 80°
1-VAL | 8 | | |
|-----------------------|-------|-------|------|-------|-------|------|------------------------|-------|-------|-------|------------------------|-----|-----|-------|------------------------|-------|--------------|---|----|----|--------------|---|---|---|
| | | | | | | | 235 | 435 | 655 | 855 | 11 | 135 | 1.6 | 80 | 150 | 350 | 80°
1-VAL | | | | | | | |
| 102 | 70408 | 02011 | 40.8 | 75.2 | 4.9 | 20.8 | 1.5+2 | 1.2+2 | 0.6+1 | 1.1+1 | 3.9+0 | | | 2.5+5 | 5.0+4 | 2.5+3 | 4.5-10 | ✓ | ✓ | ✓ | ✓ | ✓ | ✓ | ✓ |
| 103 | 70409 | 02218 | 48.0 | 105.5 | 57.6 | 22.1 | 6.1+2 | 6.1+1 | | | | | | 3.3+4 | 2.5+4 | 1.7+3 | 5.3-6 | ✓ | ✓ | ✓ | ✓ | ✓ | ✓ | ✓ |
| 104 | 70410 | 02236 | 54.3 | 167.2 | 7.6 | 22.2 | 1.3+2 | 2.7+0 | | | | | | 1.7+4 | 7.5+3 | | 6.3-8 | ✓ | ✓ | ✓ | ✓ | ✓ | ✓ | ✓ |
| 70410 | 02238 | 46.5 | | 82.9 | 6.0 | 20.5 | 1.5+2 | 4.6+1 | | | | | | 5.8+4 | 1.7+4 | 1.7+3 | 5-6 | ✓ | ✓ | ✓ | ✓ | ✓ | ✓ | ✓ |
| 105 | 70411 | 02232 | 48.5 | 249.3 | 5.7 | 21.5 | 6.1+2 | 1.5+2 | 2.1+1 | | | | | 2.5+4 | 8.3+3 | | 5-7 | ✓ | ✓ | ✓ | ✓ | ✓ | ✓ | ✓ |
| 106 | 70419 | 02297 | 58.5 | 20.6 | 14-65 | 21.7 | 4.6+3 | | | | | | | 8.3+4 | 4.2+4 | 2.5+3 | 4.4-11 | ✓ | ✓ | ✓ | ✓ | ✓ | ✓ | ✓ |
| 70419 | 02297 | 7.6 | | 10.8 | 6.7 | 9.8 | 1.5+2 | | | | | | | 8.3+4 | 4.2+4 | 2.5+3 | 4.4-11 | ✓ | ✓ | ✓ | ✓ | ✓ | ✓ | ✓ |
| 70419 | 02298 | 47.1 | | 172.3 | 4.8 | 21.7 | 4.6+2 | 4.6+1 | | | | | | 8.3+4 | 4.2+4 | 2.5+3 | 4.4-11 | ✓ | ✓ | ✓ | ✓ | ✓ | ✓ | ✓ |
| 70419 | 02299 | 54.9 | | 16.93 | 4.4 | 21.4 | 3.0+2 | 4.6+1 | | | | | | 8.3+4 | 4.2+4 | 2.5+3 | 4.4-11 | ✓ | ✓ | ✓ | ✓ | ✓ | ✓ | ✓ |
| 70419 | 02300 | 63.4 | | 130.1 | 48.53 | 22.0 | 1.5+3 | 6.1+1 | 6.8+1 | | | | | 8.3+4 | 4.2+4 | 2.5+3 | 4.4-11 | ✓ | ✓ | ✓ | ✓ | ✓ | ✓ | ✓ |
| 70419 | 02301 | 54.7 | | 35.5 | 5.7 | 19.5 | 7.7+1 | | | | | | | 8.3+4 | 4.2+4 | 2.5+3 | 4.4-11 | ✓ | ✓ | ✓ | ✓ | ✓ | ✓ | ✓ |
| 70419 | 02302 | 53.9 | | 35.5 | 57.63 | 22.9 | 1.5+2 | 1.5+1 | | | | | | 8.3+4 | 4.2+4 | 2.5+3 | 4.4-11 | ✓ | ✓ | ✓ | ✓ | ✓ | ✓ | ✓ |
| 70420 | 02304 | 42.1 | | 301.1 | 5.4 | 22.1 | 7.6+2 | 7.7+1 | 1.1+1 | | | | | 8.3+4 | 4.2+4 | 2.5+3 | 4.4-11 | ✓ | ✓ | ✓ | ✓ | ✓ | ✓ | ✓ |
| 70420 | 02305 | 45.9 | | 258.6 | 57.64 | 21.2 | 1.1+3 | 1.2+2 | 1.5+1 | | | | | 8.3+4 | 4.2+4 | 2.5+3 | 4.4-11 | ✓ | ✓ | ✓ | ✓ | ✓ | ✓ | ✓ |
| 70420 | 02306 | 43.3 | | 212.4 | 6 | 21.9 | 6.1+1 | 7.7+0 | | | | | | 8.3+4 | 4.2+4 | 2.5+3 | 4.4-11 | ✓ | ✓ | ✓ | ✓ | ✓ | ✓ | ✓ |
| 70420 | 02307 | 57.7 | | 174.8 | 5-6.6 | 21.7 | 9.2+2 | 6.1+1 | 7.8+0 | | | | | 8.3+4 | 4.2+4 | 2.5+3 | 4.4-11 | ✓ | ✓ | ✓ | ✓ | ✓ | ✓ | ✓ |
| 70420 | 02307 | 74.8 | | 132.8 | 7.1 | 21.0 | 7.7+1 | | | | | | | 8.3+4 | 4.2+4 | 2.5+3 | 4.4-11 | ✓ | ✓ | ✓ | ✓ | ✓ | ✓ | ✓ |
| 70420 | 02309 | 64.0 | | 92.2 | 5.5 | 22.6 | 1.5+2 | 4.6+1 | 1.6+1 | | | | | 8.3+4 | 4.2+4 | 2.5+3 | 4.4-11 | ✓ | ✓ | ✓ | ✓ | ✓ | ✓ | ✓ |
| 70420 | 02311 | 72.0 | | | | | | | | | | | | 8.3+4 | 4.2+4 | 2.5+3 | 4.4-11 | ✓ | ✓ | ✓ | ✓ | ✓ | ✓ | ✓ |
| 107 | 70421 | 02312 | 70.7 | 254.1 | 5.95 | 20.6 | 2.0+2 | 3.5+1 | 1.6+1 | 3.9+0 | 4.5+0 | | | 5.0+4 | 1.7+4 | | 5.5-6 | ✓ | ✓ | ✓ | ✓ | ✓ | ✓ | ✓ |
| 108 | 70422 | 02323 | 72.7 | 256.3 | 5.8 | 20.8 | 3.0+1 | | | | | | | 6.3+3 | 2.5+3 | | 6 | ✓ | ✓ | ✓ | ✓ | ✓ | ✓ | ✓ |
| 109 | 70423 | 02333 | 45.2 | 105.5 | 6.0 | 20.3 | 5.1+1 | 1.6+1 | | | | | | 1.1+4 | 8.3+3 | | 6 | ✓ | ✓ | ✓ | ✓ | ✓ | ✓ | ✓ |
| 110 | 70424 | 02347 | 48.4 | 159.1 | 5.8 | 21.3 | 7.7+1 | 1.5+1 | | | | | | 1.7+4 | 2.5+3 | | 4.8-12 | ✓ | ✓ | ✓ | ✓ | ✓ | ✓ | ✓ |
| 70424 | 02347 | 61.3 | | 160.9 | 5.6 | 21.3 | 6.1+2 | 9.2+1 | 1.1+1 | | | | | 8.3+4 | 4.2+4 | 2.5+3 | 5-8 | ✓ | ✓ | ✓ | ✓ | ✓ | ✓ | ✓ |
| 111 | 70429 | 02381 | 52.4 | 359.4 | 5.4 | 22.3 | 2.0+2 | 1.2+1 | | | | | | 3.3+4 | 8.3+3 | | 5.5-5 | ✓ | ✓ | ✓ | ✓ | ✓ | ✓ | ✓ |
| 112 | 70430 | 02384 | 43.2 | 265.9 | 6.1 | 20.9 | 4.6+1 | | | | | | | 8.3+4 | 4.2+4 | 2.5+3 | 5.5-6 | ✓ | ✓ | ✓ | ✓ | ✓ | ✓ | ✓ |

| STATION | DATE | REV | LAT | LONG | L-VAL | MLT | δ (9/1000000) | | | 80° | Σ (9/1000000) | | | 12 | 13 | 9 |
|---------|---------|-------|-------|-------|---------|------|----------------------|-------|-------|-------|----------------------|-------|-------|-------|-------|-------|
| | | | | | | | 655 | 850 | 1.1 | 1.35 | 1.6 | 80 | 110 | 350 | | |
| 115 | 70502 | P2404 | 56.3 | 275.5 | 4.6 | 21.0 | 2.5 | 4.5 | 1.5+2 | 1.5+2 | 1.5+2 | 1.5+2 | 1.5+2 | 1.5+2 | 1.5+2 | 1.5+2 |
| | (70502) | P2404 | (6.0) | | | | | | | | | | | | | |
| 116 | 70502 | P2404 | 51.7 | 192.4 | 4.6 | 20.6 | 6.1+1 | 1.5+1 | | | | | | | | |
| 117 | 70502 | M2407 | 22.7 | 66.8 | 6.6 | 22.4 | 7.4+3 | 1.4+2 | | | | | | | | |
| | 70502 | C2408 | 45.9 | 324.9 | 4.1 | 19.1 | 3.1+2 | 7.6+1 | | | | | | | | |
| | 70502 | C2408 | 56.6 | 169.4 | 6 | 11.3 | 1.5+3 | 4.6+1 | | | | | | | | |
| | (70502) | M2410 | (2.0) | | | | | | | | | | | | | |
| 118 | 70503 | P2111 | 46.7 | 239.5 | 5.7-6 | 20.5 | 1.5+2 | | | | | | | | | |
| 119 | 70506 | C2404 | 41.8 | 297.8 | 6 | 21.4 | 4.6+2 | 1.5+1 | | | | | | | | |
| 120 | 70510 | B2473 | 57.2 | 18.4 | 6 | 21.9 | 6.1+1 | | | | | | | | | |
| | 70511 | P2404 | 4.0 | 196.2 | 4.5 | 20.0 | 7.6+3 | 2.0+2 | | | | | | | | |
| | 70511 | C2477 | 49.0 | 176.2 | 4.5 | 21.0 | 1.5+1 | 2.0+1 | | | | | | | | |
| | 70511 | M2477 | 45.0 | 179.0 | 6.3 | 21.0 | 1.5+1 | 2.0+1 | | | | | | | | |
| | 70511 | M2477 | 55.1 | 66.9 | 4.6 | 21.4 | 2.0+1 | | | | | | | | | |
| 121 | 70512 | M2482 | 39.9 | 285.8 | 5.7 | 20.8 | 2.7+1 | 9.2+0 | | | | | | | | |
| | 70512 | M2482 | 40.0 | 246.0 | 4.8-5 | 20.1 | 6.1+1 | 1.1+1 | | | | | | | | |
| | 70512 | M2482 | 50.8 | 210.9 | 4.2 | 20.2 | 7.4+2 | 2.0+2 | | | | | | | | |
| | 70512 | M2482 | 49.0 | 201.8 | 4.3-4.7 | 20.1 | 1.1+2 | 3.1+1 | | | | | | | | |
| | 70512 | C2487 | 59.4 | 119.9 | 5.1 | 21.0 | 1.2+2 | | | | | | | | | |
| | 70512 | M2488 | 61.7 | 72.3 | 5.9 | 21.6 | 1.5+1 | | | | | | | | | |
| 122 | 70515 | C35M | 53.8 | 360.0 | 6 | 22.1 | 1.5+2 | 1.5+1 | | | | | | | | |
| 123 | 70516 | M253 | 41.1 | 314.5 | 5.3-5.6 | 21.1 | 1.1+3 | 1.5+2 | | | | | | | | |
| 124 | 70517 | S2538 | 64.4 | 108.0 | 6.4 | 21.1 | 1.5+2 | 1.5+1 | | | | | | | | |
| 125 | 70518 | B2533 | 51.6 | 237.1 | 7.4-7.7 | 19.8 | 1.5+1 | | | | | | | | | |
| 126 | 70518 | C2533 | 52.5 | 332 | 7.7 | 21.6 | 6.1+1 | | | | | | | | | |
| 127 | 70519 | B2546 | 63.9 | 303 | 9.0 | 21.9 | 3.5+1 | | | | | | | | | |

| S
Y
D
T | DATE | REV | LAT | LONG | L-VAL | MLT | J [°/W, K, km] | | | | J (P, L, S, Z) | | | | 80° | 12 | 97 | L-VAL | 10
(RES)
UT |
|------------------|-------|-------|------|-------|--------|------|------------------|----------------|----------------|-----|----------------|------|-----|-------|-------|-------------------------|----|---------|-------------------|
| | | | | | | | 235 | 435 | 655 | 850 | 11 | 1.35 | 1.6 | 80 | 110 | 370 | | | |
| 127 | 70520 | 02555 | 50.5 | 347.2 | 6.5 | 21.5 | 1.5+1 | | | | | | | 2.5+4 | 6.7+3 | 5.5-4 | ✓ | 6.5 | 21.7 |
| 128 | 70524 | 02587 | 55.9 | 8.6 | 6.8 | 21.5 | 4.6+1 | | | | | | | 8.3+3 | | 6-6.5 | | | 19.9 |
| 129 | 70610 | 02722 | 45.0 | 234.8 | 5.3 | 18.7 | 24.6+0
29.1+1 | 1.5+2
4.6+1 | 9.3+1
1.2+1 | | NO PA | | | 8.3+3 | 1.7+3 | 5.3-6 | | | 3.8 |
| 130 | 70702 | 02905 | 53.1 | 333.6 | 7.0 | 19.5 | 7.7+0 | | | | | | | 8.3+3 | | 5.5-7 | ✓ | 9.5 | 00.4 |
| 131 | 70710 | 02963 | 62.4 | 306.8 | 56.98 | 5.7 | 3.5+2 | 1.1+1 | | | | | | 4.2+3 | 1.1+3 | 6-9 | ✓ | 5-10 | 1.1 |
| 132 | 70710 | 02968 | 63.9 | 74.4 | 7.0 | 19.0 | 1.5+1 | | | | | | | 8.3+1 | | 5.8-7 | ✓ | 5.5 | 13.7 |
| 133 | 70710 | 02970 | 53.2 | 338.3 | 6.7 | 19.2 | 2.0+2 | 7.7+0 | | | | | | 8.3+3 | 2.5+3 | 5.5-7 | | | 19.7 |
| 134 | 70716 | 03015 | 53.4 | 324.2 | 5.5 | 5.5 | 5.0+3 | | | | | | | 3.5+4 | 2.5+3 | 5-15 | ✓ | 4.9-14 | 7.0 |
| 135 | 70716 | 03017 | 47.6 | 239 | 5.8 | 3.3 | 3.5+1 | | | | | | | 8.3+4 | | 5 | ✓ | 4.7-6 | 12.8 |
| 136 | 70716 | 03017 | 55.9 | 634 | 6.3-22 | 18.8 | 1.7+4 | | | | | | | 6.7+4 | 8.3+3 | 5-13 | ✓ | 6-12 | 13.8 |
| 136 | 70718 | 03034 | 59.0 | 200.2 | 7.2 | 3.2 | 1.5+1 | | | | | | | 2.5+3 | | 5.8-15 | ✓ | 5.5-2.5 | 15.0 |
| 137 | 70718 | 03035 | 63.5 | 182.2 | 6.6 | 3.5 | 3.5+1 | | | | | | | 8.3+2 | | 6-2 | ✓ | 6.2-20 | 18.0 |
| 137 | 70720 | 03034 | 57.8 | 76.6 | 7.3 | 4.08 | 3.1+1 | | | | | | | 2.5+3 | | 7 | ✓ | 5.5-8 | 0.8 |
| 138 | 70722 | 03065 | 46.1 | 277.2 | 6.9 | 4.3 | 2.0+1 | | | | | | | 2.5+3 | | 56.7 | ✓ | 5-7 | 10.0 |
| 139 | 70723 | 03074 | 64.4 | 49.6 | 7.0 | 3.6 | 6.1+1 | | | | | | | 4.2+3 | | 7.3 | ✓ | 7 | 2.8 |
| 140 | 70729 | 03184 | 66.0 | 5.0 | 4.5 | 4.3 | 3.1+0 | | | | | | | 8.3+3 | 2.5+3 | 7.70
8.3+2
1.7+3 | ✓ | 4.5 | 5.8 |
| 141 | 70805 | 03174 | 78.5 | 300.1 | 5.4 | 7 | 1.2+3 | 1.5+1 | | | | | | 1.7+3 | 8.3+2 | 7.5-10 | ✓ | 4.7 | 11.2 |
| 142 | 70806 | 03184 | 63.0 | 44.5 | 7-8 | 4.5 | 1.2+2 | | | | | | | 2.5+3 | 8.3+3 | 1-8 | ✓ | 7.8 | 4.4 |
| 142 | 70806 | 03184 | 43.5 | 325.0 | 6.7-8 | 4.3 | 1.5+2 | 1.5+1 | | | | | | 6.7+4 | 8.3+3 | 8.3+2
5.7-8 | ✓ | 5-10 | 6.1 |
| 142 | 70806 | 03187 | 41.8 | 285.6 | 6 | 3.6 | 1.1+2 | | | | | | | 2.5+4 | 8.3+3 | 8.3+2
5.7-8 | ✓ | 6-7 | 8.9 |
| 142 | 70806 | 03188 | 46.5 | 238.7 | 6.7 | 2.6 | 4.6+2 | 3.1+1 | | | | | | 5.8+4 | 1.7+4 | 1.7+4
2.5+3
5.4-6 | ✓ | 6-7.5 | 11.9 |
| 142 | 70806 | 03188 | 48.9 | 186.0 | 7 | 2.1 | 3.1+1 | 1.5+1 | | | | | | 1.7+4 | 4.5+3 | 6-7 | ✓ | 5.7 | 15.1 |

| EY UNIT | DATE | REF | LAT | LONG | LVAL | MIT | J (°/sec. km) | | | | T (°/sec. km) | | | 12 | 33 | LVAL | CHEN UT |
|---------|-------|-------|-----|------|-------|-----|---------------|-------|-------|------|---------------|-------|-------|-----|----|---------|---------|
| | | | | | | | 0.35 | 0.50 | 1.1 | 1.35 | 1.6 | 80 | 150 | 350 | | | |
| N3 | 70807 | B3196 | 530 | 8220 | 7.10 | 4.4 | 1.5+1 | | | | | 2.5+3 | | | ✓ | 6.5-7 | 5-7 |
| | 70807 | H3191 | 440 | 2404 | 6.8-7 | 3.6 | 1.5+2 | | | | | 1.7+4 | 2.5+3 | | ✓ | 6-7 | 8-9 |
| | 70807 | B3196 | 418 | 2488 | 6.65 | 2.8 | 1.5+2 | | | | | 8.3+4 | 1.7+4 | | | 5.5-7 | 11.4 |
| | 70807 | B3197 | 589 | 1930 | 7 | 2.1 | 1.2+2 | | | | | 4.2+4 | 8.3+3 | | ✓ | 5.9-7 | 14.6 |
| | 70807 | B3198 | 643 | 1443 | 7.9 | 2.5 | 1.5+2 | | | | | 1.7+4 | 7.5+3 | | | 6-8 | 17.6 |
| N4 | 70808 | B3200 | 484 | 2972 | 6.8 | 3.7 | 1.2+3 | | | | | 8.3+3 | 2.8+3 | | ✓ | 6-6.5 | 8.0 |
| | 70810 | P3218 | 495 | 3510 | 6 | 4.5 | 1.5+2 | 3.0+1 | | | | 4.2+3 | | | ✓ | 5.5 | 4.2 |
| N6 | 70810 | P3223 | 633 | 1207 | 57.8 | 3.0 | 1.5+2 | 1.2+1 | | | | 2.5+4 | 8.3+2 | | ✓ | 5.5-8 | 19.1 |
| | 70814 | H3354 | 430 | 2479 | 6.9 | 2.7 | 1.4+3 | 1.5+1 | | | | 1.7+4 | 4.2+3 | | ✓ | 5.3-6.0 | 11.0 |
| N7 | 70814 | B3254 | 629 | 1465 | 7 | 2.2 | 3.1+1 | | | | | 2.8+4 | 7.5+3 | | ✓ | 6-7 | 17.2 |
| | 70815 | C3260 | 418 | 2980 | 6.9 | 3.5 | 3.1+2 | 9.2+0 | | | | 8.3+3 | 6.7+3 | | ✓ | 5.5-6 | 7.6 |
| N9 | 70818 | C3285 | 453 | 2422 | 6.7 | 2.9 | 7.6+1 | | | | | 8.3+3 | 1.7+3 | | ✓ | 6-6.6 | 9.1 |
| | 70818 | C3286 | 470 | 2210 | 6.9 | 2.5 | 5.0+1 | 1.5+1 | | | | 1.7+3 | 1.7+3 | | ✓ | 6-7 | 12.1 |
| | 70818 | B3287 | 480 | 1421 | 6.7 | 3.0 | 4.6+1 | | | | | 1.7+4 | 3.3+3 | | ✓ | 6-8 | 15.0 |
| | 70818 | H3294 | 643 | 836 | 6.5 | 3.4 | 1.5+1 | | | | | 8.3+3 | 4.5+3 | | ✓ | 6-6.7 | 21.2 |
| | 70819 | C3294 | 472 | 2809 | 6.3 | 3.0 | 4.6+1 | | | | | 4.2+3 | | | ✓ | 8 | 7.8 |
| 150 | 70819 | C3294 | 472 | 2809 | 6.3 | 3.0 | 4.6+1 | | | | | 8.3+3 | 1.7+3 | | ✓ | 6-6.4 | 8.6 |
| | 70819 | C3294 | 666 | 879 | 6.588 | 1.2 | 3.1+1 | 4.6+0 | | | | 8.3+3 | 2.5+3 | | ✓ | 5.5-6 | 20.7 |
| 151 | 70820 | H3300 | 510 | 239 | 17.8 | 2.0 | 1.4+2 | 1.5+1 | | | | 2.5+3 | | | ✓ | 6.5 | 11.2 |
| | 70822 | B3353 | 435 | 2380 | 5.5 | 2.1 | 4.6+1 | 2.0+1 | 1.3+1 | | | 4.3+3 | | | ✓ | 5.5-5 | 11.1 |
| 153 | 70828 | H3360 | 562 | 2010 | 6.3 | 1.4 | 3.1+1 | | | | | 8.3+3 | | | ✓ | 6 | 13.0 |
| | 70829 | H3370 | 472 | 2575 | 7 | 2.1 | 1.5+1 | | | | | 1.7+3 | | | ✓ | 5.5-7.8 | 9.6 |
| 155 | 70830 | H3384 | 440 | 2651 | 6.8 | 2.4 | 9.2+0 | | | | | 1.7+3 | | | ✓ | 6.4 | 9.1 |
| | 70832 | C3413 | 603 | 56 | 5.5 | 2.8 | 9.2+0 | | | | | 1.7+4 | 4.2+3 | | | 6 | 22.5 |

| J | DATE | REV | LAT | (P) | LONG | L-VAL | MLT | j (e/m ² s ² km ²) | | | | J (P/m ² s ²) | | | | VAL | 12 | 33 | L-VAL | 12.0 |
|-----|-------|-------|------|-------|---------|-------|------|--|-------|-------|-------|--------------------------------------|------|-----|-------|-------|--------|----|---------|------|
| | | | | | | | | 835 | 435 | 655 | 850 | 1.1 | 1.35 | 1.6 | 80 | 150 | 550 | | | |
| 157 | 70709 | I3469 | 64.3 | 57.8 | 6.6 | 2.4 | 2.4 | 1.5+1 | | | | | | | 33+3 | 2.5+3 | 6 | ✓ | 6-6.5 | 21.9 |
| 158 | 70709 | I3470 | 60.8 | 343.5 | 6.9 | 3.3 | 3.3 | 3.1+1 | | | | | | | 1.1+5 | 2.5+3 | 6.9 | ✓ | 6-6.5 | 21.9 |
| 159 | 70710 | M3473 | 64.5 | 253.5 | 58.6 | 1.8 | 1.8 | 4.6+1 | | | | | | | 1.7+3 | 2.5+3 | 5.7 | ✓ | 5.5-6 | 9.4 |
| 160 | 70710 | M3475 | 63.2 | 65.9 | 5.9 | 2.3 | 2.3 | 1.5+2 | 4.6+0 | | | | | | 7.5+3 | 2.5+3 | 6 | ✓ | 6 | 21.4 |
| 161 | 70711 | M3476 | 61.7 | 262.2 | 5.5 | 1.95 | 1.95 | 1.1+2 | 6.1+0 | | | | | | 8.3+3 | 2.5+3 | 5-5.5 | ✓ | 5-5 | 8.8 |
| 162 | 70711 | C3472 | 61.6 | 211.4 | 5.6 | 1.1 | 1.1 | 1.4+2 | 1.2+1 | | | | | | 8.3+3 | 2.5+3 | 5-6 | ✓ | 5-5 | 11.9 |
| 163 | 70714 | M3473 | 67.7 | 163.9 | 5 | 1.4 | 1.4 | 1.4+2 | 3.1+1 | | | | | | 8.3+3 | 2.5+3 | 4.5-5 | ✓ | 4.5-5 | 14.9 |
| 164 | 70711 | C3474 | 67.5 | 110.5 | 5.1-12 | 1.7 | 1.7 | 4.6+1 | 6.1+0 | | | | | | 8.3+3 | 2.5+3 | 4.5-18 | ✓ | 5-18 | 18.0 |
| 165 | 70712 | M3476 | 64.3 | 79.3 | 6 | 2 | 2 | 1.5+1 | | | | | | | 8.3+2 | | 6 | ✓ | | 20.1 |
| 166 | 70712 | M3476 | 64.9 | 229.9 | 5.0 | 1.3 | 1.3 | 9.2+2 | 3.1+2 | 1.6+2 | 7.1+1 | | | | 2.5+3 | 1.1+4 | 4.8-5 | ✓ | 4.7-5.4 | 10.8 |
| 167 | 70715 | M3475 | 48.4 | 243.7 | 6.1 | 1.3 | 1.3 | 7.6+1 | 1.5+1 | | | | | | 2.5+3 | 2.5+3 | 5.5-15 | ✓ | 5-11 | 9.8 |
| 168 | 70715 | M3475 | 48.5 | 38.6 | 5.9-7 | 11.5 | 11.5 | 8.2+2 | | | | | | | 2.5+3 | 2.5+3 | 6 | ✓ | 6-10 | 10.9 |
| 169 | 70718 | P3528 | 48.2 | 209.8 | 6.9 | 2.6 | 2.6 | 3.1+1 | | | | | | | 7.5+3 | | 6 | ✓ | 6.9 | 5.2 |
| 170 | 70719 | C3544 | 46.0 | 274.3 | 6.6 | 1.8 | 1.8 | 1.5+1 | | | | | | | 8.3+2 | | 6.6 | ✓ | 6.6 | 7.6 |
| 171 | 70719 | I3550 | 74.6 | 92.0 | 10-10.6 | 1.2 | 1.2 | 7.7+0 | | | | | | | 8.3+3 | 8.3+3 | 6.2-10 | ✓ | 6.2-9 | 12.6 |
| 172 | 70720 | P3553 | 43.8 | 326.8 | 4.5-5 | 2.7 | 2.7 | 6.1+2 | 6.1+1 | 8.2+0 | | | | | 2.5+3 | 8.3+3 | 7.3-5 | ✓ | 7 | 4.1 |
| 173 | 70720 | P3553 | 46.2 | 330.2 | 4.5-5 | 2.8 | 2.8 | 3.1+2 | 3.1+1 | 4.9+0 | | | | | 1.7+4 | 2.5+3 | 4-6 | ✓ | 4-6 | 5.5 |
| 174 | 70720 | C3554 | 66.9 | 290.5 | 5.1 | 4.2 | 4.2 | 2.0+2 | 1.4+1 | | | | | | 2.5+3 | 3.3+3 | 5 | ✓ | 5 | 8.4 |
| 175 | 70720 | M3555 | 78.0 | 10.0 | 5-6 | 4.9 | 4.9 | 1.5+3 | | | | | | | 2.5+3 | | 6 | ✓ | 4-10 | 11.8 |
| 176 | 70720 | M3555 | 63.8 | 182.7 | 6.5-7.5 | 2.1 | 2.1 | 4.6+1 | | | | | | | 5.0+3 | 8.3+2 | 4.5-5 | ✓ | 4.5-5 | 14.4 |
| 177 | 70720 | C3555 | 51.5 | 188.1 | 5.2 | 4.4 | 4.4 | 4.6+1 | | | | | | | 2.5+3 | 2.5+3 | 4.5-14 | ✓ | 4.1-4.8 | 20.0 |
| 178 | 70720 | C3555 | 57.1 | 142.1 | 4.3-5.6 | 1.3 | 1.3 | 6.1+2 | 4.6+1 | 6.5+0 | | | | | 8.3+3 | | 5-6 | ✓ | 5-6 | 17.5 |
| 179 | 70720 | C3555 | 45.3 | 141.1 | 5.5-6 | 3.4 | 3.4 | 1.2+3 | | | | | | | 1.7+4 | 2.5+3 | 4.5-15 | ✓ | 5-6 | 20.4 |
| 180 | 70720 | I3555 | 46.6 | 97.7 | 5.4 | 1.7 | 1.7 | 3.1+1 | | | | | | | 8.3+2 | 2.5+3 | 6-9 | ✓ | 5-12 | 22.0 |
| 181 | 70720 | P3554 | 52.7 | 56.6 | 6.9 | 1.9 | 1.9 | 1.5+1 | | | | | | | 7.5+3 | 8.3+3 | 5.5-11 | ✓ | 5-6 | 23.2 |

AD-A092 545

AIR FORCE INST OF TECH WRIGHT-PATTERSON AFB OH F/G 4/1
RELATIVISTIC ELECTRON PRECIPITATION: AN OBSERVATIONAL STUDY.(U)
1980 L J ANDREOLI
AFIT-CI-80-260 NL

UNCLASSIFIED

4 of 4

NO
REPRODUCTION



END
DATE
FILMED
1-81
DTIC

Appendix D - Computation of Electron and X-ray Energy Deposition Profiles

The precipitation of energetic electrons into the atmosphere is simulated by a finite difference numerical solution to the multi-dimensional Fokker-Planck diffusion equation developed by Walt et al. (1968). The technique was slightly modified to handle other than isotropic pitch angle distributions by Spjeldvik (1974) but this modification was not used here since the distribution over the downward hemisphere at 300 km is isotropic for all cases considered. The conversion of the Walt et al. (1968) program to the UCLA computer by Spjeldvik (1974), however, was used. Spjeldvik (1974) contains the computer listing.

The Walt program solves the following final version of the Fokker-Planck equation as derived by Chappell (1968):

$$\cos \alpha \frac{\partial}{\partial s} \left(\frac{f}{n} \right) = - \frac{\partial}{\partial \alpha} \frac{\sin \alpha}{R_s L} \frac{\partial}{\partial \alpha} \left(\frac{f}{n} \right) + \frac{(E+1)^2 2\pi}{E^2 (E+2)^2} \left(\frac{q^2}{m_e c^2} \right)^2 \sum_i m_i Z_i^2 \ln \eta_i^{-1} \frac{1}{\sin \alpha} \frac{\partial}{\partial \alpha} \left[\sin \alpha \frac{\partial}{\partial \alpha} \left(\frac{f}{n} \right) \right] + \frac{2(E+1)}{E^{1/2} (E+2)^{1/2}} \frac{\partial}{\partial E} \left[\frac{(E+1) 2\pi}{E^{1/2} (E+2)^{1/2}} \left(\frac{q^2}{m_e c^2} \right)^2 \sum_i m_i Z_i \ln \sigma_i \left(\frac{f}{n} \right) \right],$$

where Table D-1 defines the symbolism. Notice that the stochastic averages $\langle (\Delta E)^2 \rangle$, $\langle (\Delta \alpha \Delta E) \rangle$, and $\langle (\Delta E \Delta r) \rangle$ (small) and higher order terms have been eliminated. Steady state ($\frac{\partial f}{\partial t} = 0$) is assumed since precipitation is steady on times scales much longer than atmospheric transit times for precipitating electrons. Also, radial

Table D-1 Nomenclature (Spjeldvik, 1974)

f = electron distribution function averaged over cyclotron phase
 t = time
 c = speed of light
 R_E = radius of the Earth
 L = L-value, field line equatorial distance in units of R_E
 E = electron energy in rest mass units
 α = local pitch angle
 α_0 = equatorial pitch angle
 r = electron gyro radius
 s = length along the field line
 q = electron charge
 m_e = electron mass
 e = the natural logarithm base, 2.7182...
 n_i = number density of atmospheric species i
 Z_i = atom number of atmospheric species i
 I_i = average excitation potential of atmospheric species i
 η_i = minimum scattering angle corresponding to maximum impact parameter (for thermal plasma, the Debye-length; for the neutral atmosphere, the atomic radius)
 $\sigma_i = (e (E+2)/I_i)^{1/2}$
 $\langle \rangle$ denotes stochastic ensemble average.

diffusion is ignored ($\frac{f}{r} = \text{constant}$).

The program outputs the amount of average energy deposited per unit volume at each altitude below the incident altitude. Also, assuming an average of 35 eV is required to produce each ion pair, the rate of ion pair production is output versus altitude.

The complete altitude profile of energy deposition by bremsstrahlung is computed from the Berger, Seltzer, Maeda (1974) Monte Carlo simulation method. This work is essentially an extension of the earlier (Berger, Seltzer, Maeda, 1970; Berger and Seltzer, 1972) Monte Carlo simulation methods by this same group. Basically, a computation is made of 10,000 electron trajectories for each incident electron energy from 2 keV to 2 MeV for electrons injected into the atmosphere at 300 km altitude. The trajectories are histories of individual primary and secondary electrons as they coulomb scatter (elastic by nuclei collisions, inelastic by orbital electron collisions) off neutral constituents and deposit energy at various altitudes. In addition, the production of bremsstrahlung quanta in these interactions and their Compton scattering and consequent photoelectron absorption of the bremsstrahlung quanta in the atmosphere is followed. The Berger, Seltzer, Maeda (1974) results of energy deposition as a function of atmospheric depth (mass thickness) by bremsstrahlung from monoenergetic incident electron beams for wide-area precipitation flux isotropic over the downward hemisphere is given in Table D-2 in the form of energy deposited per unit mass thickness (ev/g cm⁻²) per incident electron energy. From this

TABLE D-2. Energy deposition function for Bremsstrahlung, for the case of uniform wide-area precipitation of an electron flux isotropic over the downward hemisphere. The quantity given is $A_{BR} (Z_m/T_0)$, in units of $\text{cm}^2\text{gm}^{-1}$. Number in parenthesis indicates powers of ten. (Berger, Seltzer, Maeda, 1974)

| $\frac{z_0}{T_0}$
(g cm ⁻² kV V ⁻¹) | 2000 | 1000 | 500 | 200 | 100 | 50 | 20 | 10 | 5 | 2 |
|---|---|---------|---------|---------|---------|---------|---------|---------|---------|---------|
| | $A_{\text{ph}}(z)/T_0$, cm ² /g | | | | | | | | | |
| 2.0(-6) | 6.9(-4) | 1.0(-3) | 2.2(-3) | 5.0(-3) | 1.1(-2) | 7.3(-3) | 3.4(-3) | 2.0(-3) | 7.2(-4) | 8.6(-6) |
| 4.0 | 7.6 | 1.1 | 2.4 | 5.3 | 7.0(-3) | 2.2 | 1.7 | 1.7 | 1.4 | 5.1(-7) |
| 8.0 | 8.4 | 1.2 | 2.5 | 5.0 | 1.7 | 1.1 | 1.7 | 2.7 | 3.3(-5) | |
| 2.0(-5) | 9.3 | 1.3 | 2.6 | 5.0 | 1.7 | 1.1 | 1.7 | 2.7 | 3.3(-5) | |
| 4.0 | 9.9 | 1.4 | 2.6 | 5.0 | 1.7 | 1.1 | 1.7 | 2.7 | 3.3(-5) | |
| 8.0 | 1.1(-3) | 1.4 | 2.6 | 5.0 | 1.7 | 1.1 | 1.7 | 2.7 | 3.3(-5) | |
| 2.0(-4) | 1.1 | 1.2 | 1.0 | 1.8 | 1.7 | 1.1 | 1.7 | 2.7 | 3.3(-5) | |
| 4.0 | 6.8(-4) | 5.5(-4) | 5.2(-4) | 6.5(-4) | 8.4(-4) | 1.1 | 1.7 | 2.7 | 3.3(-5) | |
| 8.0 | 4.5 | 3.2 | 2.8 | 3.3 | 4.4 | 1.1 | 1.7 | 2.7 | 3.3(-5) | |
| 2.0(-3) | 2.9 | 1.0 | 1.5 | 1.5 | 1.9 | 2.3 | 3.0 | 3.9 | 5.2(-6) | |
| 4.0 | 1.0 | 1.3 | 0.9(-5) | 8.8(-5) | 1.0 | 1.1 | 1.3 | 1.4 | 1.4 | |
| 8.0 | 9.2(-5) | 8.3(-5) | 0.5 | 5.2 | 5.4(-5) | 6.4(-5) | 6.7(-5) | 9.4(-5) | 3.3(-5) | |
| 2.0(-2) | 1.7 | 2.8 | 2.8 | 2.4 | 2.3 | 2.0 | 1.6 | 2.8 | 5.2(-6) | |
| 4.0 | 1.3(-6) | 5.5(-6) | 0.5(-6) | 1.1 | 1.1 | 2.0 | 1.6 | 3.0(-6) | 1.1(-7) | |
| 8.0 | 2.4(-7) | 2.4(-7) | 1.5 | 3.8(-6) | 3.0(-6) | 3.3(-6) | 5.7(-7) | 3.9(-7) | 3.9(-7) | |
| 2.0(-1) | | | 6.0(-9) | 1.7(-7) | 5.4(-7) | 3.1(-7) | 3.9(-7) | 3.9(-7) | 3.9(-7) | |
| 4.0 | | | | 5.0(-9) | 2.4(-8) | 2.8(-8) | 2.8(-8) | 2.8(-8) | 2.8(-8) | |

starting point, we proceeded to work towards the final product, a profile of ion pair production by bremsstrahlung from an incident electron energy spectrum.

The CIRA (1965) reference atmosphere, Fig. D-1, was used to scale atmospheric depth to a representative altitude. The same reference atmosphere was used to compute the atmospheric density (g/cm^3) versus altitude (km). At each altitude the density was multiplied by the energy deposition function $A_{BR}[\text{keV/g cm}^{-2}]$, to yield the stopping ratio, $BR[\text{keV/cm, column}]$, normalized to an incident electron of a given incident energy (T_0). The resulting column stopping ratios, Br (altitude), are listed in Table D-3 and graphically represented in Fig. D-2. Due to the irregularity of the curves and diminishing contribution compared to electron production above 50 km in Fig. D-2, only values below 50 km were considered. For every 5 km of altitude between 15 and 50 km (inclusive), a linear (log-log) interpolation of incident electron energy (T_0) versus column stopping ratio of Bremsstrahlung photons was constructed. For example, at 15 km altitude, $Br = 10^x$ where $x = 1.018342561 \log T_0 (\text{keV}) - 11.85638142$ for initial energies T_0 between 200-500 keV.

A computer program using the linear (log-log) interpolation curves as described above was written to calculate the production of ion pairs versus altitude for an input electron differential energy spectrum isotropic over downward hemisphere at 300 km by solving the equation

$$\text{Prod}_{IP}(\text{alt}) = \frac{1}{4\pi} \iint Br \cdot \text{Dif}(E) \cdot d\Omega dE$$

FIG D-1. CIRA Reference Atmosphere of depth versus altitude (1965).

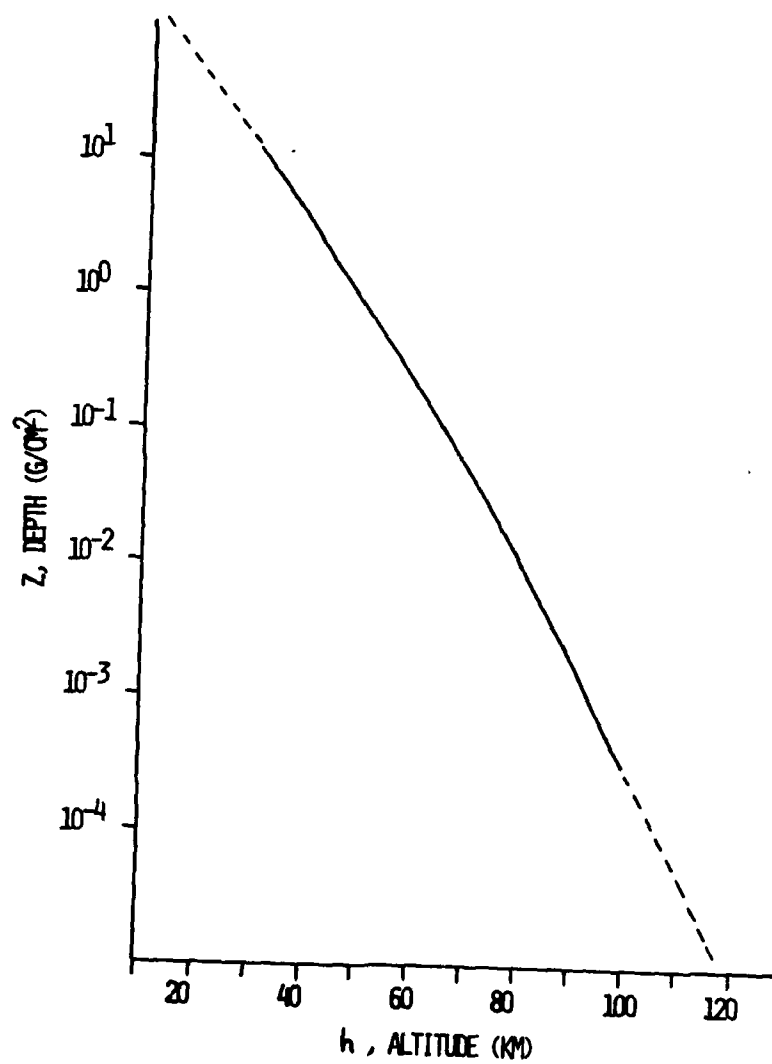


TABLE D-3. B_r (keV/cm, column), stopping ratio, versus altitude for
given incident electron energies.

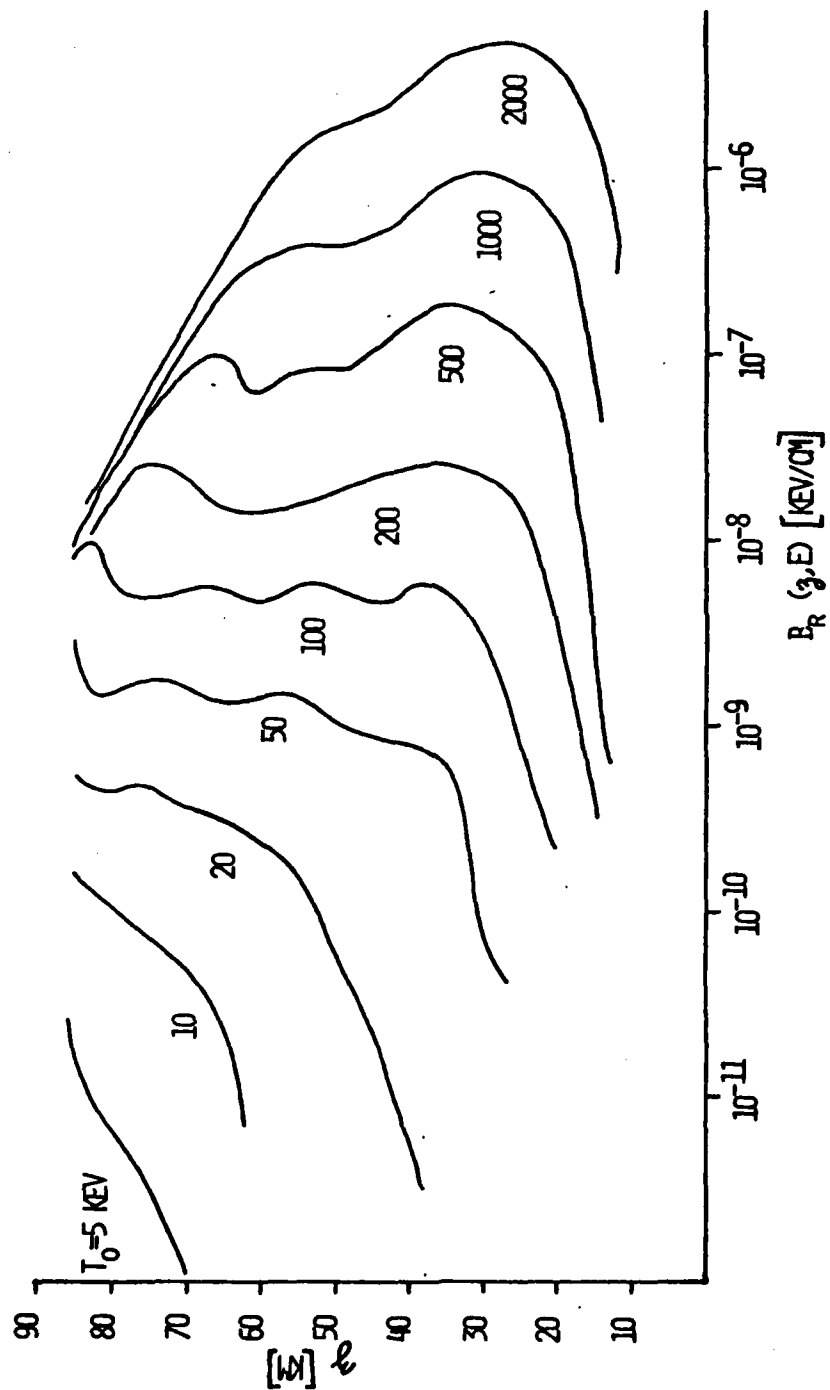
T_0 (KEV)

| | 2500 | 1000 | 500 | 200 | 100 | 50 | 20 | 10 | 5 | Z |
|----|----------|----------|-----------|-----------|-----------|-----------|-----------|-----------|-----------|-----------|
| 86 | 8.9 (-9) | 6.3 (-9) | 6.9 (-9) | 6.3 (-9) | 6.9 (-9) | 2.3 (-9) | 4.8 (-10) | 1.2 (-10) | 2.3 (-11) | 1.1 (-13) |
| 82 | 1.9 (-8) | 1.4 (-8) | 1.5 (-8) | 1.4 (-8) | 1.0 (-8) | 1.4 (-9) | 4.3 (-10) | 1.1 (-10) | 8.9 (-12) | 1.3 (-14) |
| 77 | 4.2 (-8) | 3.0 (-8) | 3.1 (-8) | 2.5 (-8) | 4.3 (-9) | 1.4 (-9) | 4.0 (-10) | 6.8 (-10) | 4.1 (-12) | |
| 72 | 1.2 (-7) | 8.1 (-8) | 7.8 (-8) | 2.2 (-8) | 5.2 (-9) | 1.8 (-9) | 3.7 (-10) | 5.8 (-10) | 1.6 (-12) | |
| 67 | 2.5 (-7) | 1.8 (-7) | 1.0 (-7) | 1.6 (-8) | 5.5 (-9) | 1.4 (-9) | 3.3 (-10) | 3.5 (-10) | 6.9 (-10) | |
| 62 | 5.4 (-7) | 2.9 (-7) | 6.3 (-8) | 1.6 (-8) | 4.6 (-9) | 1.3 (-9) | 2.8 (-10) | 7.3 (-12) | | |
| 56 | 1.1 (-6) | 2.8 (-7) | 7.2 (-8) | 1.6 (-8) | 5.2 (-9) | 1.4 (-9) | 1.5 (-10) | 2.0 (-12) | | |
| 50 | 1.4 (-6) | 2.3 (-7) | 7.8 (-8) | 1.8 (-8) | 5.6 (-9) | 1.0 (-9) | 6.9 (-10) | 4.1 (-13) | | |
| 45 | 1.8 (-6) | 3.9 (-7) | 1.0 (-7) | 2.1 (-8) | 4.7 (-9) | 8.5 (-10) | 2.3 (-11) | | | |
| 39 | 3.2 (-6) | 7.1 (-7) | 1.8 (-7) | 2.6 (-8) | 6.0 (-9) | 7.1 (-10) | 3.2 (-12) | | | |
| 33 | 1.4 (-6) | 9.5 (-7) | 1.6 (-7) | 2.5 (-8) | 4.5 (-9) | 1.8 (-10) | | | | |
| 27 | 5.2 (-6) | 7.9 (-7) | 1.3 (-7) | 2.1 (-8) | 1.5 (-9) | 4.0 (-11) | | | | |
| 20 | 3.2 (-6) | 5.8 (-7) | 7.1 (-8) | 3.2 (-9) | 2.3 (-10) | | | | | |
| 14 | 6.2 (-7) | 6.2 (-8) | 7.7 (-10) | 3.0 (-10) | | | | | | |

B_r (KEV/CM, COLUMN)

(M) 4

FIG D-2. $B_r(z,E)$ versus altitude.



where EMI = average minimum ionizing energy taken here to be 35 eV.

Dif (E) = differential electron flux at 300 km

[#/cm² sec str keV]

dΩ = solid angle ≈ 2π here

dE = 1 keV intervals

Prod (alt) = ion pair production rate at each altitude

[#/cm³ sec]

Also output is the total energy (keV) deposited at each altitude per (cm³ str sec). The computer listing follows:

TABLE D-4. Bremsstrahlung deposition computer listing.

```

C *****
C THIS PROGRAM CALCULATES THE ALTITUDE VS ENERGY DEPOSITION PROFILE FOR A
C GIVEN PRECIPITATING ELECTRON SPECTRUM. THE ENERGY DEPOSITION FUNCTION,
C BR, IS OBTAINED FROM THE BERGER, SELTZER, AND MAEDA (JATP, 1973, 36, 591)
C FULL-SCALE CALCULATIONS FOR UNIFORM, WIDE AREA PRECIPITATION OF AN
C ELECTRON FLUX ISOTROPIC OVER THE DOWNWARD HEMISPHERE. ATMO DEPTH VS ALT
C IS OBTAINED FROM CIRAS 1965 (MEAN STRUCTURE).
C *****
C DIMENSION E(2000), DIF(2000)
C *****
C INPUT - NUMBER OF DATA SETS
C
C READ (5,2) NDATA
C 2 FORMAT (I2)
C
C INPUT - DIFFERENTIAL ELECTRON FLUX (#/LL TSE) 10, 20, 50, 100, 200, 500.
C 100, 2000 KEV RESPECTIVELY.
C
C 1 READ (5,10) DIF(1), DIF(11), DIF(41), DIF( 91), DIF(191), DIF(491)
C 10 FORMAT (8E10.5)
C
C ENERGY, E, FROM 10 TO 2000 KEV
C
C DO 1 J=1,1991
C 11 E(J)= 10.* (J-1)
C
C DIFFERENTIAL FLUX SPECTRUM IS GENERATED BY LINEAR FIT (ON LOG-LOG PLOT)
C BETWEEN INPUT VALUES FROM ABOVE.
C
C 00 30 I=1,1991
C IF (I.GT.931.AND.I.LT.1981) GO TO 61
C IF (I.GT.491.AND.I.LT. 991) GO TO 59
C IF (I.GT.191.AND.I.LT. 491) GO TO 57
C IF (I.GT. 91.AND.I.LT. 191) GO TO 55
C IF (I.GT. 41.AND.I.LT.  91) GO TO 53
C IF (I.GT. 11.AND.I.LT.  41) GO TO 51
C IF (I.GT.  1.AND.I.LT.  11) GO TO 47
C GO TO 50
C
C 47 IF (I.EQ.11.NE.DIF(11)) GO TO 48
C DIF(1)=DIF(11)
C GO TO 50
C
C 48 YARG=ALOG10((DIF(11))/DIF(1))
C YARG=ALOG10(E)/DIF(11)
C Y=ALOG10(DIF(1))
C X=ALOG10(E(1))
C GO TO 99
C
C 91 IF (DIF(11).NE.DIF(41)) GO TO 89
C DIF(1)=DIF(11)
C GO TO 50
C
C 89 YARG=ALOG10((DIF(41))/DIF(11))
C YARG=ALOG10(E)/DIF(11)

```

```

V=ALC310(DIP(1))
X=ALC313(E(1))
GO TO 99
53 IF (DIP(41)-NE-DIP(91)) GO TO 54
DIP(1)=DIP(41)
GO TO 50
54 VARG=ALOG13((DIP(91))/(DIP(41)))
VARG=ALOG13((E(91))/(E(41)))
V=ALC310(DIP(41))
X=ALC310(E(41))
GO TO 99
55 IF (DIP(91)-NE-DIP(191)) GO TO 56
DIP(1)=DIP(91)
GO TO 50
56 VARG=ALOG13((DIP(191))/(DIP(91)))
VARG=ALOG13((E(191))/(E(91)))
V=ALOG13(DIP(41))
X=ALC310(E(91))
GO TO 95
57 IF (DIP(191)-NE-DIP(491)) GO TO 58
DIP(1)=DIP(191)
GO TO 50
58 VARG=ALOG13((DIP(491))/(DIP(191)))
VARG=ALOG13((E(491))/(E(191)))
V=ALOG13(DIP(191))
X=ALOG13(E(191))
GO TO 99
59 IF (DIP(491)-NE-DIP(991)) GO TO 60
DIP(1)=DIP(491)
GO TO 50
60 VARG=ALOG13((DIP(991))/(DIP(491)))
VARG=ALOG13((E(991))/(E(491)))
V=ALOG13(DIP(491))
X=ALC313(E(491))
GO TO 59
61 IF (DIP(1991)-NE-DIP(991)) GO TO 62
DIP(1)=DIP(991)
GO TO 50
62 VARG=ALOG13((DIP(1991))/(DIP(991)))
VARG=ALOG13((E(1991))/(E(991)))
V=ALC313(DIP(991))
X=ALC310(E(991))
GO TO 59
63 VARG=ALOG13((VARG/XARG)*((Z-X)+Y))
DIP(1)=10+((VARG/XARG)*((Z-X)+Y))
GO CONTINUE
PERFORM INTEGRAL OF BR-DIP*DE AT EACH 5 KM ALTITUDE FROM 15 TO 99 KM.
WRITE(6,13)
13 FORM=ALC31ML10-XVAL31ZD95-DE-CHLAIN-12L-AMR00-1-12L-AMKAL-0L-0H
12(ALLST).0X.AN(1/ALLT)
100 IF (Z-50.15) GO TO 200
100 IF (Z-50.25) GO TO 200
100 IF (Z-50.35) GO TO 200

```

```

10 IF (2.50.25.) GO TO 205
11 IF (2.50.30.) GO TO 185
12 IF (2.50.35.) GO TO 165
13 IF (2.50.40.) GO TO 145
14 IF (2.50.45.) GO TO 125
15 TOTAL=0.0
16 DO 73 1=1,1991
17 IF (1.57.91.) GO TO 110
18 X=2.736669403-ALOG10(E(1))-13.72349432
19 GO TO 120
20 IF (1.57.491.) GO TO 115
21 Y=1.534787611-ALOG10(E(1))-11.51973073
22 GO TO 120
23 X=2.332366123-ALOG10(E(1))-13.74010285
24 Y=1.534787611-ALOG10(E(1))-11.51973073
25 BR=10.0
26 XRAY=)IF(1)BR
27 TOTAL=TOTAL+XRAY
28 CONTINUE
29 GO TO 900
30 TOTAL=0.0
31 DO 71 1=1,1991
32 IF (1.57.41.) GO TO 130
33 Y=1.923061797-ALOG10(E(1))-15.73033845
34 GO TO 140
35 IF (1.57.191.) GO TO 135
36 X=2.323664191-ALOG10(E(1))-13.02100080
37 GO TO 140
38 Y=1.93720917-ALOG10(E(1))-12.1317653
39 BR=1.0
40 XRAY=)IF(1)BR
41 TOTAL=TOTAL+XRAY
42 CONTINUE
43 GO TO 900
44 TOTAL=0.0
45 DO 72 1=1,1991
46 IF (1.57.41.) GO TO 180
47 Y=3.331193138-ALOG10(E(1))-18.13209481
48 GO TO 140
49 IF (1.57.91.) GO TO 155
50 Y=2.927532307-ALOG10(E(1))-14.0663287
51 GO TO 160
52 X=2.72102793-ALOG10(E(1))-13.38446827
53 BR=10.0
54 XRAY=)IF(1)BR
55 TOTAL=TOTAL+XRAY
56 CONTINUE
57 GO TO 900
58 TOTAL=0.0
59 DO 73 1=1,1991
60 IF (1.57.91.) GO TO 170
61 Y=3.886467478-ALOG10(E(1))-16.08185425
62 GO TO 180
63 IF (1.57.131.) GO TO 175
64 X=2.474723312-ALOG10(E(1))-13.06232314

```

```

GO TO 180
178 X=2.12663A192*ALOG10(E(I))-12.64791195
180 RM=10
XRAY=JIF(I)*BR
TOTAL=TOTAL+XRAY
73 CONTINUE
GO TO 900
185 TOTAL=0.0
DO 74 I=41,1991
IR(I,GT,91.) GO TO 187
X=9.787270076*ALOG10(E(I))-18.09799954
GO TO 200
187 IF (I,GT,191.) GO TO 190
X=2.86045826*ALOG10(E(I))-14.44437471
GO TO 200
190 IF (I,GT,491.) GO TO 195
X=2.09316926*ALOG10(E(I))-12.25577687
GO TO 200
195 X=2.510322759*ALOG10(E(I))-13.60796849
200 RM=10
XRAY=JIF(I)*BR
TOTAL=TOTAL+XRAY
74 CONTINUE
GO TO 900
205 TOTAL=0.0
DO 75 I=91,1991
IF (I,GT,191.) GO TO 210
X=3.915280347*ALOG10(E(I))-16.57187825
GO TO 220
210 IF (I,GT,491.) GO TO 215
X=2.110124616*ALOG10(E(I))-12.64594502
GO TO 220
215 X=2.683161107*ALOG10(E(I))-14.19255332
220 RM=10
XRAY=JIF(I)*BR
TOTAL=TOTAL+XRAY
75 CONTINUE
GO TO 900
225 TOTAL=0.0
DO 76 I=91,1991
IF (I,GT,491.) GO TO 230
X=3.35923342*ALOG10(E(I))-16.78530729
GO TO 235
230 X=2.75125017*ALOG10(E(I))-14.8773528
235 RM=10
XRAY=JIF(I)*BR
TOTAL=TOTAL+XRAY
76 CONTINUE
GO TO 900
240 TOTAL=0.0
DO 77 I=91,1991
IF (I,GT,491.) GO TO 245
X=1.018342361*ALOG10(E(I))-11.88638142
GO TO 255

```


OUT PUT EXAMPLE

| ALTITUDE
(KM) | FLU ¹
(E/LLST) | PROD
(1/LLT) |
|------------------|------------------------------|-----------------|
| 50.0 | .628105E-01 | 11.28 |
| 48.0 | .463832E-01 | 8.33 |
| 40.0 | .412F86E-01 | 7.41 |
| 35.0 | .179902E-01 | 3.23 |
| 30.0 | .85377E-02 | 1.53 |
| 26.0 | .014803E-01 | 0.16 |
| 20.0 | .170397E-03 | 0.03 |
| 15.0 | .443316E-06 | 0.00 |

Bibliography

- Aikin, A. C. and S. J. Bauer, The Ionosphere, in Introduction to Space Science, edited by W. N. Hess, p. 161, Gordon and Breach, N. Y., 1965.
- Anderson, R. R. and K. Maeda, Explorer 45 plasma measurements, J. Geophys. Res., 82, 135, 1977.
- Ansari, Z. A., A peculiar type of daytime absorption in the auroral zone, J. Geophys. Res., 70, 3117, 1965.
- Ashour-Abdalla, M. and R. M. Thorne, The importance of electrostatic ion-cyclotron instability for quiet-time proton auroral precipitation, Geophys. Res. Ltrs., 4, 1977.
- Ashour-Abdalla, M. and C. F. Kennel, Nonconvective electron cyclotron harmonic instabilities, J. Geophys. Res., 83, 1531, 1978.
- Ashour-Abdalla, M. and R. M. Thorne, Toward a unified view of diffuse auroral precipitation, 83, 4755, 1978.
- Bailey, D. K. and M. A. Pomerantz, Relativistic electron precipitation into the mesosphere at subauroral latitudes, J. Geophys. Res., 70, 5823, 1965.
- Bailey, D. K., M. A. Pomerantz, K. W. Sullivan and C. C. Taieb, Characteristics of precipitated electrons inferred from ionospheric forward scatter, J. Geophys. Res., 71, 5179, 1966.
- Bailey, D. K., Some quantitative aspects of electron precipitation in and near the auroral zone, Rev. Geophys., 6, 289, 1968.

- Bailey, D. K., R. R. Brown and M. H. Rees, Simultaneous forward-scatter, riometer, and Bremsstrahlung observations of a daytime electron precipitation event in the auroral zone, J. Atmos. Terr. Phys., 32, 149, 1970.
- Barcus, J. R. and T. J. Rosenberg, Energy spectrum for auroral-zone X-rays, I, Diurnal and type effects, J. Geophys. Res., 71, 803, 1966.
- Berger, M. J., S. M. Seltzer and K. Maeda, Energy deposition by auroral electrons in the atmosphere, J. Atmos. Terr. Phys., 32, 1015, 1970.
- Berger, M. J. and S. M. Seltzer, Bremsstrahlung in the atmosphere, J. Atmos. Terr. Phys., 34, 85, 1972.
- Berger, M. J., S. M. Seltzer and K. Maeda, Some new results on electron transport in the atmosphere, J. Atmos. Terr. Phys., 36, 591, 1974.
- Bewersdorff, A., G. Kremser, J. Stadsnes, H. Trefall and S. Ullaland, Simultaneous balloon measurements of auroral X-rays during slowly varying ionospheric absorption events, J. Atmos. Terr. Phys., 30, 591, 1968.
- Blake, D. and R. S. Lindzen, Effect of photochemical models on calculated equilibria and cooling rates in the stratosphere, Mon. Wea. Rev., 10, 783, 1973.
- Bossen, M., R. L. McPherron and C. T. Russell, A statistical study of PC 1 magnetic pulsations at synchronous orbit, J. Geophys. Res., 81, 6083, 1976.

- Brown, R. R., A study of slowly varying and pulsating ionospheric absorption events in the auroral zone, J. Geophys. Res., 69, 2315, 1964.
- Brown, J. W. and E. C. Stone, High energy electron spikes at high latitudes, J. Geophys. Res., 77, 3384, 1972.
- Burton, R. K. and R. E. Holzer, The origin and propagation of chorus in the outer magnetosphere, J. Geophys. Res., 79, 1014, 1974.
- Chapman, S. A., A theory of upper atmospheric ozone, Quart. J. Roy. Met. Soc., 3, 103,
- Chappell, C. R., K. K. Harris and C. W. Sharp, The morphology of the bulge of the plasmasphere, J. Geophys. Res., 75, 3848, 1970.
- Chappell, C. R., Detached plasma regions in the magnetosphere, J. Geophys. Res., 79, 1861, 1974.
- Cornwall, J. M., Scattering of energetic trapped electrons by very low-frequency waves, J. Geophys. Res., 69, 1251, 1964.
- Cornwall, J. M., Cyclotron instabilities and electromagnetic emission in the ultralow frequency and very low frequency ranges, J. Geophys. Res., 70, 61, 1965.
- Cornwall, J. M., F. V. Coroniti and R. M. Thorne, Turbulent loss of ring current protons, J. Geophys. Res., 75, 4699, 1970.
- Coroniti, F. V., R. W. Fredericks and R. White, Instability of ring current protons beyond the plasmopause during injection events, J. Geophys. Res., 77, 6243, 1972.
- Crutzen, P. J. and C. J. Howard, The effect of the $\text{HO}_2 + \text{NO}$ reaction rate constant on one-dimensional model calculations of stratospheric ozone perturbations, Pure and Applied Geophys., 116, 497, 1978.

- Crutzen, P. J., Private communication, 1980.
- Davis, D. D., J. T. Herron and R. E. Huie, Absolute rate constants for reaction $O(^3P) + NO_2 \rightarrow NO + O_2$ over the temperature range $230^0 - 339^0K$, J. Chem. Phys., 58, 530, 1973.
- DeForest, S. E. and C. E. McIlwain, Plasma clouds in the magnetosphere, J. Geophys. Res., 76, 3587, 1971.
- DeVore, J. G., Photochemical damping and mesospheric circulation, Master's Degree Thesis, Department of Atmospheric Sciences, UCLA 1977.
- Dunckel, N. and R. A. Helliwell, Whistler-mode emissions on the OGO-1 satellite, J. Geophys. Res., 74, 6371, 1969.
- Dungey, J. W., Loss of Van Allen electrons due to whistlers, Planet. Space Sci., 11, 591, 1963.
- Frank, L. A., A survey of electrons $E > 40$ keV beyond 5 earth radii with Explorer 14, J. Geophys. Res., 70, 1593, 1965.
- Fredericks, R. W. and F. L. Scarf, Recent studies of the magnetospheric electric field emissions about the electron gyrofrequency, J. Geophys. Res., 78, 310, 1973.
- Gunton, R. C., R. E. Meyeroff and J. B. Reagan, Ion and neutral chemistry of the D-region during intense solar particle events of August 1972, Lockheed Report D556351, 1977.
- Gurnett, D. A., G. W. Pfeiffer, R. A. Anderson, S. R. Mosier and D. P. Cauffman, Initial observations of VLF electric and magnetic fields with the Injun 5 satellite, J. Geophys. Res., 74, 4631, 1969.

- Gurnett, D. A. and L. A. Frank, A region of intense plasma wave turbulence on auroral field lines, J. Geophys. Res., 82, 1031, 1977.
- Heaps, M. G., The effect of a solar proton event on the minor neutral constituents of the summer polar mesosphere, U.S. Army Atmospheric Sci. Laboratory Report ASL-TR-0012, 1978.
- Hones, E. W. Jr., S. Singer, L. J. Lanzerotti, J. D. Pierson and T. J. Rosenberg, Magnetospheric substorm of August 25-26, 1967, J. Geophys. Res., 76, 2977, -971.
- Herron, J. T. and R. E. Huie, The reaction between NO and O, Chemical Kinetics Data Survey, N.B.S. Report 19828, National Bureau of Standards, U.S. Dept. of Commerce, Gaithersburg, Md., 108, 1972.
- Imhoff, W. L., E. E. Gaines and J. B. Reagan, Dynamic variations in intensity and energy spectra of electrons in the inner radiation belt, J. Geophys. Res., 78, 4568, 1973.
- Imhoff, W. L., G. H. Nakano, R. G. Johnson and J. B. Reagan, Satellite observations of Bremsstrahlung from widespread energetic electron precipitation events, J. Geophys. Res., 79, 565, 1974.
- Imhoff, W. L., G. L. Nakano, E. E. Gaines and J. B. Reagan, A coordinated two-satellite study of energetic electron precipitation events, J. Geophys. Res., 80, 1975.
- Imhoff, W. L., G. H. Nakano and J. B. Reagan, Satellite observations of impulsive Bremsstrahlung X-ray events associated with substorms, J. Geophys. Res., 83, 4237, 1978.
- Jelly, D. and N. Brice, Changes in Van Allen radiation associated with polar substorms, J. Geophys. Res., 72, 5919, 1967.

- Johannesen, A. and D. Krankowski, Positive-ion composition measurement in the upper mesosphere and lower thermosphere at high latitude during summer, *J. Geophys. Res.*, 77, 2888, 1972.
- Kaye, S. M., M. G. Kivelson and D. J. Southwood, Evolution of ion cyclotron instability in the plasma convection system of the magnetosphere, *J. Geophys. Res.*, 84, 6397, 1979.
- Kennel, C. F. and N. E. Petschek, Limit on stably trapped particle flux, *J. Geophys. Res.*, 71, 1, 1966.
- Kennel, C. F. and R. M. Thorne, Unstable growth of unducted whistlers propagating at an angle to the geomagnetic field, *J. Geophys. Res.*, 72, 871, 1967.
- Kennel, C. F., Consequences of a magnetospheric plasma, *Rev. Geophys.*, 7, 379, 1969.
- Kennel, C. F., F. L. Scarf, R. W. Fredericks, J. H. McGehee and F. V. Coroniti, VLF electric field observations in the magnetosphere, *J. Geophys. Res.*, 75, 6136, 1970.
- Kindel, J. M. and C. F. Kennel, Topside current instabilities, *J. Geophys. Res.*, 76, 3055, 1971.
- Kintner, P. M., M. C. Kelley and F. S. Mozer, Electrostatic hydrogen cyclotron waves near the one earth radius altitude in the polar magnetosphere, *Geophys. Res. Ltrs.*, 5, 139, 1978.
- Kintner, P. M., M. C. Kelley, R. D. Sharp, A. G. Ghielmini, M. Temerin, C. Cattell, P. F. Mizera and J. F. Fennell, Simultaneous observations of energetic (keV) upstreaming and electrostatic hydrogen cyclotron waves, *J. Geophys. Res.*, 84, 7201, 1979.

- Kivelson, M. G., C. T. Russell, K. W. Chan and C. R. Chappell, An investigation of regions of high density cold plasma in the outer magnetosphere (Abstract), EOS Trans AGU, 53, 1103, 1972.
- Koons, H. C., A. L. Vampola and D. A. McPherson, Strong pitch-angle scattering of energetic electrons in the presence of electrostatic waves above the ionospheric trough region, J. Geophys. Res., 77, 1771, 1972.
- Kurth, W. W., M. M. Baumbach and D. A. Gurnett, Direction-finding measurements of auroral kilometric radiation, J. Geophys. Res., 80, 2764, 1975.
- Larsen, T. R., Disturbances in the high latitude lower ionosphere, REP 62, Norwegian Def. Res. Estab., Kjeller, Norway, 1973.
- Larsen, T. R. and G. R. Thomas, Energy spectra measured during a relativistic electron precipitation event on 2 Feb 1969, J. Atmos. Terr. Phys., 36, 1613, 1974.
- Larsen, T. R., J. B. Reagan, W. L. Imhoff, L. E. Montbriand and J. S. Belrose, A coordinated study of energetic electron precipitation and D-region electron concentrations over Ottawa during disturbed conditions, J. Geophys. Res., 81, 2200, 1976.
- Lerfold, G. M. and C. G. Little, D-region electron density profiles during auroras, J. Geophys. Res., 69, 2857, 1964.
- Lincoln, V. and I. Brophy, World Data Center A for solar-terrestrial physics, NOAA, Private communication, December 1978.
- Lindalen, H. R., F. S  raas, K. Aarsnes and R. Amundsen, Variations in the high latitude proton trapping boundary associated with polar magnetic substorms, Planet. Space Sci., 19, 1041, 1971.

- Lui, A. T. Y., D. Venkatesan, C. D. Anger, S.-I. Akasofu, W. J. Heikkila, J. D. Winningham and J. R. Burrows, Simultaneous observations of particle precipitation and auroral emissions by the ISIS 2 satellite in the 19-24 MLT sector, J. Geophys. Res., 82, 2210, 1977.
- Lukkari, L., J. Kangas and R. R. Heacock, Simultaneous observations of evening magnetic pulsations and morning electron precipitation events in the auroral zone during the substorm, J. Atmos. Terr. Phys., 37, 1305, 1975.
- Lukkari, L. and J. Kangas, Simultaneous ULF-wave and strong riometer absorption events at the plasmopause latitude in the afternoon sector, J. Atmos. Terr. Phys., 38, 1187, 1976.
- Lukkari, L., J. Kangas and H. Ranta, Correlated electron precipitation and magnetic IPDP events near the plasmopause, J. Geophys. Res., 82, 4750, 1977.
- Matthews, D. L. and D. J. Simons, Observation of relativistic electron precipitation at $L = 6$, J. Geophys. Res., 78, 7539, 1973.
- Matthews, D. L., M. Pongratz and K. Papadopoulos, Nonlinear production of suprathermal tails in auroral electrons, J. Geophys. Res., 81, 123, 1976.
- McPherron, R. L., G. K. Parks, F. V. Coroniti and S. H. Ward, Studies of the magnetosphere substorms, 2, correlated magnetic micropulsations and electron precipitation occurring during auroral substorms, J. Geophys. Res., 73, 1697, 1968.

- McPherson, D. A. and H. C. Koons, Dependence of the occurrence of ELF emissions on the location of the plasmopause, J. Geophys. Res., 75, 5559, 1970.
- Mizera, P. F., Observations of precipitating protons with ring current energies, J. Geophys. Res., 79, 581, 1974.
- Morfill, G., M. Scholer and D. Hovestadt, Analysis of processes leading to localized electron enhancements in the outer radiation belt, Planet. Space Sci., 23, 1495, 1975.
- Mozer, F. S., C. W. Carlson, M. K. Hudson, R. B. Torbert, B. Parody, J. Yatteau and M. C. Kelley, Observations of paired electrostatic shocks in the polar magnetosphere, Phys. Rev. Ltrs., 38, 292, 1977.
- Parks, G. K., C. Gurgiolo and R. West, Relativistic electron precipitation, Geophys. Res. Ltrs., 6, 393, 1979.
- Potemra, T. A. and A. J. Zmuda, Precipitating energetic electrons as an ionization source in the midlatitude nighttime D-region, J. Geophys. Res., 75, 7161, 1970.
- Reagan, J. B., Ionization processes, Dynamical and Chemical Coupling, B. Grandal and J. A. Holtet (eds), Spatind, Norway, 1977.
- Reagan, J. B., R. C. Gunton, J. E. Evans, R. W. Nightingale, R. G. Johnson, W. L. Imhoff and R. E. Meyerott, Effects of the August 1972 solar particle events on stratospheric ozone, Lockheed Report D 630455,
- Rees, M. H., Auroral ionization and excitation by incident energetic electrons, Planet. Space Sci., 11, 1209, 1963.

- Rosenberg, T. J., L. J. Lanzerotti, D. K. Bailey and J. D. Pierson,
Energy spectra in relativistic electron precipitation events,
J. Atmos. Terr. Phys., 34, 1977, 1972.
- Rowe, J. N., A. P. Mitra, A. J. Ferraro and H. S. Lee, An experimental
and theoretical study of the D-region-II. A semi-empirical model
for mid latitude D-region, J. Atmos. Terr. Phys., 36, 755, 1974.
- Scarf, F. L., R. W. Fredericks, C. F. Kennel and F. V. Coroniti,
Satellite studies of magnetospheric substorms on August 5, 1968,
OGO plasma wave observations, J. Geophys. Res., 78, 3119, 1973.
- Shaw, R. R. and D. A. Gurnett, Electrostatic noise bands associated
with the electron gyrofrequency and plasma frequency in the
outer magnetosphere, J. Geophys. Res., 80, 4259, 1975.
- Southwood, D. J., Plasma waves in the magnetosphere, Nature, 271, 309,
1978.
- Spjeldvik, W. N., Application of the Fokker-Planck numerical method
to describe anisotropic and energy dependent electron precipi-
tation into the atmosphere, Plasma Physics Group Tech. Report,
PPG-198, UCLA, 1974.
- Spjeldvik, W. N. and R. M. Thorne, The cause of storm after effects
in the middle latitude D-region, J. Atmos. Terr. Phys., 37,
777, 1975a.
- Spjeldvik, W. N. and R. M. Thorne, A simplified D-region model and its
application to magnetic storm after effects, J. Atmos. Terr.
Phys., 37, 1313, 1975b.

- Stix, T. H., The Theory of Plasma Waves, McGraw-Hill Book Co., New York, 1962.
- Sullivan, K. W., Institute for Telecommunications Sciences and Aeronomy (Formerly), Boulder, Colorado, Private Communication, January 1979.
- Thorne, R. M. and C. F. Kennel, Quasi-trapped VLF propagation in the outer magnetosphere, J. Geophys. Res., 72, 857, 1967.
- Thorne, R. M. and C. F. Kennel, Relativistic electron precipitation during magnetic storm main phase, J. Geophys. Res., 76, 1971.
- Thorne, R. M., A possible cause of dayside relativistic electron precipitation events, J. Atmos. Terr. Phys., 36, 635, 1974.
- Thorne, R. M., Ionosphere-magnetosphere coupling, 3. A review of the role of wave-particle interactions, Rev. Geophys. Space Phys., 13, 878, 1975.
- Thorne, R. M. and T. R. Larsen, An investigation of relativistic electron precipitation events and their association with magnetospheric substorm activity, J. Geophys. Res., 81, 5501, 1976.
- Thorne, R. M., Energetic radiation belt electron precipitation: A natural depletion mechanism for stratospheric ozone, Science, 195, 287, 1977a.
- Thorne, R. M., Influence of relativistic electron precipitation on the lower ionosphere and stratosphere, Dynamical and Chemical Coupling, B. Grandel and J. A. Holtet (eds.) Spatind, Norway, 1977b.

- Thorne, R. M., The importance of energetic particle precipitation on the chemical composition of the middle atmosphere, Middle Atmosphere Symposium, Australia, 1979.
- Tsurutani, B. J. and E. J. Smith, Postmidnight chorus: A substorm phenomenon, J. Geophys. Res., 79, 118, 1974.
- Tsurutani, B. T. and E. J. Smith, Two types of magnetospheric ELF chorus and their substorm dependences, J. Geophys. Res., 82, 5112, 1977.
- Vampola, A. L., Energetic electrons at latitudes above the outer-zone cutoff, J. Geophys. Res., 74, 1254, 1969.
- Vampola, A. L., Access of solar electrons to closed field lines, J. Geophys. Res., 76, 36, 1971a.
- Vampola, A. L., Electron pitch angle scattering in the outer zone during magnetically disturbed times, J. Geophys. Res., 76, 4685, 1971b.
- Vampola, A. L., H. C. Koons and D. A. McPherson, Outer-zone electron precipitation, J. Geophys. Res., 76, 7609, 1971.
- Vampola, A. L., The effect of strong pitch angle scattering on the location of the outer zone electron boundary as observed by low altitude satellites, J. Geophys. Res., 82, 2289, 1977.
- Vij, K. K., D. Venkatesan, W. R. Sheldon, J. W. Kern, J. R. Benbrook and B. A. Whalen, Simultaneous investigations of parent electrons and Bremsstrahlung X-rays by rocket-borne detectors, J. Geophys. Res., 80, 2869, 1975.

- Walt, M., W. M. MacDonald and W. E. Frances, Penetration of auroral electrons into the atmosphere, Physics of the Magnetosphere, McCormac, 534, 1968.
- Webber, W., The production of free electrons in the ionospheric D-layer by solar and galactic cosmic rays and the resultant absorption of radio waves, J. Geophys. Res., 67, 5091, 1962.
- Williams, D. J. and L. R. Lyons, The proton ring current and its interaction with the plasmopause: Storm recovery phase, J. Geophys. Res., 79, 1974.
- World Data Center A, Upper Atmos. Geophys. Rep., 31, Boulder, Colorado, 1974.